# Experimental Investigation and Numerical Modelling of Under Cover Ice Transport and Hanging Dam Formation Processes

by

**Waruni Randula Senarathbandara**

A thesis submitted to the Faculty of Graduate Studies of
the University of Manitoba
in partial fulfillment of the requirements for the degree of

## Doctor of Philosophy

Department of Civil Engineering
University of Manitoba

Winnipeg, Manitoba, Canada

*To my parents, my brother and my husband……*

## Publications associated with this research

### Peer Reviewed Publications

Senarathbandara R., Clark S.P., Dow K. (2024). Under Cover Ice Transport Processes under Equilibrium and Non-equilibrium Conditions. Cold Regions Science & Technology. Volume 219, 104124.

Senarathbandara, R., Clark, S.P., Dow, K. (2023). Experimental Analysis on Hanging Dam Formation and Evolution. Water, 15 (24), 4242.

### Conference Proceedings

Senarathbandara R., Clark S.P., Dow K. (2023). Investigating the Effect of Incoming Ice Supply Rate on Hanging Dam Formation. 22nd Workshop on Hydraulics of Ice Covered Rivers, Canmore, Alberta, Canada.

Senarathbandara R., Clark S.P., Dow K., Lees K. (2022). Numerical Simulation of Under Cover Ice Transport Processes and Hanging Dam Formation. 26th IAHR International Symposium on Ice. Montreal, Quebec, Canada.

Senarathbandara, R., Clark, S.P., Dow, K. (2021). Laboratory Investigation on Under Cover Ice Transport Processes. 21st CRIPE Workshop on the Hydraulics of Ice Covered Rivers. Saskatoon, Saskatchewan, Canada.

## Abstract

Under cover ice transport and hanging dam formation are river ice processes that have a significant impact on hydraulics of an ice covered river during the winter. A thick ice accumulation from a hanging dam can cause the water level to rise imposing flooding to nearby communities, and hydropower generation during the winter is often negatively impacted by hanging dams. Under cover ice transport and hanging dam formation processes are not yet well understood due to difficulties associated with obtaining field data and lack of numerical modelling efforts. This research investigates under cover ice transport and hanging dam formation processes using laboratory experiments and numerical modelling. Under cover ice transport laboratory experiments were conducted to further develop a cover load transport formula describing the relationship between dimensionless transport rate and dimensionless flow strength under equilibrium conditions and this formula is known to be the only cover load formula that is developed exclusively using simulated ice that has similar physical properties to ice in a natural river. The effect of approach Froude number in the river and the incoming ice supply rate on hanging dam formation was analyzed using a series of experiments in a scaled down physical model. This is the first study of its kind that presents the relationship between the approach Froude number and the incoming ice supply rate on hanging dam formation and evolution, contributing to improving our understanding of these processes. The current model formulation for under cover transport processes and hanging dam formation in the CRISSP2D numerical model was evaluated and the laboratory developed cover load transport formula was incorporated in the model to improve the model in this application.

## Acknowledgements

As I have reached the end of this challenging yet rewarding journey of completing my Ph.D., I would like to extend my heartfelt gratitude to everyone who supported me throughout these years. I would like to sincerely thank my advisor Dr. Shawn Clark and my co-advisor Dr. Karen Dow for their guidance and mentorship throughout this journey. Your support was a pillar of strength during the years I spent at the university. Thank you for inspiring me to be better in both professional and personal aspects.

I would also like to thank my committee members Dr. Mark Tachie and Dr. Jarrod Malenchak for their valuable feedback and comments at all stages of the research that helped me to improve the quality of my thesis.

My sincere thanks go to Alexandar Wall for his technical support that enabled me to successfully complete the laboratory experiments presented in this thesis.

I would like to acknowledge the generous funding provided by Manitoba Hydro and the Natural Sciences and Engineering Research Council of Canada which made this research possible.

To my friends at the university, Kevin Lees, Mina Rouzegar, Brittany Peters, Su Jin Kim and all the other wonderful people that I had the chance to work with during my years at HRTF, thank you for the cherished memories.

Dilini, I am grateful that you embarked on this journey with me and for being by my side on good and bad days. Dilini and Theja, thank you for taking care of me during difficult times, for being wonderful companions for the past few years. I wouldn't be able to do this without you.

My heartfelt gratitude goes to Dr. Udaya Annakkage and Dr. Dilruskhi Annakkage for being my family in Winnipeg. Thank you Akbo and Gayamini (my brother and sister in-law) for making Winnipeg feel like home and my mother in-law and father in-law for supporting me throughout this journey.

Amma and Appachchi (my parents), my heartfelt gratitude goes to both of you for your unwavering love and support throughout my life. Thank you for teaching me the qualities of perseverance and resilience which helped me to successfully complete this thesis. Malli (my little brother) for cheering me on even if you are thousands of miles away. My loving husband Sapumal thank you for taking good care of my heart so that my mind can be at ease as I completed my thesis.

I hope I made all of you proud.

*Randula Senarathbandara*

*November 2024*

# Table of Contents

## List of Figures

## List of Tables

## Nomenclature

| | |
|---|---|
| $\alpha$ | empirical coefficient in transport rate equation (-) |
| $\beta$ | empirical coefficient in transport rate equation (-) |
| $\beta_{re}$ | rate of surface ice entrainment (1/s) |
| $\gamma$ | specific weight of water (N/m$^3$) |
| $\Delta$ | difference between specific gravities of water and ice (-) |
| $\Delta_s$ | difference in specific gravities of bed material and water (-) |
| $\eta$ | rate of frazil rise (m/s) |
| $\Theta_c$ | critical dimensionless flow strength (-) |
| $\Theta_n$ | dimensionless flow strength for ice transport (-) |
| $\Theta_s$ | dimensionless flow strength for bed load transport (-) |
| $\theta_b$ | bed slope angle (-) |
| $\theta_i$ | ice cover slope angle (-) |
| $\nu$ | kinematic viscosity of water (m$^2$/s) |
| $\rho_w$ | density of water (kg/m$^3$) |
| $\rho_i$ | density of ice (kg/m$^3$) |
| $\varepsilon_y$ | vertical mixing coefficient (-) |
| $\tau_b$ | boundary shear stress (Pa) |
| $\tau_{bc}$ | critical boundary shear stress (Pa) |
| $\tau_i$ | shear stress on the underside of the ice cover (Pa) |
| $\Phi_n$ | dimensionless ice transport rate (-) |
| $\Phi_E$ | dimensionless equilibrium transport rate (-) |
| $\Phi_{in}$ | dimensionless incoming ice supply rate (-) |
| $\Phi_{out}$ | dimensionless ice output rate (-) |
| $\Phi_s$ | dimensionless bed load transport rate (-) |

| | |
|---|---|
| $\phi_i$ | dynamic internal friction angle of ice particles (-) |
| $\phi_s$ | dynamic internal friction angle of bed material (-) |
| $\omega$ | fall velocity (m/s) |
| $\omega_i$ | buoyant velocity (m/s) |
| $A_0$ | initial cross-sectional area (m$^2$) |
| $A_i$ | cross-sectional area of the under cover moving frazil layer (m$^2$) |
| $A_w$ | cross-sectional flow area (m$^2$) |
| $B$ | buoyant velocity coefficient (-) |
| $B'_b$ | net buoyancy force of moving granular ice per unit area (N/m$^2$) |
| $B_0$ | open water width (m) |
| $b$ | flume/channel/river width (m) |
| $C$ | Chezy's roughness coefficient for water passage (m$^{1/2}$/s) |
| $C_D$ | drag coefficient (-) |
| $C_f$ | volumetric concentration of suspended frazil (-) |
| $C_i$ | surface ice concentration (-) |
| $D_*$ | dimensionless particle parameter |
| $d_n$ | nominal diameter of an ice particle (m) |
| $d_s$ | nominal diameter of bed material (m) |
| $e_i$ | efficiency coefficient for cover load transport (-) |
| $e_b$ | efficiency coefficient for bed load transport (-) |
| $F$ | fall velocity coefficient (-) |
| $Fr$ | Froude number |
| $F_d$ | tractive force (Pa) |
| $g$ | gravitational acceleration (m/s$^2$) |
| $h$ | water depth (m) |
| $h_{fc}$ | Maximum allowable thickness of a frazil deposit (m) |

| | |
|---|---|
| $h_{f0}$ | Initial thickness of a frazil deposit (m) |
| $H_{avg}$ | average flow depth underneath the ice cover (m) |
| $H'$ | water depth under ice (m) |
| $k_1$ | empirical coefficient in Rubey (1993) formula (-) |
| $k_2$ | empirical coefficient in Rubey (1993) formula (-) |
| $M_{uc}$ | initial parcel mass (kg) |
| $N_{uc}$ | concentration of the undercover particle accumulation (-) |
| $n_b$ | Manning's bed roughness coefficient |
| $n_i$ | Manning's ice cover roughness coefficient |
| $n_c$ | Manning's composite roughness coefficient |
| $p$ | porosity of the accumulation (-) |
| $Q_{in}$ | ice discharge input ($m^3$/s) |
| $Q_{ic}$ | volumetric ice transport capacity ($m^3$/s) |
| $Q_{it}$ | total volumetric under cover ice discharge ($m^3$/s) |
| $Q_{out}$ | ice discharge output ($m^3$/s) |
| $Q_w$ | water discharge ($m^3$/s) |
| $q_i$ | volumetric ice transport rate per unit width ($m^3$/s/m) |
| $q_{uc}$ | volumetric under cover ice transport rate per unit width ($m^3$/s/m) |
| $q_s$ | volumetric rate of bed load transport per unit width ($m^3$/s/m) |
| $r$ | fraction of ice covered length in the considered reach (-) |
| $R$ | hydraulic radius (m) |
| $R_i$ | hydraulic radius under ice cover (m) |
| $Re$ | particle Reynolds number (-) |
| $S_w$ | water surface slope (-) |
| $S_f$ | friction slope (-) |

| | |
|---|---|
| $\Delta S$ | change in storage within the control volume ($m^3$) |
| $T$ | dimensionless transport stage parameter (-) |
| $t_i$ | thickness of the under cover moving frazil layer (m) |
| $t_{avg}$ | average thickness of the ice cover (m) |
| $t_{uc}$ | thickness of the under cover ice parcel (m) |
| $\Delta t$ | time interval between two measurements (s) |
| $U$ | mean flow velocity (m/s) |
| $U_i$ | velocity of the moving frazil layer (m/s) |
| $\bar{u}_b$ | moving particle velocity in the moving bed load layer (m/s) |
| $\bar{u}_i$ | mean ice particle velocity (m/s) |
| $u_*$ | shear velocity (m/s) |
| $u_{*i}$ | ice cover shear velocity (m/s) |
| $u_{*c}$ | critical ice cover shear velocity (m/s) |
| $u_{*,cr}$ | critical ice grain shear velocity (m/s) |
| $V$ | volume of a single particle ($m^3$) |
| $V_{fm}$ | maximum ice volume that can deposit with a uniform ice thickness ($m^3$) |
| $V_{cr}$ | critical velocity for deposition (m/s) |
| $V_w$ | average flow velocity (m/s) |
| $V_{uc}$ | under cover ice transport velocity (m/s) |
| $W_b'$ | submerged weight of the moving bed material per unit area of bed load transport ($N/m^2$) |
| $\Delta x$ | length of the control volume (m) |

# Chapter 1 Introduction

## 1.1 Background and Motivation

The hydraulics of rivers and lakes in cold regions are vastly impacted by various ice processes during the winter. There are socio-economic as well as ecological implications associated with ice cover formation in a northern climatic river or a lake. Ice roads are often used as transportation corridors to remote communities during the winter and recreational activities such as ice-skating and ice fishing heavily rely on the formation of a strong, competent ice cover. Ice-related flooding is disastrous and causes damage to human lives, property, and infrastructure. Hydro-electric generation is often negatively impacted by ice formation during the winter due to the head loss in the presence of an ice cover. River morphology is altered by the presence of ice, where sediment transport, deposition, and erosion processes with the presence of river ice are different to that of open water conditions. Aquatic life in rivers and lakes can incur both beneficial and adverse effects due to ice formation in rivers during the winter.

At the onset of winter, the heat loss from a water body to the environment through the air-water and the bed-water interfaces results in a decrease in water temperature. When the water temperature falls below its freezing point of 0˚C (for pure water) without any state change, water is said to be supercooled, and it is one of the two conditions that should be satisfied for ice formation in a water body. Nucleation is the second condition required for ice formation, and pure water must be cooled to approximately -40˚C for water to be the nucleus (homogeneous nucleation). Ice formation which initiates with a seed crystal such as an organic material in water, air bubble, water droplet or snowflake is another source of initial nuclei. Secondary nucleation, where ice particles in water break apart through collisions and turbulence to form new nuclei is the primary cause of a dramatic increase in frazil ice concentration in a natural water body (Daly, 1984).

River ice formation processes are dynamic in nature compared to the ice formation in a lake. Border ice formation is often one of the initial ice formation processes in a river. Border ice in a river initiate along the shorelines where the water velocities are considerably lower than the central portion of the river. As the winter progresses, the border ice cover grows inwards towards the center of the river. Border ice width can increase primarily by two mechanisms. With thermal growth, the border ice edge will grow smoothly outwards over time. If frazil ice pans are simultaneously being transported on the river, border ice width will increase by depositing ice along the existing border ice edge as the ice pans collide with the border ice edge (also known as buttering). Both river hydraulics and heat transfer at the air-water interface are altered with the presence of a border ice cover in a river. The resistance to the flow increases with the border ice cover, thus causing more water to be conveyed in the middle of the river. The insulation provided by the border ice cover prevents heat transfer at the air-water interface slowing the overall heat loss from the river. In small rivers, border ice from either side of the shorelines may eventually bridge, thereby potentially halting the surface ice transport from upstream. The ice cover progresses upstream when frazil pans and frazil slush accumulate at the leading edge. The ice cover becomes stronger as the interstitial water within the porous ice cover freezes and then the ice cover grows thermally in the vertical direction (Beltaos, 2013).

Skim ice formation is another process which may contribute to ice cover formation in both rivers and lakes. Skim ice is prominent in lakes where there is little to no water movement. Skim ice can also form in a river with supercooled water temperature, when the vertical turbulence intensity of the water is low, it is insufficient to entrain the ice particles into the flow. Skim ice can grow laterally across a water surface at a very fast rate and create large thin ice floes that can be the initiation of an ice cover under appropriate hydraulic conditions. If the water velocity in the river is high, it will transport skim ice downstream, which is referred to as a skim ice run.

Frazil ice forms in turbulent river reaches when the water is supercooled. Frazil ice particles are typically disc shaped with diameters ranging from a few micrometers to a few millimeters. Laboratory studies have shown that the mean frazil particle diameter is a function of turbulence intensity (Clark and Doering, 2009). The vertical turbulence intensity of the flow and the rise velocity of the frazil particles govern the vertical distribution of frazil ice particles in a water column. When water is being supercooled, and frazil ice is being formed, it is referred to as active frazil ice. Active frazil is sticky and frazil ice particles may stick together to form frazil flocs or they may stick to rocks in the river bottom to form anchor ice. The buoyant force on frazil flocs increases as they grow in size which will cause the frazil flocs to rise to the surface. The frazil flocs at the surface will combine to form frazil pans which are more competent than individual frazil flocs. Larger ice floes are formed when frazil pans that are close in contact freeze together at the surface. A solid ice layer is created at the surface when the interstitial water within the porous frazil floes freezes.

Frazil ice entrained in the flow will get transported downstream in a river, and the frazil ice movement underneath a stable ice cover is known as under cover ice transport or cover load transport. Frazil ice can deposit beneath an ice cover based on the flow conditions such as the critical velocity and/or the approach Froude number and the geometric conditions of the river. These ice accumulations may grow in thickness to form hanging ice dams if there is continuous ice supply from upstream. River ice formation processes with an emphasis on hanging dam formation is illustrated in Figure 1.1 below.

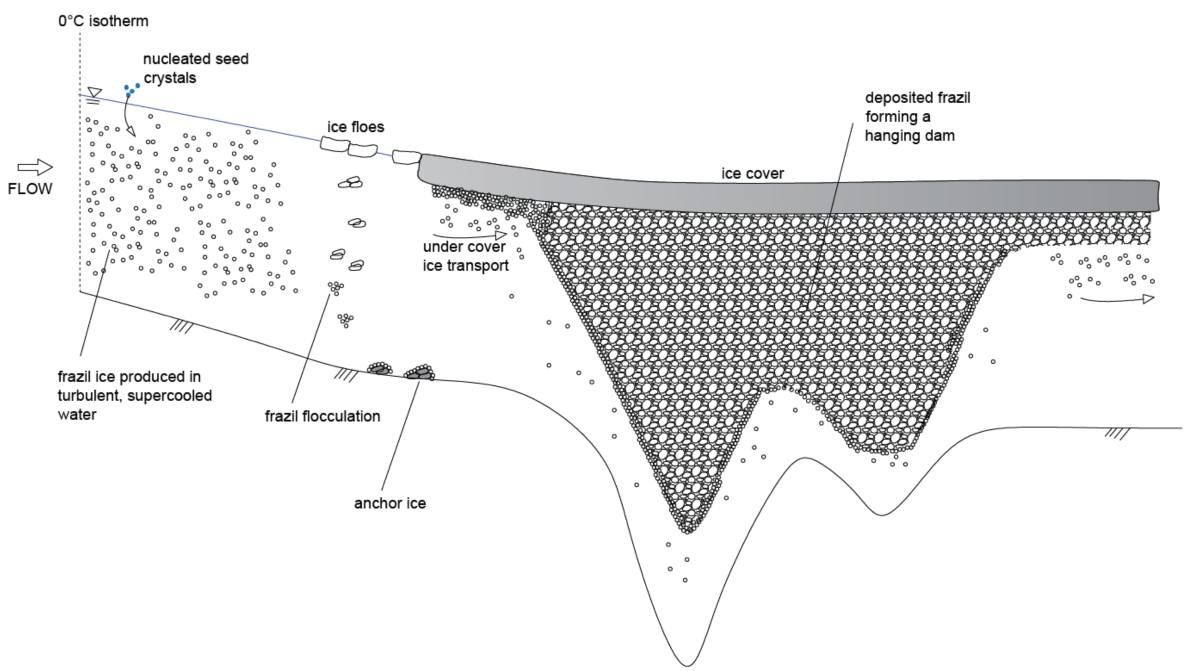


Figure 1.1. River ice and hanging dam formation.

Previous literature specifically focusing on under cover transport processes is limited, but there are a few studies that discuss the stability and the movement of an ice floe beneath an ice cover with regard to ice jam development. Despite the difference in particle size of an ice floe and a frazil ice particle, some of these theories can be used to better understand the under cover ice transport processes. Critical velocity beneath an ice accumulation and the critical Froude number of the flow at the leading edge of the ice cover had been considered as limiting criterion for ice deposition in early ice transport studies (Ashton, 1974; MacLachlan, 1926; Kivislid, 1959). Later Shen and Wang (1995) introduced the concept of ice transport capacity that is more representative of the actual field processes with regard to under cover ice transport. In this study under cover ice transport was considered to be analogous to bed load transport, hence indicating the potential of using bed load transport theories which are comparatively well-known, to analyze the under cover ice transport processes. Many bed load studies focused on developing an equation to link the relationship between the dimensionless flow strength and the dimensionless transport rate. Shen and Wang (1995) showed that a similar relationship can be adapted for ice transport processes using a series of laboratory experiments and analysis of field data from a long-term field study in Hequ Reach, Yellow River, China (Wang, 1992).

Depending on the hydraulic and ice supply conditions of a river, ice accumulations can develop to form a hanging dam which is a thick accumulation of frazil ice beneath an ice cover (Beltaos and Dean, 1981). Hanging dams can be typically found at locations where the geometry of the river changes in a manner that causes a significant reduction in water velocity, such as an increase in river width, an increase in river depth, or reduction in channel slope. River mouths or the entrance to reservoirs/lakes are another common location for hanging dam formation. Previous field studies (Beltaos and Dean, 1981; Gold and Williams, 1963) have shown that the amount of frazil ice supply from upstream can be a major contributing factor for formation of a large hanging dam.

## 1.2 Research Objectives

Hanging dam formation has various environmental and social implications. The flow restriction caused by the formation alters river hydraulics by increasing the under ice roughness, water surface elevation, and the flow velocity beneath the hanging dam formation. During the breakup period, ice accumulations from hanging dams can significantly contribute to ice jam flooding that affects people living in areas vulnerable to ice jam flooding. From a hydropower perspective, the increase in water surface elevation is detrimental to power generation as lower head difference results in less power generation. Despite being one of the crucial components of river ice, hanging dams and the under cover ice transport processes that govern hanging dam formation are still not well understood. There are limited field and lab studies and numerical modelling efforts of under cover ice transport and hanging dam formation in the literature. Under cover ice transport processes determine the rates of ice erosion and deposition beneath an existing ice cover which formulates the basis for the development of a hanging dam. Therefore, a better understanding of under cover ice transport processes is necessary to predict the formation and evolution of a hanging dam. The objectives of this research are listed as follows:

1. Further develop a formula for cover load transport rate based on the analogous nature of bed load and cover load transport processes, using experiments conducted in laboratory flumes with simulated frazil ice and a simulated ice cover. Investigate the effect of incoming ice supply rate on under cover ice transport processes.

2. Investigate hanging dam formation and evolution process by conducting a series of experiments in a scaled-down laboratory physical model, where a river issues water to

a lake. This will advance the existing knowledge on hanging dam formation under various flow and incoming ice supply rate conditions.

3. Evaluate the numerical simulation of under cover ice transport processes and hanging dam formation using existing numerical formulations of the two-dimensional Comprehensive River Ice Simulation System Project (CRISSP2D) model in an ideal channel model setup. Assess the performance of the numerical model relative to the experimental results and propose modifications based on the results from objectives (1) and (2).

## 1.3 Organization of Thesis and Contributions of the Author

Chapter 2 of the thesis consists of a literature review on under cover ice transport processes, hanging dam formation and numerical models that can simulate these processes. The laboratory studies related to ice floe stability and under cover ice transport processes are discussed in this section focusing on several governing parameters such as the critical velocity, Froude number, and the ice transport capacity of the flow. The field studies on hanging dams in several cold region rivers are discussed in detail with an emphasis on conditions that would facilitate hanging dam formation, hydraulic and societal impacts of hanging dam formation, and components of a hanging dam.

Chapter 3 of this thesis presents work completed on under cover ice transport processes using a series of laboratory experiments. A journal paper titled, "Under cover ice transport processes under equilibrium and non-equilibrium conditions" is presented in this chapter which has been published in the journal Cold Regions Science and Technology. The objective of this paper was to improve the current knowledge on the under cover ice transport processes that lead to hanging dam formation. The experimental methods presented in the paper were primarily designed by the author, with the guidance of Dr. Shawn Clark and Dr. Karen Dow (program co-advisors). The author independently conducted the experiments and analyzed the results. The paper was written solely by the author of the thesis with revisions and suggestions provided by the program co-advisors. The paper was published in January 2024.

Chapter 4 comprises of a set of laboratory experiments that were conducted to analyze the formation and evolution of a hanging dam beneath a simulated ice cover using simulated frazil ice. The experimental methods were designed primarily by the author, with the guidance from program co-advisors. The author independently conducted the experiments, and technical assistance was provided by Alexander Wall (lab technician) when needed. The results of the experiments were independently analyzed by the author of this thesis. The paper titled "Experimental analysis on hanging dam formation and evolution" is included in this chapter and this paper was solely written by the author with the revisions and suggestions provided by the program co-advisors. The paper was submitted to the special issue of the journal Water, on Advances in River Ice Science and its Environmental Implications and was published in December 2023.

In Chapter 5, the background and modeling capabilities of the two dimensional river ice numerical model, Comprehensive River Ice Simulation Systems Project (CRISSP2D) is discussed in detail. This chapter presents the results of numerical modeling efforts to simulate under cover ice transport processes and hanging dam formation in a two-dimensional numerical river ice model, CRISSP2D. The discussion of this chapter highlights the model strengths and identifies areas of improvements with respect to the model performance in simulating under cover ice transport and hanging dam formation.

Chapter 6 of the thesis is a conclusion of the major findings of this research. Suggested future work with respect to laboratory experiments and numerical modeling of under cover ice transport and hanging dam formation are presented in this chapter.

# Chapter 2 Literature Review

## 2.1. Under Cover Ice Transport Processes

In the winter, frazil ice is generated in large quantities in high velocity river sections as a result of continuous supercooling. Frazil ice particles are transported downstream in the river either in suspension or at the open water surface and these particles can be entrained beneath an existing downstream ice cover.

Entrained ice may continue to be transported beneath the ice cover (termed under cover ice transport) or get deposited on the underside of the ice cover depending on the hydraulic conditions of the flow. Frazil ice particles that are entrained under an ice cover mostly consist of coarse granules that are formed from flocculated ice. These suspended ice particles rise to the ice cover within a short distance from the leading ice edge. Wang (1992) and Shen and Wang (1995) have conducted the most detailed analysis of under cover ice transport processes up to date. Shen and Wang (1995) claimed that the concept of critical velocity and critical Froude number is inadequate to describe the erosion and deposition processes beneath an ice cover and it should be related to the hydraulic and ice conditions of the river.

The ice transport capacity of the flow is defined as the equilibrium rate of ice discharge for a given flow condition and set of ice particle characteristics with the assumption that supercooling is not present beneath the ice cover and the ice particles are no longer active (and sticky). If the ice supply from upstream is higher than the ice transport capacity of the flow, deposition occurs. Ice deposits that are not frozen erode if the ice supply from upstream is lower than the ice transport capacity. When the incoming ice supply is equal to the ice transport capacity there is a dynamic equilibrium where the rate of deposition is equal to the rate of erosion, and ice output from the reach is equal to the ice input to the reach.

Cover load transport is analogous to bed load transport in many aspects, but the granular frazil ice layer under an ice cover can be fully mobilized unlike bed load transport. The concentration and velocity profiles of under cover ice transport is shown in Figure 2.1, where the highest ice concentration is observed closer to the ice cover boundary. The partially mobilized velocity profile shows transport in the ice boundary layer is minimal and typically it is observed before incipient motion. The fully mobilized velocity profile shows the ice movement after passing the threshold for incipient ice motion. In both bed load and cover load transport processes, submerged solid particles move along a boundary and the movement is caused by the shear stress acting on the particles. Figure 2.2(a) and Figure 2.2(b) show the shear stresses acting on a sediment and an ice particle, respectively.

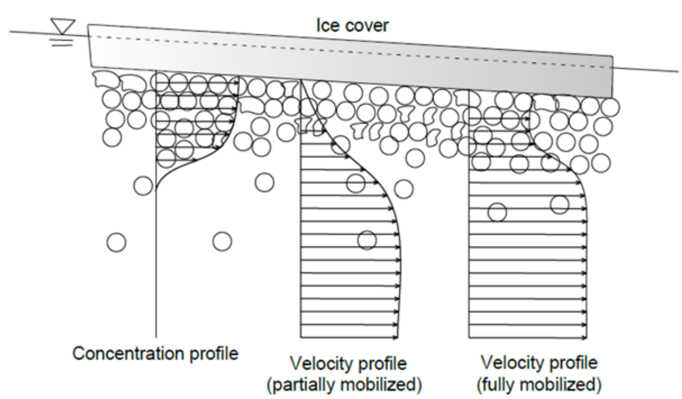


Figure 2.1 Concentration and velocity profiles for under cover ice transport (adapted from Shen and Wang, 1995).

(a)

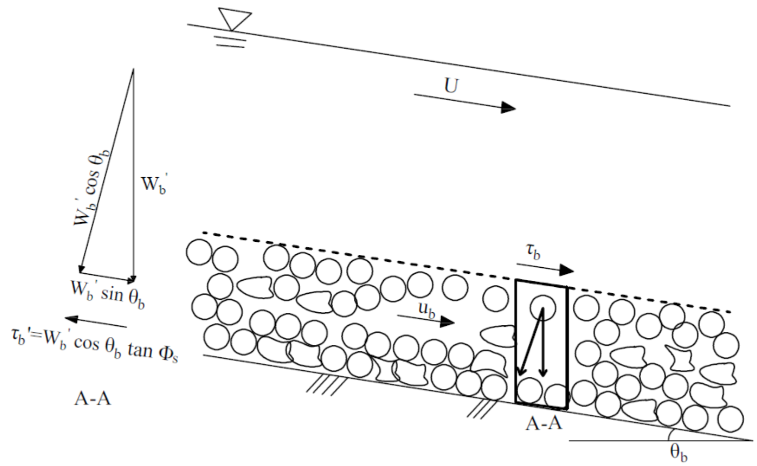


(b)

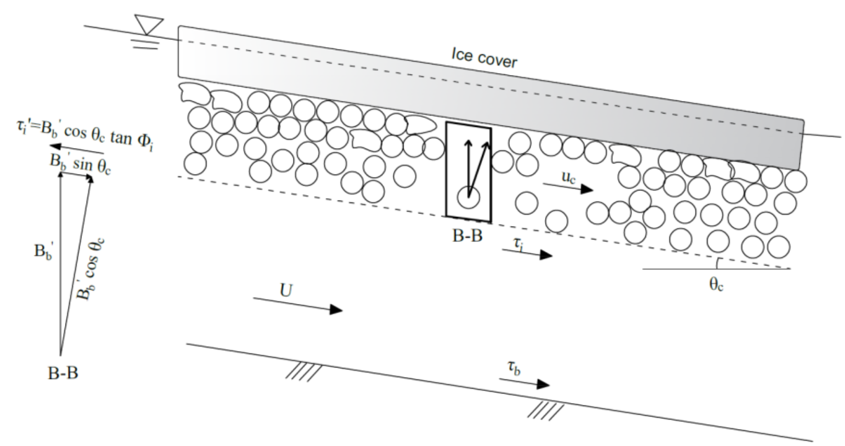


Figure 2.2 Shear stresses acting on (a) a sediment particle, and (b) an ice particle (adapted from Shen and Wang, 1995).

The stream power concept by Bagnold (1966, 1973) states that the rate of bed load transport can be determined from the balance of the rate of energy input and the rate of work done to move the bed material which is expressed by Equation 2.1 where $W_b'$ is the submerged weight of the moving bed material per unit area of bed load transport (N/m$^2$), $\bar{u}_b$ is the moving particle velocity in the moving bed load layer (m/s), $\theta_b$ is the bed slope angle (-), $\phi_s$ is the dynamic internal friction angle (-) (approximately 33˚ for sand), where $tan\ \phi_s$ would give the ratio of shear to normal stress, $\tau_b$ is the shear stress on the bed (Pa), $U$ is the mean flow velocity (m/s), and $e_b$ is the efficiency coefficient for bed load transport (-). The shear stress acting on the bed is calculated using Equation 2.2 where $\rho$ is the density of water (kg/m$^3$), $g$ is the gravitational acceleration (m/s$^2$), and $h$ is the water depth (m). The efficiency coefficient for bed load transport ($e_b$) is calculated using Equation 2.3 (Bagnold, 1966; 1973).

$$W_b'\bar{u}_b(cos\theta_b tan\phi_s - sin\theta_b) = \tau_b U e_b \qquad [2.1]$$

$$\tau_b = \rho g h\ sin\theta_b \qquad [2.2]$$

$$e_b = \frac{\bar{u}_b}{U} \qquad [2.3]$$

A similar relationship was developed for cover load transport by Shen and Wang (1995) which is given in Equation 2.4 where $B_b'$ is the net buoyancy force of moving granular ice per unit area (N/m$^2$), $\bar{u}_i$ is the mean ice particle velocity (m/s), $\theta_i$ is the cover slope angle (-); $\phi_i$ is the dynamic internal friction angle of ice particles (-), $\tau_i$ is the shear stress on the underside of the ice cover (Pa), $e_i$ is the efficiency coefficient for cover load transport (-). The shear stress acting on the under side of the ice cover is calculated using Equation 2.5 where $R$ is the hydraulic radius (m), and $S$ is the energy slope (-). The efficiency coefficient for cover load transport ($e_i$) is calculated using Equation 2.6.

$$B_b'\bar{u}_i(cos\theta_i tan\phi_i - sin\theta_i) = \tau_i U e_i \qquad [2.4]$$

$$\tau_i = \rho g R S \qquad [2.5]$$

$$e_i = \frac{\overline{u}_i}{U} \tag{2.6}$$

In natural rivers, the values of bed and ice cover slopes ($\theta_b$ and $\theta_i$) are negligible compared to the dynamic internal friction angle of sand and ice ($\phi_s$ and $\phi_i$), which further simplify Equation 2.1 and 2.4.

According to Chien (1956; 1980) many existing bed load formulae can be arranged to obtain a relationship between dimensionless flow strength ($\Theta$) and dimensionless transport rate ($\Phi$). The dimensionless flow strength for bed load transport ($\Theta_s$) is calculated using Equation 2.7 where $\Delta_s$ is the difference in specific gravities of bed material and water (-), $d_s$ is the particle diameter of bed material (m) and the dimensionless bed load transport rate ($\Phi_s$) is calculated using Equation 2.8, where $q_s$ is the volumetric rate of bed load transport per unit width ($m^3/s/m$).

$$\Theta_s = \frac{\tau_b}{\Delta_s \rho g d_s} \tag{2.7}$$

$$\Phi_s = \frac{q_s}{\sqrt{\Delta_s g d_s^3}} \tag{2.8}$$

Depending on the similarity between bed load and cover load transport processes, Shen and Wang (1995) introduced the dimensionless flow strength ($\Theta_i$) for ice transport, and dimensionless ice transport rate ($\Phi_i$) given by Equation 2.9 and Equation 2.10, respectively where $\Delta$ is the difference in specific gravities of water and frazil ice (-), $d_n$ is the nominal diameter of frazil ice (m), and $q_i$ is the volumetric ice transport rate per unit width ($m^3/s/m$).

$$\Theta_i = \frac{\tau_i}{\Delta \rho g d_n} \tag{2.9}$$

$$\Phi_i = \frac{q_i}{\sqrt{\Delta g d_n^3}} \qquad [2.10]$$

The shape of the frazil ice particles is an important parameter that should be taken into consideration when estimating the cover load transport rate. The particle shape depends on factors such as the distance travelled from frazil generation point to the deposition point, slope, flow velocity and the turbulence intensity of the river. The field study from Hequ Reach, China showed that the frazil flocs were round shaped, and the particles had travelled a long distance through a section of rapids with high flow velocities (Sun et al, 1986; Wang, 1992). A similar field study was conducted in the St. Lawrence River, Canada where the flow velocity in the river was lower when compared with the Hequ Reach and the frazil ice particles were disc-shaped (Morse and Richard, 2009). The study by Mantz (1980) which was on the effect on the particle shape on the bed load transport rate suggested that under similar shear stress conditions, the circular disks move slower than rounded or angular particles with the same submerged density and nominal diameter.

The shape of the particle influences the hydrodynamic forces acting on the particle causing distinct types of particles to have dissimilar transport rates. The shape factor can be introduced to dimensionless flow strength and transport rate equations to account for the effect of particle shape. In bed load transport processes, fall velocity coefficient ($F$) is used as the particle shape factor and it is determined based on the fall velocity ($\omega$) of the bed material. The modified dimensionless flow strength and transport rate equations which include the particle shape factor (Shen and Wang, 1995) are given in Equation 2.11 and 2.12 respectively, where $u_*$ is the shear velocity (m/s).

$$\Theta_i = \frac{u_*^2}{F^2 \Delta g d} \qquad [2.11]$$

$$\Phi_i = \frac{q_i}{F\sqrt{\Delta g d^3}} \qquad [2.12]$$

Shen and Wang (1995) introduced the following relationship between the dimensionless transport rate and dimensionless flow strength given in Equation 2.13, where $\Theta_c$ is the critical dimensionless flow strength (-) that was determined to be 0.041. This equation was developed based on a series of laboratory experiments that will be discussed in detail in Chapter 3 of this thesis.

$$\Phi_i = 5.487(\Theta_i - \Theta_c)^{1.5} \qquad [2.13]$$

## 2.2 Hanging Dam Formation and Evolution

Under cover ice depositions may develop to high accumulations over the duration of the winter, depending on the flow and ice supply conditions. Hanging dams are thick accumulations beneath an ice cover that often alter the hydraulic characteristics of a river. Hanging dams are usually found at locations where the flow velocity significantly reduces due to increase in width, depth, and/or decrease in the slope of the channel. River mouths and entrance to reservoirs are typical locations that would facilitate hanging dam formation. A hanging dam forms at the mouth of Moira River at the bay of Quinte (Lake Ontario, Canada), where the river upstream of the inlet has a very steep slope and remains open long after lake ice cover has formed (Beltaos, 2013).

The amount of frazil ice supply from upstream is a major contributing factor for initiation and evolution of a hanging dam. Hanging dams can be commonly found at slow velocity regions that are immediately downstream of a reach of rapids which is a continuous source of frazil ice generation. The first records of the hanging dam in Ottawa River, Canada is dated back to 1686, but the hanging dam was not observed after 1963 since the reach of rapids supplying ice was submerged by the construction of a downstream dam (Gold and Williams, 1963; Beltaos, 2013)

Hanging dams can have negative impacts on the flow regime of a river during the winter. Scour of the channel bed can occur under a hanging dam due to the high flow velocity caused by flow restriction. In Yellow River, China near Hequ, bed scour of 2 m was observed but it was covered from the subsequent sediment depositions and a stable cross-sectional shape was maintained over the long term (Sui et al., 2006). Flooding due to hanging dams is a common and recurrent issue in many northern climatic rivers. The lower portion of the Kaministiquia River in Thunder Bay, Ontario, Canada has a very flat bed slope, and the water surface elevation is controlled by the water level of Lake Superior. Frazil accumulation at the location where the bed slope changes from normal to a near zero value causes a rise in the water level that may cause flooding based on hydro-climatic conditions (Beltaos et al., 2007).

The knowledge from field studies on hanging dams can be used to understand the formation and evolution processes. Field data spanning over two or more winters are valuable when comparing a recurring hanging dam at a specific location such as data for 1986-1987 and 1987-1988 winters from Hequ reach of the Yellow River, China (Sun et al., 1986; Wang, 1992). In a laboratory study, there is an advantage of precisely controlling hydraulic and geometric parameters to analyze the fundamentals of hanging dam formation process. Insights from a field study are often valuable when developing and designing a laboratory study. Details from several field studies on hanging dams are presented highlighting the existing knowledge on hanging dams.

A field study was conducted at the St. Raymond reach hanging dam of St. Anne River in Quebec by Vergeynst, Morse and Turcotte (Vergeynst et al., 2017) in 2014-2015 to quantify transported frazil ice, combining data from the field samples and a complete heat budget approach. St. Raymond reach of the St. Anne River is located at the head of a 4.5 km long reservoir created by a 105 m long concrete overflow dam on a rock sill at Chute-Panet. The St. Anne River is a gravel-bed river that changes from riffle pool geomorphology with a slope of 0.2% to rapids with a slope of 0.6% over a short distance, (several tens of kilometers) upstream of St. Raymond reach. A significant amount of frazil slush is produced in these sections of the river which would be transported downstream. At the beginning of each winter, the reservoir ice cover is formed by the process of frazil slush interception, consolidation and freezing. A hanging dam is subsequently formed at this reach by deposition of frazil ice under the existing ice cover. Frazil slush interception and secondary consolidation events along multichannel riffle ponds cause the grounded frazil jam to progress upstream.

In 2014-2015 winter, the hanging dam spanned over a length of 9.2 km and 20 cross-sections were selected to obtain measurements corresponding to river depth, water level, ice thickness and density. Instead of acoustic methods, simple apparatus and experimental procedures were used for acquiring measurements. The ice discharge in the rapids was measured to quantify the amount of frazil ice transported to the hanging dam location by using a manual sampler made of a pole with circular rings that were covered with nylon stockings. A home-made shear vane was used to measure the shear strength and a homemade Shelby tube was used for sampling at 20 cross sections along the streamwise direction. The river surface upstream of the sampling site was photographed every hour to gain additional information on frazil transport. The results from the study showed the presence of distinct layers of frazil indicating that a series of discontinuous deposition events had occurred. The thickness of frazil layers varied between 10 cm to 270 cm. There were only single density frazil layers across all cross-sections closer to the toe of the hanging dam. The complexity and the variation of stratigraphy increased in the upstream direction up to the middle of the hanging dam formation and it reduced from the middle of the hanging dam to the head of the dam. The study was concluded with an estimation of net frazil ice production in the reach which quantified the deposition using manual sampling methods to provide recommendations for ice management strategies to reduce the flood risk in the area.

A field investigation was conducted in 1971 -1972 at a reservoir formed by the intake dam of Gamlebrofoss power plant in Kongsberg, Norway to study the hanging dam formed at the site (Tesaker, 1975). The intake pond was 500 m long, 350 m wide with a depth of 7.5 m which could hold a total water volume of 250,000 m$^3$. The ice cover formation in the intake pond usually precedes the ice cover formation in the upstream section of the river. A survey was conducted to measure solid and frazil ice thickness by drilling boreholes through the accumulation twice each year. Ice thicknesses were measured with an accuracy of 5 cm using a round plate that was mounted on a rod. The velocities in the cross sections of the reservoir were measured once a year using a propeller flow meter. A hanging dam with a maximum thickness of 4.2 m and a total volume of 28,000 m$^3$ was formed in the winter of 1971. The maximum velocity underneath the hanging dam was 0.6 m/s and the average velocity varied in the range of 0.3 to 0.4 m/s. This study compared the areal extent and the shape of the hanging dam with sand entering from a river getting deposited in a reservoir and concluded that the pattern is significantly similar. A larger hanging dam was observed in winter of 1972, where the volume of the accumulation was estimated to be 43,000 $m^3$. The shear stresses were calculated based on the logarithmic velocity profiles obtained in the study and they were used to determine the critical particle diameter for frazil ice deposition underneath the ice cover using the Shield's formula.

Ice management strategies incorporated with hydro power operations can alter or sometimes prevent hanging dam formation in a river. A 50 m thick hanging dam that used to form below the Muskrat Falls on the Lower Churchill River before construction of Muskrat Falls Hydroelectric Generating Station is one such example. Muskrat Falls is located on the Lower Churchill River in Newfoundland, Canada and the river has a dynamic ice regime with numerous ice formation and breakup events. Before commissioning of Muskrat Falls Generating Station, the river upstream of Muskrat Falls remained open throughout the winter generating a large quantity of frazil ice and the deep pool below the fall provided the perfect conditions for the formation of a very thick hanging dam. The hanging dam formation had a significant impact on the water level downstream of Lower Muskrat Falls and would cause the water level to rise by more than 15 m prior to construction of the generating station. After the construction of the generating station, stable ice cover formation was promoted in the reservoir upstream which eliminated the open water reach upstream that produced frazil ice throughout the winter. The post construction data shows that winter stages are 7 to 9 m lower than the pre-project conditions, and the ice cover thickness is only 0.5 m in the area where a 50 m hanging dam used to form (Groeneveld et al., 2022). Table 2.1 provides a summary of literature on hanging dams and under cover ice transport processes highlighting their main contributions.

With the absence of laboratory studies which exclusively focus on hanging dam formation, ice jam studies can be a valuable resource to understand the present state of knowledge on the subject. A laboratory study on formation and movement of ice accumulation waves was conducted by Wang et al. (2019) which focused on developing a suitable criterion for ice accumulation wave formation and determining the speed of wave propagation. It was observed that the wave formation is strongly dependent on the flow intensity (which was demonstrated through effect of Froude number) and incoming ice supply rate. The relationship between dimensionless water depth and critical Froude number for ice accumulation wave development was investigated by the authors. Based on the experimental results for the same discharge, the smaller water depths did not produce an ice accumulation wave because the flow intensity underneath the ice cover was high compared to higher water depths. It was also found that higher Froude number would result in larger ice accumulation wave height. The propagation speed of the ice accumulation wave was found to be dependent on the flow intensity, water depths and the incoming ice supply according to the experimental results.

A formula for ice transport capacity for a waved accumulation was developed based on mass conservation equation, and the developed equation was validated through experimental results. According to the authors, the ice transport capacity for a waved accumulation is primarily dependent on the flow intensity, water depth, incoming ice supply rate, and the ice particle size.

Table 2.1. Summary of Literature on hanging dams and under cover transport processes.

| **Authors** | **Study site (nature of the study)** | **Hanging dam thickness and extent** | **Measurement** | **Measurement techniques/devices** |
|---|---|---|---|---|
| Gold and Williams (1961) | Ottawa River, Canada (field study) | Length: 450 m and 600 m<br>Width: 150 m<br>Thickness: 10-12 m | bathymetry survey | echo sounder |
| Tesaker (1975) | Kongsberg, Norway (field study) | Volume: 43,000 $m^3$<br>Thickness: 4.2 m | ice thickness | borehole drilling |
| | | | velocity | propeller flow meter |
| Beltaos and Dean (1981) | Smoky River, Canada (field study) | Length: varied 300 -700 m<br>Thickness: varied 11-16 m | formation | movie camera |
| | | | velocity | magnetic flowmeter |
| | | | roughness | calculated using velocity |
| | | | shear strength | torque wrench |
| | | | dry density of frazil | weight measurements |
| Shen & Van deValk (1984) | St. Lawrence River, Canada (field study) | Length: 2000 ft (~ 61 m)<br>Thickness: 20 ft (~ 6.1 m) | velocity | stream-tube analysis |
| | | | roughness | calculated using velocity |
| Sun, Yang and Yao (1986) | Yellow River, China (field study) | - | ice cover thickness | |
| | | | water levels | |
| | | | flow velocity | |
| Shen and Wang (1995) | Laboratory study | - | flow strength | |
| | | | transport rate | |
| Vergeynst, Morse and Turcotte (2017) | St Raymond reach, Canada (field study) | Length: 9.2 km<br>Thickness: varied 0.1- 2.7 m | ice discharge | manual sampler |
| | | | shear strength | homemade shear vane |
| | | | sample collection | homemade Shelby tube |
| | | | formation | camera |
| Groeneveld et al. (2022) | Muskrat Falls, Canada (field study) | Thickness: 50 m | ice cover thickness | |
| | | | water levels | |

## 2.3 Numerical Modeling of Under Cover Ice Transport Processes and Hanging Dam Formation

River ice numerical models are used to simulate the complex river ice processes, using analytical or empirical equations under simplified assumptions. Numerical modeling is far more cost and time efficient when compared to other forms of analyzing river ice processes, such as physical modeling or field studies. River ice numerical models can vary in level of complexity, where basic models usually simulate the effect of an ice cover on the water surface profile of a river and complex models can simulate thermal and transient effects of ice on hydraulics of a river. River ice numerical models may be designed to be site-specific, to formulate the model under simplified assumptions to reduce the modeling complexity and usage of computational resources.

There are several river ice numerical models that are capable of simulating the under cover ice transport processes in a river. River1D is a river ice numerical model developed by the University of Alberta which is available in the public domain. The model was initially designed as a hydrodynamic model which solved the Saint-Venant equations using characteristic-dissipative-Galekin (CDG) finite element scheme. Later the model was developed to simulate supercooling of water, frazil accretion, frazil re-entrainment, anchor ice formation and release, border ice formation, and under cover ice transport processes (Blackburn and She, 2019).

Under cover ice transport in River1D numerical model is simulated based on the ice transport rate equation proposed by Shen and Wang (1995). The ice transport capacity of the flow is estimated using Equation 2.14, where $Q_{ic}$ is the volumetric ice transport capacity ($m^3/s$); $B_0$ is the water surface width between border ice (m).

$$Q_{ic} = 5.487FB_0\sqrt{gd_n^3\Delta}(\Theta - \Theta_c)^{1.5} \qquad [2.14]$$

The total under cover ice discharge is estimated using Equation 2.15, where $Q_{it}$ is the total volumetric under cover ice discharge ($m^3/s$); $A_i$ is the cross sectional area of the under cover moving frazil layer ($m^2$); $U_i$ is the velocity of the moving frazil layer (m/s); $p$ is the porosity of frazil slush layer (-), that is set to be 0.4; $A_w$ is the cross sectional flow area ($m^2$), and $C_f$ is the volumetric concentration of suspended frazil (-).

$$Q_{it} = A_iU_i(1 - p) + A_wUC_f \qquad [2.15]$$

The amount of frazil ice transported beneath the ice cover is estimated from the difference between the total under cover ice discharge given in Equation 2.15 and the under cover transport capacity given in Equation 2.14. The River1D model uses the relationship given in Equation 2.16 to estimate the transport of frazil underneath a stationary ice cover, where $t$ and $x$ are time and space notations; $\eta$ is the rate of frazil rise (m/s); $C_i$ is the surface ice concentration (-); $\beta_{re}$ is the rate of surface ice entrainment (1/s); $t_i$ is the thickness of under cover moving frazil layer (m); $L$ is the length of ice cover between computational nodes (m) which is approximated using the streamwise discretization.

$$\frac{\partial A_i}{\partial t} + \frac{\partial U_iA_i}{\partial x} = \frac{B_0\eta C_f}{(1-p)} - B_0C_i\beta_{re}t_i - \frac{(Q_{it}-Q_{ic})}{L} \qquad [2.16]$$

RICE is a one-dimensional river ice numerical model developed by Lal and Shen (1990) that has the capability of simulating the river hydraulics, distributions of water temperature and ice discharge, formation of an ice cover, under cover ice transport, thermal growth/decay of an ice cover and ice cover stability. RICE model uses the critical velocity criterion to model the under cover ice transport processes. The model considers a two-layer formulation which consists of a surface layer and layer below the ice cover when modeling the ice transport (Lal and Shen, 1990).

In the model, the ice supply rate that would reach the underside of the ice cover is considered as one of the main factors that would affect the rate of deposition underneath the ice cover. The one-dimensional form of mass conservation of frazil ice in suspension in the model is expressed by Equation 2.17, where $\omega_i$ is the buoyant velocity of frazil ice (m/s); $\varepsilon_y$ is the vertical mixing coefficient (-) and $h$ is the flow depth under ice cover (m).

$$\frac{\partial(C_f A_w)}{\partial t} + \frac{\partial(C_f A_w U)}{\partial x} = B_0\left[\left(\epsilon_y \frac{\partial C_i}{\partial y} - \omega_i C_i\right)_{y=h} - \left(\epsilon_y \frac{\partial C_i}{\partial y} - \omega_i C_i\right)_{y=0}\right] \qquad [2.17]$$

Based on the assumption that there is no exchange at the bed, the right-hand side of Equation 2.17 was modified to obtain Equation 2.18, where $\theta_1$ is an empirical coefficient (-) and the term $\theta_1\omega_i C_f$ gives the rate of frazil deposition. The RICE manual suggests that the parameter $\theta_1\omega_i$ should be obtained by calibration against field data.

$$\frac{\partial(C_f A_w)}{\partial t} + \frac{\partial(C_f A_w U)}{\partial x} = -B_0\theta_1\omega_i C_f \qquad [2.18]$$

If the flow is steady and uniform, Equation 2.18 can be further simplified to obtain Equation 2.19.

$$A_w U \frac{dC_f}{dx} = -B_0\theta_1\omega_i C_f \qquad [2.19]$$

The streamwise variation of depth averaged frazil ice concentration in the model was estimated using Equation 2.20, where $C_0$ is the frazil ice concentration at the upstream end (-)

$$C_v(x) = C_0 exp\left(-\frac{B_0\theta_1\omega_i x}{A_w U}\right) + constant \qquad [2.20]$$

The downstream frazil ice concentration of a river reach that has a length of $\Delta x$ can be determined in terms of the upstream ice concentration as given in Equation 2.21, where $C_1$ is the average concentration at the beginning of the river reach (-); $C_2$ is the average concentration at the end of the river reach (-).

$$C_2 = C_1 exp\left(-\frac{B_0\theta_1\omega_i x}{A_w U}\right) \qquad [2.21]$$

The reduction of ice concentration along the reach over the distance $\Delta x$ was represented as a fraction in the model formulations using the coefficient $\beta$ as shown in Equation 2.22. After depositions, the concentration of frazil ice in suspension is equal to $(1-\beta)C_1$.

$$\beta = \frac{C_1 - C_2}{C_1} = 1 - exp\left(-\frac{B_0\theta_1\omega_i x}{A_w U}\right) \qquad [2.22]$$

In the RICE model, ice deposition initiates at the downstream leading ice edge and it progresses upstream. Critical flow velocity is used as the criterion for ice deposition where ice particles moving underneath the cover will deposit at the first ice covered reach as long as the flow velocity exceeds the critical velocity for deposition. The excess ice concentration which is unable to deposit because of the critical velocity criterion will travel further downstream. The critical velocity for deposition of frazil was determined using

Equation 2.23, where $Q_w$ is the water discharge (m$^3$/s); and $V_{cr}$ is the critical velocity for deposition (m/s).

$$\frac{Q_w}{A_w} \leq V_{cr} \qquad [2.23]$$

The limiting condition for frazil deposition is based on several factors such as concentration that is available for deposition and the hydraulic conditions of the river. Typically, the hydraulics of a river such as the water surface elevation change with frazil accumulation since it limits the available flow area. In the RICE model it had been assumed that there was no significant change in water surface elevation and flow depth with frazil accumulation during a certain time step. Equation 2.24 for maximum allowable thickness for a frazil deposit is obtained based on the assumption that the ice cover freely floats and the cross-sectional flow area before frazil ice deposition is equal to the cross-sectional flow area after frazil ice deposition, where $h_{fc}$ is the maximum allowable thickness of a frazil deposit (m); $h_{f0}$ is the initial thickness of the frazil deposit (m); $A_0$ is the initial net cross-sectional area (m$^2$); $\rho_i$ is the density of frazil ice (kg/m$^3$).

$$h_{fc} = h_{f0} + \frac{\rho}{B_0\rho_i}\left(A_0 - \frac{Q_w}{V_{cr}}\right) \qquad [2.24]$$

The maximum ice volume that can deposit with a uniform ice thickness ($V_{fm}$) is given in Equation 2.25, where $r$ is the fraction of ice covered length in the considered reach (-).

$$V_{fm} = B_0 r \Delta x(1-p)\left(h_{fc} - h_{f0}\right) \qquad [2.25]$$

The critical velocity for erosion of a frazil ice deposit is higher than the critical velocity required for deposition since the inter-particle bond of frazil ice increases due to freezing.

In the RICE model, the critical velocity for erosion is a user input which can be either obtained directly from field data or it can be calibrated using observed flow and ice conditions. Since there were no theories for predicting the erosion rate when RICE model was developed, the model simulates erosion such that the concentration of frazil ice generated from erosion is equal to the current ice concentration in the reach (Lal and Shen, 1990).

RIVICE was developed by Environment Canada and several other collaborative agencies. RIVICE is a comprehensive one-dimensional model that can simulate the transient ice regime of a river considering the geometric, hydraulic, and meteorologic conditions of a river. Supercooling of water, ice generation, ice transport, ice cover formation, and ice cover break-up are the various river ice processes that can be simulated in the RIVICE numerical model. The model uses an implicit finite difference scheme and consists of a modular structure where each module is designed to simulate an ice process or control the inputs and the outputs of the model (Lindenschmidt, 2017; Martinson et al., 1993).

The under cover ice transport processes in the RIVICE model are managed by a separate subroutine where deposition and erosion are determined based on a certain criterion. The model has three criteria for deposition underneath an ice cover, and the user can choose the preferred criterion based on the requirement. The first option is having a user-defined critical velocity within the range permitted by the model specifications (0.7 m/s-1.5 m/s). If the under cover velocity is below the user defined critical velocity, there will be depositions underneath the ice cover. The second option is using the Meyer-Peter sediment transport equation given in Equation 2.26 to calculate the ice discharge per unit width ($q_i$)

that can be transported underneath the ice cover, where $C$ is the Chezy's roughness coefficient for water passage ($m^{1/2}/s$).

$$3281\frac{U^2}{C^2} = 12.3d_n + 0.84q_i \qquad [2.26]$$

The third option is having a user defined densimetric Froude number (Equation 2.27) that will govern the deposition process. Using a critical velocity or a critical Froude number are the commonly used methods to determine the deposition process underneath an ice cover.

$$Fr = \frac{U}{\sqrt{gd\Delta}} \qquad [2.27]$$

Similar to deposition, erosion processes in the model can also be simulated based on two criteria. The first method is defining a maximum velocity that would range from 0.9 m/s to 2.0 m/s and the ice will start to erode when the under cover velocity exceeds the user specified maximum velocity. The model is setup to send a notification when the thickness of the ice cover reaches 0.15 m, and the user will be notified that the erosion limit is unachievable. The second option is to use the tractive force (shear stress) as limiting criterion for ice deposition. Erosion occurs when the tractive force underneath the ice cover calculated according to Equation 2.28 is above the user defined minimum tractive force, where $F_d$ is the tractive force (Pa); $\gamma$ is the specific weight of water ($N/m^3$); $R_i$ is the hydraulic radius under the ice cover (m); and $S_f$ is the friction slope (-).

$$F_d = \gamma R_i S_f \qquad [2.28]$$

Both RICE and RIVICE numerical models use a critical velocity criterion for under cover transport simulations and the River1D model uses the Shen and Wang (1995) equation to determine the under cover ice transport rate for a certain flow strength condition.

The numerical modeling simulations presented in this thesis were conducted using the two-dimensional Comprehensive River Ice Simulation System Project (CRISSP2D) numerical model. CRISSP2D is an advanced two-dimensional river ice numerical model that can simulate various thermal and dynamic river ice processes such as skim ice formation, thermal ice growth, anchor ice formation, and under cover ice transport. This river ice model can simulate unsteady flow conditions, which is an advantage when simulating ice processes during freeze-up and breakup periods.

CRISSP2D was developed based on two river ice numerical models, RICEN (Shen et al., 1995) and DynaRICE (Shen et al., 2001). The RICEN numerical model is a one-dimensional unsteady river ice model that is capable of modeling supercooling, anchor ice formation, wind effects, and flow resistance due to moving ice etc. RICEN is capable of simulating under cover ice transport processes and frazil accumulation based on transport capacity formulations introduced by Shen and Wang (1995). DynaRICE is a two-dimensional river ice dynamics model which was validated using many field scenarios such as ice control operations for the Niagara Power Project and ice jam formation at the Missouri-Mississippi River confluence (Shen, 2000). The thermal effects of ice were not included in the DynaRICE model. The CRISSP2D river ice model was developed by applying the thermal formulations used in RICEN model to the two-dimensional DynaRICE model (Shen, 2002).

CRISSP2D is one of the most advanced and comprehensive river ice numerical models that is currently available to simulate river ice processes. It was primarily developed to model ice related issues in hydropower operations in North America. CRISSP2D can be used for various applications, including analysis of flow and ice conditions for post-construction assessment of proposed hydropower stations, the examination of the impact of flow control measures on ice formation, and the investigation of the long-term climate change effects on river ice conditions, just to name a few.

CRISSP2D consists of different modules responsible for hydrodynamic and various ice dynamic formulations. The hydrodynamic module determines river hydrodynamics by solving the depth-averaged Navier-Stokes equations using the explicit Petrov-Galerkin finite element method (Liu and Shen, 2004). In the ice dynamics module, Lagrangian Discrete Parcel Method (DPM) based on Smoothed Particle Hydrodynamics (SPH) is used to simulate the ice transport and ice dynamics within the model. The surface ice in the CRISSP2D model is considered as a continuum that is made of individual ice parcels with mass, momentum, and energy. These ice parcels are made of open water areas and ice areas which consist of a solid and porous frazil ice component. In Chapter 5, the under cover ice transport module of the program will be discussed in detail since it is the main focus of this research. CRISSP2D Programmer's Manual presents a detailed description of the modeling capabilities and information on each module of the numerical model (Liu and Shen, 2004).

## 2.4 Research Gap

Wang (1992) and Shen and Wang (1995) have conducted the most detailed analysis of under cover ice transport processes up to date, where they highlighted that the concept of critical velocity and/or critical Froude number itself is inadequate to describe the erosion and deposition processes. Shen and Wang (1995) proposed an under cover ice transport formula with a relationship between dimensionless transport rate and dimensionless flow strength based on a laboratory study. It is beneficial to investigate under cover ice transport processes using a material that has similar properties to ice particles with a focus on the effect of particle shape, and incipient motion of simulated ice particles which has not been analyzed in previous literature.

There are several field studies which report the physical parameters of hanging dams formed in natural rivers or lakes. However, it is difficult to conduct a detailed field study to investigate the fundamentals of formation and evolution of a hanging dam with careful isolation of contributing variables to identify the impact of each variable. This intensifies the need for a detailed laboratory study where the hydraulic and geometric parameters can be precisely controlled, and each contributing variable can be analyzed in detail.

CRISSP2D numerical model has the capability of simulating under cover ice transport processes, but a detailed analysis of model capabilities has not been reported in the previous literature. In fact, the under cover ice transport module of the CRISSP2D model is one of the least investigated components of the model. Numerical modelling efforts of under cover ice transport processes and hanging dam formation using the CRISSP2D model would add a valuable contribution to better understand these processes.

# Chapter 3 Under Cover Ice Transport Processes

## 3.1 Introduction

There is a knowledge gap on under cover ice transport processes and equations that can quantify the ice transport rate based on the flow strength of a river compared to sediment transport processes, despite the analogous nature of the two processes. This chapter is based on laboratory experiments conducted on equilibrium and non-equilibrium under cover transport processes using simulated ice and ice cover. The paper presented in this chapter discusses the experimental design, methodology and the results of a series of experiments that lead to the development of a new cover load formula. The effect of incoming ice supply rate on under cover transport processes is discussed in the paper, introducing the equilibrium, and non-equilibrium conditions of under cover ice transport. The paper was accepted to the journal Cold Regions Science and Technology in January 2024 (doi.org/10.1016/j.coldregions.2024.104124).

## 3.2 Paper 1: Under Cover Ice Transport Processes under Equilibrium and Non-Equilibrium Conditions

### 3.2.1 Abstract

The transport of ice particles beneath a stable ice cover (referred to as cover load transport), and the processes leading to ice deposition and erosion are highly dynamic and complex.

Based on the strong analogous relationship between bed load and cover load transport processes, knowledge from bed load transport research can be used when developing experiments for cover load transport processes. This paper presents a detailed experimental study of cover load transport rate in a laboratory flume with simulated ice particles and a simulated ice cover. The effect of the particle shape and size on cover load transport rate is quantified using the buoyant velocity and its velocity coefficient. The critical dimensionless flow strength is identified as an important parameter which determines the incipient motion of the under cover ice particles, and was calculated using hydraulic measurements obtained through laboratory experiments. A new cover load transport formula is introduced based on regression analysis of experimental data for a wide range of dimensionless flow strength conditions. The impact of incoming ice supply rate on the under cover ice transport rate was also investigated by altering the ice supply rate to the flume. A control volume analysis of ice discharge underneath the ice cover is used as the approach to quantify the dimensionless ice transport rate at different sections of the flume. The concept of equilibrium ice transport rate is introduced based on the experimental observations with variable incoming ice supply rates. The experimental observations on the impact of incoming ice supply were supported by an analysis of field data from Hequ Reach, China (Sun et al., 1986; Wang, 1992). The introduction of a cover load transport formula developed exclusively with simulated ice particles that have similar physical properties to ice forming in a natural environment, and the discussion on equilibrium ice transport rate are important contributions to advance the present understanding on under cover ice transport processes.

### 3.2.2 Introduction

The hydraulics of a river in a cold region climate is vastly impacted by various river ice processes during the winter. Steep fast flowing river sections with high turbulence can remain open throughout the winter season (Hicks, 2009). As a result of continuous supercooling, frazil particles will be generated in large quantities in these high velocity river sections, which can flocculate as the ice is transported downstream. The generated ice particles are transported downstream in suspension or at the open water surface at a certain rate determined primarily by meteorological conditions and can be entrained beneath an existing downstream ice cover. Depending on the hydraulic conditions, this ice may continue to be transported beneath the ice cover (termed under cover ice transport herein), or the ice can be deposited on the underside of the ice cover. Ice deposition will result in a local increase in ice thickness and can develop into a hanging dam if conditions are appropriate. In a deposition zone, the ice cover will continue to grow in thickness unless the supply of frazil slush from upstream is discontinued or the shear stress on the ice cover exceeds a limiting value. The basic river ice processes including formation of frazil ice, frazil ice dynamics, transportation of frazil ice, accumulation and growth are illustrated in Figure 3.1 (adapted from Gebre et al., 2013).

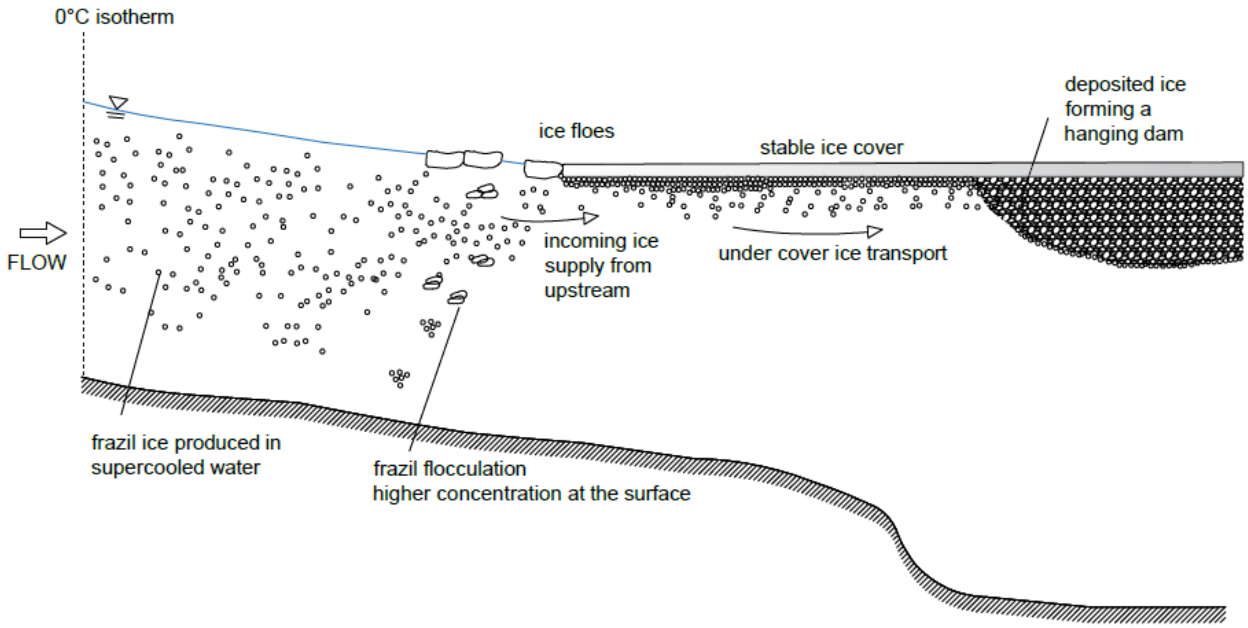


Figure 3.1. Under cover ice transport process in a river (adapted from Gebre et al., 2013).

The ice transport rate beneath an ice cover likely depends on the incoming ice supply rate, the ice properties (including freezing of interstitial water between ice granules), as well as local hydraulic conditions. The principles of under cover ice transport processes could be investigated using field monitoring, but this is often challenging due to accessibility issues at remote sites, hazardous conditions associated with the potential of ice movement, high cost, time, and level of effort associated with field data collection. Investigating under cover ice transport processes in a laboratory flume study is an effective alternative to understand the basic principles, while allowing for carefully controlled conditions and isolation of specific variables that are relevant to the processes being studied.

The objectives of this paper are to analyze the equilibrium cover load transport using a series of laboratory experiments and investigate the impact of incoming ice supply rate on the cover load transport rate. The experimental methodology to obtain the properties of simulated ice particles such as shape factor, buoyant velocity, critical dimensionless flow strength is summarized. Since these are site/study specific properties, this summary could be used as a resource in future studies related to under cover ice transport. A new cover load transport formula is proposed based on the cover load transport experiments conducted using simulated ice particles and a simulated ice cover. It is anticipated that in addition to improving our understanding of under cover ice transport processes, these results will also be useful for future work on hanging dam formation as well as for ongoing numerical modelling efforts that include under cover ice transport.

### 3.2.3 Background

Under cover ice transport, also termed cover load transport, refers to the movement of ice beneath a stable ice cover. Cover load transport is comparable to bed load transport, where the ice cover and ice particles are analogous to the riverbed and sediment, respectively. Sediment deposition is caused by gravitational forces, while ice deposition underneath the ice cover is governed by buoyancy forces. The two processes are illustrated in Figure 3.2 adapted from Shen and Wang (1995). In both cases the shear stress exerted by the water onto the ice and/or sediment causes the downstream movement.

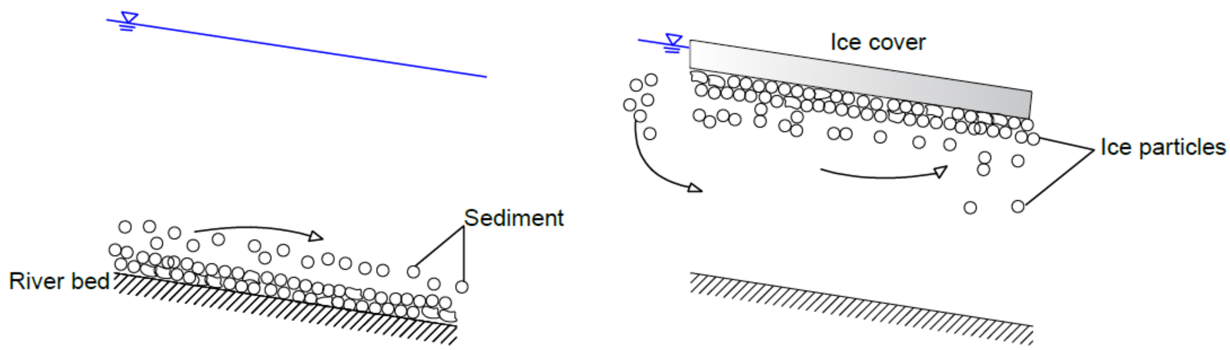


Figure 3.2. Bed load transport (left), cover load transport (right) adapted from Shen and Wang (1995).

Bed load transport processes are widely studied and there are many formulae to predict the bed load transport rate based on a hydraulic parameter such as the flow strength. There is no universal formula for bed load transport rate in a river due to the high variability in the parameters affecting the transport processes such as the particle specific gravity, angularity, and the particle size distribution (Bagnold, 1966). Bed load transport rate formulae for non-cohesive sediment often specify the range of specific gravity and/or the particle diameter for which the formulae can be used. Based on the analogous nature of the relationship between bed load and cover load transport processes, the basic theories in bed load transport can be used when developing a cover load transport formula.

Many bed load transport formulae can be arranged in the form shown in Equation 3.1, where $\Phi_n$ = dimensionless transport rate (-); $\Theta_n$ = dimensionless flow strength (-); $\Theta_c$ = critical dimensionless flow strength (-); and $\alpha$ and $\beta$ are empirical coefficients (-) (Chien, 1956; 1980).

$$\Phi_n = \alpha(\Theta_n - \Theta_c)^\beta \quad [3.1]$$

One of the prominent differences between bed load and cover load transport processes is the availability of material to be transported. Bed materials are available in large quantities and often can be considered as an infinite supply, but the incoming ice supply in a river primarily depends on the atmospheric conditions and the energy budget.

This paper discusses the concept of equilibrium and non-equilibrium ice transport rates. At equilibrium ice transport, ice cover thickness and the water surface elevation remain constant as the ice output from a certain control volume is equal to the ice input to that control volume and there will be no deposition or erosion of the ice cover. At non-equilibrium ice transport, the ice cover thickness and the water surface elevation change with varying incoming ice supply depending on whether the incoming ice supply is higher or lower than the equilibrium ice supply. Ice output from a control volume will no longer be equal to the ice input, erosion or deposition will occur based on the incoming ice supply rate.

*3.2.3.1 Previous studies on under cover ice transport processes*

A laboratory study was conducted by Wang, (1992) and Shen and Wang, (1995) to measure the under cover ice transport rate using a tilting glass-sided flume which was 7.5 m long, 0.3 m wide and 0.32 m deep. Six piezometric taps were installed 1.25 m apart along the centerline at the bottom of the flume to obtain the water depth measurements. Triangular and square-shaped plastic chips with a thickness of 1 mm were used for the experiments. The corresponding nominal diameter (diameter of a sphere of identical volume) was calculated as 2.41 mm. The plastic chips had a specific gravity of 1.055, so they were transported along the flume bed, which was therefore conceptually considered as the ice cover boundary in the experiments.

The first set of experiments were conducted with open water conditions and the second set of the experiments were conducted with a floating stationary cover. A layer of plastic chips was set up on the flume bed prior to each experiment and the flume slope was adjusted to an estimated value to obtain uniform flow conditions. The water discharge was set to a predetermined rate which varied between 1 L/s to 30 L/s and the chip (ice) discharge was fed from upstream at a constant rate. The ice discharge rate from upstream and the channel slope were then adjusted until uniform flow and equilibrium transport conditions were reached. Uniform flow was ensured when the flow depth was constant along the channel and equilibrium transport was ensured by supplying ice at a constant rate such that the thickness of the accumulation on the bed remained constant. The ice discharge output was determined using the weight of the plastic chips collected at the downstream end. The line of best fit for the laboratory flume data was determined through regression analysis and given in Equation 3.2, where $\Theta_c$ was estimated to be 0.041.

$$\Phi_n = 5.487(\Theta_n - \Theta_c)^{1.5} \qquad [3.2]$$

Extensive measurements of frazil slush accumulation and transport beneath an ice cover were conducted on the 70 km Hequ Reach of the Yellow River, China for a period of 6 years starting in the winter of 1982 (Sun et al., 1986; Wang, 1992). The Hequ Reach has a width on the order of 1000 m, with an upstream channel slope of 1 x $10^{-3}$ and a significantly milder downstream channel slope of 7.9 x $10^{-5}$. The study site consisted of 22 cross sections where river stage, discharge, water temperature, ice cover thickness, and frazil slush accumulation thickness were collected daily for each winter. If the ice cover was thin and unstable at a cross-section, only occasional measurements were collected. The river upstream of cross-section 1 was narrow, with a width of 300 m, and had a high flow velocity, which caused the section upstream of the study site to be open throughout the winter. This produced a large quantity of frazil ice, causing a hanging dam to form at cross-section 1. The mean diameter of the frazil granules deposited in this reach was estimated to be about 1 cm.

The field data from Sun et al. (1986) was compared with the Bagnold (1956) and Luque and Beek (1976) bed load transport formulae in the study by Shen and Wang (1995). The plot of dimensionless transport rate vs. dimensionless flow strength of the field study showed considerable scatter, but a simple linear regression obtained from the field data agreed with the Bagnold (1956) formula.

### 3.2.4 Equilibrium Transport Rate Experiments

#### *3.2.4.1 Methods*

The first set of experiments to investigate cover load transport were conducted in an acrylic flume (Fig. 3.3) in the Hydraulics Research & Testing Facility (HRTF) at the University of Manitoba. The flume was 22 m long and, 0.20 m wide with a height of 0.25 m. The flume consisted of three sections with two different bed slopes. The most upstream section that is 2 m long had a bed slope of 0.1%, the mid-section that is 8 m long had a steep bed slope of 1% and the downstream section that is 12 m long had a mild bed slope of 0.1%. A recirculating flow system equipped with a flow meter pumped water from an upstream reservoir at a maximum allowable flow of $3.5 \times 10^{-3}$ $m^3/s$ (3.5 L/s), and a minimum allowable flow of $0.5 \times 10^{-3}$ $m^3/s$ (0.5 L/s).

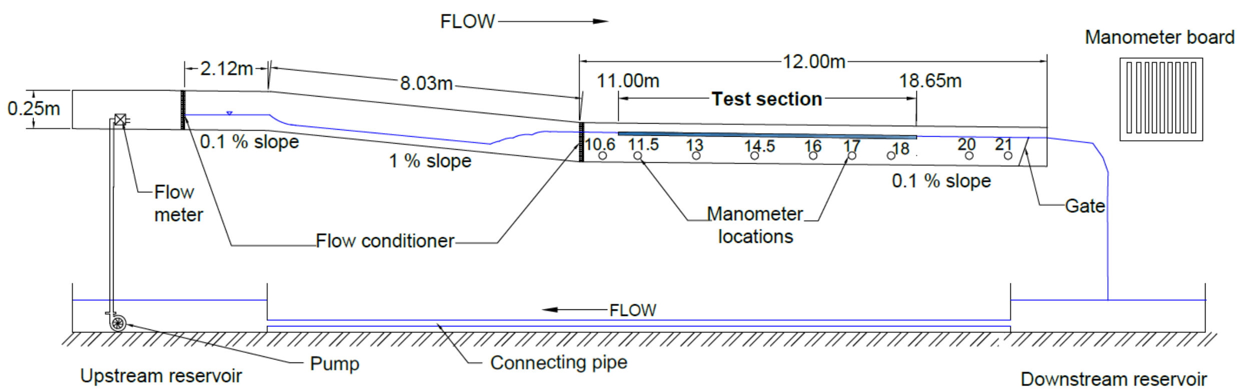


Figure 3.3. Acrylic flume schematic with the test section from station 11 to 18.65 m.

Flow conditioners were installed at the transition section from the steep to mild bed slope to force the hydraulic jump further upstream in the steep section, thereby reducing its influence on the flow in the downstream mild section where the cover load transport rate experiments were conducted. Nine manometer holes were tapped into the flume wall approximately every 1.5 meters, to obtain the water depths and water surface slope. A gate at the end of the flume controlled the water depth. Water flowed freely over the gate into a downstream reservoir that was connected to the upstream reservoir with a pipe, thus completing the recirculating flow system.

High density polyethylene (HDPE) pellets were used as simulated ice particles and standard packing bubble wrap as the simulated ice cover as shown in Figure 3.4(a) and Figure 3.4(b), respectively. The pellets were oval-shaped with a nominal diameter of 3.1 mm and a density of 950 $kg/m^3$. In comparison, the frazil granules at the Hequ Reach of the Yellow River had a mean diameter of 1 cm and a density of 917 kg/m$^3$. Frazil ice in a river is cohesive in the active stage and can often be found as flocs or porous slush. In contrast, the HDPE pellets that simulated ice particles in this experimental study did not possess cohesive properties. A floating rigid foam ledge which had a thickness equal to the pellet layer thickness and width equal to the flume width was installed at station 18.65 m to act as a 'sediment' (ice) trap.

(a)

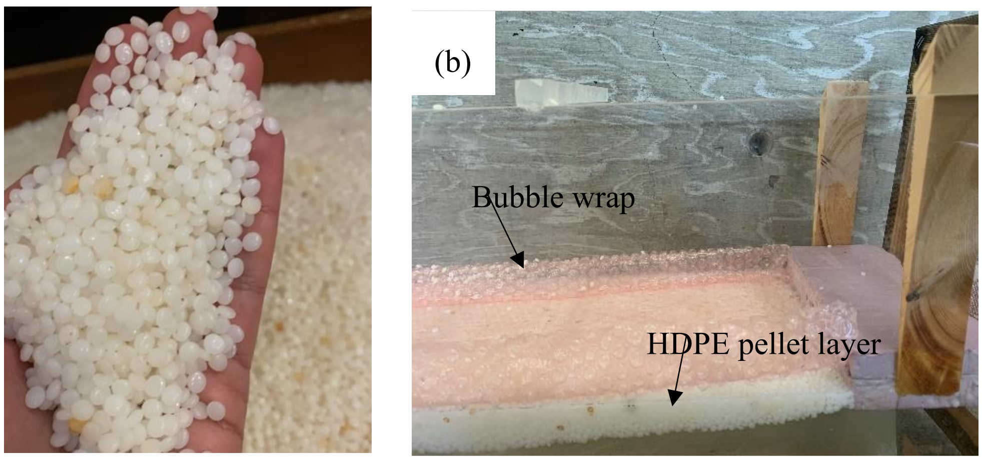


Figure 3.4. (a) HDPE pellets, (b) cover load experimental setup in the acrylic flume with HDPE pellets as simulated ice particles and bubble wrap as the simulated ice cover.

To accommodate a wider range of flow strengths in the cover load transport formula, a second set of experiments was conducted in a 13 m long, 0.94 m wide, and 0.72 m deep glass-walled flume with an adjustable slope located in the HRTF (Fig. 3.5). A flow straightener was placed at the flume inlet and water was supplied to the flume using a recirculating flow system which can provide flow at a maximum discharge of 0.3 m$^3$/s (300 L/s). The glass-walled experimental setup with the bubble wrap and HDPE pellets is shown in Figure 3.6. Water depth was measured at six locations using a ruler attached to the flume wall. The accuracy of the ruler reading was confirmed under open water conditions, by comparing the ruler measurement to the water depth obtained using a point gauge that has an accuracy of 0.2 mm.

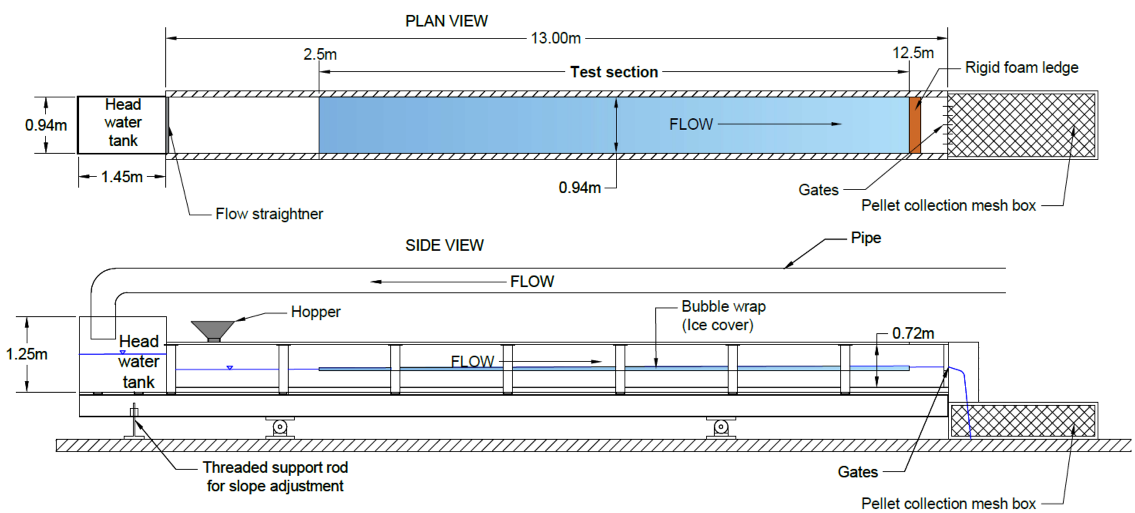


Figure 3.5. Glass-walled flume schematic with the test section from station 2.5 to 12.5 m.

The dimensionless flow strength ($\Theta_n$) and the dimensionless transport rate ($\Phi_n$) (Chien, 1956; 1980) for cover load transport experiments were calculated using Equation 3.3 and Equation 3.4 respectively, where $u_*$ is the shear velocity (m/s), $B$ is the buoyant velocity coefficient (-), $g$ is the gravitational acceleration (m/s$^2$), $d_n$ is the nominal diameter of HDPE pellets (m), $q_i$ is the volumetric transport rate of pellets per unit width (m$^3$/s/m), and $\Delta$ is the difference between specific gravities of water and ice (-).

$$\Theta_n = \frac{u_*^2}{B^2 g d_n \Delta} \quad [3.3]$$

$$\Phi_n = \frac{q_i}{B\sqrt{g d_n^3 \Delta}} \quad [3.4]$$

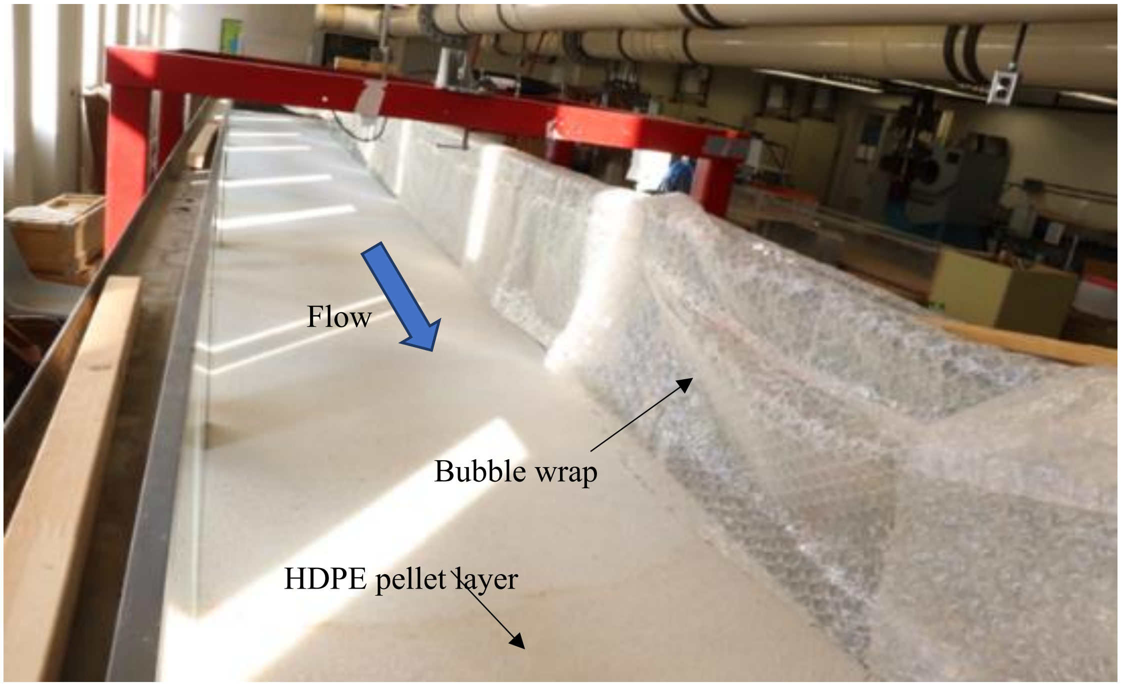


Figure 3.6. Cover load experimental setup in the glass-walled flume with HPDE pellet layer and bubble wrap in pellet layer establishment stage.

The tailwater gate setting, discharge, and bed slope (only in the glass-walled flume) were adjusted to attain a specific dimensionless flow strength at uniform flow conditions as given in Table 1. Initially, the pump was set to supply a low discharge, and a rigid foam ledge and a temporary mesh screen were placed at the flume outlet to prevent pellets from passing through. The first step was to establish a pellet layer with a uniform thickness of 2 cm throughout the channel from station 11.00 m to 18.65 m in the acrylic flume and from station 2.5 m to 12.5 m in the glass-walled flume. Then the bubble wrap was placed on the pellet surface. Discharge was then set to a pre-determined value and the mesh screen was removed from the downstream end of the flume allowing the pellets to be collected in the downstream end of the flume for a period of time, typically between 25 and 30 minutes for the acrylic flume and between 7-10 minutes for the glass-walled flume. The duration of the glass-walled flume experiments was shorter compared to the acrylic flume, as the flume was considerably larger, resulting in a large volume of pellets being collected over a brief time period. A constant supply of pellets was added to the flow throughout the duration of an experiment using a hopper system to maintain the uniform ice thickness and the ice thickness measurements were obtained using the rulers pasted along the flume wall, several times during the experiment. The equilibrium pellet supply rate for each experimental condition was determined by conducting preliminary experiments to maintain a uniform ice layer thickness. The collected pellets were air dried for 24 hours and the weight of the pellets was obtained using a scale that has an accuracy of 0.2 g for the acrylic flume and a scale with an accuracy of 0.1 kg for glass-walled flume. The experimental conditions for all uniform, steady state cover load experiments are summarized in Table 3.1.

Table 3.1. Experimental conditions and measured dimensionless transport rate for cover load transport rate experiments

| Flume | Bed slope (-) | $\Theta_n$ | $\Phi_n$ | Discharge (L/s) | Water velocity (m/s) | Water depth (m) | Water surface slope (-) |
|---|---|---|---|---|---|---|---|
| **Acrylic flume** | 0.0010 (constant bed slope) | 0.40 | critical shear | 1.6 | 0.09 | 0.086 | 0.0010 |
| | | 0.43 | 0.15 | 1.3 | 0.10 | 0.067 | 0.0012 |
| | | 0.45 | 0.14 | 1.9 | 0.11 | 0.086 | 0.0010 |
| | | 0.52 | 0.43 | 2.4 | 0.15 | 0.081 | 0.0012 |
| | | 0.53 | 0.33 | 2.5 | 0.13 | 0.094 | 0.0011 |
| | | 0.53 | 0.15 | 2.5 | 0.13 | 0.095 | 0.0011 |
| | | 0.56 | 0.36 | 2.1 | 0.12 | 0.086 | 0.0012 |
| | | 0.61 | 0.26 | 1.9 | 0.13 | 0.077 | 0.0015 |
| **Glass walled flume** | 0.0020 | 0.43 | critical shear | 5.2 | 0.18 | 0.035 | 0.0020 |
| | | 0.70 | 0.69 | 6.8 | 0.15 | 0.050 | |
| | | 0.81 | 0.32 | 9.2 | 0.17 | 0.058 | |
| | | 0.84 | 0.36 | 10.5 | 0.19 | 0.059 | |
| | | 0.93 | 0.50 | 12.9 | 0.20 | 0.067 | |
| | | 0.97 | 1.00 | 14.9 | 0.23 | 0.070 | |
| | | 1.33 | 1.17 | 18.5 | 0.20 | 0.099 | |
| | | 1.47 | 1.13 | 29.5 | 0.29 | 0.110 | |
| | | 1.70 | 1.85 | 32.2 | 0.26 | 0.129 | |
| | 0.0030 | 2.02 | 1.88 | 21.0 | 0.22 | 0.097 | 0.0030 |
| | | 2.02 | 3.00 | 22.3 | 0.24 | 0.100 | |
| | | 2.56 | 3.46 | 43.1 | 0.35 | 0.130 | |
| | 0.0050 | 3.07 | 5.50 | 31.6 | 0.37 | 0.089 | 0.0050 |
| | | 3.37 | 6.45 | 40.2 | 0.43 | 0.100 | |
| | | 3.37 | 6.25 | 41.5 | 0.44 | 0.100 | |
| | 0.0090 | 3.79 | 7.10 | 25.2 | 0.45 | 0.059 | 0.0090 |

The shear stress exerted on the ice cover boundary was calculated using Equation 3.5, where $\tau_b$ is the boundary shear stress (Pa), $\gamma$ is the specific weight of water (N/m$^3$), $R$ is the hydraulic radius (m), and $S_w$ is the water surface slope (-). Detailed acoustic Doppler velocimeter measurements of flow beneath a simulated ice cover in a rectangular channel by Peters et al. (2018) showed that the shear stress applied to the ice cover can be approximated by multiplying the cross sectional-averaged shear stress by a factor of 1.2. In the current study, the velocity profile underneath the ice cover in the glass walled flume was obtained using the acoustic Doppler velocimeter and log-law fitting was used to confirm that the same factor of 1.2 can be applied to the experiments in this study. The critical boundary shear stress was determined to be 0.31 Pa by observing the incipient motion of HDPE pellets. The corresponding critical shear velocity was calculated to be 0.02 m/s using Equation 3.6 where $u_*$ is the shear velocity (m/s), and $\rho$ is the density of water (kg/m$^3$).

$$\tau_b = 1.2\gamma R S_w \quad [3.5]$$

$$u_* = \sqrt{\frac{\tau_b}{\rho}} \quad [3.6]$$

The buoyant velocity was measured to be 0.042 m/s in still water and was compared to the theoretical velocity that was calculated as 0.045 m/s using the Rubey (1993) formula given by Equation 3.7, where $\omega_i$ is the buoyant velocity (m/s), $k_1$, $k_2$ are empirical coefficients ($k_1$=1.22, $k_2$=4.27) (-), $\nu$ is the kinematic viscosity of water (m$^2$/s), and $\rho_i$ is the density of HDPE pellets (kg/m$^3$). The measured buoyant velocity was used in the subsequent calculations for this study.

$$\omega_i = -4\frac{k_2}{k_1}\frac{\nu}{d_n} + \sqrt{\left(4\frac{k_2}{k_1}\frac{\nu}{d_n}\right)^2 + \frac{4}{3k_1}\frac{|\rho_i - \rho|}{\rho} g d_n} \qquad [3.7]$$

The HDPE pellets were oval-shaped, and the effect of particle shape was considered by incorporating the buoyant velocity coefficient in transport rate calculations according to the methodology presented in Swamee and Ojha (1992). For a single HDPE pellet, the lengths along the principal axes were measured as 5 mm, 4 mm, and 1.5 mm, respectively. The nominal diameter of the pellets was calculated to be 3.1 mm using Equation 3.8, where $V$ is the volume of a single HDPE pellet ($m^3$). The shape factor accounts for the hydrodynamic forces acting on the particle and was calculated using Equation 3.9, where $\alpha$ is the shape factor (-), and $a, b, c$ are the lengths of longest, intermediate, and shortest the principal axes (m), respectively.

$$d_n = \left(\frac{6V}{\pi}\right)^{1/3} \qquad [3.8]$$

$$\alpha = \frac{c}{\sqrt{ab}} \qquad [3.9]$$

The buoyant velocity coefficient, B (-), was determined to be 0.72 using Equation 3.10, where $C_D$ is the drag coefficient (-). The drag coefficient was determined to be 2.58 using Equation 3.11, in which $Re$ is the particle Reynolds number (-), which was calculated as 117.5 using Equation 3.12.

$$B = \sqrt{\frac{4}{3C_D}} \qquad [3.10]$$

$$C_D = \left[\frac{48.5}{(1+4.5\alpha^{0.35})^{0.8} Re^{0.64}} + \left(\frac{Re}{Re+100+1000\alpha}\right)^{0.32} + \frac{1}{(\alpha^{18}+1.05\alpha^{0.8})}\right]^{1.25} \qquad [3.11]$$

$$Re = \frac{\omega_i d_n}{\nu} \qquad [3.12]$$

*3.2.4.2 Results and Discussion*

The results for the equilibrium transport experiments conducted in both acrylic and glass-walled flumes are shown in Figure 3.7.

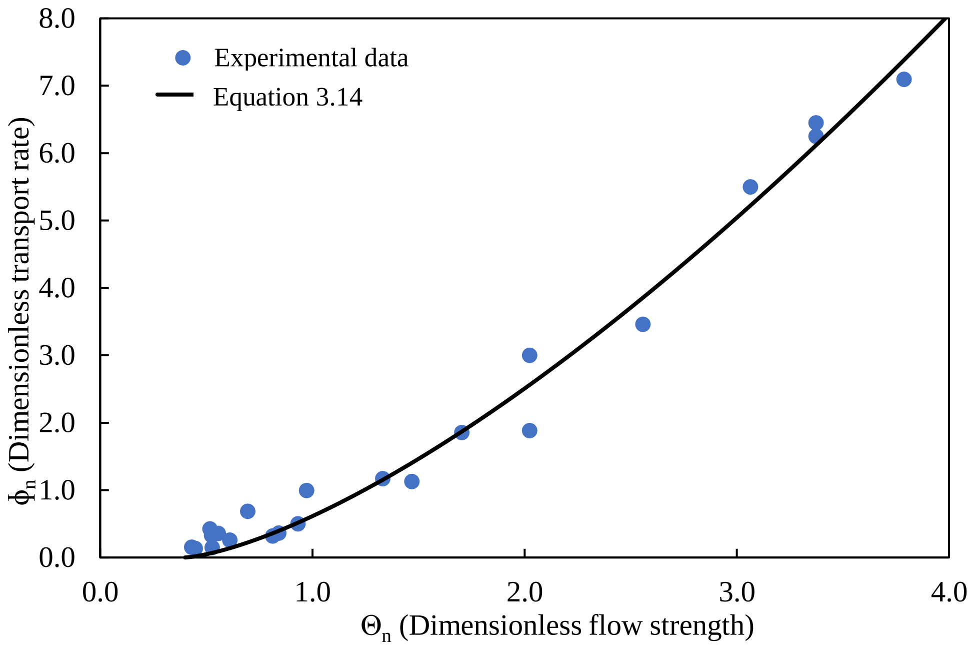


Figure 3.7. Equilibrium transport experimental results with the new cover load transport formula.

Regression analysis was conducted to obtain the line of best fit for the experimental data by minimizing the root mean squared error (RMSE) according to Equation 3.13. The new cover load transport formula corresponding to equilibrium ice transport rate for a certain flow strength is presented in Equation 3.14 where the ice thickness and water surface elevation remained constant throughout the entire duration of the experiment and the ice output was equal to the ice input.

$$RMSE = \sqrt{\frac{1}{N}\sum_{i=1}^{N}\left[\left(\Phi_{n,calculated} - \Phi_{n,measured}\right)\right]^2} \quad [3.13]$$

$$\Phi_n = 1.27(\Theta_n - 0.396)^{1.44} \qquad [3.14]$$

The experimental uncertainties for both the dimensionless flow strength and the dimensionless transport rate were quantified using the methodology presented in Coleman and Steele (1999). The uncertainty of the dimensionless flow strength ranged between 4% to 12% and the uncertainty of dimensionless transport rate was determined to vary between 2% to 5%. The results of equilibrium transport rate experiments are compared to the previously reported results of Shen and Wang (1995) in Figure 3.8. The Shen and Wang (1995) transport rate formula given in Equation 3.2 with a critical dimensionless flow strength ($\Theta_c$) of 0.041 and the same formula with a $\Theta_c$ of 0.396 to match with the $\Theta_c$ obtained from this experimental study are also shown on Figure 3.8.

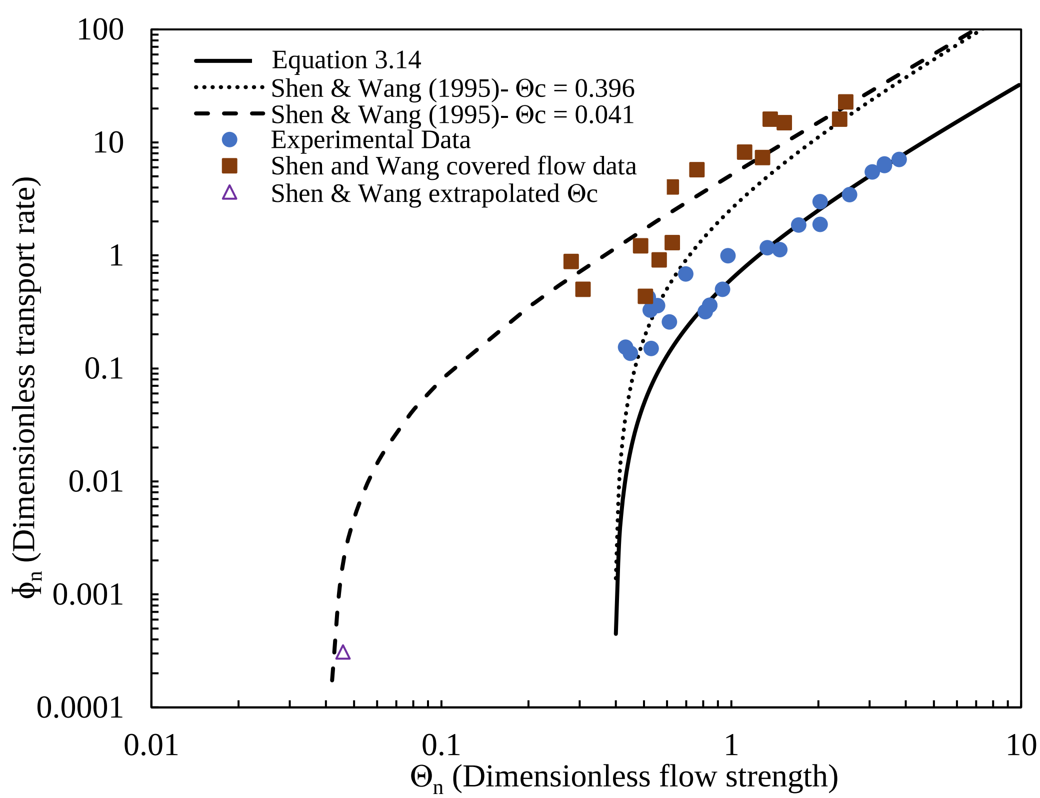


Figure 3.8. Comparison of equilibrium transport experiments to Shen and Wang (1995).

The observed dimensionless transport rate for a specific flow strength during the experiments is lower than that for the Shen and Wang (1995) cover load transport formula. This difference in transport rates could be explained by factors such as the particle shape, presence or absence of dunes during an experiment and the dependence of critical dimensionless flow strength on the particle properties.

In the present study, HDPE pellets with a uniform nominal diameter of 3.1 mm were used as simulated ice for the experiments whereas random shaped (triangular and square) 1.0 mm thick plastic chips with a range of $d_{50}$ varying from 1.0 mm to 5.6 mm were used for Shen and Wang (1995) experiments. Even though the effect of particle shape and size is considered through fall/buoyant velocity coefficients, the forces in between the adjacent particles are not taken into consideration when developing the cover load formula. Straight-edged thin particles have a higher likelihood of projecting into the flow and experiencing a downstream drag force compared to more spherical particles. In the present experiment, it could be noted that the HDPE pellets were tightly packed with minimal void spaces between particles as shown in Figure 3.9 and that a relatively high shear stress was required to initiate the pellet transport.

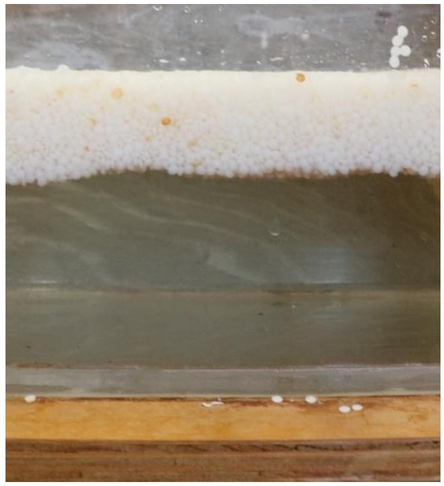

Figure 3.9. A layer of tightly packed HDPE pellets in a cover load transport rate experiment.

The presence or absence of dunes is another main difference between the Shen and Wang (1995) study and the current study which might help explain the differences in transport rates. In the current study, the flow was set to uniform, steady state conditions and a constant incoming ice supply rate was maintained. The initial ice cover thickness, water surface slope and the water depth were consistent throughout the duration of the experiment, and no dunes were observed. The transport rate was determined using the weight of the pellets collected at the downstream end over the duration of the experiment. This methodology was based on the assumption that the transport rate is equal in all sections of the flume, throughout the duration of the experiment. Shen and Wang (1995) reported dunes which typically had an amplitude of 1 to 2 cm, a wavelength of 40 to 125 cm, that travelled with a velocity of 2 cm/min to 11 cm/min. It is also stated in Shen and Wang (1995) that there were distinct layered structures that appeared in the bed deposits when the dunes were present. These dunes will have increased the flow resistance and may have caused the flow conditions to differ from the initial uniform conditions.

Critical dimensionless flow strength ($\Theta_c$), corresponds to the dimensionless shear stress applied by the flow that is required to initiate consistent cover load transport. In the present study, $\Theta_c$ was determined by observing the incipient motion of pellets. The critical boundary shear stress was calculated at incipient motion using the water depth and the water surface slope measurements in both the acrylic and glass walled flumes. The critical dimensionless flow strength was determined to be 0.396 using Equation 3.3, which is an order of magnitude higher than the previously reported value of 0.041 by Shen and Wang (1995), which was estimated by extrapolating data in the $\Phi$ vs. $\Theta$ plot (extrapolated value is shown in Fig. 3.8). The order of magnitude difference of $\Theta_c$ between the present study and the Shen and Wang (1995) study indicates that a higher shear stress was required to initiate the transportation of pellets in the current laboratory study, and that a smaller volume of pellets was moved with an equivalent flow strength compared to the previous study. The disparity between these values warrants further explanation by assessing a few key contributing factors.

It is important to note that the critical dimensionless flow strength is dependent on many factors including the size, density, and buoyant velocity coefficient of the particle. To highlight the importance of these factors, Table 3.2 presents a comparison of several parameters that were used when estimating $\Theta_c$ for cover load transport processes in this study to those used to estimate $\Theta_c$ for bed load transport processes (1 mm diameter sand) in the same flume (Senarathbandara et al., 2021).

Table 3.2. Comparison of parameters used for $\Theta_c$ calculation for cover load and bed load processes in the same flume.

| Parameter | Cover load experiments | Bed load experiments |
|---|---|---|
| $\boldsymbol{d_n}$ (mm) | 3.1 | 1.0 |
| $\boldsymbol{\rho_s}$ (kg/m$^3$) | 950 | 2650 |
| $\boldsymbol{\Delta}$ | 0.05 | 1.65 |
| Buoyant/fall velocity coefficient | 0.72 | 0.77 |
| Critical boundary shear stress (Pa) | 0.31 | 0.38 |
| Critical shear velocity (m/s) | 0.02 | 0.02 |
| $\boldsymbol{\Theta_c}$ | 0.396 | 0.041 |

The order of magnitude difference between $\Theta_c$ of cover load transport and bed load transport experiments can be explained by the order of magnitude difference in the specific gravities of ice and water compared to that of sediment and water ($\Delta$). One of the important contributions of this study is to introduce a new $\Theta_c$ value based on hydraulic measurements and experimental observations that is more representative of ice particles.

### 3.2.5 Non-equilibrium Transport Rate Experiments

#### *3.2.5.1 Methods*

Additional experiments were conducted in the acrylic flume (Fig. 3.3) to investigate the effect of different incoming ice supply rates on the ice transport rate underneath the ice cover. The experiments were designed by first setting the dimensionless flow strength ($\Phi_n$) and determining the corresponding equilibrium dimensionless transport rate ($\Phi_E$) using

Equation 3.14. The incoming ice supply rate ($\Phi_{in}$) was then set at a rate that was either greater than or less than $\Phi_E$. The dimensionless flow strength for each experimental condition was achieved by setting the water discharge and downstream water depth according to the values specified in Table 3.3.

Table 3.3. Experimental conditions for varying incoming ice supply rate experiments.

| Case | Condition | $\Phi_{in}$ | $\Phi_E$ | $\Theta_n$ | Water discharge (L/s) | Average water depth (m) |
|---|---|---|---|---|---|---|
| **Case 1** | Ice supply = 0 | 0.00 | 1.44 | 1.49 | 1.46 | 0.040 |
| **Case 2** | Ice supply < equilibrium | 0.05 | 1.44 | 1.49 | 1.46 | 0.040 |
| **Case 3** | Ice supply > equilibrium | 0.60 | 0.04 | 0.48 | 1.46 | 0.066 |

Initially, a HDPE pellet layer with a constant thickness of 2 cm was established between stations 11.0 and 18.65 m. HDPE pellets were supplied to the channel using the upstream hopper system at a constant supply rate ($\Phi_{in}$) for the full 60-minute duration of the experiment. Thickness of the pellet layer (ice thickness) and the flow depth were measured at 8 cross-sectional locations (stations 11, 12, 13, 14, 15, 16, 17, and 18 m) in the flume using a ruler attached to the flume wall at 5 minute intervals in the first half (0-30 minutes) and 10 minute intervals in the second half (30-60 minutes) of the experiment.

For the analysis of ice transport rate underneath the ice cover, the test section of the flume from 11 to 18 m was divided into 7 control volumes each with a length of 1 m. As shown in Figure 3.10, the ice discharge input to the most upstream control volume was the incoming ice supply rate to the flume. The ice discharge input to each control volume starting from the 2nd control volume was determined as the ice discharge output from the previous control volume.

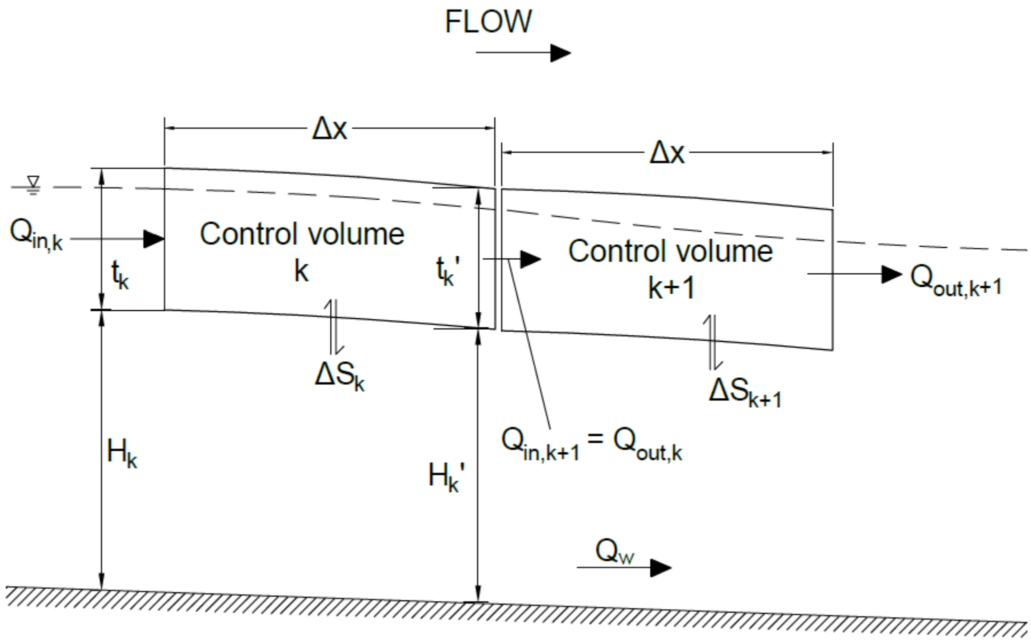


Figure 3.10. Definition sketch for under cover ice transport from an upstream control volume to the consecutive downstream control volume.

Ice discharge output from a control volume was calculated using Equation 3.15, where $Q_{out,k}$ is the ice discharge output from the kth control volume ($m^3/s$), $Q_{in,k}$ is the ice discharge input to the kth control volume ($m^3/s$), $\Delta S_k$ is the change in storage within the kth control volume ($m^3$), $\Delta t$ is the time interval between two measurements (s), and $p$ is the porosity of the accumulation which was determined to be 0.3 for the experiments. In comparison, the porosity of frazil slush in the Hequ Reach was determined to be 0.4 from the field measurements. The change in storage was calculated using Equation 3.16, where $A_{initial,k}$ and $A_{final,k}$ are the initial and the final cross-sectional areas of the kth control volume respectively ($m^2$), and $\Delta x$ is the length of the control volume (m).

$$Q_{out,k} = Q_{in,k} + \frac{(1-p)\Delta S_k}{\Delta t} \quad [3.15]$$

$$\Delta S_k = \left(A_{final,k} - A_{initial,k}\right)\Delta x \quad [3.16]$$

If there was no change in storage within the control volume ($\Delta S_k = 0$), the ice transport rate underneath the ice cover within that control volume was in equilibrium, so $Q_{out,k}$ was equal to $Q_{in,k}$. According to Equation 3.16, if the change in storage was greater than zero ($\Delta S_k > 0$), there was net deposition within the control volume, and $Q_{out,k}$ was less than $Q_{in,k}$. If the change in storage was less than zero ($\Delta S_k < 0$), there was net erosion within the control volume, and $Q_{out,k}$ was greater than $Q_{in,k}$.

Average values were obtained for ice thickness and under ice flow depth of each control volume using Equation 3.17 and Equation 3.18 respectively, where $t_{k,avg}$ is the average thickness of the ice cover (m),$t_k$ and $t_k{}'$ (m), are the ice thickness at the upstream and downstream nodes of the k$^{th}$ control volume, respectively. $H_{k,avg}$ is the average flow depth underneath the ice cover (m), $H_k$ and $H'_k$ are the flow depths at the upstream and downstream nodes of the k$^{th}$ control volume (m), respectively.

$$t_{k,avg} = \frac{t_k + t_k'}{2} \quad [3.17]$$

$$H_{k,avg} = \frac{H_k + H_k'}{2} \quad [3.18]$$

For each control volume the shear velocity underneath the ice cover ($u_{*,k}$), the hydraulic radius ($R_k$) and the friction slope ($S_{f,k}$) were determined based on Equation 3.19, Equation 3.20, and Equation 3.21, respectively.

$$u_{*,k} = \sqrt{gR_k S_{f,k}} \quad [3.19]$$

$$R_k = \frac{H_{k,avg}}{1+\left({n_b}/{n_i}\right)^{3/2}} \quad [3.20]$$

$$S_{f,k} = \frac{V_{w,k}^2 n_c^2}{\left(H_{k,avg}/2\right)^{4/3}} \quad [3.21]$$

The average flow velocity for each control volume was calculated using Equation 3.22, where $V_{w,k}$ is the average flow velocity for the k$^{th}$ control volume (m/s), $Q_w$ is the water discharge (m$^3$/s) and $b$ is the flume width (m). Bed, ice cover and composite Manning's roughness coefficients are denoted by $n_b$, $n_i$, and $n_c$ respectively.

$$V_{w,k} = \frac{Q_w}{H_{k,avg} b} \quad [3.22]$$

The dimensionless flow strength for each control volume was calculated using Equation 3.3. The dimensionless ice transport rate underneath the ice cover for each control volume was determined based on Equation 3.23.

$$\Phi_n = \frac{\left({Q_{out,k}}/{b}\right)}{B\sqrt{g d_n^3 \Delta}} \quad [3.23]$$

*3.2.5.2 Results and Discussion*

Case 1: No ice supply

Figure 3.11 shows the dimensionless transport rate at various control volumes of the flume at different time increments for Case 1 when there was no incoming ice supply. Each control volume is indicated in Figure 3.11 by the start and the end streamwise distance of the control volume, for example S11-S12 indicates the control volume between stations 11 and 12 m of the flume. When there was no ice supply to the flume, the thickness of the ice cover decreased due to erosion. The observed dimensionless transport rates were lower than the dimensionless transport rates obtained from Equation 3.14 which was developed based on the uniform, steady state experiments with an equilibrium ice supply rate. Due to the continuous erosion of the ice cover, the water surface elevation and the water surface slope decreased during the experiment, reducing the resistance to the flow. As a result, the dimensionless flow strength at the end of the experiment was lower than the initial dimensionless flow strength.

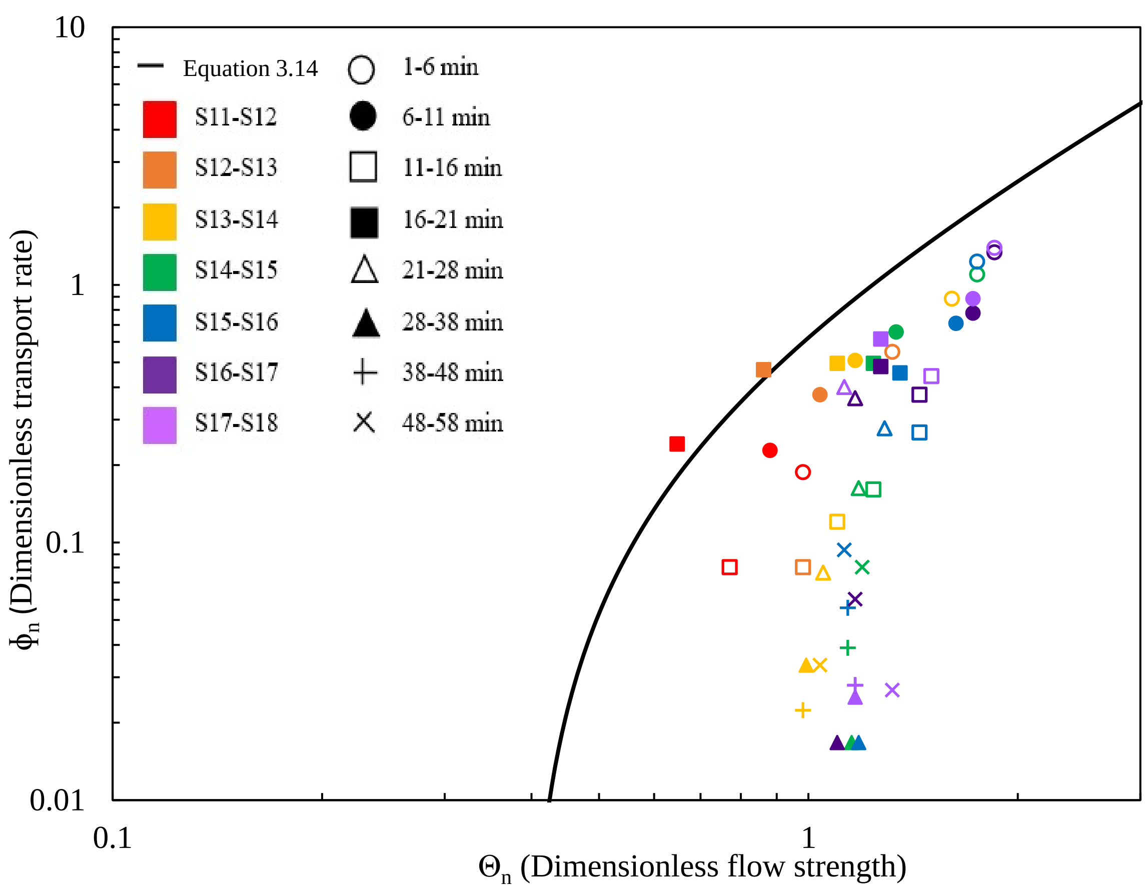


Figure 3.11. Transport rates at various control volumes of the flume for Case 1: no ice supply.

Figure 3.12 presents the same data, colored according to the time period that the measurements were taken, rather than grouped by control volume location. During the initial stages of the experiment, the dimensionless transport rates are closer to the values predicted by the experimentally derived Equation 3.14, compared to the second half of the experiment. This is because even though there was no incoming ice supply, ice eroded from upstream control volumes provided sufficient ice supply to the downstream control volumes to stay close to the equilibrium dimensionless transport rate. As time progressed, the total ice volume in the flume became scarce, which caused the dimensionless transport rates to drop across all control volumes in the flume.

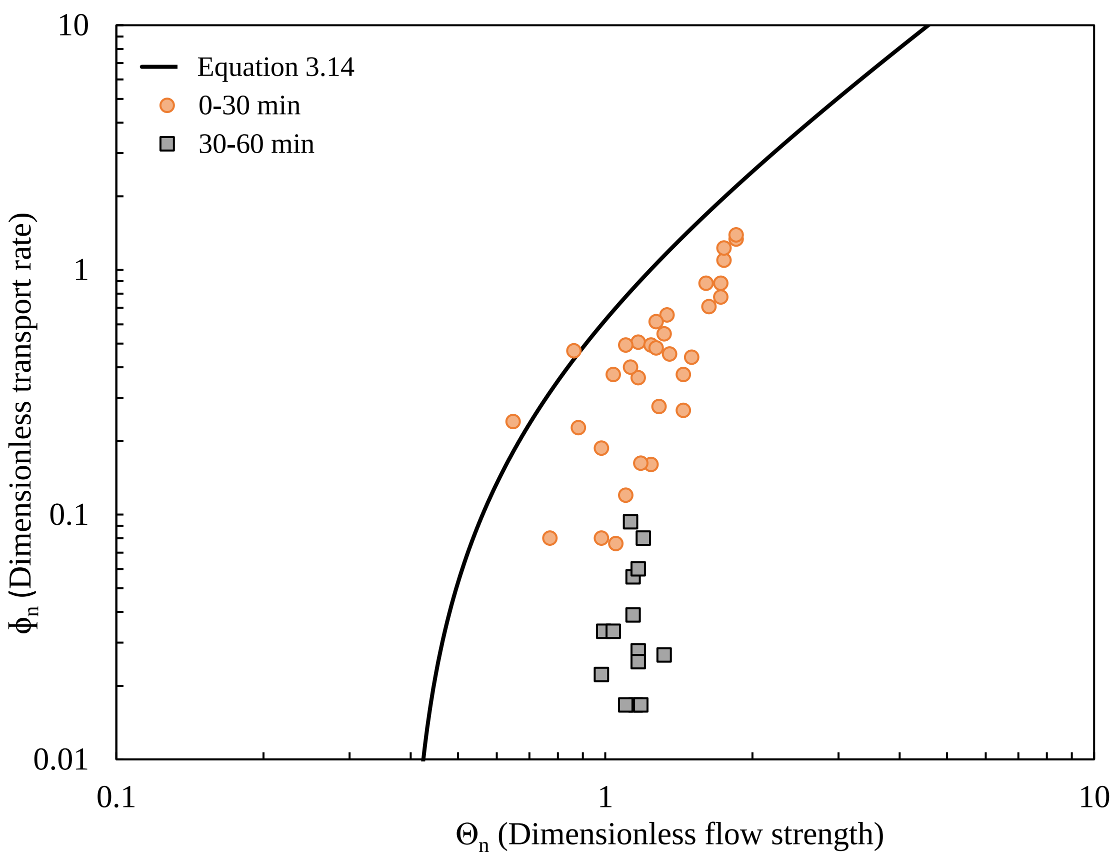


Figure 3.12. Transport rates at various times for Case 1: no ice supply.

Case 2: Lower than equilibrium ice supply

Figure 3.13 shows the dimensionless transport rate at various control volumes of the flume at different time increments for Case 2 for low incoming ice supply. When the incoming ice supply was lower than the rate required for equilibrium, there was net erosion in the flume and the flow strength decreased similar to Case 1; however, the low incoming ice supply slowed the rate of erosion. The dimensionless transport rates in Case 2 are lower than the experimentally derived Equation 3.14 for equilibrium conditions, but higher than the dimensionless transport rates for Case 1.

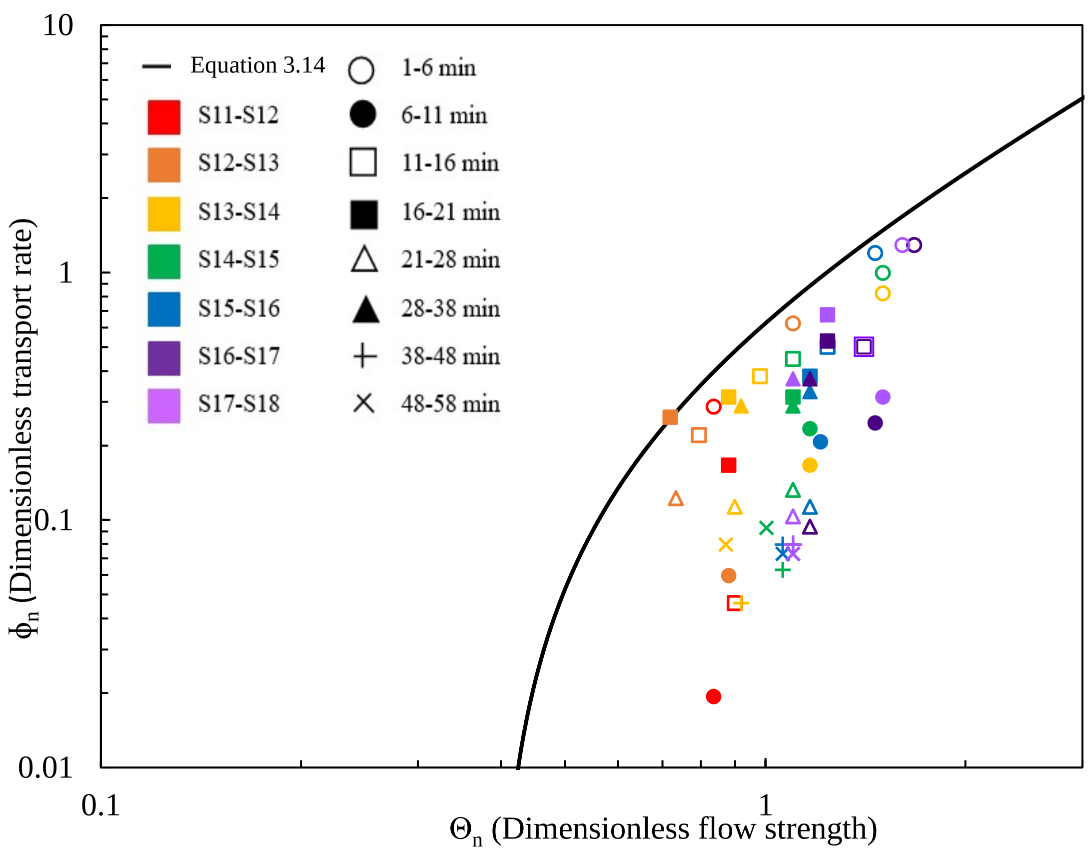


Figure 3.13. Transport rates at various control volumes of the flume for Case 2: lower than equilibrium ice supply.

Figure 3.14 presents the results colored according to time where the dimensionless transport rates were observed to drop as time progressed because the incoming ice supply was still not sufficient to maintain equilibrium. Since ice from upstream control volumes provided the ice supply for downstream control volumes, the transport rates at some downstream control volumes were higher even during the latter half of the experiment than the transport rates at the upstream cross-sections during the first half.

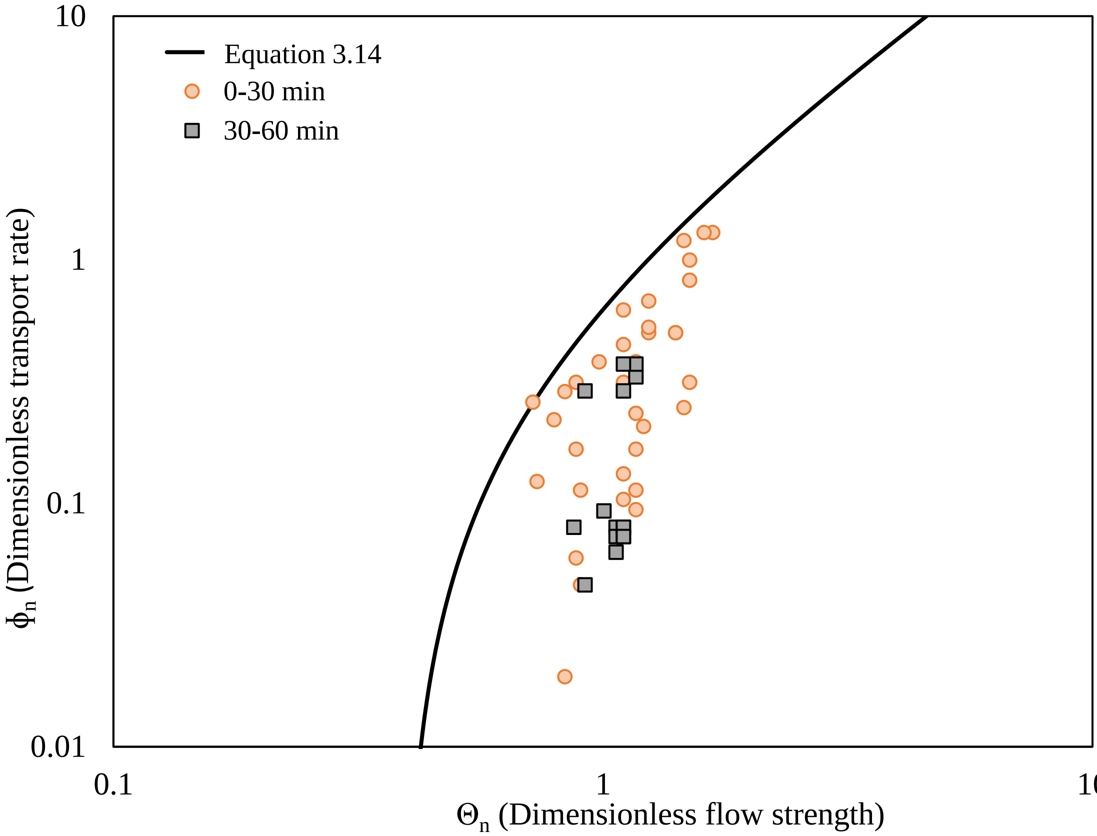


Figure 3.14. Transport rates at various times for Case 2: lower than equilibrium ice supply.

Case 3: Higher than equilibrium ice supply

Figure 3.15 shows the dimensionless transport rate at various control volumes of the flume at different time increments for Case 3 for high incoming ice supply. A lower flow strength was used for Case 3 compared to Case 1 and Case 2, since it was difficult to maintain the ice supply exceeding the equilibrium transport rate for a high flow strength condition. When the incoming ice supply was higher than the rate required for equilibrium, it was observed that the thickness of the ice cover increased, hence causing net deposition in the flume. The observed dimensionless transport rates were higher than the transport rates obtained from Equation 3.14 for uniform, steady state conditions. The water surface elevation and the water surface slope increased during the experiment due to the deposition underneath the ice cover. As the thickness of the ice cover increased, the flow resistance also increased. As a result, the dimensionless flow strength at the end of the experiment was higher than the initial dimensionless flow strength.

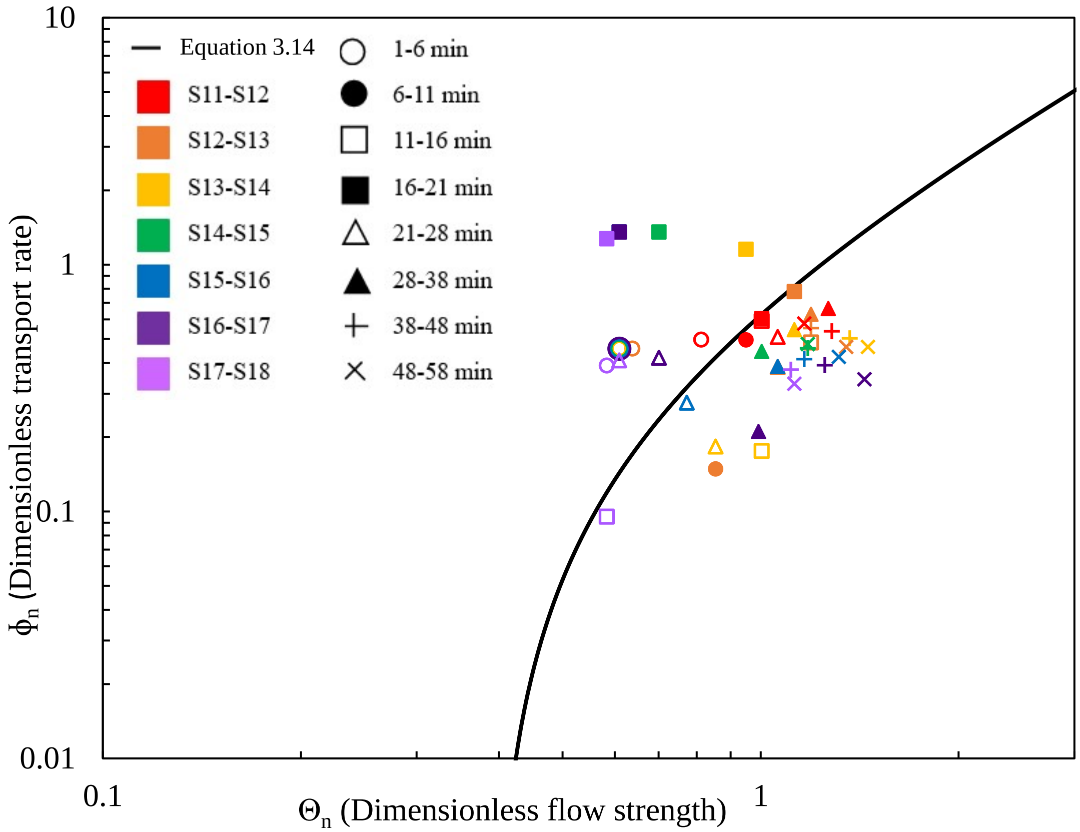


Figure 3.15. Transport rates at various control volumes of the flume for Case 3: higher than equilibrium ice supply.

The same data are presented in Figure 3.16, categorized according to the time period of the measurements. Initially the dimensionless transport rates were higher than the values predicted using Equation 3.14 because there was a high incoming ice supply rate in the flume. The dimensionless flow strength increased as a result of deposition in the flume and towards the second half of the experiment the observations began to shift towards the experimentally derived equilibrium equation. It was observed that the flow strength in the flume adjusts itself towards the line for equilibrium ice transport when there is abundant ice supply in the flume.

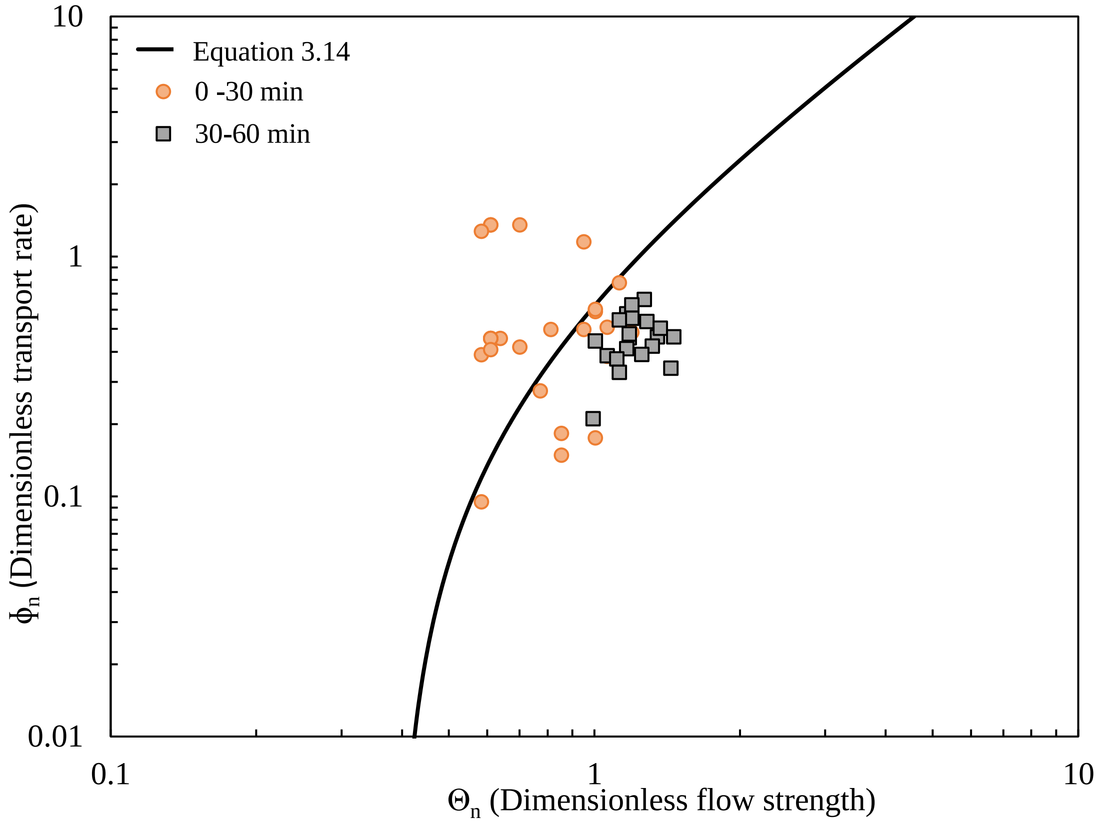


Figure 3.16. Transport rates at various times for Case 3: higher than equilibrium ice supply.

*3.2.5.3 Comparison to Previous Field Studies*

The data from the Hequ Reach, China for 1986-1987 and 1987-1988 winters (Sun et al., 1986; Wang, 1992) was analyzed to further understand the impact of incoming ice supply rate on the under cover ice transport rate. The river reach between any 2 cross-sections was treated as a control volume. Unlike the laboratory ice supply rate experiments, the incoming ice supply to the reach from the upstream was an unknown. The analysis by Wang (1992) used an approach of proceeding from downstream to upstream when estimating ice transport rates based on the field observation that the ice discharge at the most downstream boundary was negligible. Therefore, Equation 3.24 (Wang, 1992) was used to obtain the under cover ice transport rate output of successive cross-sections proceeding from downstream to upstream, where $Q_k^m$ is the time averaged ice transport rate during the m$^{th}$ time interval at the k$^{th}$ cross-section (m$^3$/s), $Q_{k+1}^m$ is the time averaged ice transport rate during the m$^{th}$ time interval at the k+1$^{th}$ (downstream from k$^{th}$ cross-section) cross-section (m$^3$/s), $A_k^m$ is the time averaged cross-sectional area of ice accumulation during the m$^{th}$ time interval at the k$^{th}$ cross-section (m$^2$), $A_k^{m-1}$ is the time averaged cross-sectional area of ice accumulation during the m-1$^{th}$ time interval at the k$^{th}$ cross-section (m$^2$), $\Delta x_k$ is the distance between k$^{th}$ and k+1$^{th}$ cross-sections (m), $\Delta t_m$ is the m$^{th}$ time interval (s) and, $p$ = porosity of frazil ice accumulation which is 0.4 according to the field measurements (-).

$$Q_k^m = Q_{k+1}^m + \frac{(1-p)\Delta x_k}{\Delta t_m}(A_k^m - A_k^{m-1}) \qquad [3.24]$$

The ice discharge calculations for cross-sections 1-7 were used in the analysis since the ice discharges in the downstream cross-sections were very small in comparison to the upstream cross-sections and also to be consistent with the field data analysis by Wang (1992). The dimensionless ice transport rate at each cross-section was calculated using Equation 3.25, where $b_k$ is the average top width of the river between k$^{th}$ and k+1$^{th}$ cross-sections (m), and $B$ is the buoyant velocity coefficient that was set as 1.0 in the analysis based on the field observation that particles were nearly spherical (Wang, 1992). The nominal diameter of an ice particle ($d_n$) was reported as 0.007 m in the 1986/87 winter, and 0.011 m in 1987/88. The density of ice was reported as 917 kg/m$^3$, therefore Δ is equal to 0.083.

$$\Phi_n = \frac{\left(Q_k^m / b_k\right)}{B\sqrt{g d_n^3 \Delta}} \qquad [3.25]$$

The dimensionless flow strength for each cross-section was calculated using Equation 3.3. The river cross-section was assumed to be rectangular when calculating the flow area, wetted perimeter, and the hydraulic radius since the field data only provides a single value at each cross-section for water surface elevation and the thickness of the ice cover.

The dimensionless transport rates for the Hequ Reach during both winters are shown in Figure 3.17. The field observations showed that there was a large hanging dam formation in the Hequ Reach, which explains the cluster of points located above the experimentally derived Equation 3.14 for equilibrium ice transport. These points correspond to depositions in the reach where the flow strength was not high enough to transport the incoming ice further downstream in the reach. This field data analysis is comparable with the high ice supply experiments conducted in the acrylic flume. The dimensionless transport rates are categorized according to the incoming ice supply rate for each control volume to understand the impact of incoming ice supply rate on the under cover ice transport rate. At low incoming ice supply rates (0-1 $m^3/s$), the transport rates are in the vicinity of Equation 3.14 for equilibrium transport, which means the flow strength had the capacity to transport the incoming ice supply and the equilibrium ice transport capacity can be closely maintained. At medium ice supply rate (1-2 $m^3/s$), the flow strength of the river was not sufficient to maintain the equilibrium transport rate, and this contributed to depositions in the reach. There is a more pronounced effect on ice transport rates at high ice supply rates (2-10 $m^3/s$) which lead to large depositions underneath the ice cover.

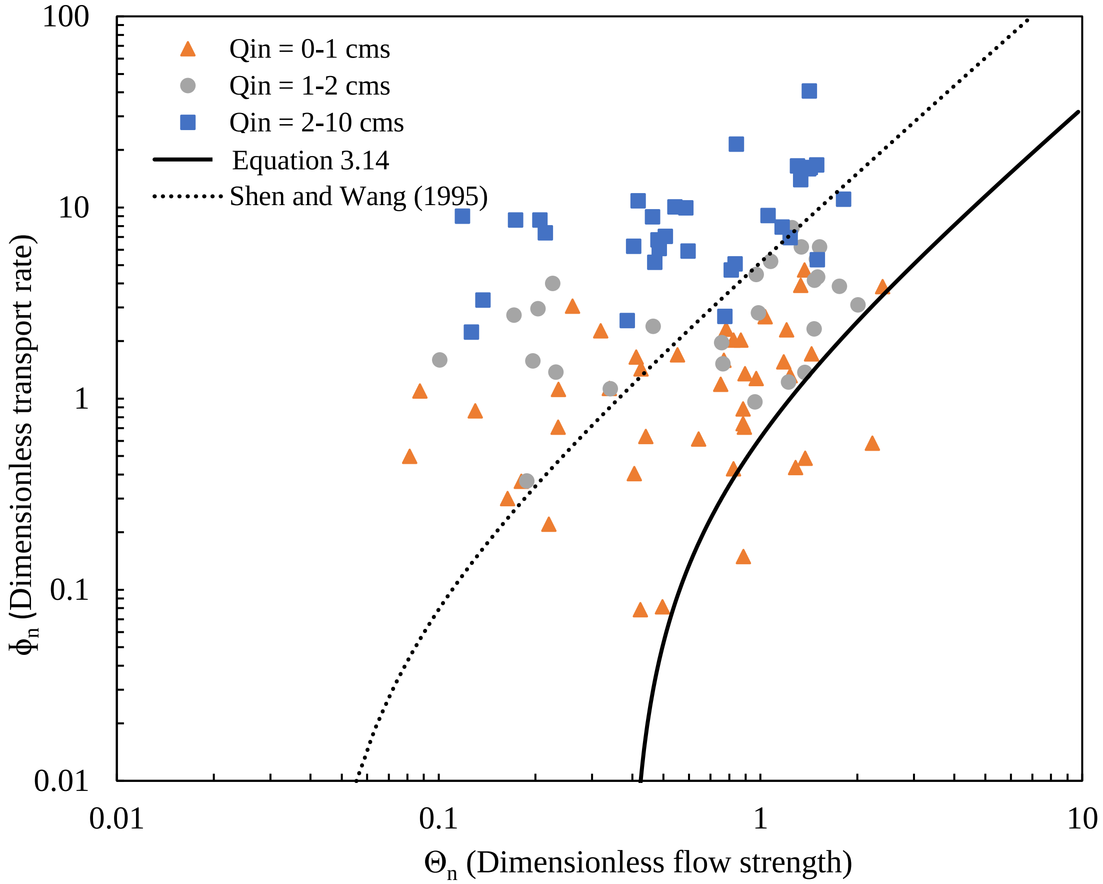


Figure 3.17. Hequ Reach field data (Wang, 1992) analysis of ice transport rates.

The change in average ice thickness between 15 days at each control volume (reach between 2 cross-sections) was analyzed to further understand the erosion and deposition within the Hequ Reach. The results of the analysis are shown in Figure 3.18, where a negative change in thickness denotes erosion and a positive change in thickness specifies deposition when compared with the previous timestep. Deposition within the reach was clearly more prominent than erosion, which aligns with the observation of a high number of data points that lie above the equilibrium line in Figure 3.17. The equilibrium line given by equation 3.14 can be used to determine the criterion for ice cover erosion and deposition processes in a river.

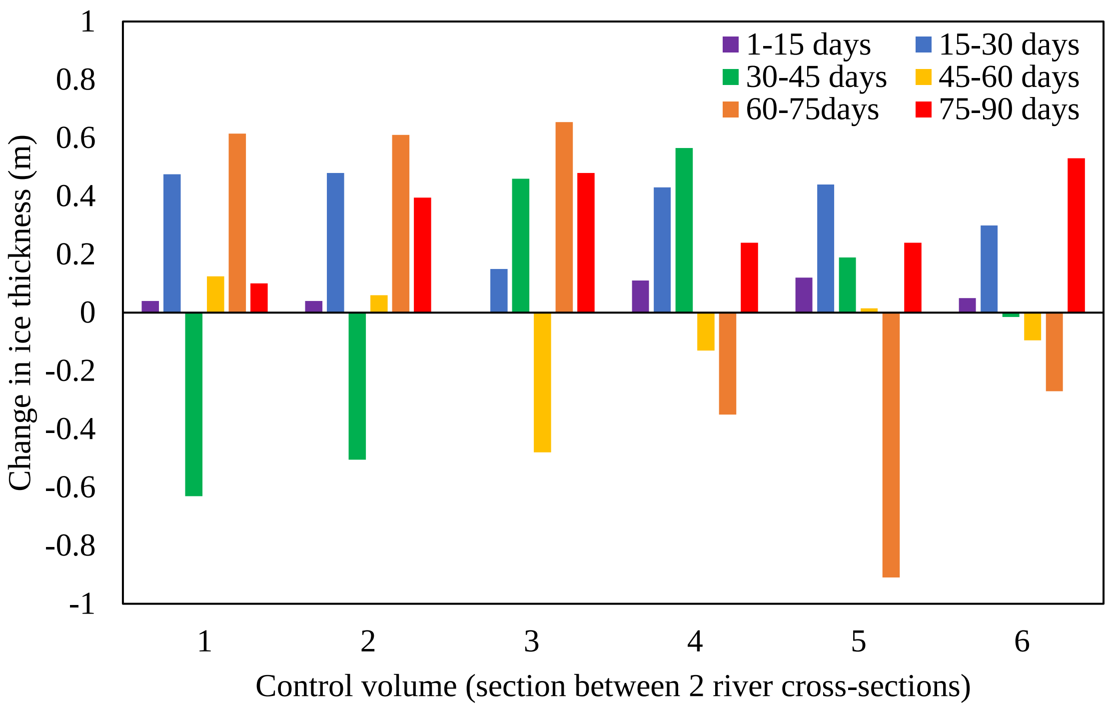


Figure 3.18. Change in ice thickness for Hequ Reach field data (positive values indicate deposition).

### 3.2.6 Conclusion

Under cover ice transport can be a vital component of the river ice processes in a cold region river during the winter. This study presents a cover load transport formula to describe the relationship between dimensionless transport rate and dimensionless flow strength under equilibrium conditions. The formula was developed based on a series of laboratory experiments under uniform flow conditions using HDPE pellets as simulated ice particles and bubble wrap as a simulated ice cover. The critical dimensionless flow strength which corresponds to the critical boundary shear stress underneath the ice cover was identified as an important parameter during the analysis and it was determined experimentally at the point of incipient pellet motion. It is recognized that critical dimensionless flow strength is dependent on several particle properties like the size, density, and buoyant velocity coefficient. A comparison of critical dimensionless flow strength for HDPE pellets and 1 mm diameter sand is presented in the paper highlighting the importance of these parameters.

This study explores the relationship between equilibrium ice transport rate for a certain flow strength condition and the upstream ice supply. When the incoming ice supply rate is equal to the equilibrium ice transport rate, the thickness of the initial ice cover remains constant, without major depositions that will lead to a hanging dam formation or erosion that will reduce the thickness of the ice cover. Since there are no net changes in the under cover ice thickness, the flow strength remains constant throughout the entire duration and the ice output rate from the reach (control volume) will be equal to the ice supply rate to the reach.

The impact of the incoming ice supply rate on under cover ice transport rate was further analyzed by conducting experiments with varying incoming ice supply rates. Results showed that the observed transport rates drop below the equilibrium line (Equation 3.14) when there is insufficient ice supply in the reach, which leads to erosion of the ice cover. Both the laboratory experiments and field data analysis showed that when there is high ice supply in the reach that exceeds the equilibrium transport rate for the given flow strength, deposition occurs. Therefore, the line for equilibrium ice transport rate given by Equation 14 could be used as an initiation criterion for ice cover thickening and eventual hanging dam formation.

When the incoming ice supply was varied from the required equilibrium ice supply, it was observed that the flow strength adjusted itself such that the under cover ice transport rate tended towards the equilibrium ice transport rate given by the experimentally derived equation. The flow strength in a river has the potential to change when there is either insufficient ice supply or an abundant ice supply from the upstream, making conditions quite dynamic. These results were supported by an analysis of previously reported field data from Hequ Reach, China (Wang, 1992). The difference in time and space scales of a river compared to a laboratory flume might have an impact on change of flow strength.

The cover load transport formula introduced in this study was developed exclusively with simulated ice that has similar physical properties to ice in a natural river. This formula can be used to estimate the equilibrium cover load transport rate for a certain flow strength condition in a river. The subsequent experiments on the effect of incoming ice supply rate can be used to determine the criterion for ice cover erosion and deposition processes in a river. Application of the proposed cover load transport formula and the concept of equilibrium transport capacity should be relevant to further studies related to numerical modeling of under cover ice transport processes as well as hanging dam formation and evolution.

### 3.2.7 Acknowledgements

The authors would like to thank Alexander Wall for his assistance with the experimental setup. The authors would like to acknowledge the project funding contributions from a Collaborative Research & Development Project with the Natural Sciences and Engineering Research Council of Canada and Manitoba Hydro.

### 3.2.8 References

Bagnold, R.A., 1956. The flow of cohesionless grains in fluids. Philosophical Transactions. Royal Society, London, England, Series A, Vol 249, 235-297.

Bagnold, R. A., 1966. An approach to the sediment transport problem from general physics. Geological Survey Profile. Paper 422-I, U.S. Geological Survey, Washington, D.C.

Chien, N., 1956. The present status of research on sediment transport. Transactions, ASCE, Vol. 121.

Chien, N., 1980. A comparison of the bed load formulas. Journal of Hydraulic Engineering, Chinese Hydraulic Engineering Society, Beijing, No 4, 1-11.

Coleman, H. W., & Steele, W. G., 1999. Experimentation and Uncertainty Analysis for Engineers (2nd ed.). Wiley.

Gebre, S., Alfredsen, K., Lia, L., Stickler, M., & Tesaker, E., 2013. Review of Ice Effects on Hydropower Systems. Journal of Cold Regions Engineering, 27(4), 196–222. https://doi.org/10.1061/(ASCE)CR.1943-5495.0000059 .

Hicks, F., 2009. An overview of river ice problems: CRIPE07 guest editorial. Cold Regions Science and Technology. 55(2), 175–185. https://doi.org/10.1016/j.coldregions.2008.09.006.

Peters, M. R., Clark, S. P., Dow, K., Malenchak, J., & Danielson, D., 2018. Flow Characteristics beneath a Simulated Partial Ice Cover: Effects of Ice and Bed Roughness. Journal of Cold Regions Engineering, 32(1). https://doi.org/10.1061/(ASCE)CR.1943-5495.0000143

Rubey, W.W., 1993. Settling velocities of gravel, sand, and silt particles. American Journal of Science, 25(148), 325-338.

Senarathbandara, R., Clark, S.P., & Dow, K., 2021. Laboratory Investigation of Under Cover Ice Transport Processes, Proc. 21st Workshop on the Hydraulics of Ice Covered Rivers, Saskatoon, Saskatchewan, Canada.

Shen, H. T. & Wang, D. S., 1995. Under Cover Transportation and Accumulation of Frazil Granules, Journal of Hydraulic Engineering, 121(2), 184–195.

Sun, Z., Yang, S. & Yao, K., 1986. Prototype observation and study of ice jam at Hequ section of the Yellow River. Proceedings of IAHR Symposium, Iowa City, Iowa, Vol. II, 39-48.

Swamee, P.K., Ojha, C.S.P., 1991. Drag coefficient and fall velocity of non-spherical particles. Journal of Hydraulic Engineering, 117(5), 660-667.

Wang, D.S., 1992. Frazil Jam Evolution and Transport of Low Density Granules [master's thesis, Lulea University of Technology].

## 3.3 Conclusions and Contributions of this Work

A cover load transport formula to describe the relationship between dimensionless transport rate and dimensionless flow strength under equilibrium conditions was further developed exclusively using simulated ice and ice cover using the laboratory experiments presented in this paper. The relationship between ice supply and transport rate was further analyzed to identify the equilibrium and non-conditions of under-cover ice transport. The critical dimensionless flow strength was determined using hydraulic measurements at incipient motion and it was identified as an important parameter that governs under cover ice deposition and erosion.

# Chapter 4 Hanging Dam Formation and Evolution

## 4.1 Introduction

The significance of incoming ice transport rate was highlighted in the under cover ice transport experiments presented in Chapter 3. Further laboratory experiments were conducted to investigate the effect of incoming ice supply rate as well as hydraulic conditions of the flow on hanging dam formation and evolution. The journal paper on hanging dam experiments is presented in this chapter where the ice supply rate and Froude number were altered to measure its effect on several physical parameters of the hanging dam formation. The paper was published in the special issue on Advances in River Ice Science and Its Environmental Implications in Water Journal in December 2023 (doi.org/10.3390/w15244242).

## 4.2 Paper 2: Experimental Analysis on Hanging Dam Formation and Evolution

### 4.2.1 Abstract

Hanging dams are thick accumulations of frazil ice beneath an existing ice cover that are formed during the freeze-up period at locations where a fast-flowing river section enters a section with relatively low velocity. Hanging dams can have a substantial impact on the hydraulics of an ice-covered river. This paper presents an experimental study on hanging

dam formation and evolution conducted using a laboratory physical model of a river issuing water into a relatively large reservoir using simulated frazil ice and a simulated ice cover. The incoming ice supply rate and the approach Froude number of the river are the two parameters that have an impact on the hanging dam formation with respect to several physical characteristics of the hanging dam. Hanging dam erosion was observed by increasing the approach Froude number of the river after a hanging dam had already formed. Both the formation and erosion of the hanging dam were qualitatively compared with field observations of hanging dam occurrences using satellite imagery and hydrometric data to support the applicability of the experimental results to a field scenario. The results presented in this paper comprise the first published quantitative laboratory data on hanging dam formation, helping to improve our understanding of the fundamental mechanisms of hanging dam formation and evolution.

### 4.2.2 Introduction

In a cold-region river, large quantities of frazil ice are generated in steep, fast flowing, open water river sections during the winter as a result of continuous super-cooling and high turbulence (Hicks, 2009). The generated frazil ice particles are transported downstream and can become entrained underneath an existing downstream ice cover. The frazil ice entrained in the flow will either be transported as undercover ice or get deposited underneath the ice cover, depending on the hydraulic and geomorphic conditions of the river.

According to Ashton (1974), the entrainment or the deposition of an ice floe at the leading edge of an ice cover is determined primarily based on the critical velocity and/or critical

Froude number of the approach flow. MacLachlan (1926) stated that the limiting velocity for ice deposition beneath an ice cover is 0.69 m/s and the ice cover may thicken if the flow velocity is lower than the critical velocity, which was based on data from the St. Lawrence River, Quebec, Canada. In the study on hanging ice dams by Kivisild (1959), the critical Froude number of the approach flow was determined to be 0.08 for ice to become entrained beneath an ice cover, and the corresponding critical velocity was calculated as 0.61 m/s.

A thick frazil accumulation known as a hanging dam will form if there is a continuous frazil ice supply from upstream (Beltaos and Dean, 1981). Hanging dams can be found at locations where there are significant decreases in the water velocity due to changes in the channel geometry, such as width expansions, depth increases, or channel slope reductions that promote ice deposition (Beltaos, 2013). Depending on the size of the formation, hanging dams can have a substantial impact on the hydraulics of an ice-covered river. Channel bed scours can occur under a hanging dam due to the high flow velocity caused by the flow restrictions. In the Yellow River, China, near Hequ, a bed scour of 2 m was observed (Sui et al., 2006). Hanging dam formation in a river can reduce the cross-sectional flow area, causing a flow restriction that may increase the flooding potential. Understanding the hanging dam formation process and quantifying the hanging dam evolution under various hydraulic and incoming ice supply conditions are important and may help address the flood risks that may be posed to communities near locations that are vulnerable to hanging dam formation. Minimizing hanging dam formation also enhances the hydraulic efficiency of hydropower generation.

It is often difficult to conduct field studies to monitor hanging dam formation due to the lack of accessibility to remote sites, safety conditions associated with potential ice cover failure, and cost considerations. Laboratory studies are an effective alternative to further understand the fundamental processes of hanging dam formation and evolution under various hydraulic and ice supply conditions with precise control of the hydraulic and geometric parameters.

The main objective of this study was to analyze the hanging dam formation under various hydraulic and incoming ice supply rate conditions using a laboratory physical model with a river issuing water into a relatively large reservoir with a simulated ice cover. Several parameters, such as the maximum length along the centerline, maximum thickness, location of maximum thickness, maximum width, and areal extent of the hanging dam, were quantified for various hydraulic and incoming ice supply rate conditions. The results of this study will improve the existing knowledge on hanging dam formation processes and its governing factors, and they will be beneficial to improve numerical modelling applications of hanging dam formation.

### 4.2.3 Background

Hanging dams are defined as thick accumulations of frazil ice beneath an existing ice cover (Beltaos and Dean, 1981). Frazil ice particles generated in upstream, supercooled, turbulent, open water sections (following a 0°C isotherm, where the water temperature drops below 0°C) are transported downstream in the river and may become entrained beneath an existing ice cover. The entrained frazil ice will be transported as undercover ice and get deposited on the underside of the ice cover if the applied shear stress on the underside of the ice cover is insufficient to transport it further downstream (Shen and Wang, 1995). The thickness of the accumulation will grow continuously to form a hanging dam unless the incoming frazil ice supply from upstream is limited/discontinued or the applied shear stress exceeds a limiting value. Previous field studies (Beltaos and Dean, 1981; Gold and Williams, 1961) show that an abrupt change in the geometry of a river that causes a reduction in the flow velocity, as well as the amount of the frazil ice supply from upstream, are two major contributing factors to hanging dam formation. The hanging dam formation process beneath a lake ice cover during the winter is illustrated in Figure 4.1 (adapted from Gebre et al., 2013).

Several previous field studies report large hanging dam formations when the geometry of the river changes. In the winter of 1962, a field study was conducted at a hanging dam formation site in the Ottawa River. It was reported that there was a 75 m deep trench in the river with a width of 90 m that spanned over a length of 1.2 km. The flow velocity in the trench was considerably lower than the velocity of the river, which facilitated large depositions of frazil ice underneath the ice cover. The Long Sault Rapids are located immediately upstream of the hanging dam formation site. A large quantity of frazil ice was generated due to the high turbulence in the rapids and supercooled water temperature during the winter, which was transported in suspension to become deposited underneath the ice cover at the low-velocity downstream section. Two hanging dam formations with lengths of 450 m and 600 m and a width of 150 m were observed at this site (Gold and Williams, 1961).

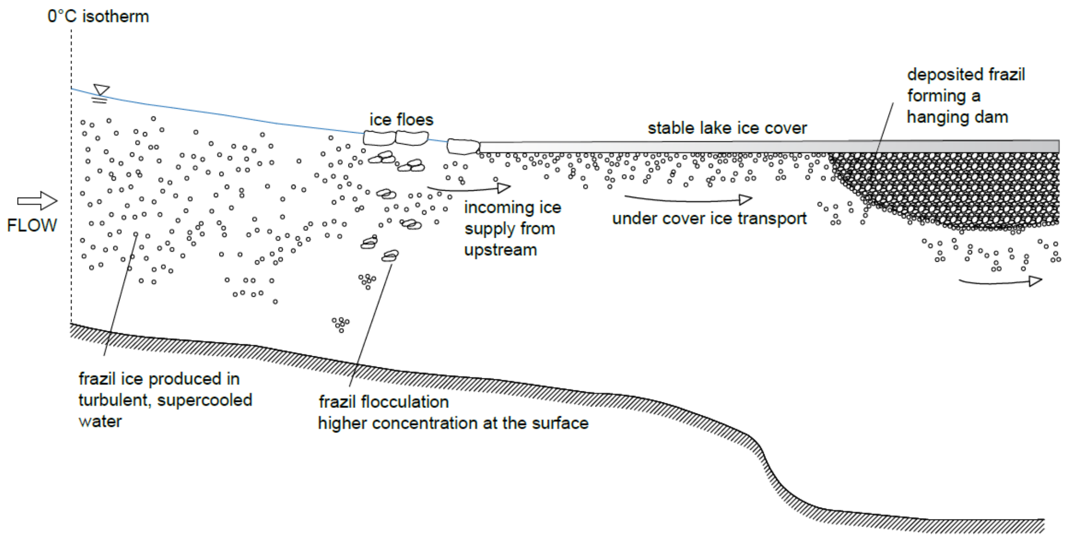


Figure 4.1. Hanging dam formation beneath a lake ice cover (adapted from Gebre et al., 2013).

A hanging dam formation in the Smoky River, Alberta, was monitored in a series of field studies from 1975 to 1979. The field investigation showed that the length of the hanging dam formation varied from 300 m to 700 m and the maximum frazil accumulation thickness under the water surface varied from 11.0 m to 16.3 m during the study period. Similar to the Ottawa River hanging dam, this hanging dam was also located at a deep and wide section of the river immediately downstream of a rapids section. The non-submerged portion of the hanging dam (overburden) consisted of a layer of snow and weak granular ice. There was a 6 cm layer of thick solid ice on top of the overburden close to the riverbanks. The submerged portion comprised dense frazil slush with the pores saturated similar to those of the overburden, but with less cohesion. The frazil slush had a shape that varied between spheroid and discoid, with a diameter ranging from 1 to 6 mm. By weight, 60% of the frazil slush was in the range of from 1.1 mm to 2.4 mm in diameter, 35% was in the range of from 2.4 mm to 4.8 mm, and 5% was in the range of from 4.8 mm to 6.0

mm. The velocity underneath the hanging dam was measured using a magnetic flow meter, and the average velocity was reported as 0.12 m/s. Field tests were conducted to measure the shear strength and the bearing capacity using shear vanes from 1976 to 1979, and a scattered trend was obtained for both parameters. The authors suggested that this could be a result of the crudeness of the measuring technique and the natural variability in the shear strength (Beltaos and Dean, 1981).

Hanging dams can significantly impact the hydraulics of an ice-covered river by forming large accumulations that reduce the flow area, disrupt the flow, and even cause flooding. Each year, frazil ice accumulates in the St. Raymond reach of the St. Anne River, Quebec, in the form of grounded frazil jams or hanging dams. Even though flood-controlling structures were built to reduce the impacts from ice jam flooding, St. Raymond is repeatedly flooded during and after the break-up season each year. The study by Vergeynst, Morse, and Turcotte (2017) showed that 40% of the floods have occurred in the presence of ice in the river. The lack of knowledge on hanging dam formation processes and the river's ice regime were identified as the main reasons for the inability to successfully address the ice-related flooding issues in the St. Raymond reach, irrespective of the flood-controlling structures (Vergeynst et al., 2017). A comprehensive understanding of the processes leading to hanging dam formation and evolution will contribute to minimizing the flood risks posed to local communities near vulnerable locations.

Hopper and Raban (1980) investigated hanging dams in the Manitoba Hydro system and discussed their effects on river hydraulics and hydropower generation. The winter flows in the Burntwood River, Manitoba, increased from 20–34 $m^3/s$ to 950 $m^3/s$ as a result of the Lake Winnipeg Regulation and the diversion of the flow from the Churchill River to the

Nelson River via the Burntwood River. It was predicted that a major hanging dam would form in the Burntwood River close to Thompson, Manitoba, causing high-river stages. After identifying this problem, a control structure and an ice boom were installed 6 km upstream from the potential hanging dam site to promote a stable ice cover and eliminate the ice-generating open water reach in the river. The authors concluded that this operation was successful and that the river stages were reduced by 8 m from the previous predicted levels (Hopper and Raban, 1980).

The ice stabilization program in the Lake Winnipeg Regulation (LWR) was implemented in 1984 by cutting back flows at the Jenpeg control structure to facilitate ice cover formation in open water sections. During the operation, the cycling of the flow cutback was implemented such that the flows were decreased at night and increased during the day to minimize the effect of the flow cutback on the energy production (Zbigniewicz, 1997). The flow cutback procedure at the Jenpeg Generating Station decreased the discharge and the Froude number, which allowed the leading edge of the ice cover to progress over the rapids section, thereby decreasing the frazil ice production (Lees et al., 2021). Through the ice stabilization program, Manitoba Hydro has successfully reduced the size of under-ice de-posits in the reaches surrounding the Jenpeg Generating Station (Zbigniewicz, 1997).

### 4.2.4 Methodology

Experiments were conducted in the hanging dam physical model shown in Figure 4.2, located at the Hydraulics Research and Testing Facility (HRTF) at the University of Manitoba. The physical model, initially constructed for work by Badhan (2020), consisted of a narrow channel issuing into a much wider reservoir, hereafter referred to as the river and lake sections, respectively. The river section was 2.74 m long, 0.28 m in height, and had a width of either 0.16 m or 0.31 m to accommodate a range of approach Froude numbers. The lake section was 5.80 m long, 3.88 m wide, and 0.61 m in height. There was a difference in elevation of 0.31 m from the riverbed to the lakebed. The ratios of the lake width to the river width were 24 and 13 for river widths of 0.16 m and 0.31 m, respectively. The Dauphin River in Manitoba, Canada, enters Lake Winnipeg and a hanging dam forms at this confluence. In comparison, the ratio of the Dauphin River width to the width of the bay where the Dauphin River enters Lake Winnipeg was calculated as 17.

Water was pumped from a reservoir using either one or two pumps that had a combined capacity of 20 L/s. The flow was then conveyed to a headwater tank through a 0.1 m diameter pipe equipped with a paddlewheel flow meter. The upstream head water tank was 1.20 m wide, 1.20 m long, and 1.22 m in height and consisted of a flow straightener with an array of cylindrical pipes and a furnace filter to minimize the effects of turbulence on the flow. The outflow from the lake entered the downstream tailwater system via an opening at the downstream wall of the lake. A hopper system, as shown in Figure 4.3(a), was installed to supply simulated ice upstream of the river section.

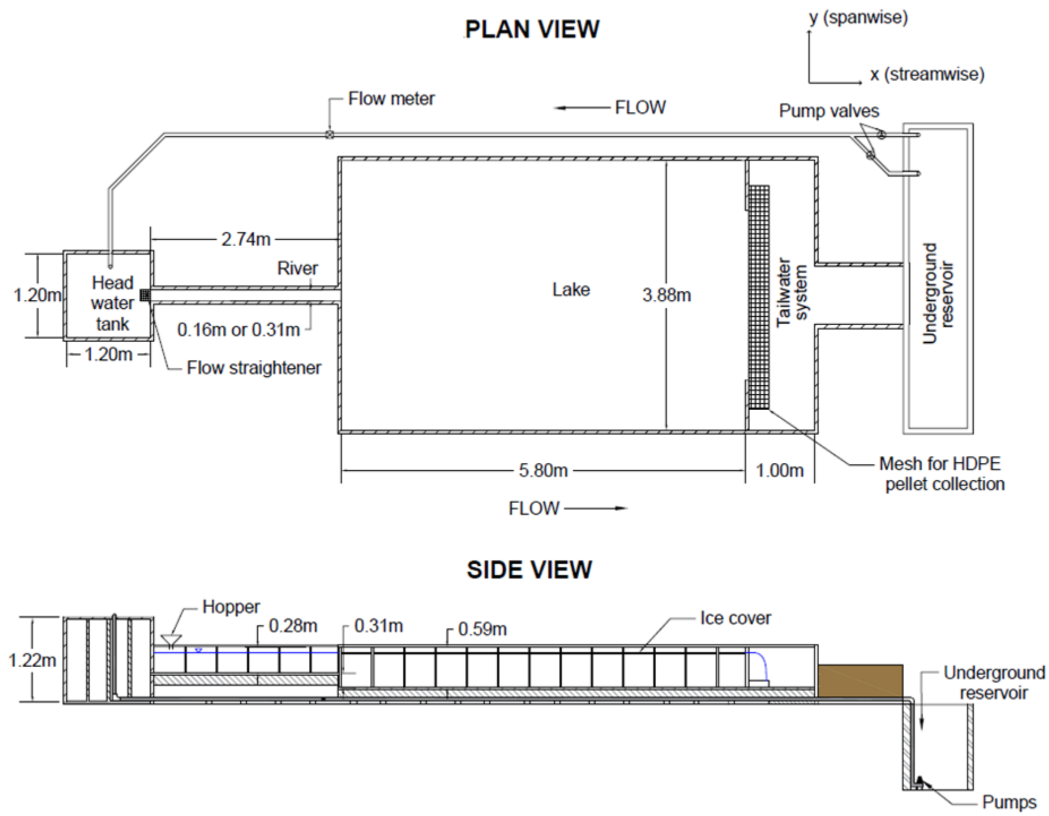


Figure 4.2. Schematic of the hanging dam experimental setup.

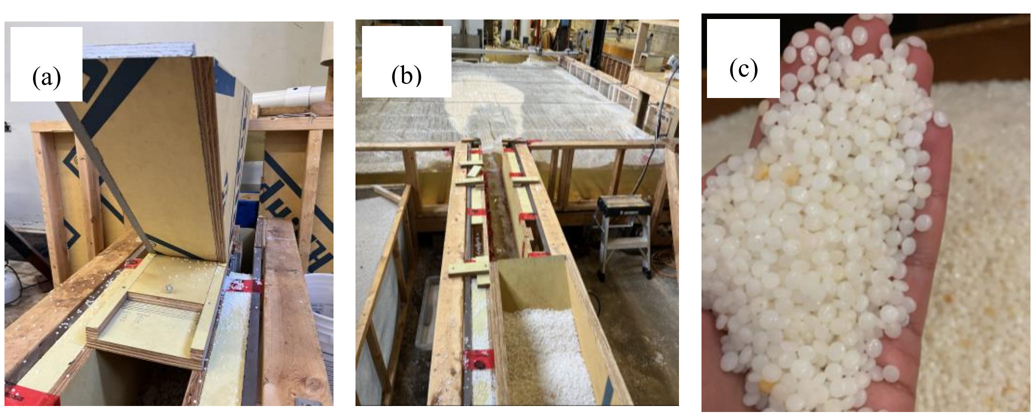


Figure 4.3. (a) Hopper system installed to supply pellets; (b) hanging dam experimental setup during an experiment; (c) HDPE pellets.

As shown in Figure 4.3(c), high-density polyethylene (HDPE) pellets with a specific gravity of 0.95 and a nominal diameter of 3.1 mm were used as simulated frazil ice, and standard packing bubble wrap was used as a simulated ice cover. Initially, the flume was filled with water and the bubble wrap was set to cover the lake section (Figure 4.3 (b)). Then, the pumps were set to achieve the discharge specified in the experimental conditions presented in Table 4.1. For each water discharge condition, simulated ice was supplied with two volumetric incoming ice supply rates per unit width of 0.0001 $m^3/s/m$ and 0.001 $m^3/s/m$ to observe the effect of the incoming ice supply rate on the hanging dam formation. For each experiment, the hanging dam was formed by supplying a total ice volume of 216 L from the hopper upstream of the river section. The time of the experiment varied according to the incoming ice supply rate. Ice was supplied for 72 min for an incoming supply rate of 0.0001 $m^3/s/m$, and for 18 min for an incoming supply rate of 0.001 $m^3/s/m$.

The water depth in the river was measured using a point gauge, and the water depth in the lake was measured using a ruler attached to the lake wall. The average approach velocity (V) and the approach Froude number (Fr) in the river were calculated using Equation 4.1 and Equation 4.2, respectively, where Q is the water discharge ($m^3/s$), b is the river width (m), d is the water depth in the river (m), and g is the gravitational acceleration ($m/s^2$):

$$V = \frac{Q}{bd} \tag{4.1}$$

$$Fr = \frac{V}{\sqrt{gd}} \tag{4.2}$$

Initially two methods were considered to obtain the shape and the dimensions of the hanging dam. A comparison was made between a 3D point cloud generated by scanning the hanging dam using an underwater laser scanner during an experiment and a digital elevation model (DEM) of an orthomosaic created using photogrammetry. For this comparison, a smaller hanging dam with a total ice volume of 72 L was used since it was difficult to conduct an under-water laser scan for an accumulation of 216 L while maintaining the minimum distance between the laser scanner and hanging dam.

A 2G Robotics underwater laser scanner with ULS-100 class 1 laser was used to scan the hanging dam. A 50 degree laser swath was emitted by the laser scanner on the target to calculate the position of points along a laser line projected on the target. Then the position of the scanner was mechanically changed to a new angle that depended on the step size specified by the user. A step size of 45 was used in this experiment. Step size determines the laser return quality, and a lower step size produces a higher quality point cloud with the drawback of taking a longer time. The scanning process took approximately 6 minutes at each location. The laser scanner was mounted on a board with nylon strings attached to the two ends so that the scanner could be moved along tracks on the lakebed to complete a full scan of the hanging dam formation.

The point cloud data from the laser scanner was post-processed using CloudCompare, which is a 3D point cloud processing open-source software developed by Daniel Girardeau-Monteau (Girardeau-Monteau, 2003). Initially the point cloud was filtered for noise reduction. The scans at different grid locations were merged to create a combined point cloud from which the centerline length from the lake inlet, maximum thickness and the location of maximum thickness were obtained. Figure 4.4(a) shows the plan view of the merged laser scans overlaid on top of an aerial view image of the hanging dam and Figure 4.4(b) shows the side view of the same point cloud obtained from the underwater laser scanner. The location of the maximum thickness of the hanging dam was measured as 2.1 m from the lake inlet and the maximum thickness of the hanging dam was measured as 0.17 m using the CloudCompare software as shown in Figure 4.4(b).

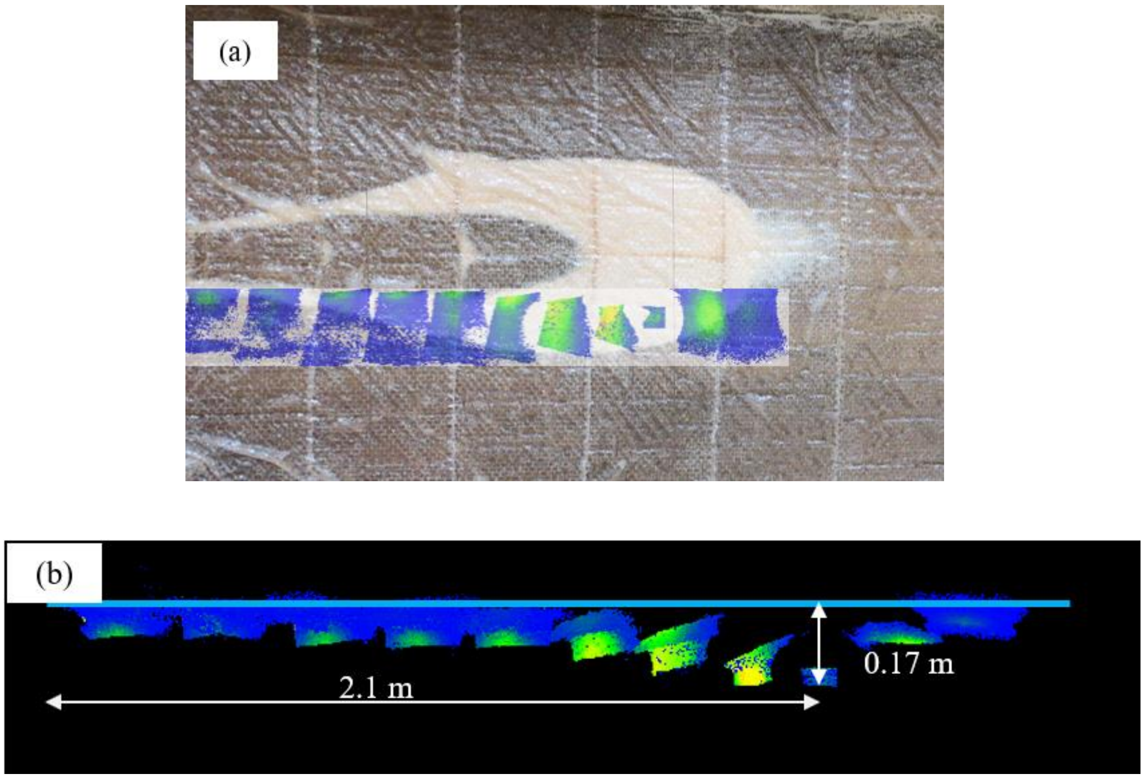


Figure 4.4. (a) Plan view; and (b) side view of the point cloud obtained from the laser scanner.

Water in the flume was slowly drained after the experiment and the ice cover was carefully lifted off to the side. Four targets with known geometric coordinates with respect to the walls and the bed of the lake section were placed around the hanging dam as shown in Figure 4.5. The photos of the hanging dam were taken using a Canon DSLR camera. It was important to obtain photos that have a considerable (50%-80%) overlap with the adjacent photos to generate a high-quality dense point cloud. Therefore, the number of photos for each experiment were based on the size of the formation and typically varied between 25-30 photos. The photos were imported to Agisoft Metashape photogrammetric processing software (Agisoft LLC, 2019) to form an orthomosaic of the hanging dam. As the initial step the photos were aligned to create a sparse point cloud. The geometric coordinates of the 4 targets were used to conduct georectification for the sparse point cloud and a dense point cloud was generated as shown in Figure 4.6(a). A digital elevation model (DEM) was generated using the dense point cloud as shown in Figure 4.6(b).

Figure 4.5. Hanging dam with 4 targets on the lakebed for photogrammetry.

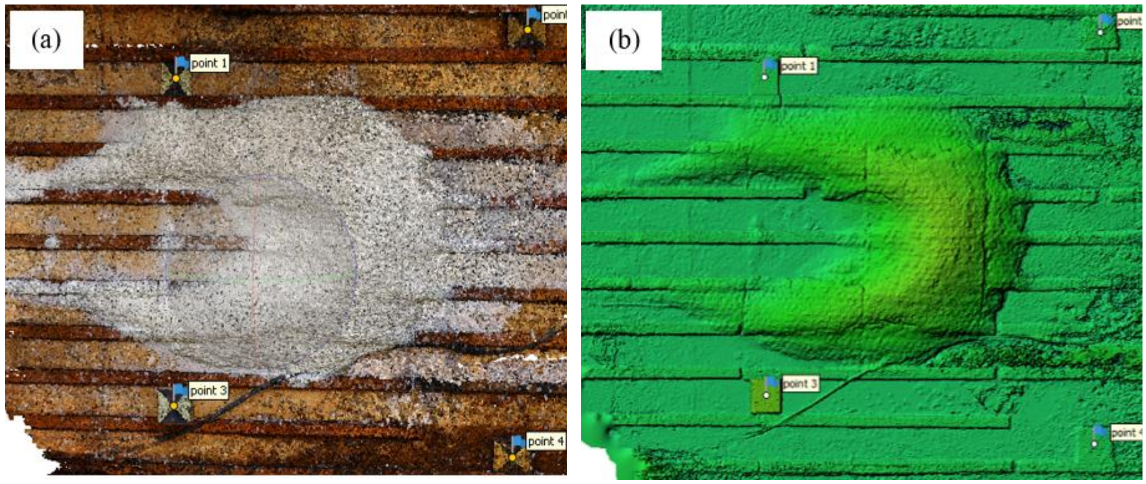


Figure 4.6. Orthomosaic created using photogrammetry; (a) dense point cloud and (b) digital elevation model.

Table 4.1 shows a comparison of the hanging dam centerline length from the lake inlet, maximum width, maximum thickness, and the location of the maximum thickness obtained from the underwater laser scanner and photogrammetry. The centerline length of the hanging dam from the lake inlet is similar for both photogrammetry and laser scan methods. The maximum thickness of the hanging dam and the location of the maximum thickness obtained using the laser scanner are slightly higher than the values obtained using photogrammetry. The maximum width was only measurable using the photogrammetry method.

There are several disadvantages associated with obtaining the shape and the dimensions of the hanging dam using the underwater laser scanner. It takes a considerable amount of time (approximately 6 minutes) to complete scanning at one grid location in order to obtain a high-quality point cloud. Therefore, the total scanning time for the entire hanging dam will take a few hours depending on the extent of the hanging dam. During this time, erosion of existing formation can be observed since there is no ice supply from upstream.

Table 4.1. Comparison of hanging dam dimensions using laser scanner and photogrammetry.

| Dimension | Laser scanner | Photogrammetry |
|---|---|---|
| Centerline length from the lake inlet (m) | 2.62 | 2.63 |
| Maximum width (m) | Not measured | 1.24 |
| Maximum thickness (m) | 0.17 | 0.15 |
| Location of maximum thickness from the lake inlet (m) | 2.10 | 2.05 |

Due to the long scanning time, only one side of the hanging dam was scanned with the assumption that the hanging dam formation was symmetric along the centerline of the lake section. This assumption was not perfectly accurate, specifically at higher Froude numbers where the hanging dam formed at a further downstream location. Due to time constraints, laser scans were obtained with a spacing of 20 cm between 2 consecutive scanning locations. It was difficult to produce an accurate DEM since there was no overlap between point clouds. During the post-processing step, the scans need to be aligned based on the grid measurements and the length of the hanging dam obtained from aerial view photos. This is a manual process that involves a high amount of quality control, and it is not as accurate as generating a DEM using an orthomosaic. There are disturbances caused to the hanging dam when moving the laser scanner from one track to another which is problematic when scanning must be done in several tracks for a spread-out hanging dam formation. It was also noted that the scanner does not have enough space to rotate when the thickness of the hanging dam is high. Since it is evident that photogrammetry is able to produce a high-quality point cloud with an accurate estimate of the hanging dam dimensions, photogrammetry was used to obtain the hanging dam properties for the subsequent experiments of this study.

The aerial views of the hanging dam were captured using a GoPro Hero6 camera mounted to an overhanging wire above the hanging dam flume every 1 min during the ice supply. A Matlab package for georectifying oblique digital images developed by Bourgault et al. was used to orthorectify the aerial view images of the hanging dam (Bourgault et al., 2015). The centerline length, maximum width, and areal extent of the hanging dam for each experiment were obtained from the orthorectified aerial view images. The image processing software ImageJ was used to measure the dimensions of the hanging dam formation (ImageJ, 2018), which were then divided by the lake depth to obtain dimensionless parameters.

Photogrammetry was used to obtain the maximum thicknesses of the hanging dam and their locations. To conduct the photogrammetry, water in the flume was slowly drained upon reaching a total ice supply volume of 216 L after the experiment, and the ice cover was carefully lifted off to the side. Four targets with known geometric coordinates with respect to the walls and the bed of the lake section were placed around the hanging dam. The photos of the hanging dam were taken using a Canon DSLR camera. The photos were imported to Agisoft Metashape photogrammetric processing software (Agisoft LLC, 2019) to form an orthomosaic of the hanging dam. A digital elevation model (DEM) created using the orthomosaic was used to obtain the maximum thicknesses of the hanging dam and their locations.

Table 4.2. Experimental conditions for hanging dam experiments.

| Water Discharge (L/s) | Ice Discharge ($m^3/s/m$) | River Width (m) | River Depth (m) | Approach Velocity (m/s) | Approach Froude Number (-) | Lake Depth (m) |
|---|---|---|---|---|---|---|
| 2.5 | 0.0001 | 0.31 | 0.057 | 0.14 | 0.19 | 0.38 |
| 2.5 | 0.001 | 0.31 | 0.057 | 0.14 | 0.19 | 0.38 |
| 4.0 | 0.0001 | 0.31 | 0.068 | 0.19 | 0.23 | 0.39 |
| 4.0 | 0.001 | 0.31 | 0.068 | 0.19 | 0.23 | 0.39 |
| 3.0 | 0.0001 | 0.16 | 0.063 | 0.30 | 0.38 | 0.38 |
| 3.0 | 0.001 | 0.16 | 0.063 | 0.30 | 0.38 | 0.38 |
| 4.2 | 0.0001 | 0.16 | 0.061 | 0.43 | 0.56 | 0.36 |
| 4.2 | 0.001 | 0.16 | 0.061 | 0.43 | 0.56 | 0.36 |
| 10.0 | 0.0001 | 0.16 | 0.095 | 0.66 | 0.69 | 0.37 |
| 10.0 | 0.001 | 0.16 | 0.095 | 0.66 | 0.69 | 0.37 |

### 4.4.5 Results and Discussion

#### *4.4.5.1 Hanging Dam Formation*

Figure 4.7 shows the orthorectified aerial views of the hanging dam for all approach Froude numbers and two incoming ice supply rates upon reaching the final ice volume of 216 L. The hanging dam formed immediately at or very close to the lake inlet for lower approach Froude numbers (Fr = 0.19 and 0.23), and the formation shifted further downstream as the approach Froude number increased. Flow from a narrow river into a lake is analogous to a three-dimensional wall jet, where the flow is directed along a wall to an ambient fluid. A wall jet is defined as a shear flow directed along a wall where the streamwise velocity over some region within the flow exceeds that in the external stream at any downstream location because of the initially supplied momentum (Launder and Rodi, 1981). The presence of a wall (ice cover) that directs the shear flow and the zero streamwise velocity at the wall (ice cover) due to the no-slip boundary condition are the primary similarities between a three-dimensional wall jet and the flow from a narrow river to a wide lake section. The high velocity of the wall jet for the approach Froude numbers 0.38, 0.56, and 0.69 did not allow under-ice deposition at the lake inlet, and the jet section can be seen in all these cases, where no ice was deposited immediately downstream of the river.

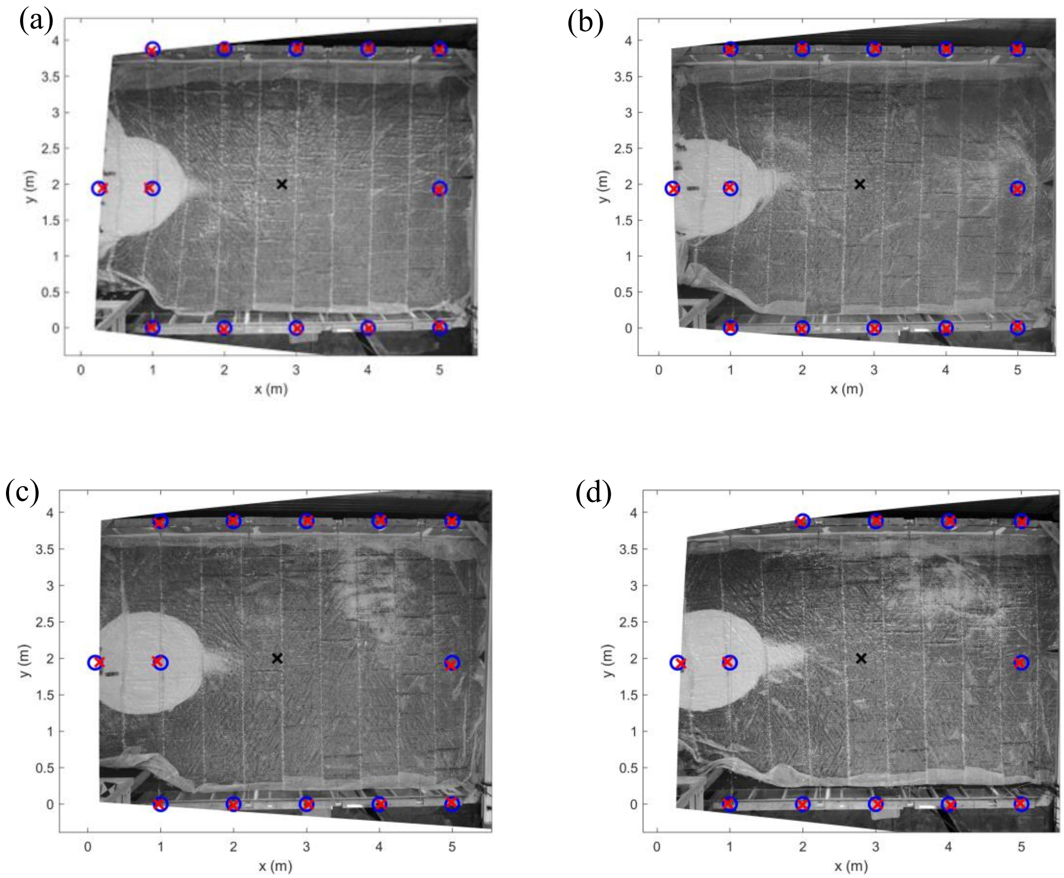

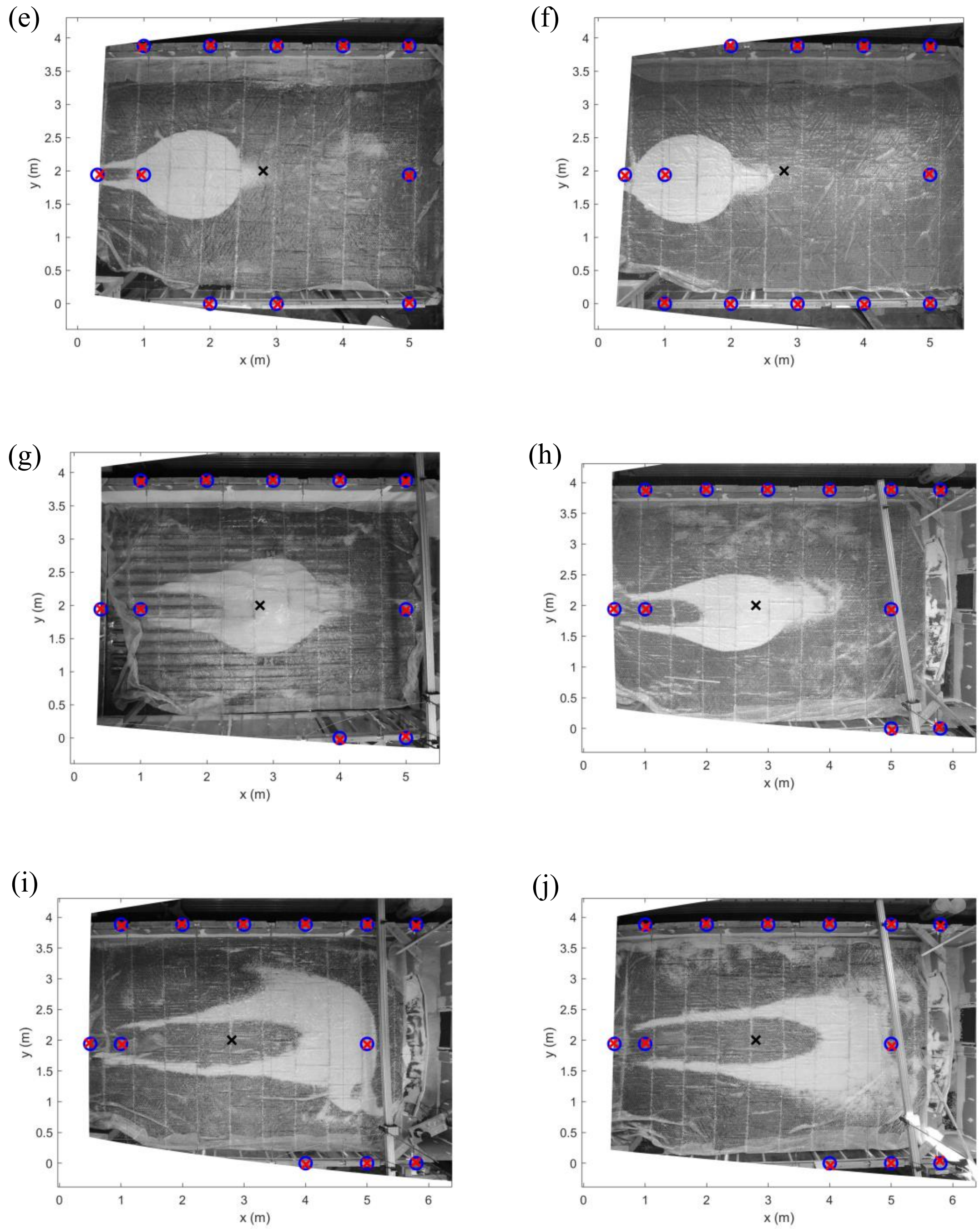


Figure 4.7 Aerial views of hanging dam formation for various Froude numbers and incoming ice supply rates: (a) Fr = 0.19, qi = 0.0001 $m^3/s/m$; (b) Fr = 0.19, qi = 0.001 $m^3/s/m$; (c) Fr = 0.23, qi = 0.0001 $m^3/s/m$; (d) Fr = 0.23, qi = 0.001 $m^3/s/m$; (e) Fr = 0.38, qi = 0.0001 $m^3/s/m$; (f) Fr = 0.38, qi = 0.001 $m^3/s/m$; (g) Fr = 0.56, qi = 0.0001 $m^3/s/m$; (h) Fr = 0.56, qi = 0.001 $m^3/s/m$; (i) Fr = 0.69, qi = 0.0001 $m^3/s/m$; (j) Fr = 0.69, qi = 0.001

$m^3$/s/m (flow direction: from left to right; white area: hanging dam extent; pink markers: ground control points; black cross marker: camera location).

The spatial evolution of the hanging dam in terms of the maximum length along the centerline and the maximum width was analyzed for the three lowest Froude numbers (Fr = 0.19, 0.23, and 0.38), as the approach Froude number of an ice-covered river during the winter is typically of a low value. Figure 4.8 shows the evolution of the dimensionless maximum centerline length (maximum centerline length/lake depth) of the hanging dam for various approach Froude numbers for the two incoming ice supply rates. Initially there was a rapid increase in the centerline length, but the length plateaued and approached a constant value when the $t/t_{final}$ was approximately 0.2, where t is the time at a specific moment and $t_{final}$ is the time taken to reach an ice supply volume of 216 L. This can be explained based on the momentum supplied by the velocity of the jet. Initially, the incoming ice supply to the flume is transported along the flow of the jet and deposited beneath the ice cover when the velocity is not adequate to transport the ice further downstream. The subsequent ice supply to the flume is deposited in the area in between the initially reached centerline length and the lake inlet, increasing the thickness of the accumulation. The final centerline length of the hanging dam has a direct relationship with the approach Froude number of the flow, where the centerline length increases when the approach Froude number increases, as ice is transported further downstream due to the high velocity of the jet at high approach Froude numbers.

The spatial evolution of the dimensionless maximum width (maximum width/lake depth) of the hanging dam is shown in Figure 4.9. For all the cases, the maximum width of the hanging dam increased as more ice was supplied to the flume. Irrespective of the Froude number and incoming ice supply rate, the dimensionless maximum width of the hanging dam reached a constant value upon reaching the final volume of the hanging dam. Even though it is not possible to produce a similar plot for the evolution of the maximum thickness of the hanging dam, it would have increased with the increasing ice supply in a trend similar to that of the maximum width.

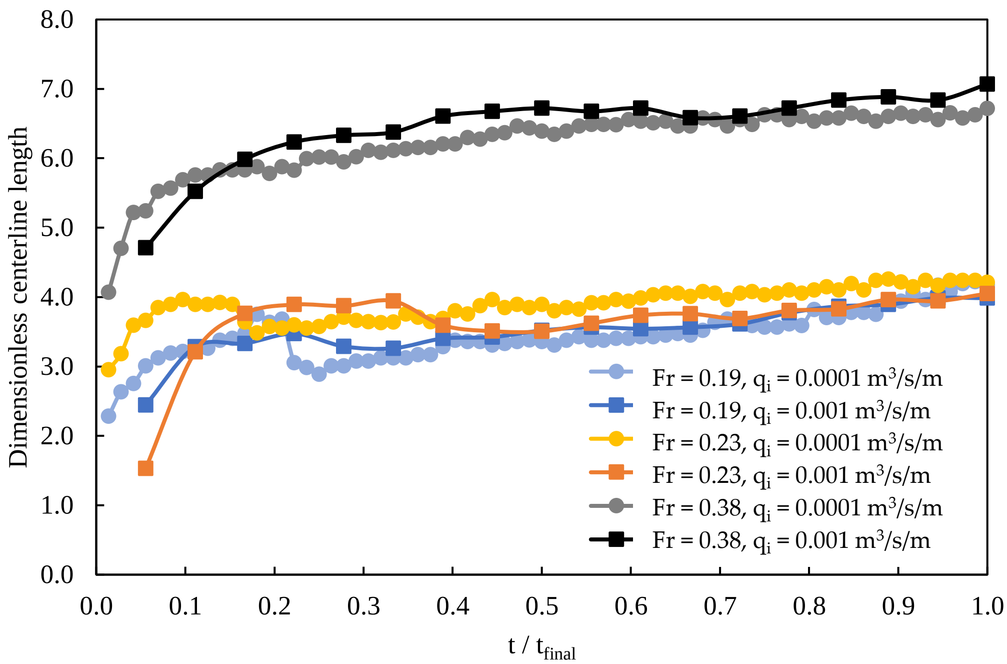


Figure 4.8. Evolution of dimensionless centerline length (centerline length/lake depth) for various approach Froude numbers.

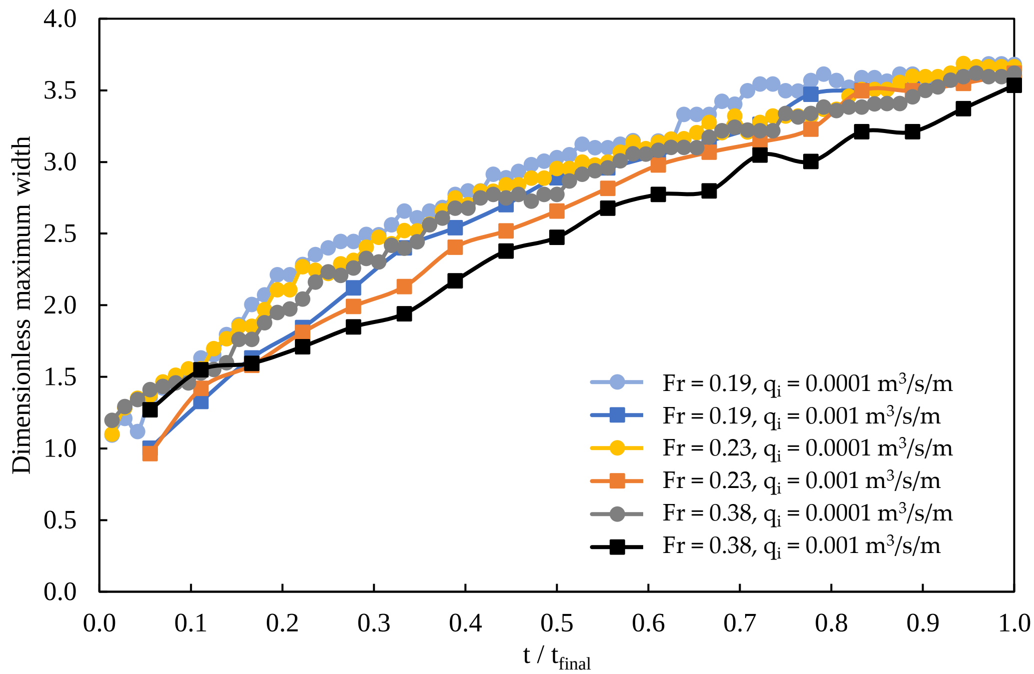


Figure 4.9. Evolution of dimensionless maximum width (maximum width/lake depth) for various approach Froude numbers.

The final longitudinal profiles of the hanging dams obtained from photogrammetry at the centerline of the lake section for various Froude numbers are shown in Figure 4.10. For the lowest-Froude number (Fr = 0.19) experiment, the hanging dam formed immediately at the lake inlet for both high and low incoming ice supply rates. The hanging dam formed immediately at the lake inlet only at the high incoming supply rate for the Froude number 0.23. As the Froude number increased, the hanging dam formed further downstream due to the high shear stress exerted by the flow of the jet. For all the approach Froude numbers, the maximum thickness of the hanging dam occurred closer to the lake inlet at the higher incoming ice supply rate when compared with the low incoming ice supply rate.

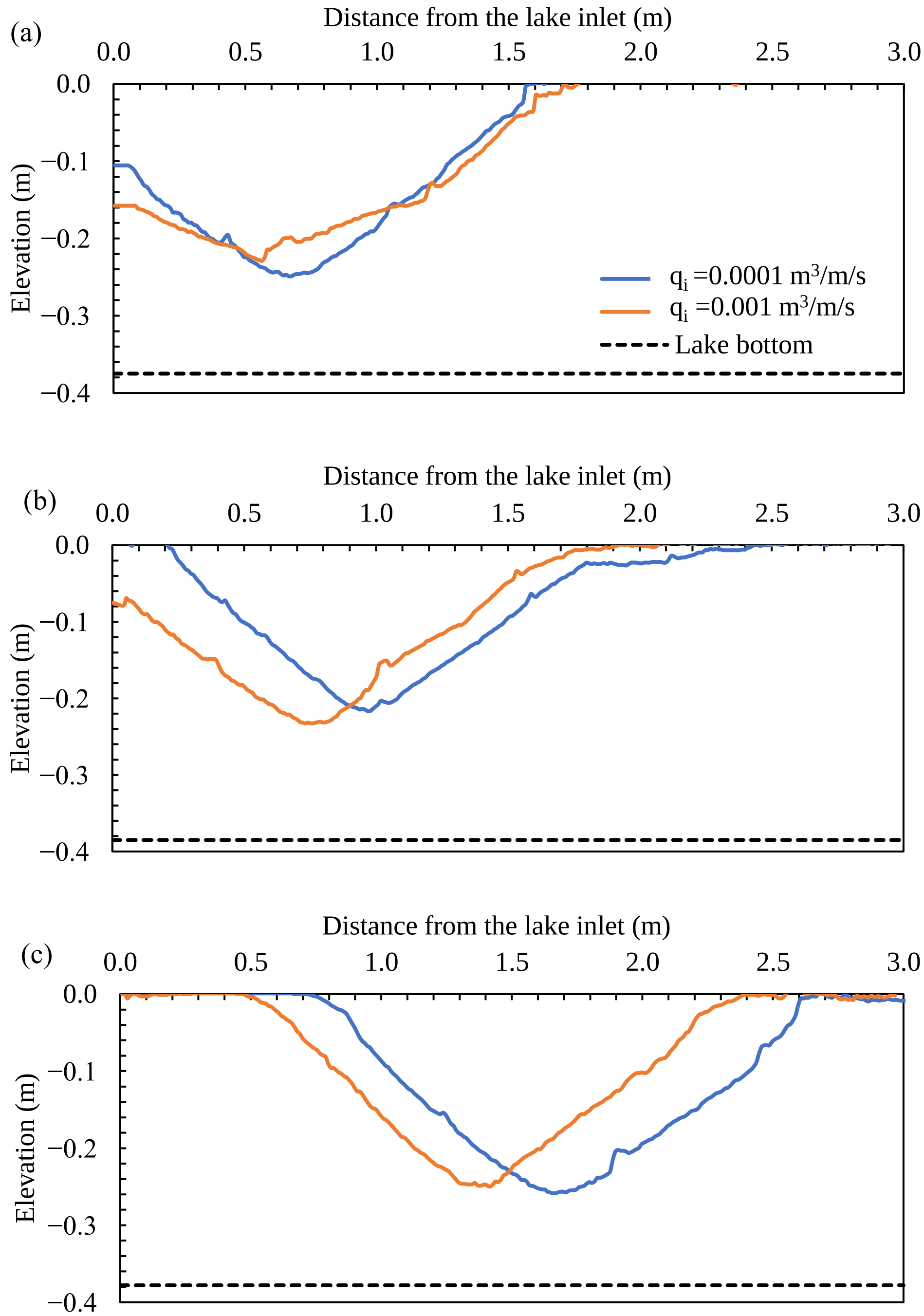
(a)
Distance from the lake inlet (m)
0.0
0.5
1.0
1.5
2.0
2.5
3.0
0.0
−0.1
−0.2
−0.3
−0.4
Elevation (m)
q_i =0.0001 m³/m/s
q_i =0.001 m³/m/s
Lake bottom
(b)
Distance from the lake inlet (m)
Elevation (m)
(c)
Distance from the lake inlet (m)
Elevation (m)

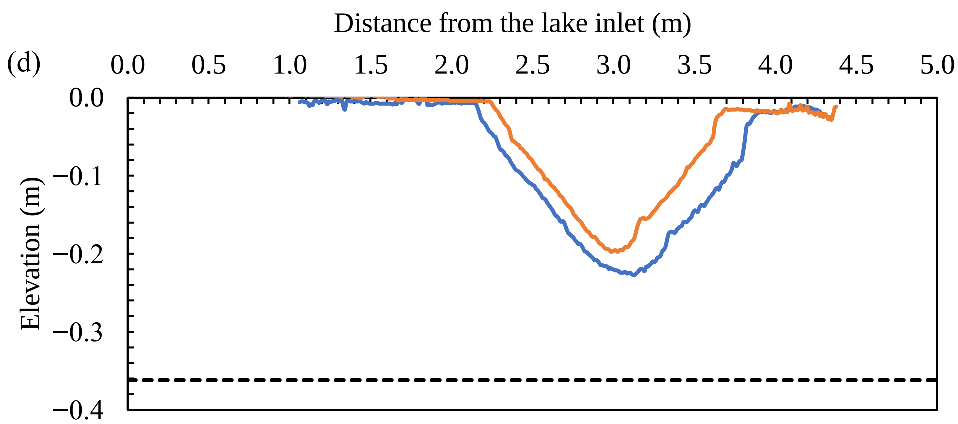


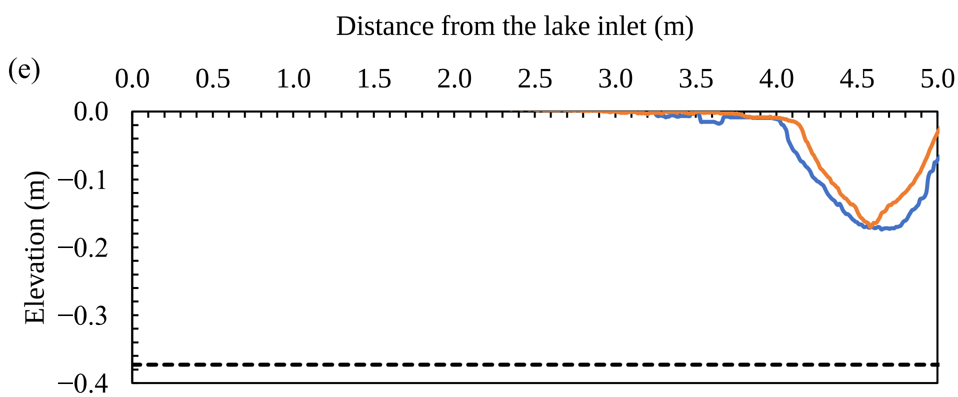


Figure 4.10. Longitudinal profiles of the hanging dam at the centerline of the lake section for various Froude numbers: (a) Fr = 0.19; (b) Fr = 0.23; (c) Fr = 0.38; (d) Fr = 0.56; (e) Fr = 0.69.

The maximum thicknesses of the hanging dam formation ($T_{max}$) for the two incoming ice supply rates and various approach Froude numbers are shown in Figure 4.11. The highest thickness was observed at an approach Froude number of 0.38. The maximum thicknesses for the approach Froude numbers of 0.19 and 0.23 were just slightly lower than the maximum thickness at a Froude number of 0.38. For the low Froude number conditions, the maximum dimensionless thickness of the hanging dam plateaued around a dimensionless length of 0.68, which corresponds to a thickness of 0.25 m. The growth of the thickness of the hanging dam was hindered by several factors, such as the fixed lakebed that only allowed a flow depth of 0.12 m during the thick hanging dam formation, and the absence of cohesion due to freezing. Figure 4.12 shows the side view of the hanging dam formation at the lake inlet for an approach Froude number of 0.19 after reaching the maximum thickness of 0.25 m. The maximum thickness of the hanging dam decreased with increasing approach Froude numbers because the velocity of the jet was high at higher Froude numbers and the hanging dam accumulation was pushed further downstream in the lake section. At a specific approach Froude number, the maximum thicknesses of the hanging dam reached similar values irrespective of the incoming ice supply rate. The maximum thickness of the hanging dam was governed by the fixed lakebed and the absence of cohesion in the HDPE pellets. The shear stress on the underside of the accumulation increases as the hanging dam grows in thickness and non-cohesive pellets easily erode due to this high shear stress. On the contrary, a hanging dam in a natural environment could reach extremely high thicknesses as long as there is a sufficient water depth such that the applied shear stress underneath the hanging dam is lower than the critical shear stress that initiates erosion. During the initial ice formation stages, the thermal effects of ice play an important role in forming an ice cover near the water surface. The thermal ice cover can grow in thickness, which may also contribute to a portion of the hanging dam, which was not simulated in this laboratory study.

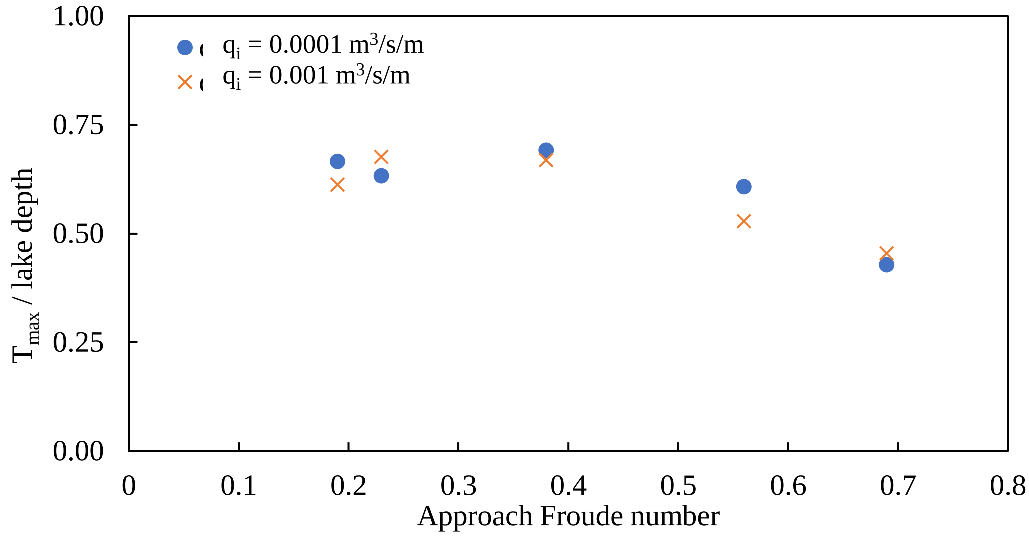


Figure 4.11. Maximum thicknesses of the hanging dam for various approach Froude numbers and incoming ice supply rates.

Figure 4.12. Side view of the hanging dam at the lake inlet for an approach Froude number of 0.19.

The locations of the maximum thicknesses of the hanging dam ($L_{max}$) for various approach Froude numbers and the two incoming ice supply rates are shown in Figure 4.13. The maximum thickness of the hanging dam occurred further downstream as the approach Froude number increased due to the high-velocity jet coming out of the river that pushed the formation downstream. The maximum thicknesses for lower incoming ice supply rates were located further downstream when compared with the locations of the higher supply rates for the same Froude number. During the ice supply stage of hanging dam formation, both deposition and erosion processes happen at the same time at different locations, making the process quite dynamic. Erosion is facilitated through the shear force exerted by the jet flow, and if the incoming ice supply from upstream is not adequate to maintain the rate of erosion, the subsequent depositions happen further downstream.

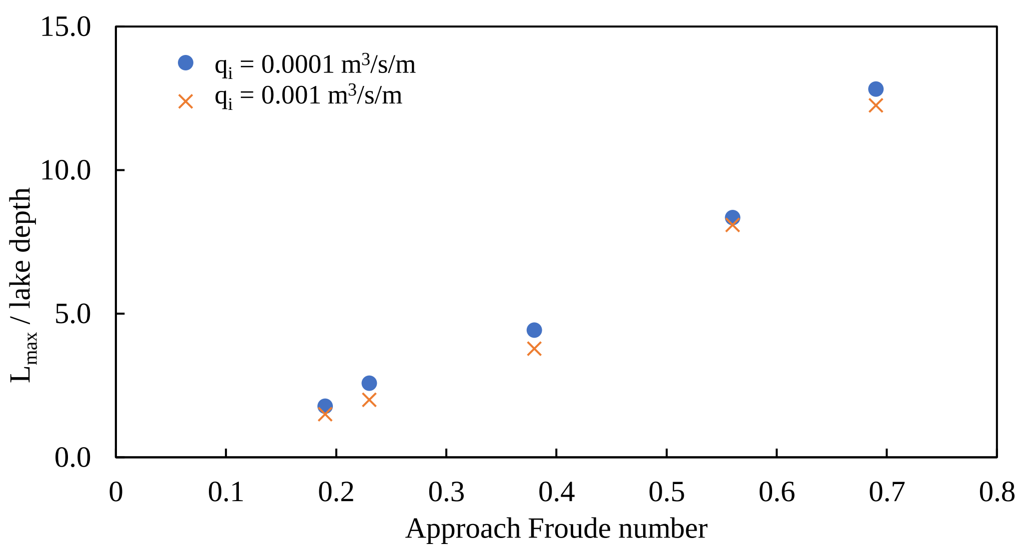


Figure 4.13. Locations of maximum thicknesses of the hanging dam for various approach Froude numbers and incoming ice supply rates.

The areal extents of the hanging dam ($A_{max}$) for various approach Froude numbers and two incoming ice supply rates are shown in Figure 4.14. The areal extent of the hanging dam increased with increasing Froude numbers, and the areal extent for the lower incoming ice supply rate experiment was higher than that of the high ice supply rate experiment for the same approach Froude number. At a low ice supply rate, the rate of supply was not adequate to overcome the rate of erosion; therefore, the eroded ice was transported in both the streamwise and spanwise directions and became deposited at a location further away from the high erosive power of the jet. This also means that if the incoming ice supply from upstream is abruptly terminated and the water discharge is maintained the same, the hanging dam will evolve with erosion and finally reach a stable state. An erosion experiment was conducted to further investigate this theory.

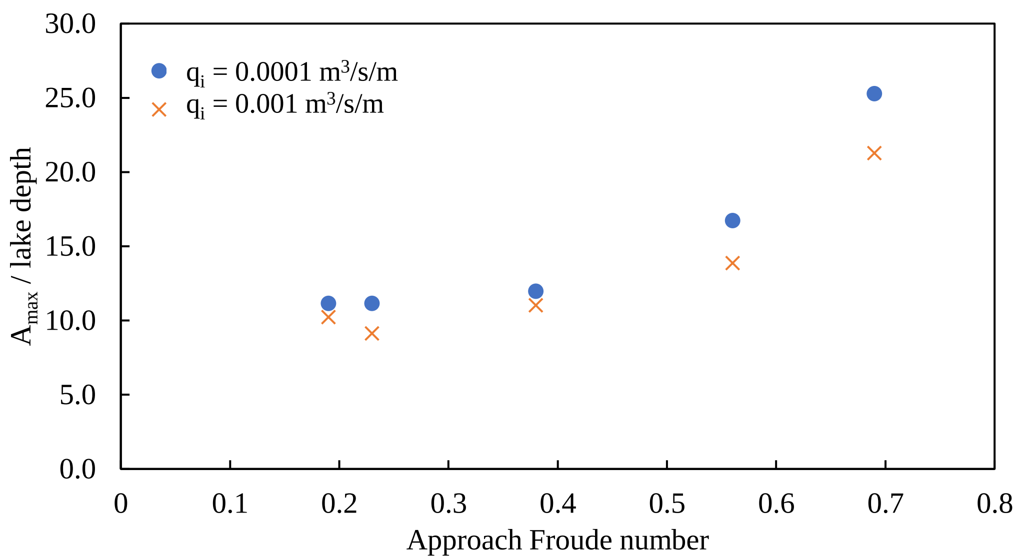


Figure 4.14. Areal extents of the hanging dam for various approach Froude numbers and incoming ice supply rates.

The experimental uncertainty for Froude number was quantified using the methodology presented in Coleman and Steele (1999). The uncertainty of the Froude number ranged between 1% to 2% and uncertainty of length measurements ranged 0.03% to 3.3%.

#### *4.4.5.2 Hanging Dam Erosion*

For the erosion experiment, a hanging dam was formed with a volumetric incoming ice supply rate of 0.0001 $m^3/s/m$ and an approach Froude number of 0.19. Ice was supplied to the flow until a total ice volume of 216 L was reached. Figure 4.15(a) shows the hanging dam formation immediately after finishing the ice supply. The water discharge was incremented in two steps, as specified in Table 4.3, until erosion was observed, and an aerial photo was taken using a GoPro camera every minute to observe the erosion process.

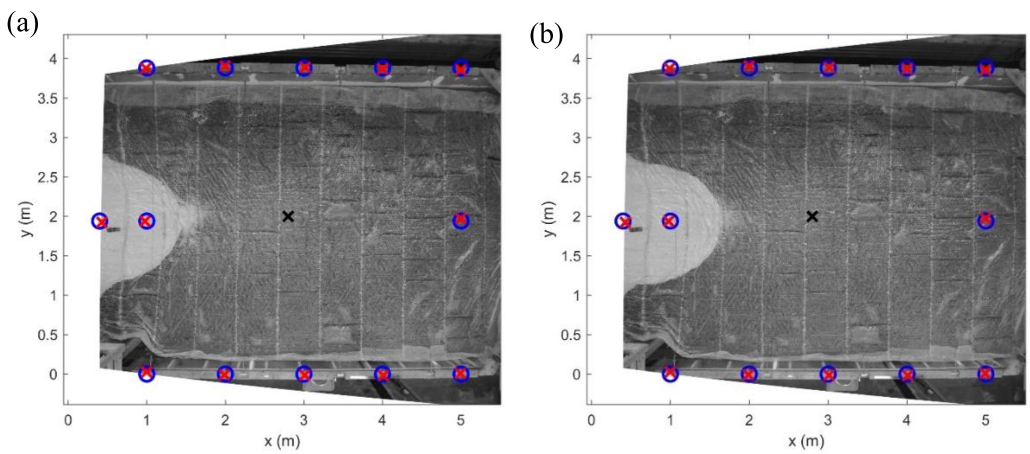


Figure 4.15. Aerial views of the hanging dam (a) immediately after terminating the ice supply and (b) 15 min after setting an approach Froude number of 0.25 (flow direction: from left to right; white area: hanging dam extent; pink markers: ground control points; black cross marker: camera location).

Table 4.3. Experimental conditions for hanging dam erosion experiments.

| Condition | Water Discharge (L/s) | Approach Froude Number (-) | Approach Velocity (m/s) |
|---|---|---|---|
| **Formation** | 2.5 | 0.19 | 0.14 |
| **First step for erosion** | 4.6 | 0.25 | 0.21 |
| **Second step for erosion** | 7.9 | 0.33 | 0.30 |

As the first step, the discharge was set to 4.6 L/s with an approach Froude number of 0.25. Figure 4.15(b) shows the aerial view of the hanging dam after 15 min with the first flow condition; only a modest amount of erosion can be inferred from the slightly larger aerial extent of the hanging dam. The discharge was increased to 7.9 L/s with an approach Froude number of 0.33, and the hanging dam started to erode noticeably. Figure 4.16(a–d) show the aerial views of the hanging dam at 5, 15, 25, and 35 min after setting the second discharge condition. The total centerline length and the open water jet length were measured from the aerial view images and plotted against time, as shown in Figure 4.17. Initially, the total centerline length of the hanging dam increased due to erosion; however, the rate of change in the total centerline length was reduced 15 min after setting the discharge. The rate of change in the open-water jet length also dropped and reached a steady state approximately 25 min after setting the discharge. The erosion of the hanging dam formation was caused by the shear stress exerted on the underside of the ice cover from the jet flow. The wall jet theory explains that the streamwise velocity in the region close to the jet initiation (lake inlet) is higher than the streamwise velocity at any downstream location because of the initially supplied momentum. At the start of the erosion process, the ice deposited close to the lake inlet is transported further downstream based on the shear stress supplied by the flow of the jet and is deposited in an area where the velocity is very low or negligible. The outline of the wall jet can be seen in the aerial view photos as an open-water section.

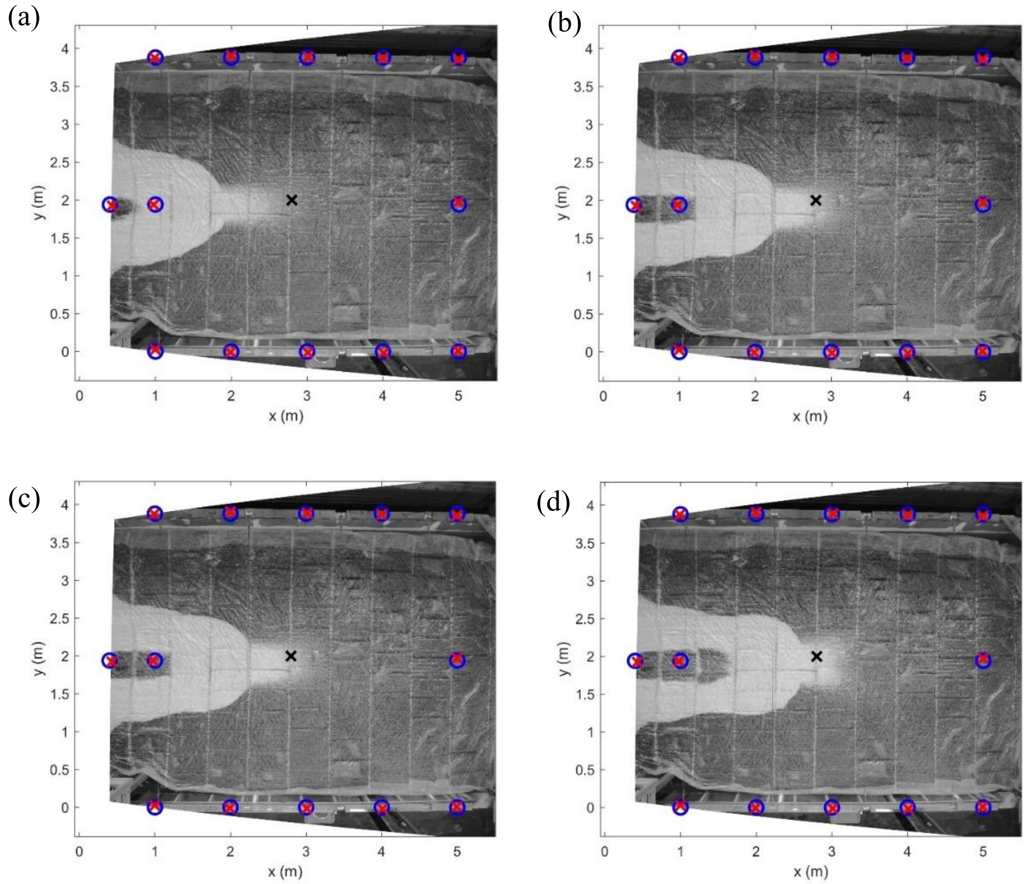


Figure 4.16. Aerial views of hanging dam erosion (a) 5 min, (b) 15 min, (c) 25 min, and (d) 35 min after stopping the ice supply (flow direction: from left to right; white area: hanging dam extent; pink markers: ground control points; black cross marker: camera location).

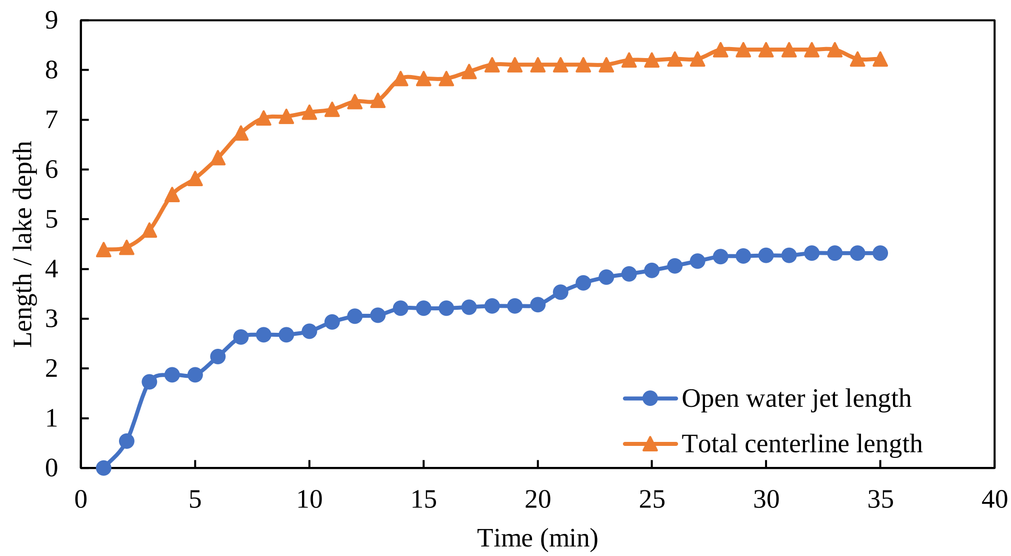


Figure 4.17. Evolution of the total centerline length and open-water jet length of the hanging dam during erosion.

### *4.4.5.3 Comparison to Field Data*

The experimental results were qualitatively compared with two hanging dam occurrences in the field using optical imagery from satellites and hydrometric data. The first case was the hanging dam formation at the confluence of the Dauphin River and Lake Winnipeg in central Manitoba. The Dauphin River is about 52 km long and drains into Lake Winnipeg. Based on the difference in the channel slope, this river can be classified into two reaches: an upper reach with a slope of 0.029% over 40 km and a lower reach with a slope of 0.16% over 11.2 km. The steep lower reach of the river has open-water areas with velocities that exceed 1.5 m/s and can generate a significant volume of frazil ice during the freeze-up season (Clark and Wall, 2016). A hanging dam forms at the outlet to Lake Winnipeg when the frazil ice is deposited under the lake ice cover (KGS Group and North/South Consultants, 2014). The ice-affected water levels in the steep lower reach can rise 4–5 m or more above those of the open-water conditions due to thick ice jams (Wazney, 2019).

The shape and areal extent of the hanging dam were visible from satellite images when the lake ice cover was relatively thin, typically at the end of the winter during the months of April and May. Optical imagery was obtained from Landsat 8/9 and Sentinnel-2 satellites from the US Geological Survey's EarthExplorer (USGS Sentinel-2 and Landsat) for days with low cloud coverage.

An HEC-RAS model of the Dauphin River (Wazney, 2019) was used to estimate the Froude number at the most downstream cross section of the river. The mean monthly discharge and the mean monthly water level at the Dauphin River Water Survey of Canada gauge (05LM006) were used as the upstream and downstream boundary conditions for the HEC-RAS model, respectively. The model was set to run in a steady state for each month during the ice-affected period (from November to April), and the Froude number at the downstream cross section of the river was obtained. The average ice-affected Froude number for 2017–2018 was estimated as 0.06 from HEC-RAS model simulations.

The ice discharge in a river is correlated to the air temperature. A field estimation of the incoming ice discharge in the Dauphin River was previously conducted using an analysis of unmanned aerial vehicle (UAV) videos taken at a site 25 km upstream of the lake inlet for the 2017–2018 season. The ice discharge was calculated using Equation 4.3, where $Q_{ice}$ is the ice discharge ($m^3/s$), $V_{ice}$ is the average surface ice velocity (m/s), N is the average surface ice concentration (-), B is the river width (m), and $t_{ice}$ is the average thickness of a surface ice floe (m):

$$Q_{ice} = V_{ice} N B t_{ice} \tag{4.3}$$

The average thickness of the ice floes was considered a major unknown when using this method and was estimated to vary between 0.05 m and 0.15 m according to field measurements. The ice discharge in the river for the 2017–2018 season was calculated to vary between 1.1 $m^3/s$ and 3.4 $m^3/s$ (Wazney, 2019). The corresponding volumetric incoming ice discharge ($q_i$) at the lake inlet was calculated to vary between 0.004 $m^3/s/m$ and 0.01 $m^3/s/m$ using Equation 4.4, where the width of the river immediately upstream of the lake inlet was determined to be 120 m using the bathymetry data:

$$q_i = \frac{Q_{ice}}{B} \qquad [4.4]$$

Figure 4.18(a) shows the hanging dam formation at the Dauphin River–Lake Winnipeg confluence for the 2017–2018 season, where the average approach Froude number is equal to 0.06. This case from the field can be compared with the lowest Froude number experiment shown in Figure 4.18(b), where the approach Froude number was 0.19 and the incoming ice supply rate was 0.001 $m^3/s/m$. In both cases, ice deposition occurred immediately at the lake inlet, where the flow velocity was reduced due to the abrupt increase in the channel width and depth. Ice was deposited in a semi-circular shape around the inlet of Lake Winnipeg, similar to the experimental case, suggesting that there was a high incoming ice supply during the formation stage of this hanging dam. In comparison, the ratio of the lake width (at the bay where the Dauphin River enters Lake Winnipeg) to the Dauphin River width was 17, whereas the physical model had a lake width–river width ratio of 13. The field observations and analysis by Wazney (2019) indicated that the ice discharge in the Dauphin River was as high as 3.4 $m^3/s$, based on the thickness of the ice floes, during the 2017–2018 freeze-up season.

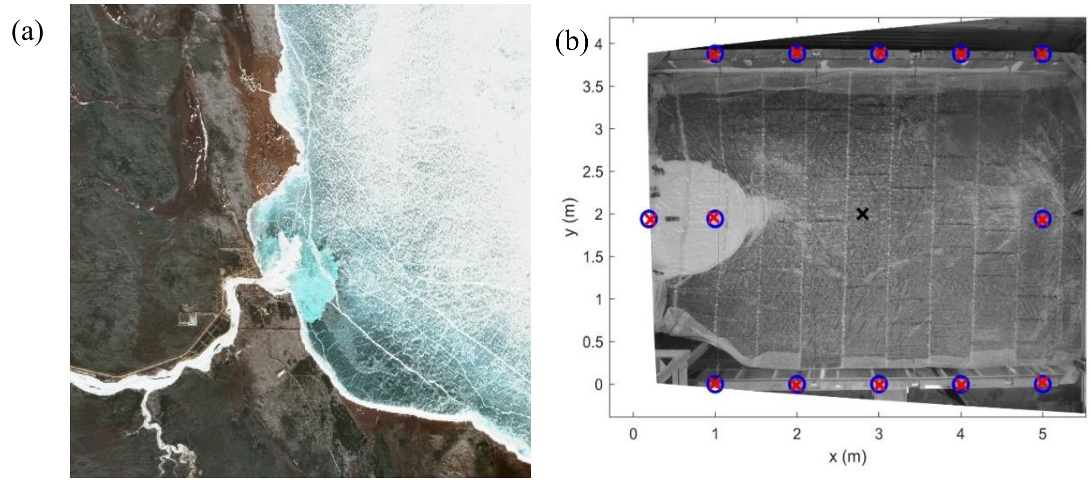


Figure 4.18. Hanging dam formation (a) at Dauphin River–Lake Winnipeg confluence on 21 April 2018 (image courtesy of the USGS) and (b) for the experiment with an approach Froude number of 0.19, qi = 0.001 $m^3/s/m$ (flow direction: from left to right; white area: hanging dam extent; pink markers: ground control points; black cross marker: camera location).

Figure 4.19(a) shows the hanging dam on 3 May 2018 during the breakup season. The higher river discharge and warmer water temperature seem to have caused the hanging dam to have eroded (either mechanically, thermally, or likely a combination of both) along a preferential path. Figure 4.19(b) shows the aerial view of the hanging dam 35 min after setting an approach Froude number of 0.33 during the erosion experiment, where the erosion was caused by the higher river discharge. In both cases, the open-water jet section that results from the higher river discharge is clearly visible. The thermal effect on erosion is an important difference between a field study and a laboratory study. In the Dauphin River field study, rising air temperatures might have contributed to the erosion of the hanging dam, whereas the erosion in the experiments was caused entirely by the flow of the jet.

(a) (b)

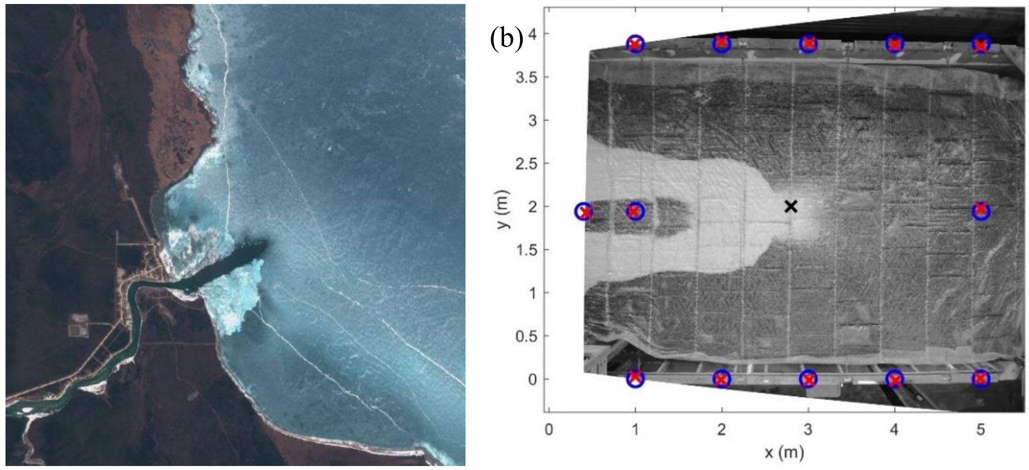


Figure 4.19. Hanging dam erosion (a) at Dauphin River–Lake Winnipeg confluence on 3 May 2018 (image courtesy of the USGS) and (b) for the experiment with an approach Froude number of 0.33 (flow direction: from left to right; white area: hanging dam extent; pink markers: ground control points; black cross marker: camera location).

Another hanging dam can be found downstream of the Keeyask Generating Station on the lower Nelson River, Manitoba. The Keeyask Generating Station is located between the outlet of Split Lake and the inlet to Stephens Lake, with average winter flows of 3300 $m^3/s$. The lower Nelson River is a complex, fast-flowing hydraulic system that contains reaches that are separated by rock controls, rapids, and lakes. The ice processes in this river are complex due to the presence of rapids that produce a large quantity of frazil ice during the winter and the interconnected system of river reaches and lakes. During the winter, a large hanging dam forms at the inlet to Stephens Lake that is located immediately downstream of the Gull Rapids. There is a 13 m drop in elevation from Gull Lake to Stephens Lake, and the majority of the drop spans across the Gull Rapids.

Prior to commissioning of the Keeyask Generating Station, the lake ice cover on Stephens Lake formed in early fall, causing the frazil ice generated in the Gull Rapids to collect at the leading edge of the ice cover. The ice cover progressed upstream until reaching the rapids section downstream of the Keeyask Generating Station, where it stalled. The incoming frazil ice from upstream was deposited beneath the ice cover and formed a hanging dam at this location. This hanging dam initially grew very rapidly, but the growth rate slowed down later depending on whether an ice bridge formed upstream of Gull Lake. The frazil ice supply from upstream was reduced substantially if the ice cover bridged upstream of Gull Lake, which impacted the size of the hanging dam formation (Groeneveld et al., 2017).

The size and the location of the hanging dam at this site can be seen in satellite imagery when the lake ice cover is thin, typically in mid-May. Satellite images of the hanging dam from Sentinel-2 and Landsat 8/9 satellites were obtained from the US Geological Survey's EarthExplorer (USGS Sentinel-2 and Landsat) for a period of 10 years from 2013 to 2023. The hanging dam was not visible in some years due to high cloud coverage. Figure 4.20 shows the hanging dam downstream of the Keeyask Generating Station in 2013 and 2023. A significant decrease in the areal extent can be observed when comparing the formation of 2013 with that of 2023.

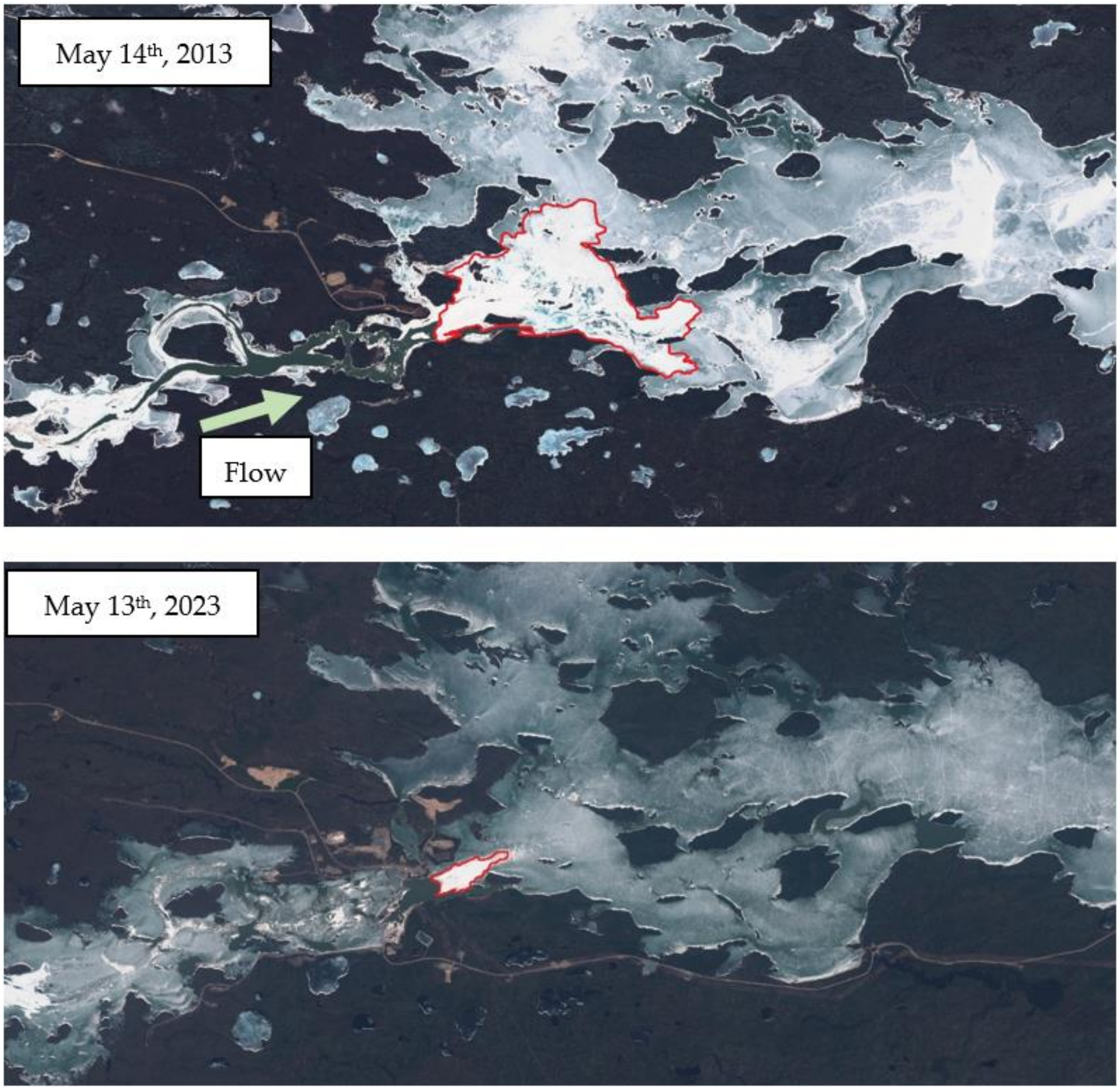


Figure 4.20. Hanging dam formation downstream of Keeyask Generating Station in 2013 and 2023 (the extent of the hanging dam is outlined in red).

The Keeyask Generating Station started operations in March 2022, which is the main difference between the 2012–2013 and 2022–2023 seasons. The ice boom installed at Gull Lake and the flow control procedures taken by the generating station as part of their operations may have ensured the formation of a competent ice cover upstream of the rapids section, lowering the frazil ice production. There are open water sections visible in the

2013 satellite image upstream of the hanging dam location, but these sections are ice-covered in the 2023 satellite image.

The mean daily air temperatures at Gillam Airport (the closest meteorological site to the Keeyask Generating Station) were analyzed for the two winter seasons (October–May) for 2012–2013 and 2022–2023. The cumulative degree days of freezing (CDDF) for the 2012–2013 winter were calculated as 3323, while the 2022–2023 winter had 3065 cumulative degree days of freezing, indicating that the 2022–2023 winter was warmer than the 2012–2013 winter.

The results presented in this paper comprise the first published quantitative laboratory data on hanging dam formation, but there are several limitations of this study that need to be highlighted. The thermal effects on the hanging dam formation were not taken into consideration, as it is practically difficult to incorporate the thermal component in a laboratory environment. Frazil ice is cohesive and easily freezes together, unlike the HDPE pellets that were used as simulated ice in this laboratory study. In a natural river, hanging dams can attain extremely high thicknesses if the applied shear stress beneath them is less than the critical shear stress that initiates erosion. In this laboratory study, the flow depth was limited; therefore, the maximum thickness of the hanging dam reached similar values for all the different ice supply rate conditions.

The under-ice roughness, shear stress, and velocity change as the accumulation increases in thickness. Quantifying these parameters would be beneficial when validating numerical models as well as provide an additional insight when making comparisons with field data. An acoustic Doppler velocimeter (ADV) was considered to obtain the velocity measurements in this study, but it could not be used during the ice supply stage because the ADV probe disturbed the hanging dam formation. The use of an alternative technique to measure the velocity beneath the hanging dam is suggested for future studies, as it will be a valuable addition to the existing hanging dam literature.

### 4.2.6 Conclusion

The effects of the approach Froude number of a river and the incoming ice supply rate on the hanging dam formation and evolution processes were analyzed in this study. Hanging dam erosion that is enabled by a higher river discharge (at a higher approach Froude number) was also discussed. The results of this study were obtained from a series of laboratory experiments in a hanging dam physical model using HDPE pellets and bubble wrap as simulated frazil ice and simulated ice cover, respectively.

The hanging dam formed immediately at or very close to the lake inlet at lower approach Froude numbers when compared with higher approach Froude numbers, as the high velocity of the three-dimensional wall jet did not allow under-ice deposition at the lake inlet at higher Froude numbers. The maximum centerline length of the hanging dam increased with increasing Froude numbers, but the maximum width was not dependent on either the Froude number or the incoming ice supply rate. The maximum width of the hanging dam reached a constant value for all low approach Froude number experiments at the final volume of the hanging dam.

The maximum thickness decreased, and the location of the maximum thickness was further downstream with increasing approach Froude numbers due to the high velocity of the jet that pushes the hanging dam formation further downstream at high approach Froude numbers. The areal extent of the hanging dam increased with increasing Froude numbers. The low incoming ice supply rate experiments had higher areal extents compared to the high incoming ice supply rate experiments for the same Froude number, as the low incoming ice supply rate was not adequate to overcome the under ice erosion rate exerted by the flow of the jet.

The satellite imagery of the hanging dam at the Dauphin River–Lake Winnipeg confluence was compared to the laboratory experiments to note the similarities in the formation and erosion of the hanging dam. Decades apart satellite images (2013 and 2023) of the hanging dam downstream of the Keeyask Generating Station were compared, and a considerable reduction in the areal extent of the hanging dam was noticed. The effects of the flow control procedures implemented by the generating station as a part of their operations, and the construction of the reservoir and forebay of the generating station altered the hydraulics and ice conditions upstream of the hanging dam location.  The milder winter might be another reason for the reduction in the hanging dam size.

This is the first study of its kind that presents the relationship between the approach Froude number and the incoming ice supply rate on hanging dam formation and evolution, contributing to improving our understanding of these processes. The wall jet comparison to hanging dam formation is of interest for numerical modelling applications simulating hanging dam formation and evolution.

#### 4.2.7 Acknowledgements

The authors would like to thank Alexander Wall for his assistance with the experimental setup, and Danica Bodino for orthorectifying the aerial view images.

### 4.2.8 References

Agisoft Metashape Professional Edition (Version 1.5) [Computer Software], 2019. Agisoft LLC.: St. Petersburg, Russia.

Ashton, G. D., 1974. Froude criterion for ice block stability. Journal of Glaciology, 13, 307-313.

Badhan, M. A. 2020. An Experimental Investigation of Hanging Dam Formation. M.Sc. Thesis, University of Manitoba, Winnipeg, MB, Canada.

Beltaos, S., Dean, A.M., 1981. Field investigations of a hanging dam. In Proceedings of the IAHR Symposium on Ice, Quebec, QC, Canada.

Beltaos, S., 2013. Ice Cover Formation. In River Ice Formation; Beltaos, S., Ed.; Committee on River Ice Processes and the Environment; Canadian Geophysical Union, Hydrology Section : Edmonton, AB, Canada, 181–251.

Bourgault, D., Richards, C., Pawlowicz, R. A Matlab Package for Georectifying Oblique Digital Images (g rect). Retrieved from GitLab. Available online: http://demeter.uqar.ca/g_rect/index.php/A_Matlab_package_for_georectifying_oblique_digital_images_(g_rect) (accessed on 10 May 2023).

Clark, S.P., Wall, A., 2016. Freeze-up monitoring on the Dauphin River, Manitoba, Canada. In Proceedings of the 23rd International Symposium on Ice, Ann Arbor, MI, USA.

Gebre, S., Alfredsen, K., Lia, L., Stickler, M., Tesaker, E., 2013. Review of Ice Effects on Hydropower Systems. Journal of Cold Regions Engineering. 27, 196–222.

Gold, L.W., Williams, G.P., 1961. An unusual ice formation on the Ottawa River. Journal of Glaciology. 4, 569–573.

Groeneveld, J., Malenchak, J., Morris, M., 2017. Numerical Model Studies of Ice Conditions during the Design and Construction of the Keeyask Generating Station. In Proceedings of the 19th Workshop on the Hydraulics of Ice Covered Rivers, Whitehorse, Yukon, Canada.

Hicks, F., 2009. An overview of river ice problems: CRIPE07 guest editorial. Journal of Cold Regions Science and Technology 55, 175–185.

Hopper, H.R., Raban, R.R., 1980 Hanging dams in the Manitoba Hydro system. In Proceedings of the Workshop on River Ice, Burlington, ON, Canada.pp. 195–208.

ImageJ (Version 1.51) [Computer Software], 2018. National Institutes of Health and Laboratory for Optical and Computational Instrumentation (LOCI), University of Wisconsin: Madison, WI, USA.

KGS Group; North/South Consultants, 2014. Emergency Reduction of Lake Manitoba and Lake St. Martin Water Levels; Manitoba Infra-structure and Transportation: Winnipeg, MB , Canada.

Kivisild. H.R., 1959. Hanging ice dams. In Proceedings of the 8th Congress International Association for Hydraulic Research, Montreal, QC, Canada. 2, paper no. 23-F,-1-30.

Launder, B.E., Rodi, W., 1981. The turbulent wall jet. Prog. Aerosp. Sci., 19, 81–128.

Lees, K., Clark, S.P., Malenchak, J., Chanel, P., 2021. Characterizing ice cover formation during freeze-up on the regulated Upper Nelson River, Manitoba. Journal of Cold Regions Engineering, 35.

MacLachlan, D. W., 1926. Appendix E. In St. Lawrence Waterways Project Report; Joint Board of Engineers: Ottawa, Canada.

Senarathbandara, R., Clark, S.P., Dow, K., 2023. Investigating the effect of incoming ice supply rate on hanging dam formation. In Proceedings of the 22nd Workshop on the Hydraulics of Ice Covered Rivers, Canmore, AB, Canada.

Shen, H.T., Wang, D.S., 1995. Under cover transportation and accumulation of frazil granules. ASCE Journal Hydraulic Engineering, 121, 184–195.

Sui, J., Hicks, F.M., Menounos, B., 2006.i Observations of river bed scour under a developing hanging dam. Canadian Journal of Civil Engineering. 33, 214-218.

USGS Sentinel-2 EarthExplorer. Available online: https://apps.sentinel-hub.com/sentinel-playground (accessed on 7 June 2023).

USGS Landsat EarthExplorer. Available online: https://earthexplorer.usgs.gov (accessed on 8 June 2023).

Vergeynst, J., Morse, B., Turcotte, B., 2017. Quantifying frazil production, transport and deposition in a gravel-bed river: Case study of the St. Raymond hanging dam. Cold Regions Science and Technology, 141, 109–121.

Wazney, L.E., 2019. Investigation of River Ice Cover Formation Processes at Freeze-Up. Ph.D. Thesis, University of Manitoba, Winnipeg, MB, Canada.

Zbigniewicz, H.S., 2017. Lake Winnipeg Regulation Ice Stabilization Program. In Proceedings of the Workshop on River Ice, Fredricton, NB, Canada, pp. 43–53.

## 4.3 Conclusions and Contributions of this Work

This chapter presents effects of the approach Froude number of a river and the incoming ice supply rate on the hanging dam formation and evolution processes, analyzed using laboratory experiments with simulated ice and ice cover. The discussion on hanging dam erosion and relating it to the high velocity of the river advances the present understanding of the effect of river hydraulics on the formation and evolution hanging dam processes.

# Chapter 5 Numerical Modeling of Under Cover Ice Transport and Hanging Dam Formation Processes

## 5.1 Introduction

Two-dimensional Comprehensive River Ice Simulation System Project (CRISSP2D) was used to model the under cover ice transport and hanging dam formation presented in this chapter. The objective of this chapter was to provide an evaluation of current numerical formulations in the CRISSP2D model with respect to the under cover ice transport module. A simplified model was run where the effect of under cover ice transport could be easily identified for comparison to the laboratory experiments presented in Chapter 3 and 4, so the thermal effects and ice dynamics were not taken into consideration. The under cover ice transport scenarios presented in this chapter were simulated under free drift model conditions, where the parcels were transported by setting the parcel velocity to the water velocity without considering the interactions between the parcels using the Smoothed Particle Hydrodynamics (SPH) method. When modeling a field scenario, it is crucial to integrate both ice dynamics and the thermal effects of ice for a comprehensive representation of the physical processes in the field.

The current numerical formulation for under cover ice transport processes are evaluated using model simulations in an idealized rectangular channel under uniform flow conditions. The results are compared with the Shen and Wang (1995) equation for transport of under cover ice granules. A channel expansion is introduced to the same idealized channel to facilitate ice deposition. This model setup is used to investigate the impact of incoming ice supply rate, approach Froude number, and the critical dimensionless flow strength on transport processes and ice deposition. The model results are compared with under cover ice transport and hanging dam formation laboratory experiment results presented in Chapters 3 and 4 of the thesis.

## 5.2 Background

The two main sources of under cover ice in the CRISSP2D model are from the ice floes that underturn upon reaching the leading edge of an ice cover based on a critical Froude number criterion, and suspended frazil ice in the flow. The ice floes approaching the leading edge of an ice cover will underturn if the Froude number is higher than the critical Froude number, prescribed in the model parameters. In the CRISSP2D model, the transport of under cover ice (frazil granules) is treated similar to sediment transport based on the analogous relationship between the two processes. The Shen and Wang (1995) ice transport equation, (Equation 5.1) is used as the numerical formulation for modeling ice transport processes in the current CRISSP2D model, where $\Phi_n$ is the dimensionless transport rate (-), $\Theta_n$ is the dimensionless flow strength (-), and $\Theta_c$ is the critical dimensionless flow strength (-) that is set in the code as 0.041.

$$\Phi = 5.487(\Theta - \Theta_c)^{1.5} \qquad [5.1]$$

The dimensionless transport rate and the dimensionless flow strength are defined in the model using Equation 5.2 and Equation 5.3, respectively where $q_{uc}$ is the volumetric transport rate per unit width (m$^3$/s/m), $d_n$ is the nominal diameter of under cover ice particles (m), $\Delta$ is the difference between specific gravities of water and ice particles (-), $u_{*i}$ is the ice cover shear velocity (m/s), and $F$ is the fall velocity coefficient (-). $F$ is set to 1.0 in the current model with the assumption that the frazil ice is spherical in shape.

$$\Phi_n = \frac{q_{uc}}{F\sqrt{g d_n^3 \Delta}} \quad [5.2]$$

$$\Theta_n = \frac{u_{*i}^2}{F^2 g d_n \Delta} \quad [5.3]$$

Ice cover shear velocity, $R_i$ and the friction slope $S_f$ are determined using Equation 5.4, 5.5, and 5.6 where $V_w$ is the depth averaged flow velocity (m/s), $n_c$ is the composite roughness coefficient for bed and ice cover (-), $n_b$ is the bed roughness coefficient (-), $n_i$ is the ice roughness coefficient (-), and $H'$ is the water depth under ice (m). The composite roughness ($n_c$) was determined using Equation 5.7 based on Sabaneev's method for composite roughness calculation.

$$u_{*i} = \sqrt{g R_i S} \quad [5.4]$$

$$R_i = \frac{H\prime}{1+\left(\frac{n_b}{n_i}\right)^{3/2}} \quad [5.5]$$

$$S_f = \frac{V_w^2 n_c^2}{(H\prime/2)^{4/3}} \quad [5.6]$$

$$n_c = \left(\frac{n_b^{1.5}}{2} + \frac{n_i^{1.5}}{2}\right)^{2/3} \quad [5.7]$$

The model uses the Lagrangian discrete parcel method to simulate the under cover ice transport. The transport rate is calculated for the flow beneath each under cover parcel using Equation 5.8.

$$q_{uc} = \begin{cases} 5.487(\Theta - \Theta_c)^{1.5} F\sqrt{g d_n^3 \Delta} & if\ \Theta > \Theta_c \\ 0.0 & if\ \Theta \leq \Theta_c \end{cases} \qquad [5.8]$$

Calculated transport rate is used to determine the thickness of ice that will be eroded from the under cover ice parcel ($t'_{uc}$) using Equation 5.9, where $N_{uc}$ is the concentration of the undercover particle accumulation (-) and $V_{uc}$ is the under cover ice transport velocity (m/s). Equation 5.10 is an adaptation from van Rijn (1984) and Wu et al. (2006) that is used to determine $V_{uc}$ where $T$ is the dimensionless transport stage parameter (-), $\rho_i$ is the density of frazil ice (kg/m$^3$), and $\rho_w$ is the density of water (kg/m$^3$).

$$t'_{uc} = \frac{|q_{uc}|}{|V_{uc}| N_{uc}} \qquad [5.9]$$

$$V_{uc} = 1.64\left[T\left(1 - \frac{\rho_i}{\rho_w}\right) g d_n\right]^{0.5} \qquad [5.10]$$

Dimensionless transport stage parameter is calculated using Equation 5.11, and the critical ice grain shear velocity is determined according to the method suggested by van Rijn (1984) presented in Equation 5.12, where $D_*$ is the dimensionless particle parameter (-). $D_*$ is calculated using Equation 5.13, where $\nu$ is the kinematic viscosity of water (m$^2$/s).

$$T = \frac{u_{*i}^2 - u_{*,cr}^2}{u_{*,cr}^2} \qquad [5.11]$$

$$\frac{u_{*,cr}^2}{(1-s)gd_n} = \begin{cases} 0.240D_*^{-1.00} & for \quad D_* \leq 4 \\ 0.140D_*^{-0.64} & for \quad 4 < D_* \leq 10 \\ 0.040D_*^{-0.10} & for \; 10 < D_* \leq 20 \\ 0.013D_*^{0.29} & for \; 20 < D_* \leq 150 \\ 0.055 & for \; 150 < D_* \end{cases} \qquad [5.12]$$

$$D_* = d_n \left(\frac{\Delta g}{\nu^2}\right)^{1/3} \qquad [5.13]$$

$D_*$ is a dimensionless particle parameter that is used for Shield's criteria in sediment transport rate estimations. The same parameter and the Shield's criteria were adapted to estimate the critical ice grain shear velocity required to transport under cover ice in the CRISSP2D model based on the following factors. The effect of density has been accounted for when calculating $D_*$, the ice and sediment particle diameters are in the same order of magnitude and the velocity field near moving particles has the same profile for both ice and sediment particles.

The thickness that will be eroded from the ice parcel ($t'_{uc}$) is calculated using Equation 5.9, and it is compared with the thickness of the initial parcel. If $t'_{uc}$ is less than or equal to the initial parcel thickness, the calculated thickness ($t'_{uc}$) is eroded from the ice parcel. If $t'_{uc}$ is greater than the thickness of the initial parcel, the entire initial parcel is eroded. The amount eroded from the initial parcel is referred to as the eroded parcel. The mass of the eroded parcel ($M'_{uc}$) is calculated according to Equation 5.14, where $M_{uc}$ is the initial parcel mass. The parcel mass is proportional to the thicknesses of initial and eroded parcels.

$$M'_{uc} = M_{uc} \frac{t'_{uc}}{t_{uc}} \qquad [5.14]$$

The mass and the thickness of the new parcel after erosion are updated as given in Equation 5.15 and 5.16, respectively.

$$M_{uc} = M_{uc} - M'_{uc} \quad [5.15]$$

$$t_{uc} = t_{uc} - t'_{uc} \quad [5.16]$$

The portion of an initial parcel that remains uneroded will remain stationary, maintaining its position. Meanwhile, the eroded parcels will move along the channel with under cover ice transport velocity in the next time step. To prevent an excessive number of parcels in the model, an eroded parcel is merged with a stationary parent parcel at the new location at each coupling time step.

## 5.3 Model simulations with uniform flow conditions

### 5.3.1 Methods

The first set of model simulations were conducted under uniform flow conditions to evaluate the current numerical model formulation in CRISSP2D for under cover ice transport processes. A prismatic rectangular channel with a uniform bed slope of 0.001 was used as the idealized channel for these model simulations. A finite element mesh of a straight, rectangular idealized channel with a length of 10 km, and a width of 200 m was created using the Surface Water Modeling System (SMS) software (Aquaveo, 2021). A sensitivity analysis on mesh discretization was performed using three meshes; fine mesh with 10 m by 20 m, medium mesh with 50 m by 20 m and coarse mesh with 100 m by 20 m in streamwise and spanwise directions, respectively. The results of the mesh sensitivity analysis are presented in Appendix A. The spatial discretization in the streamwise and spanwise directions of the mesh was set to be 50 m and 20 m, considering the balance between computational efficiency and model accuracy. The first 1 km of the channel was set up as an open water section and the ice-covered section was set from 2 km to 10 km with a stationary ice cover of thickness 0.01 m (Figure 5.1).

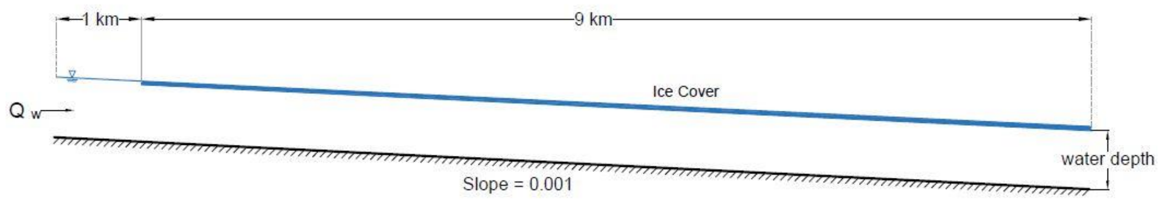


Figure 5.1. Streamwise schematic of the model setup for uniform flow simulations.

Water and ice discharge were the upstream boundary conditions. The water surface elevation was the downstream boundary condition which was determined by calculating the normal depth of flow for a specific water discharge under ice-covered conditions using Manning's equation with a composite roughness of 0.023. The model simulations were conducted for various hydraulic conditions summarized in Table 5.1. Each testing condition was set to run for 24 hours to analyze the effect of incoming ice supply rate on the ice output rate and under cover ice deposition in the channel.

A new output file called *.$uco$ was added to the CRISSP2D code to summarize the ice mass input to the model domain, the ice mass that exited the model domain, and the ice mass retained in the model at the end of each hour. The dimensionless ice output rate ($\Phi_{out}$) was calculated using Equation 5.17, where $Q_{out}$ is the ice output rate (total ice volume that exited the model domain over the simulation time) ($m^3/s$), and $b$ is the river width (m). The fall velocity coefficient ($F$) was set to a constant value of 1.0 as specified in the CRISSP2D model.

$$\Phi_{out} = \frac{\left(Q_{out}/_{b}\right)}{F\sqrt{gd_n^3\Delta}} \qquad [5.17]$$

The dimensionless flow strength ($\Theta_n$) was calculated based on the hydraulic radius and friction slope using the same procedure which was followed to calculate $\Theta_n$ in Chapter 3. For each case, the average flow velocity ($V_w$) was determined using Equation 5.18, where $Q_w$ is the water discharge (m$^3$/s), and $H_{avg}$ is the average flow depth along the centerline of the ice-covered section of the channel (m).

$$V_w = \frac{Q_w}{H_{avg}b} \qquad [5.18]$$

The incoming ice supply rate ($Q_{in}$) was varied in each case and the corresponding dimensionless ice input rate ($\Phi_{in}$) was calculated using Equation 5.17 by replacing $Q_{out}$ with $Q_{in}$. The uniform flow model simulations were conducted using the existing model formulation with the Shen and Wang (1995) equation.

Table 5.1. Testing conditions for uniform flow simulations in an idealized rectangular channel.

| $Q_{in}$ ($m^3/s$) | $\phi_{in}$ | $Q_w$ ($m^3/s$) | Average water depth (m) | Average flow velocity (m/s) | $\Theta_n$ | $\phi_{out}$ | Water surface slope (-) |
|---|---|---|---|---|---|---|---|
| 0.1 | 0.55 | 50 | 0.52 | 0.49 | 0.36 | 0.07 | 0.001 |
| | | 200 | 1.16 | 0.87 | 0.46 | 0.39 | |
| | | 250 | 1.33 | 0.94 | 0.52 | 0.42 | |
| 0.2 | 1.11 | 100 | 0.79 | 0.63 | 0.28 | 0.83 | |
| 0.3 | 1.66 | 138 | 0.94 | 0.74 | 0.36 | 1.42 | |
| 0.4 | 2.22 | 150 | 0.99 | 0.76 | 0.38 | 1.85 | |
| 0.5 | 2.77 | 200 | 1.17 | 0.85 | 0.45 | 2.27 | |
| | | 250 | 1.33 | 0.94 | 0.52 | 2.33 | |
| | | 350 | 1.62 | 1.08 | 0.64 | 2.39 | |
| | | 500 | 2.01 | 1.24 | 0.79 | 1.56 | |
| 0.6 | 3.32 | 50 | 0.53 | 0.47 | 0.18 | 2.47 | |
| | | 100 | 0.81 | 0.62 | 0.27 | 2.68 | |
| | | 138 | 0.94 | 0.74 | 0.36 | 2.85 | |
| | | 150 | 1.00 | 0.75 | 0.37 | 2.78 | |
| 1.0 | 5.54 | 50 | 0.54 | 0.46 | 0.17 | 3.97 | |
| | | 100 | 0.81 | 0.62 | 0.27 | 4.72 | |
| | | 138 | 0.97 | 0.71 | 0.33 | 4.37 | |
| | | 150 | 1.01 | 0.75 | 0.36 | 4.73 | |
| | | 350 | 1.63 | 1.07 | 0.63 | 5.23 | |
| | | 500 | 2.00 | 1.25 | 0.80 | 4.87 | |
| 2.0 | 11.08 | 50 | 0.56 | 0.45 | 0.16 | 6.82 | |
| | | 350 | 1.66 | 1.05 | 0.61 | 9.89 | |
| 2.5 | 13.85 | 138 | 0.97 | 0.71 | 0.33 | 10.70 | |
| 3.0 | 16.62 | 350 | 1.65 | 1.06 | 0.61 | 14.62 | |

| | | | | | | |
|---|---|---|---|---|---|---|
| 4.0 | 22.16 | 250 | 1.39 | 0.90 | 0.47 | 19.93 |
| | | 350 | 1.65 | 1.06 | 0.61 | 19.82 |
| 5.0 | 27.71 | 100 | 0.83 | 0.60 | 0.25 | 13.46 |
| | | 138 | 1.00 | 0.69 | 0.31 | 16.22 |
| | | 150 | 1.06 | 0.71 | 0.32 | 15.81 |
| | | 350 | 1.68 | 1.04 | 0.59 | 24.47 |

### 5.3.2 Results and Discussion

The results of uniform flow model simulations are shown in Figure 5.2, along with the Shen and Wang (1995) equation. The results are classified according to the incoming ice supply rate to demonstrate the impact of incoming ice supply on the dimensionless ice output rate ($\Phi_{out}$). As previously described in Chapter 3, the Shen and Wang equation was developed under equilibrium transport conditions maintaining a constant ice thickness in the channel. The line corresponding to the Shen and Wang equation defines the equilibrium condition for transport, and the depositions in the channel are denoted by points that are plotted above the line while points that are plotted below the line indicate ice erosion.

The dimensionless ice output rates are in the vicinity of the Shen and Wang (1995) line at low incoming ice supply rates (0-1 $m^3/s$) indicating that the flow strength has the capacity to transport the low ice supply rates through the model. Ice depositions start to occur for medium ice supply rates (1-2 $m^3/s$) at low flow strengths since the flow strength is not adequate enough to transport the ice supplied through the reach. The dimensionless ice output rates for medium ice supply rates with higher flow strengths do fall closer to the Shen and Wang line than medium ice supply rates with low flow strengths, since the flow has capacity to transport the incoming ice. When the incoming ice supply was further increased (2-5 $m^3/s$) it can be observed that $\Phi_{out}$ will move further away from the Shen and Wang (1995) line indicating major depositions. This observation was compatible with the Hequ Reach field data analysis presented in Chapter 3, where ice major ice depositions in the reach corresponded to the higher incoming ice supply rates from upstream.

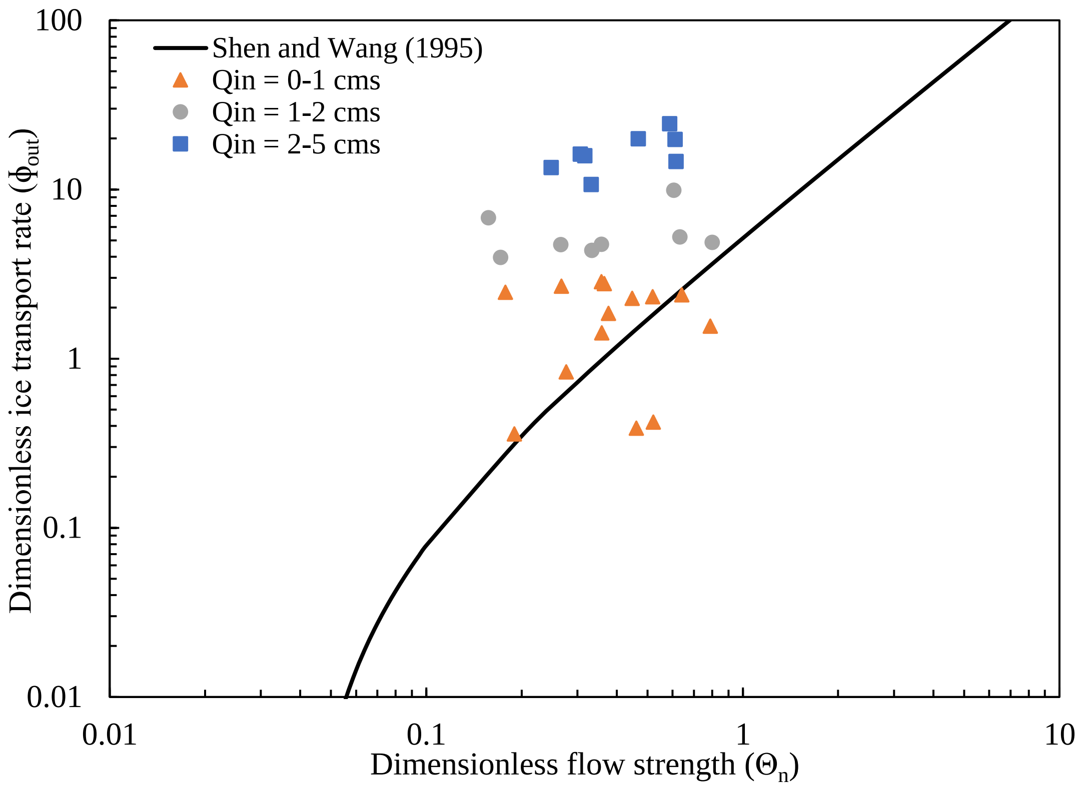


Figure 5.2. Uniform flow model simulations using Shen and Wang (1995) equation.

Figure 5.3 shows the variation of maximum under cover ice thickness in the channel at the end of the simulation period with the incoming ice supply rate to further validate the above findings. It shows that the magnitude of the under cover ice thickness increased with increasing incoming ice supply to the model indicating thicker depositions in the channel for higher incoming ice supply rates.

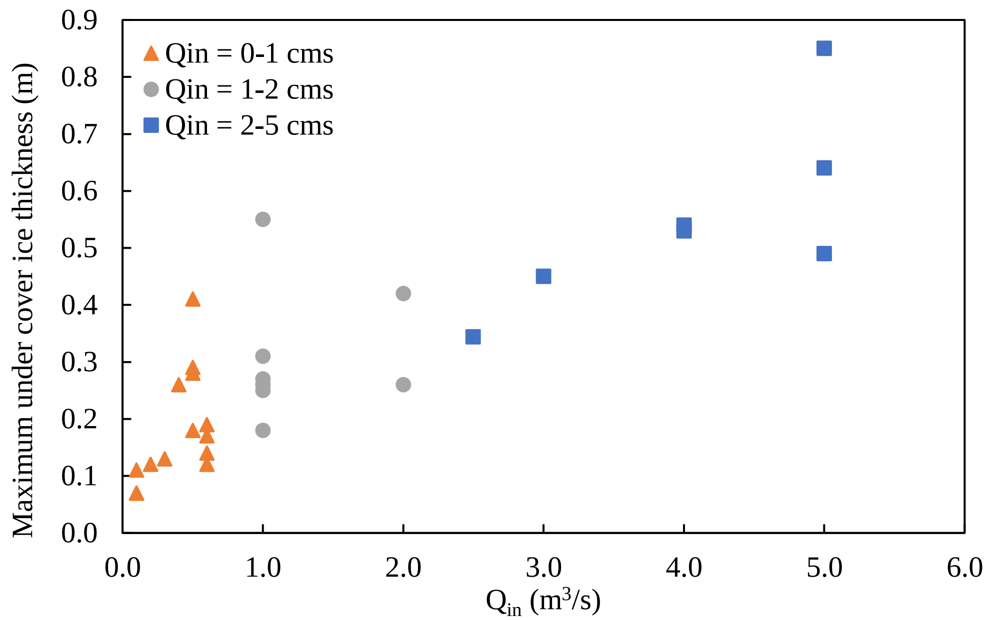


Figure 5.3 Variation of maximum under cover ice thickness with incoming ice supply rate.

The under cover ice deposition profile for uniform flow model simulations was evaluated to assess the model capability of producing an ice deposition profile for varying incoming ice supply rates. The ice deposition profile for uniform flow model simulations (a) $Q_w$ = 250 $m^3$/s, $Q_{in}$ = 0.5 $m^3$/s and (b) $Q_w$ = 250 $m^3$/s, $Q_{in}$ = 4.0 $m^3$/s at the end of the simulation period are shown in Figure 5.4.

For the case of low ice supply rate ($Q_{in}$ = 0.5 $m^3$/s) where the ice supply was close to the equilibrium ice supply determined by the Shen and Wang equation, only a small deposition can be observed at the end of the simulation period, indicating that the initial ice cover thickness was not significantly altered by the incoming ice supply to the model. The incoming ice supply did not contribute to increasing the ice cover thickness, instead it exited the model as ice output from the downstream end, which agrees in principle with the definition of equilibrium conditions as defined in Chapter 3 of the thesis.

The deposition profile at the end of the simulation period for the higher ice supply rate ($Q_{in}$ = 4.0 $m^3/s$) case shows there were depositions at various locations in the channel (ice deposited in these locations by travelling as a propagating wave). Based on the non-equilibrium experimental investigations presented in Chapter 3, it was expected that the under cover ice thickness in the entire channel length should have increased, creating an ice deposition profile throughout the channel, thereby increasing the dimensionless flow strength of the entire channel as a result of the overall increase in flow resistance.

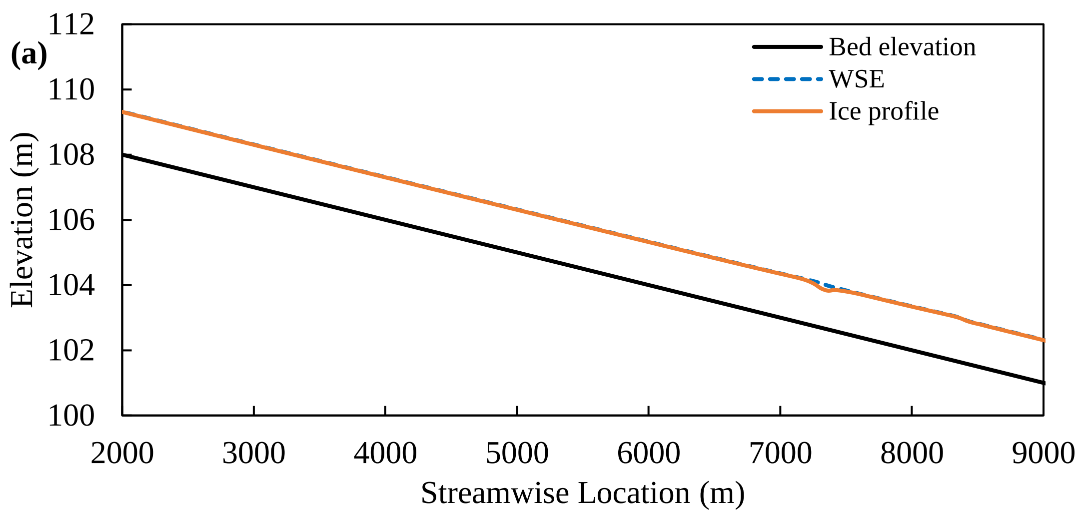

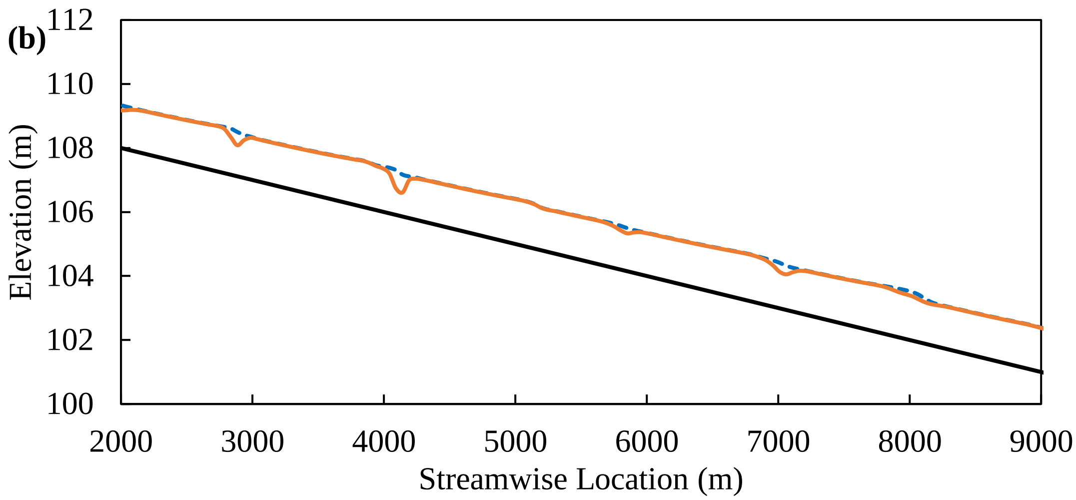


Figure 5.4. Ice deposition profile for uniform flow model simulations (a) $Q_w = 250$ m$^3$/s, $Q_{in} = 0.5$ m$^3$/s and (b) $Q_w = 250$ m$^3$/s, $Q_{in} = 4.0$ m$^3$/s

The localized depositions shown in Figure 5.4 (b) at higher incoming ice supply rates only caused localized changes in water depth and velocity at the locations where the depositions happen, which did not affect the overall flow strength in the channel.

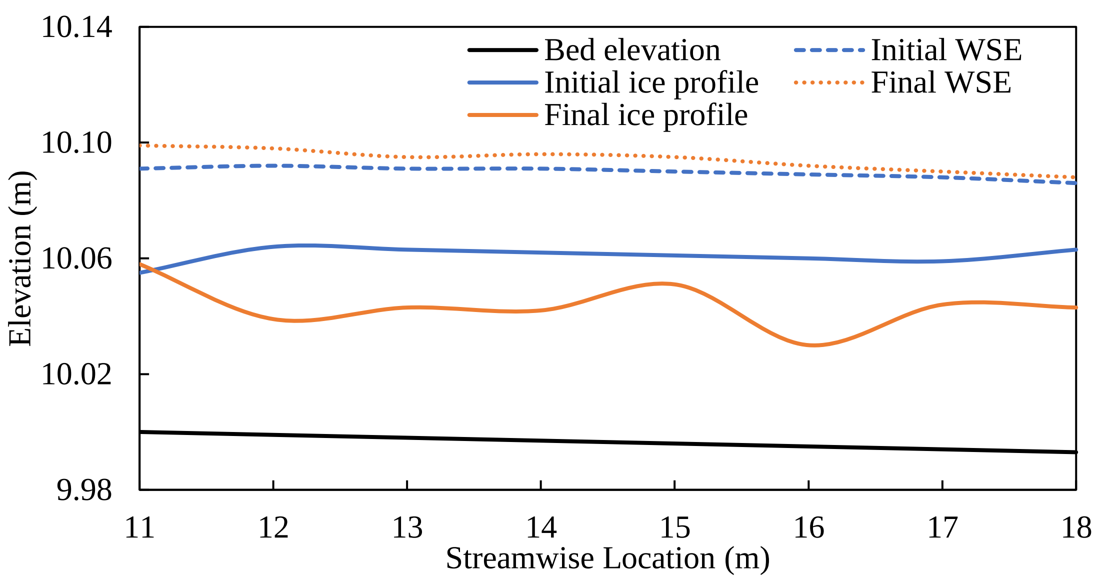


Figure 5.5. Ice deposition profile for higher than equilibrium ice supply rate (Case 3) experiment.

Figure 5.5 shows the experimental results for a higher than the equilibrium ice supply rate which resulted in an increased under cover ice thickness throughout the flume length at the end of experimental period. The ice mass within the model was conserved with 1% maximum difference between mass within the model and the mass that was input to the model at the end of each simulation period. The final water surface elevation and the water surface slope have increased due to deposition underneath the ice cover. Since the thickness of the ice cover has increased, the resistance to flow also increased causing an increase in the final dimensionless flow strength. The numerical model simulation results showed that the model is not currently equipped with a numerical formulation to simulate the physical process when the incoming ice supply rate deviates from the equilibrium ice transport determined by under cover transport rate equation.

To further understand the cause of this, it was important to investigate the model formulation and the key factors that would determine the deposition profile in the CRISSP2D model. The under cover transport rate that is calculated using Equation 5.1 (Shen and Wang ,1995) and the under cover transport velocity that is determined using Equation 5.10 (van Rijn, 1984) are the two main model components that would determine the amount of ice that is being eroded from an ice parcel and the velocity with which the eroded ice would transport until the next coupling time step, respectively. It is also evident that the user defined coupling time has a direct impact on the distance an eroded ice parcel travels until it gets combined with a stationary ice parcel.

Coupling timestep determines the communication frequency of the ice dynamic and the hydrodynamic models. Typically for other module simulations in CRISSP2D such as skim ice formation, thermal ice growth, and anchor ice formation, a coupling time of 900 s (15 minutes) is deemed to be sufficient to generate accurate model results. As indicated by the model results, due to the dynamic nature of under cover transport processes, a 15-minute coupling time interval is too large to capture the changes occurring at a smaller time scale. A sensitivity analysis was conducted for a series of coupling time steps using the same channel geometry under uniform flow conditions and continuous incoming ice supply for a simulation period of 24 hours to further investigate the effect of coupling time on under cover ice deposition. The plan view of the channel showing the thickness of under cover ice deposition for various coupling times at end of the simulation period is shown in Figure 5.6.

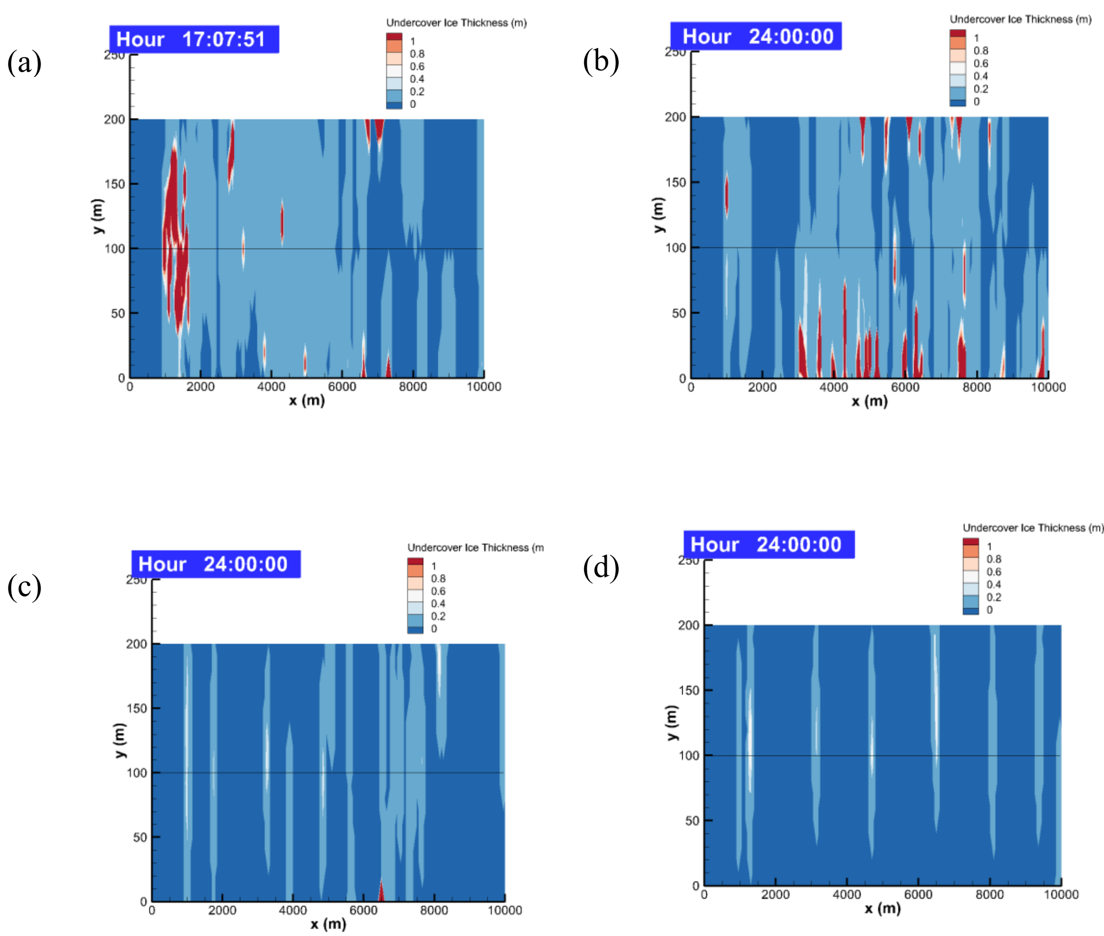

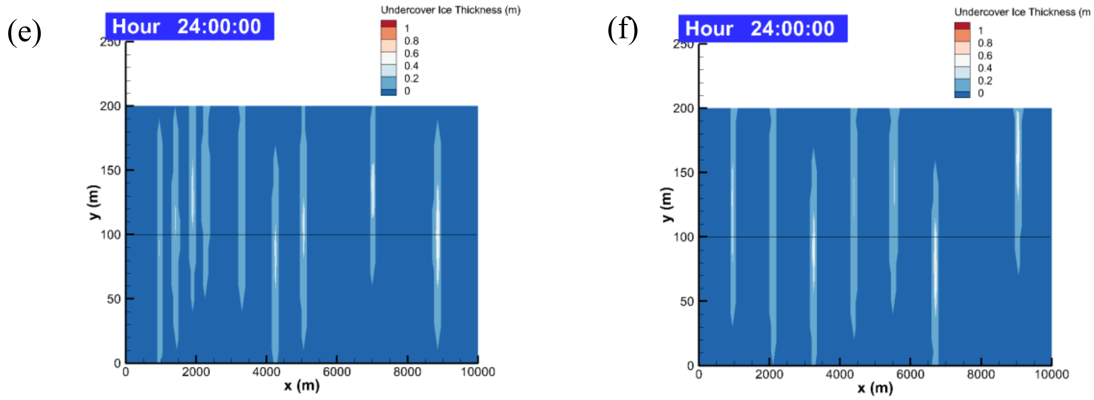


Figure 5.6. Sensitivity analysis for coupling times (a) 2s, (b) 5s, (c) 60s, (d) 240s, (e) 360s, (f) 900s.

The results show that the lower coupling times (2s and 5s) were successful in generating a uniform ice deposition profile since the eroded ice parcels were combining with the stationary ice parcels at a higher frequency compared to high coupling time model runs. For high coupling time interval model simulations, an ice parcel would travel further downstream in the channel for the duration of the coupling time interval before it has the opportunity to deposit under the ice cover.

Running an under cover model simulation at a low coupling time step seemed to generate a uniform ice deposition profile by capturing the dynamic nature of under cover ice transport processes. However model simulations with low coupling time steps caused the ice to deposit in extremely large quantities at the edges of the channel (shown in red), eventually causing the model to crash (the model crashed at approximately 17 hours for the 2s coupling time simulation). Even though this problem of extremely high ice depositions at model side boundaries occurred when the coupling time interval was reduced to a small number, this is primarily related to the model's treatment of ice at the channel boundaries which needs to be addressed. The variation of maximum ice thickness at the edges of the channel with the coupling time highlighting the extremely high ice thicknesses for low coupling time steps is shown in Figure 5.7.

The sensitivity analysis on coupling timestep showed that uniform ice deposition can be simulated by using a low coupling time step. According to the model formulation, an eroded ice parcel will transport with under cover velocity until the next coupling time step to be combined with a stationary ice parcel. By lowering the coupling time step the model will be able to simulate a uniform ice deposition profile as observed in laboratory experiments.

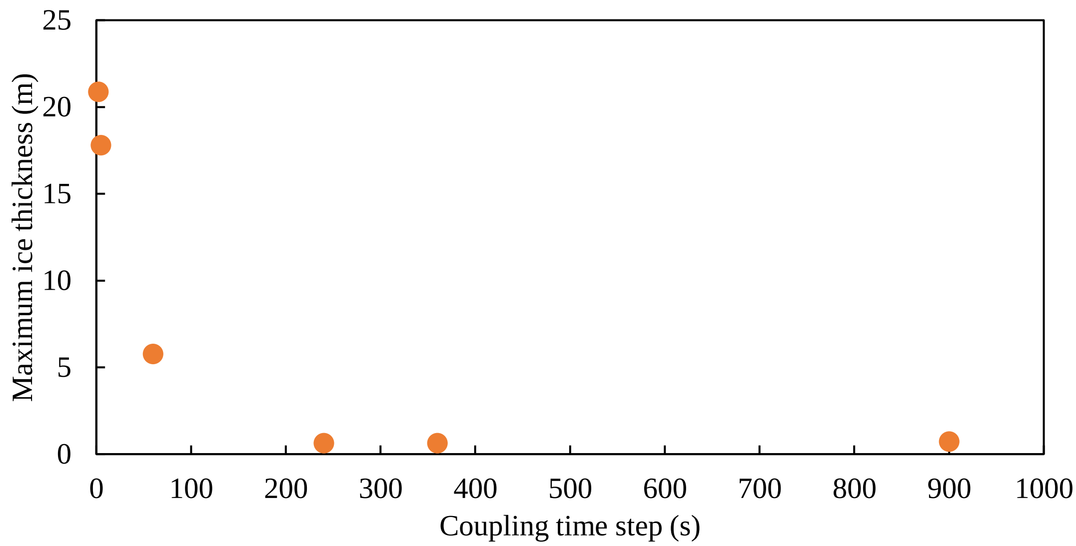


Figure 5.7. Variation of maximum ice thickness at the edges of the channel with the coupling time.

## 5.4 Model Simulations with a Channel Expansion

The second part of the numerical study focused on simulating the ice deposition underneath an ice cover leading to hanging dam formation, similar to the laboratory experiments presented in Chapter 4 of the thesis. Hanging dams are formed when a large quantity of under cover ice accumulates beneath an existing ice cover. Such depositions are facilitated by low flow velocities that typically occur with geometry changes in a river such as width expansions, drop in the bed elevation, or slope reductions. Two channel geometries with a drop in bed elevation were used to simulate ice accumulation and the effect of approach Froude number on the maximum thickness of the accumulation and its location.

### 5.4.1 Model Setup

*Geometry 1*

The first geometry was a rectangular ideal channel with a length of 10 km, and a width of 200 m. At a streamwise distance of 2 km from the upstream end, a drop of 5 m in the bed elevation was introduced over the next 50 m. The section upstream and downstream of the drop had a bed slope of 0.001. During the freeze-up period there can be open water sections in a river that enable continuous frazil ice generation and transport downstream, therefore the upstream shallow river section was modeled as an open water section. A thin stable ice cover with a thickness of 0.01 m was set from 2.0 km in the deep river section to the channel outlet at 10 km. The cross-sectional and the plan view of geometry 1 is shown in Figure 5.8. The drop in the channel bed significantly reduced the water velocity in the downstream section of the channel promoting ice deposition.

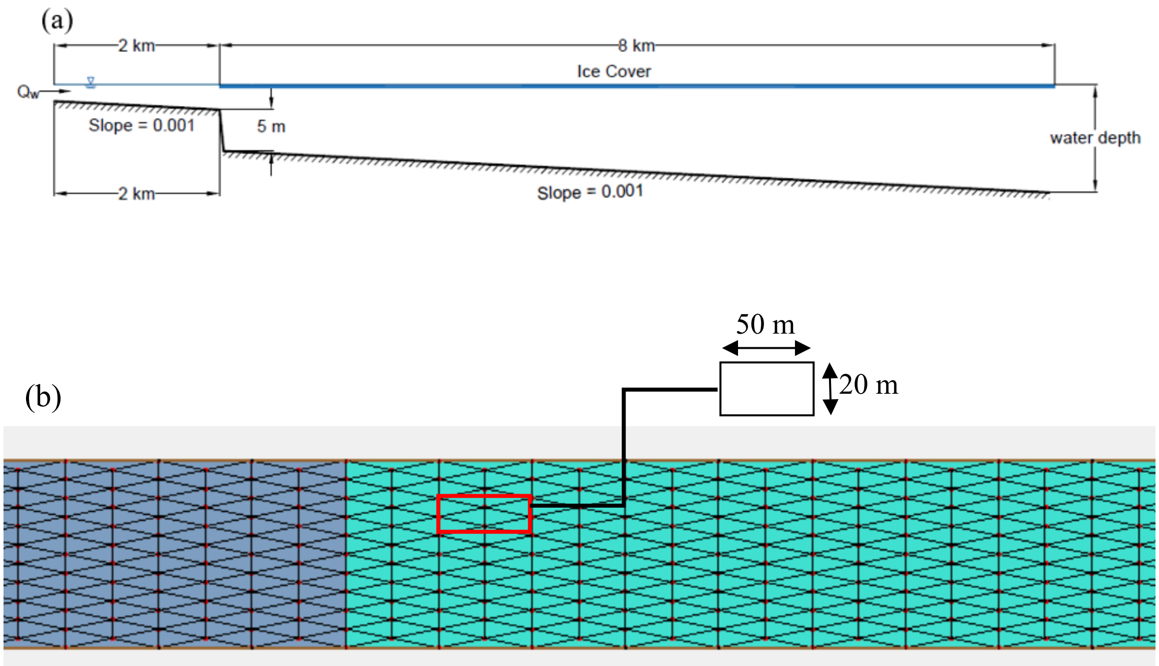


Figure 5.8. (a) Streamwise cross-sectional and (b) plan view of geometry 1

*Geometry 2*

In the second geometry the width of the channel increased from 200 m to 400 m in addition to the 5 m channel drop. This channel can be divided into 3 reaches. The most upstream reach had a width of 200 m, and a bed slope of 0.001. The following transition reach had a 5 m drop in the channel bed elevation at 2 km, and the bed slope was 0.025. At 2 km, the channel width also increased from 200 m to 400 m over a streamwise distance of 200 m. The most downstream reach extended from 2.2 km to 10 km with a width of 400 m and a bed slope of 0.001. The ice cover was placed at a distance of 2.4 km from the inlet instead of at 2.0 km to reduce the effect of dynamic changes at the channel expansion interface. The cross-sectional and the plan view of geometry 2 is shown in Figure 5.9.

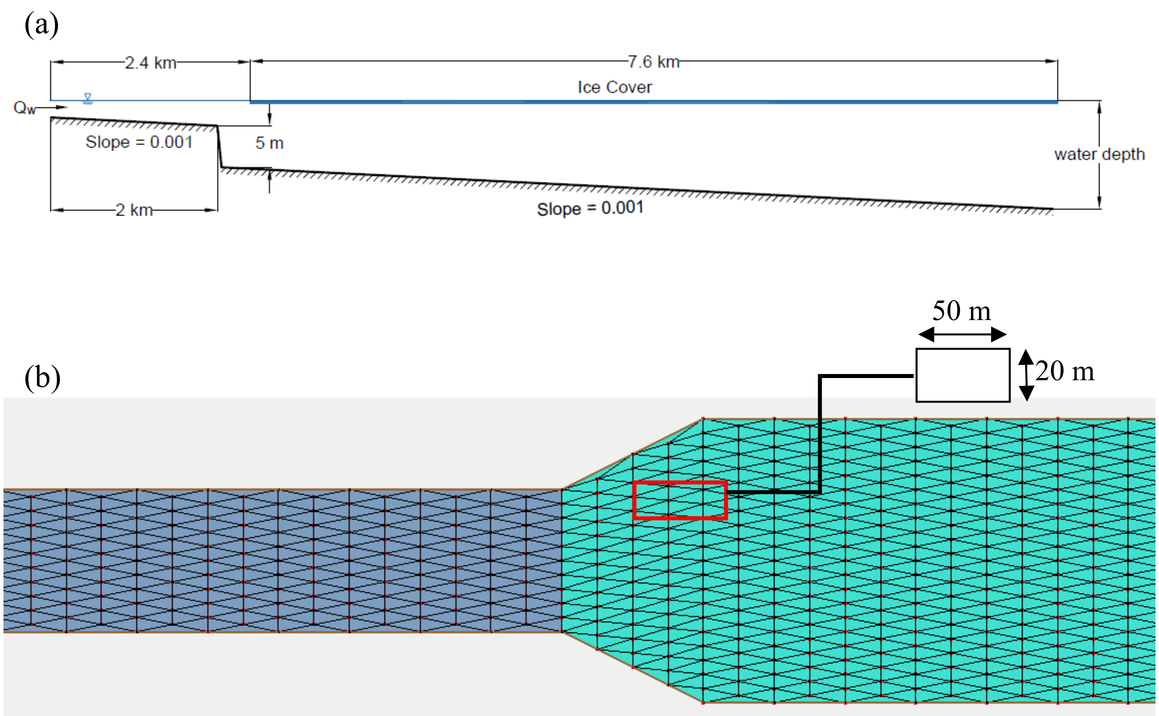


Figure 5.9. (a) Streamwise cross-sectional and (b) plan view of geometry 2

The water surface slope and the water depth in the deep river section were the two important aspects considered when setting up the downstream boundary condition. The water surface slope should be low enough to reduce the applied boundary shear stress, hence reduce the flow strength and allow deposition. The water depth in the downstream section should be deep to have a higher cross sectional flow area and therefore a lower flow velocity that would support deposition underneath the ice cover. Firstly, the water discharge and the water depth at the leading ice edge (2.0 km for geometry 1 and 2.4 km for geometry 2) were determined for each Froude number condition. The water surface elevation at the leading ice edge was calculated, and this elevation was then used as the water surface elevation at the downstream boundary condition. This imposed a high water level at the downstream boundary of the model similar to a lake that backs up into the channel or the backwater caused by a hydraulic structure downstream. A constant water discharge calculated according to the Froude number at the leading ice edge was used as the upstream boundary condition. The ice discharge input to the model was introduced through the channel inlet. The coupling time was set as 15 minutes for all simulations with a channel expansion.

### 5.4.2 Model Simulations to analyze the effect of $\Theta_c$

Model simulations were conducted to analyze the effect of critical dimensionless flow strength ($\Theta_c$) since it is an important parameter which defines the incipient motion of under cover ice transport. The effect of $\Theta_c$ was analyzed using two values, $\Theta_c$ = 0.041 based on the under cover ice transport study by Shen and Wang (1995) and $\Theta_c$ = 0.396 based on laboratory experiments presented in Chapter 3 of this thesis. The critical shear velocity ($u_{*c}$) was determined using Equation 5.19 and was calculated to be 0.02 m/s for $\Theta_c$ = 0.041 and 0.06 m/s for $\Theta_c$ = 0.396. Equation 5.20 was used to calculate the critical boundary shear stress ($\tau_{bc}$). Critical boundary shear stress was determined to be 0.33 Pa, and 3.26 Pa for $\Theta_c$ = 0.041 and $\Theta_c$ = 0.396, respectively.

$$u_{*c}^2 = \Theta_c F^2 \Delta g d_n \qquad [5.19]$$

$$\tau_{bc} = u_{*c}^2 \rho \qquad [5.20]$$

Several incoming ice supply rates were used to investigate whether the ice supply rate has an effect on the hanging dam formation along with the critical dimensionless flow strength parameter. Model conditions are given in Table 5.2.

Table 5.2. Testing conditions for simulations to investigate the effect of $\Theta_c$ on ice deposition in an idealized rectangular channel with a drop in bed elevation.

| Geometry | Lake flow area ($m^2$) | River flow area ($m^2$) | Flow area ratio (-) | $\Theta_c$ (-) [Equation] | $Q_w$ ($m^3$/s) | $Q_i$ ($m^3$/s) |
|---|---|---|---|---|---|---|
| **Geometry 1** | 1800 | 800 | 2.25 | 0.041 [Shen & Wang] | 790 | 0.01 |
| | | | | 0.396 [Senarathbandara et al.] | | 0.1 |
| | | | | | | 1.0 |
| **Geometry 2** | 3600 | 800 | 4.50 | 0.041 [Shen & Wang] | 790 | 0.01 |
| | | | | 0.396 [Senarathbandara et al.] | | 0.1 |
| | | | | | | 1.0 |

Figure 5.10 shows geometry 1 streamwise ice deposition profiles for $Q_{in}$ = 0.01 $m^3$/s, simulated using Shen and Wang (1995) and Senarathbandara et al. (2024) equations after a duration of 5, 10, 15, 20, 25, and 30 days of simulation. The model simulations conducted using Shen and Wang (1995) equation are referred to as $\Theta_c$ = 0.041 simulations and the simulations conducted using Senarathbandara et al. (2024) equation are referred to as $\Theta_c$ = 0.396 simulations in the following sections of this chapter. The ice deposition profile is plotted at the channel bed drop location, where the flow strength is reduced due to increased flow area facilitating ice deposition. After a simulation time of 5, 10, and 15 days, both $\Theta_c$= 0.041 and $\Theta_c$= 0.396 simulations showed ice starting to deposit at the leading ice edge creating a small hanging dam formation. After 15 days, the ice depositions for $\Theta_c$= 0.041 simulation started to erode, and the eroded ice was deposited at a location further downstream. Figures 5.10 (d, e, f) for durations of 20, 25, and 30 days for the $\Theta_c$= 0.041

simulations show the ice accumulation at the channel transition undergoing erosion. On the contrary, the $\Theta_c$= 0.396 simulations showed continuous deposition of ice at the leading edge forming a hanging dam that grows in thickness with time as depicted in Figures 5.10 (g-l).

$\Theta_c$ is a measure of critical shear stress that is dependent on particle size, density, and buoyant velocity. The model results showed that the hanging dam accumulation was prone to erosion for low $\Theta_c$ when compared with high $\Theta_c$. The critical dimensionless flow strength of 0.396 from Senarathbandara et al. (2024) equation was calculated based on hydraulic measurements at incipient motion of HDPE pellets (simulated ice) as described in Chapter 3 of the thesis. Numerical simulations showed that a thick under cover ice accumulation can be simulated with a higher $\Theta_c$ value of 0.396, similar to the results from the hanging dam laboratory experiments in Chapter 4. For all simulations, the ice mass within the model was conserved with 1% maximum difference between mass within the model and the mass that was input to the model.

The plan view for $\Theta_c$= 0.041 simulations is shown in Figure 5.11 where ice was undergoing constant erosion and was transported downstream, instead of forming a hanging dam at the leading ice edge. The plan view of the hanging dam accumulation for $\Theta_c$= 0.396 simulations with $Q_i$ = 0.01 $m^3/s$ at the leading ice edge is shown in Figure 5.12.

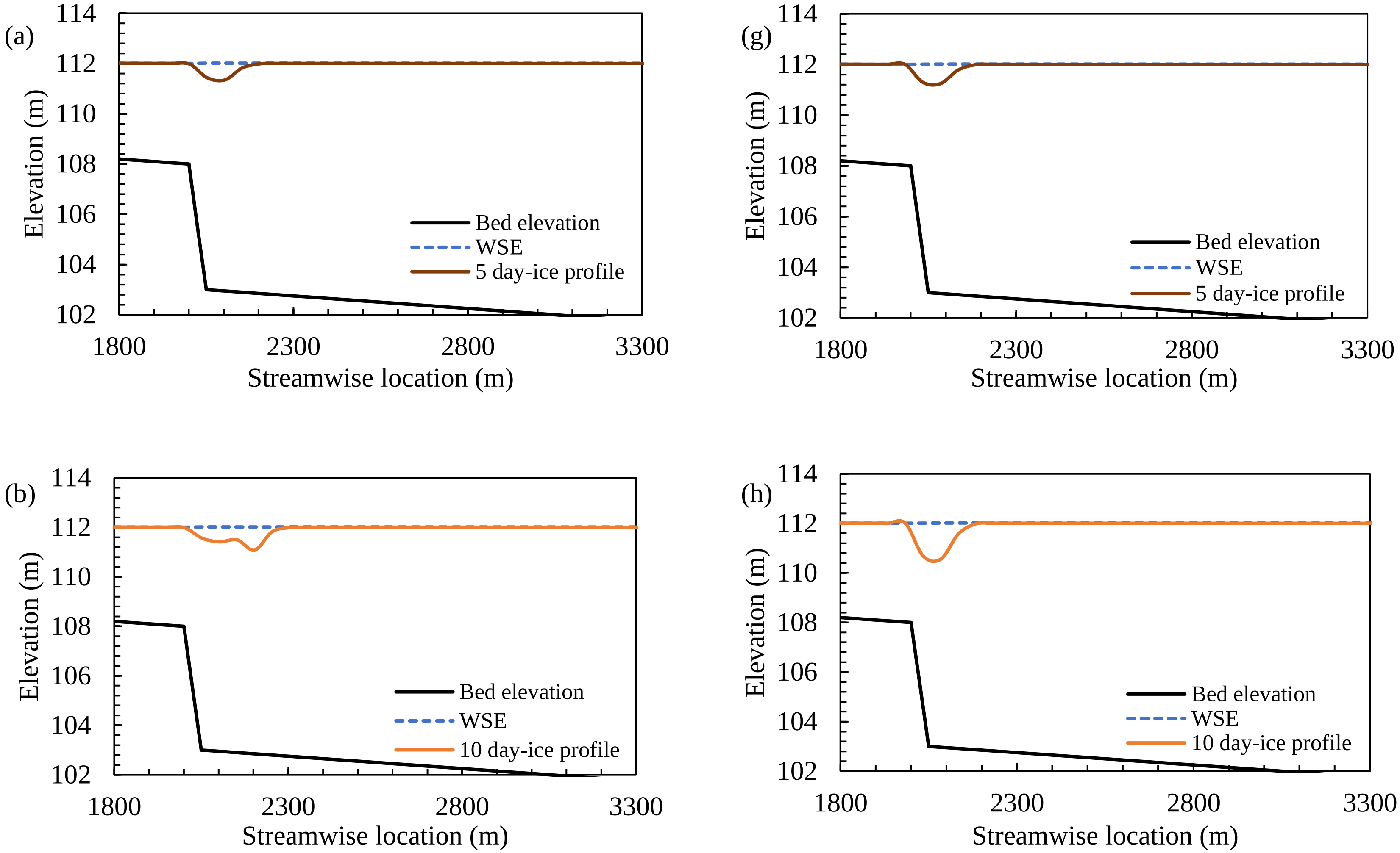
(a)
Elevation (m)
Streamwise location (m)
Bed elevation
WSE
5 day-ice profile
(g)
Elevation (m)
Streamwise location (m)
Bed elevation
WSE
5 day-ice profile
(b)
Elevation (m)
Streamwise location (m)
Bed elevation
WSE
10 day-ice profile
(h)
Elevation (m)
Streamwise location (m)
Bed elevation
WSE
10 day-ice profile

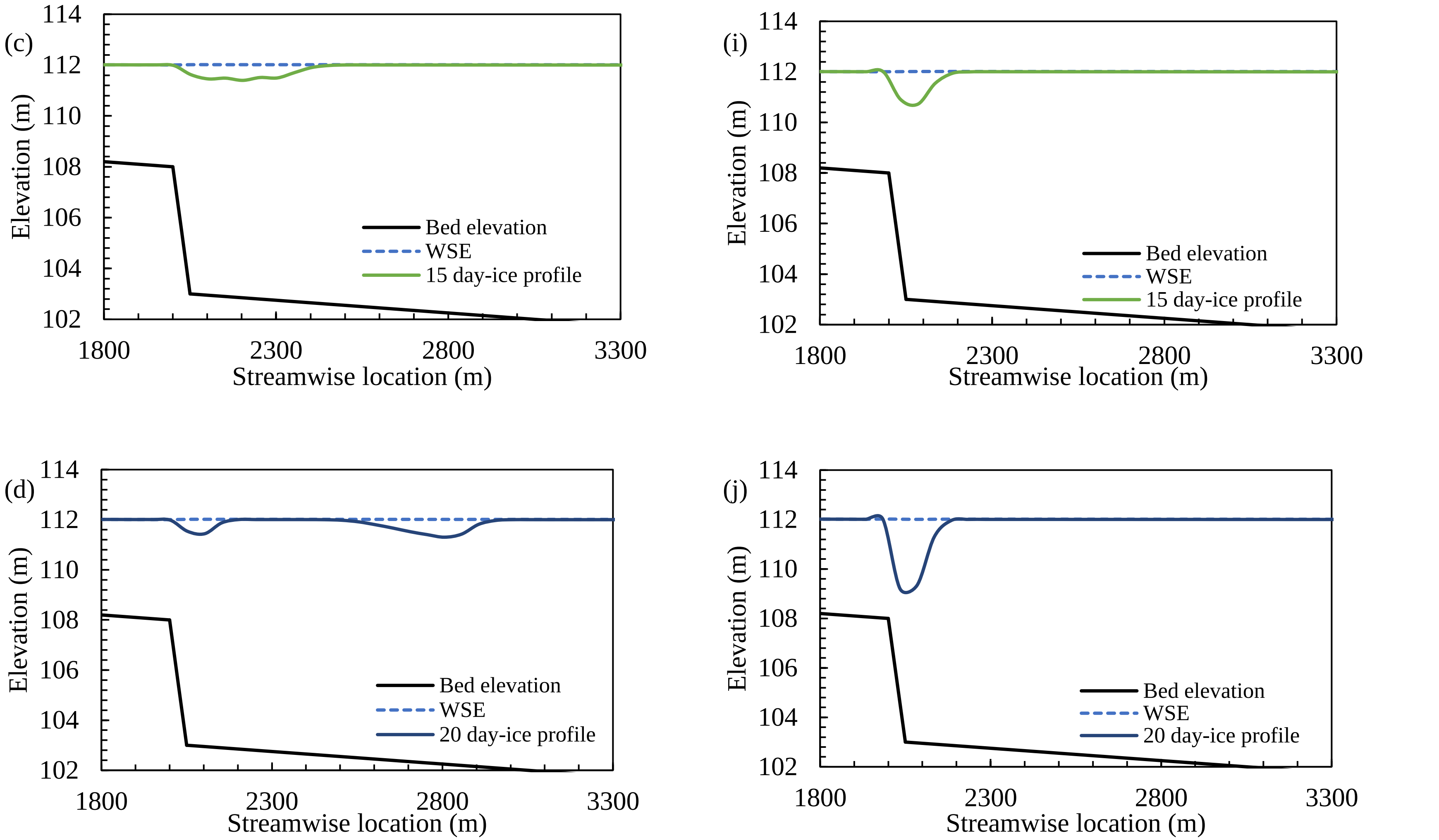
(c)
Elevation (m)
114
112
110
108
106
104
102
1800
2300
2800
3300
Streamwise location (m)
Bed elevation
WSE
15 day-ice profile
(i)
Elevation (m)
Streamwise location (m)
Bed elevation
WSE
15 day-ice profile
(d)
Elevation (m)
Streamwise location (m)
Bed elevation
WSE
20 day-ice profile
(j)
Elevation (m)
Streamwise location (m)
Bed elevation
WSE
20 day-ice profile

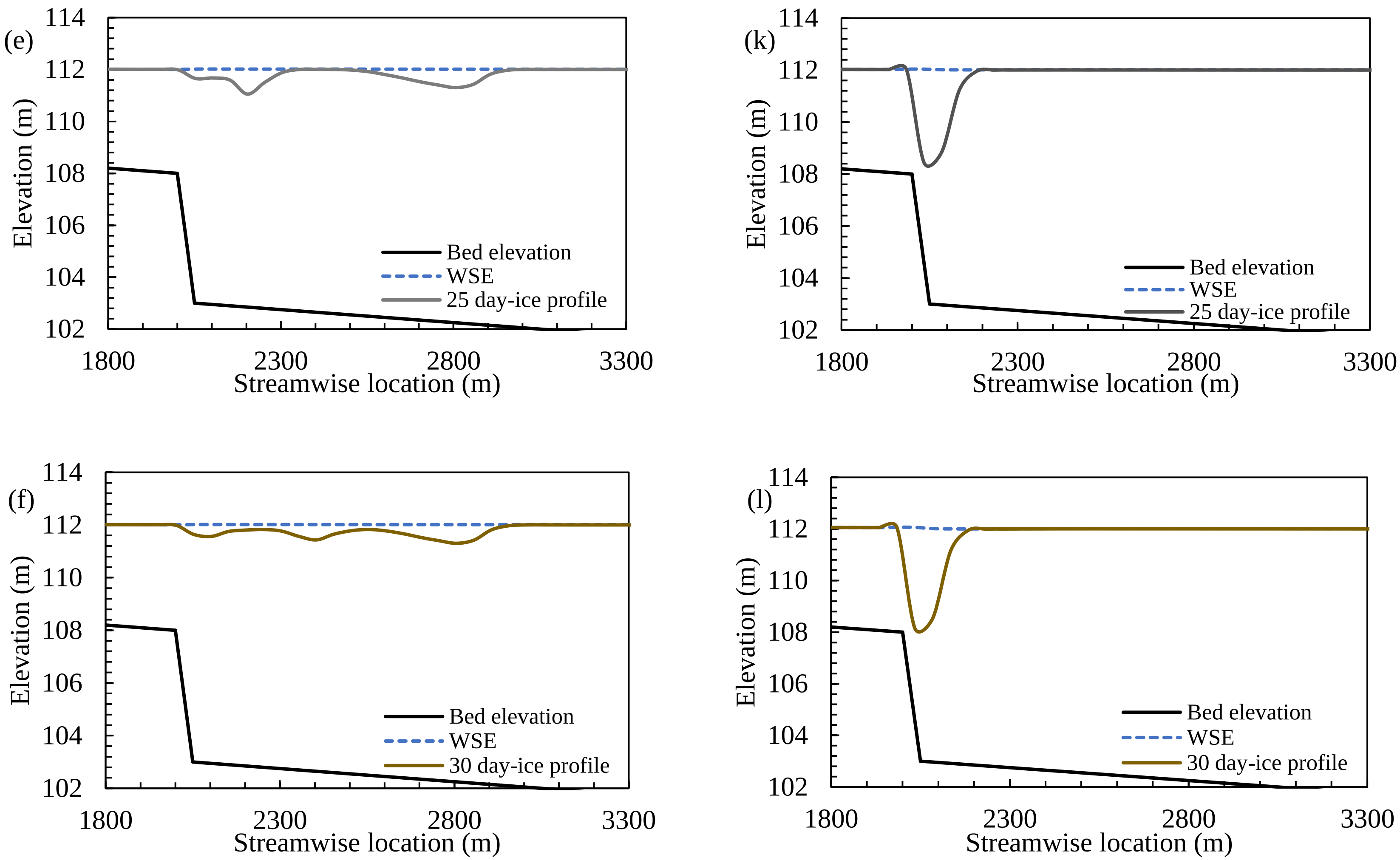


Figure 5.10. Streamwise ice deposition profiles for geometry 1(ice cover at 2.0 km), Qi = 0.01 $m^3/s$ on 5, 10, 15, 20, 25, and 30 days; (a)-(f) $\Theta_c$= 0.041 simulations, (g)-(l) $\Theta_c$= 0.396 simulations.

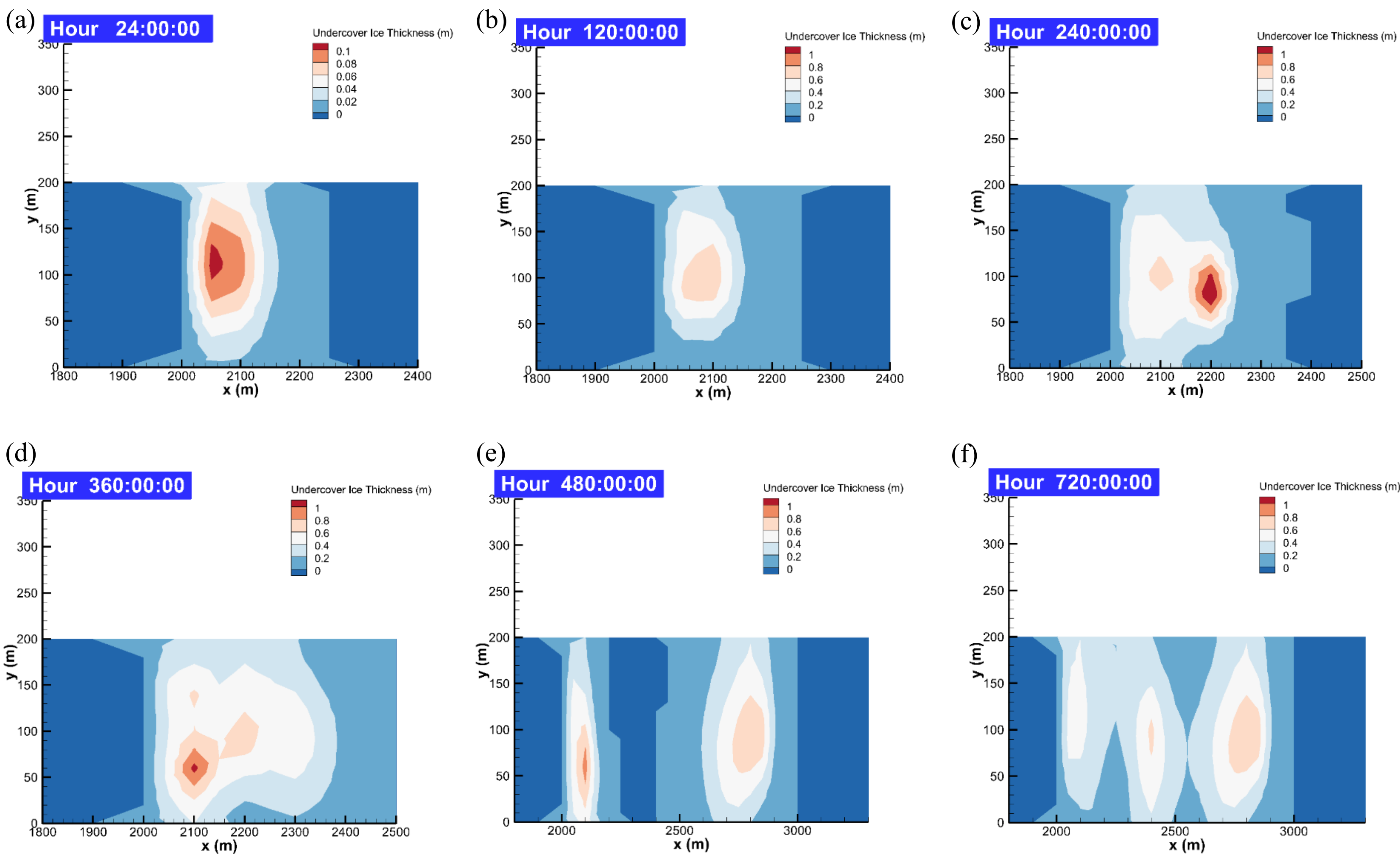


Figure 5.11. Plan view of the hanging dam for geometry 1 (ice cover at 2.0 km), Qi = 0.01 $m^3/s$ on 1, 5, 10, 15, 20 and 30 days; $\Theta_c$= 0.041simulations.

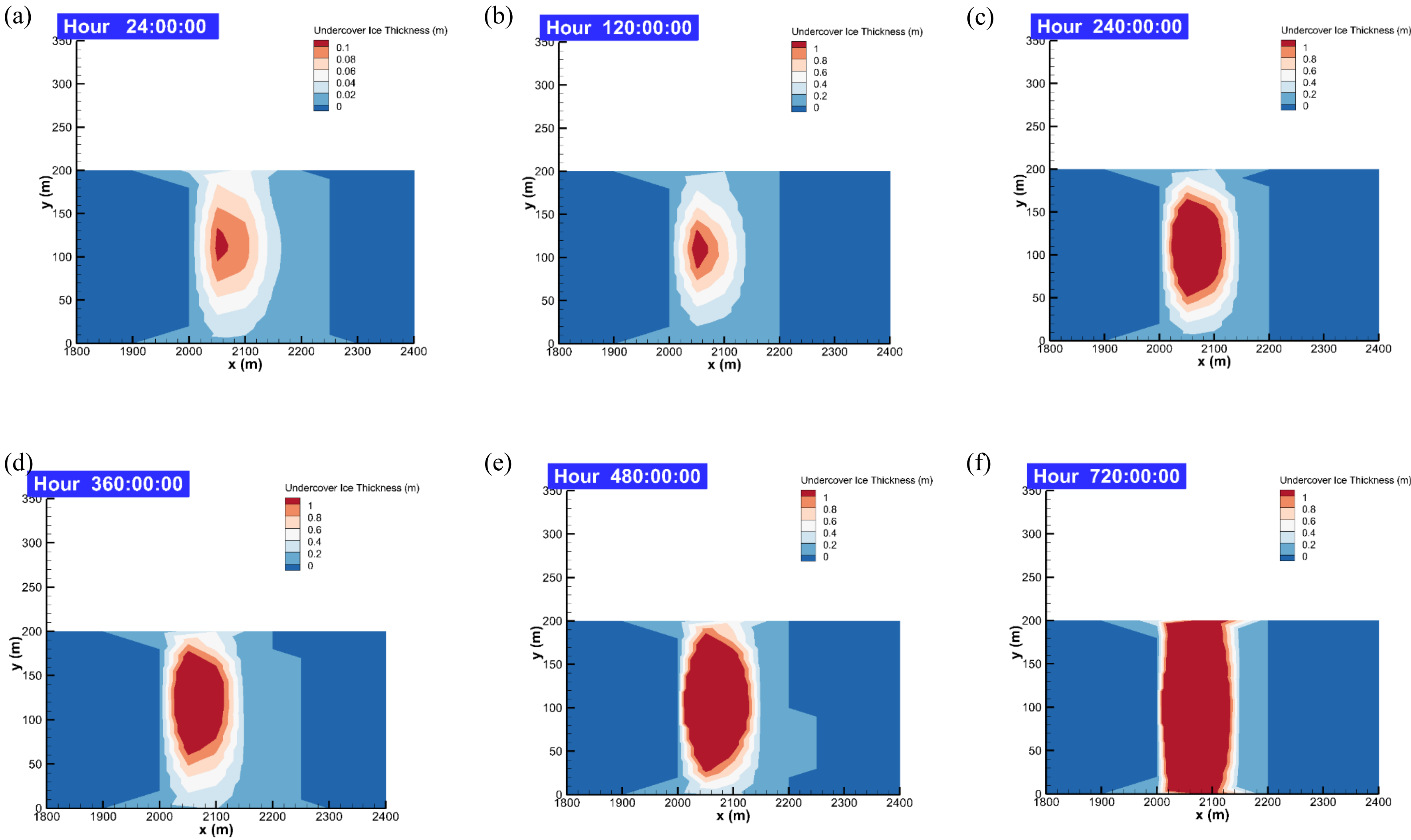


Figure 5.12. Plan view of the hanging dam for geometry 1 (ice cover at 2.0 km), Qi = 0.01 m$^3$/s on 1, 5, 10, 15, 20 and 30 days; $\Theta_c$= 0.396 simulations.

The streamwise ice deposition profiles for $Q_i$ = 0.1 $m^3/s$ and $Q_i$ = 1 $m^3/s$ for $\Theta_c$= 0.041 and $\Theta_c$= 0.396 simulations are shown in Figure 5.13 and Figure 5.14, respectively. Similar to the model results for $Q_i$ = 0.01 $m^3/s$, both $Q_i$ = 0.1 $m^3/s$ and $Q_i$ = 1 $m^3/s$ simulations develop a hanging dam formation when $\Theta_c$= 0.396, and the deposition undergoes erosion when $\Theta_c$= 0.041. In both cases, the hanging dam reached a high thickness faster since the incoming ice supply rates are higher compared to the initial case of $Q_i$ = 0.01 $m^3/s$. In $\Theta_c$= 0.396 simulations, a considerable backwater effect caused by the hanging dam accumulation can be observed for ice supply rates $Q_i$ = 0.1 $m^3/s$ and 1 $m^3/s$. In a situation when there are concerns about upstream flooding due to ice accumulations, this is an important factor to consider in the numerical model.

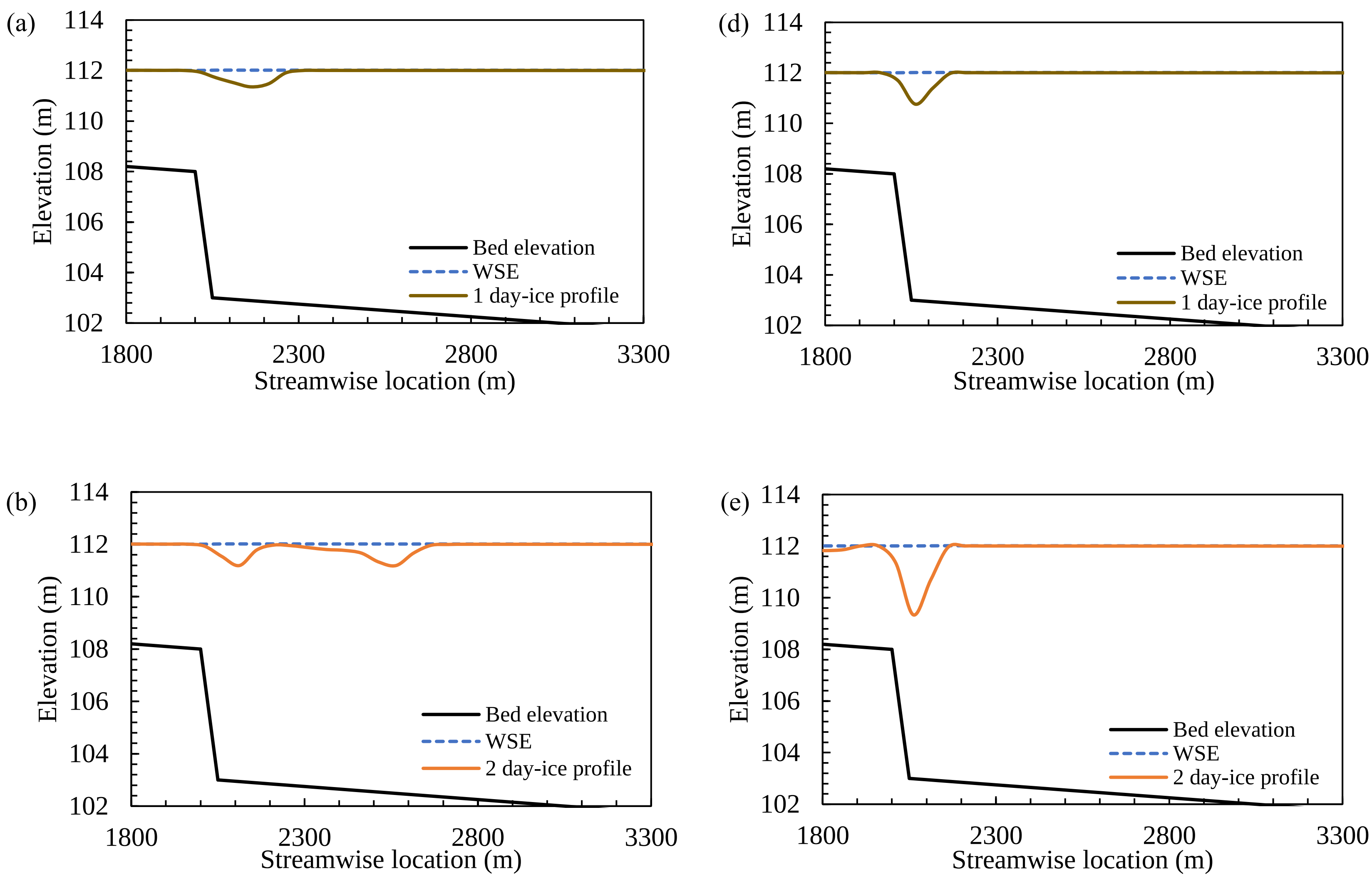
(a)
(d)
(b)
(e)
Elevation (m)
Streamwise location (m)
114
112
110
108
106
104
102
1800
2300
2800
3300
Bed elevation
WSE
1 day-ice profile
2 day-ice profile

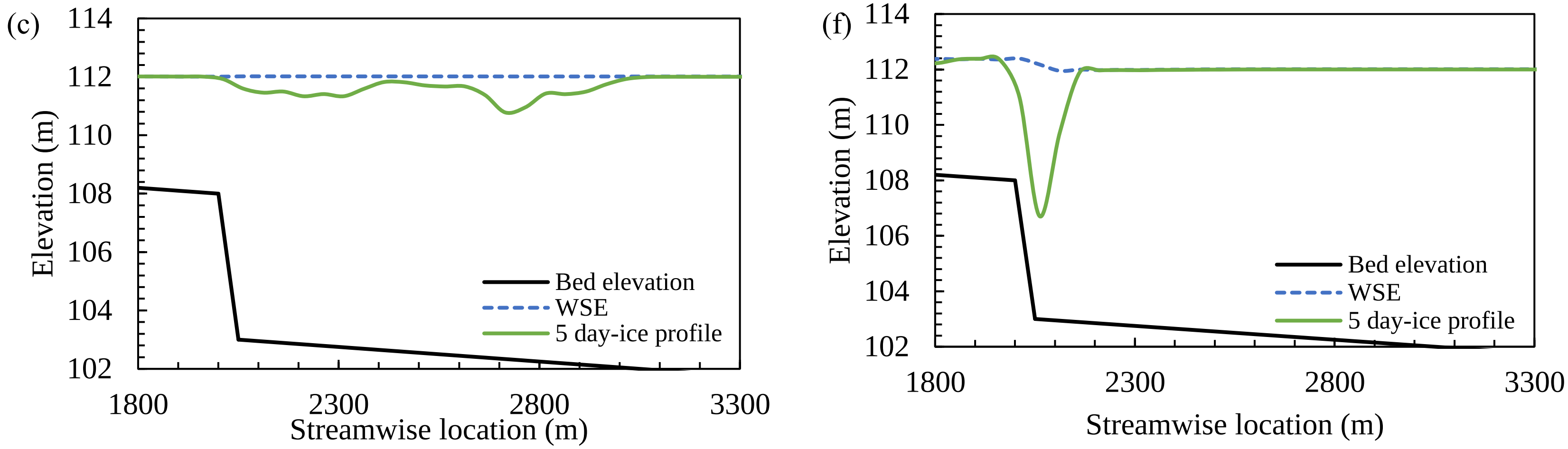


Figure 5.13. Streamwise ice deposition profiles for geometry 1 (ice cover at 2.0 km), Qi = 0.1 $m^3/s$ on 1, 2, and 5 days; (a)-(c) $\Theta_c$= 0.041 simulations, (d)-(f) $\Theta_c$= 0.396 simulations.

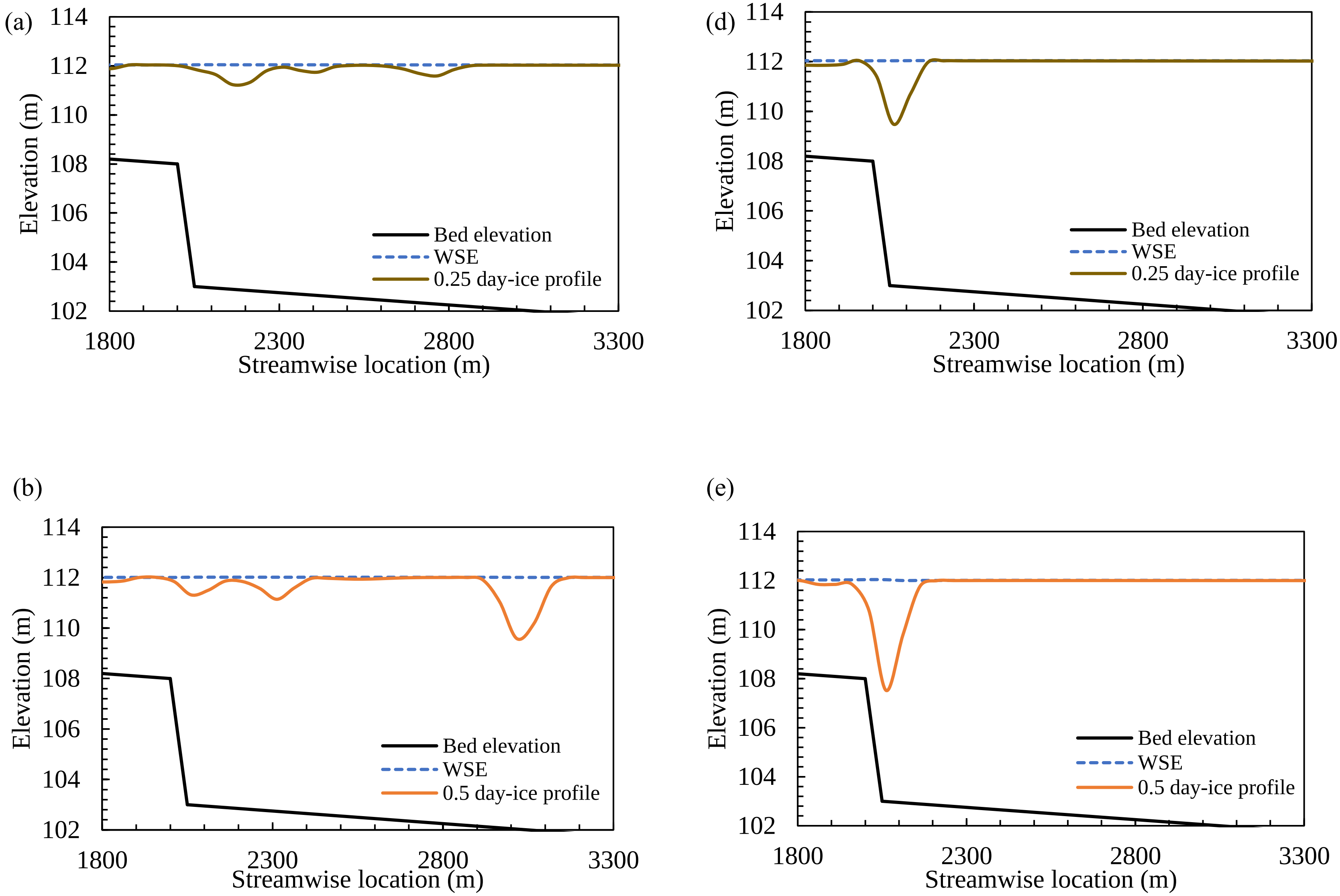
(a)
114
112
110
108
106
104
102
1800
2300
2800
3300
Elevation (m)
Streamwise location (m)
Bed elevation
WSE
0.25 day-ice profile
(d)
0.25 day-ice profile
(b)
0.5 day-ice profile
(e)
0.5 day-ice profile

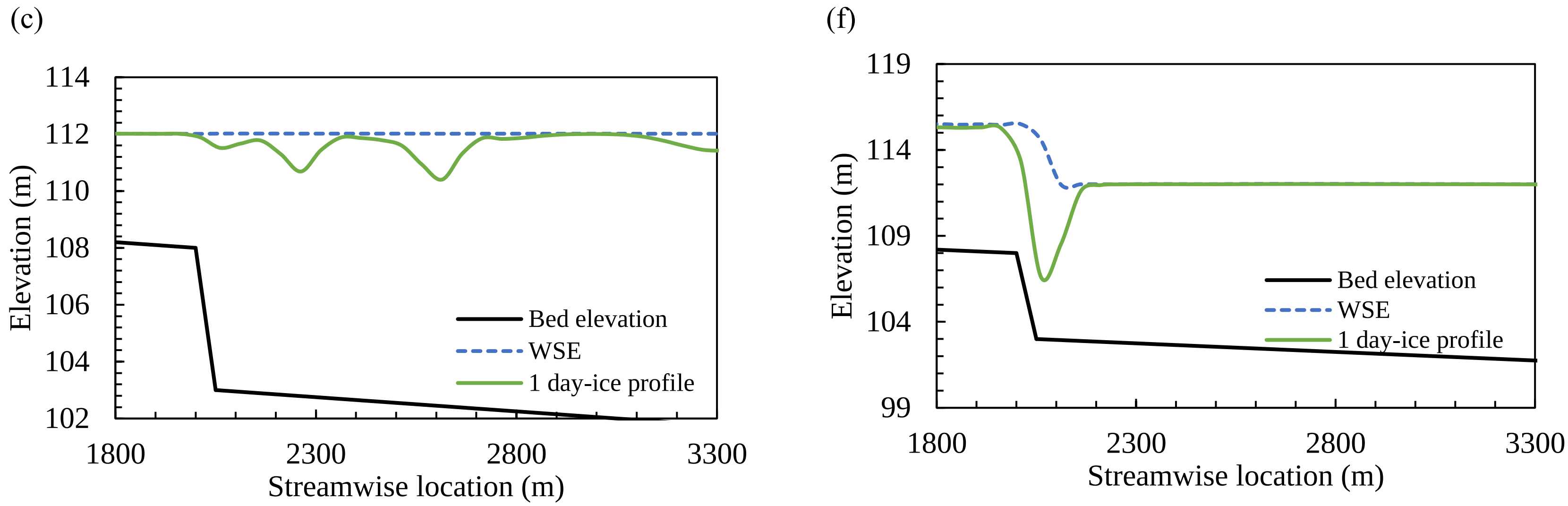


Figure 5.14. Streamwise ice deposition profiles for geometry 1 (ice cover at 2.0 km), Qi =1 $m^3/s$ for 0.25, 0.5 and 1 days; (a)-(c) $\Theta_c$= 0.041 simulations, (d)-(f) $\Theta_c$= 0.396 simulations.

A similar comparison was done for geometry 2 which has a higher flow area expansion ratio due to the added increase in channel width at the channel expansion interface and the ice cover was placed at 2.4 km (instead of 2.0 km for geometry 1) from the channel inlet. Figure 5.15, Figure 5.18, and Figure 5.19 show the streamwise ice deposition profiles for both $\Theta_c$= 0.041 and $\Theta_c$= 0.396 simulations for $Q_i$ = 0.01 $m^3/s$, 0.1 $m^3/s$, and 1 $m^3/s$, respectively. Unlike the geometry 1 model runs, $\Theta_c$= 0.041 simulations using geometry 2 lead to a hanging dam formation at the leading ice edge. This deposition is facilitated by the reduction in flow strength at the leading ice edge caused by the more significant flow area expansion. Geometry 2 simulations with $\Theta_c$= 0.396 showed a backwater effect of the hanging dam accumulation for $Q_i$ = 0.1 $m^3/s$ and 1 $m^3/s$ similar to geometry 1 simulations.

$\Theta_c$= 0.396 simulations for geometry 2 runs show a similar deposition profile compared to geometry 1 runs and the plan view of geometry 2 runs with $Q_i$ = 0.01 $m^3/s$ for $\Theta_c$= 0.041 and $\Theta_c$= 0.396 simulations are shown in Figure 5.16 and Figure 5.17, respectively. Geometry 1 simulations yielded thicker ice depositions at the channel centerline compared to geometry 2 simulations for both cases. In geometry 2, the increase in channel width allows ice to transport in both streamwise and spanwise directions reducing the ice thickness at the channel centerline for the same volume of ice input. The plan view of deposition profiles for $Q_i$ = 0.1 $m^3/s$ and 1 $m^3/s$ ice supply rates simulated using $\Theta_c$= 0.041 and 0.396 for both geometry 1 and 2 are presented in Appendix B of the thesis.

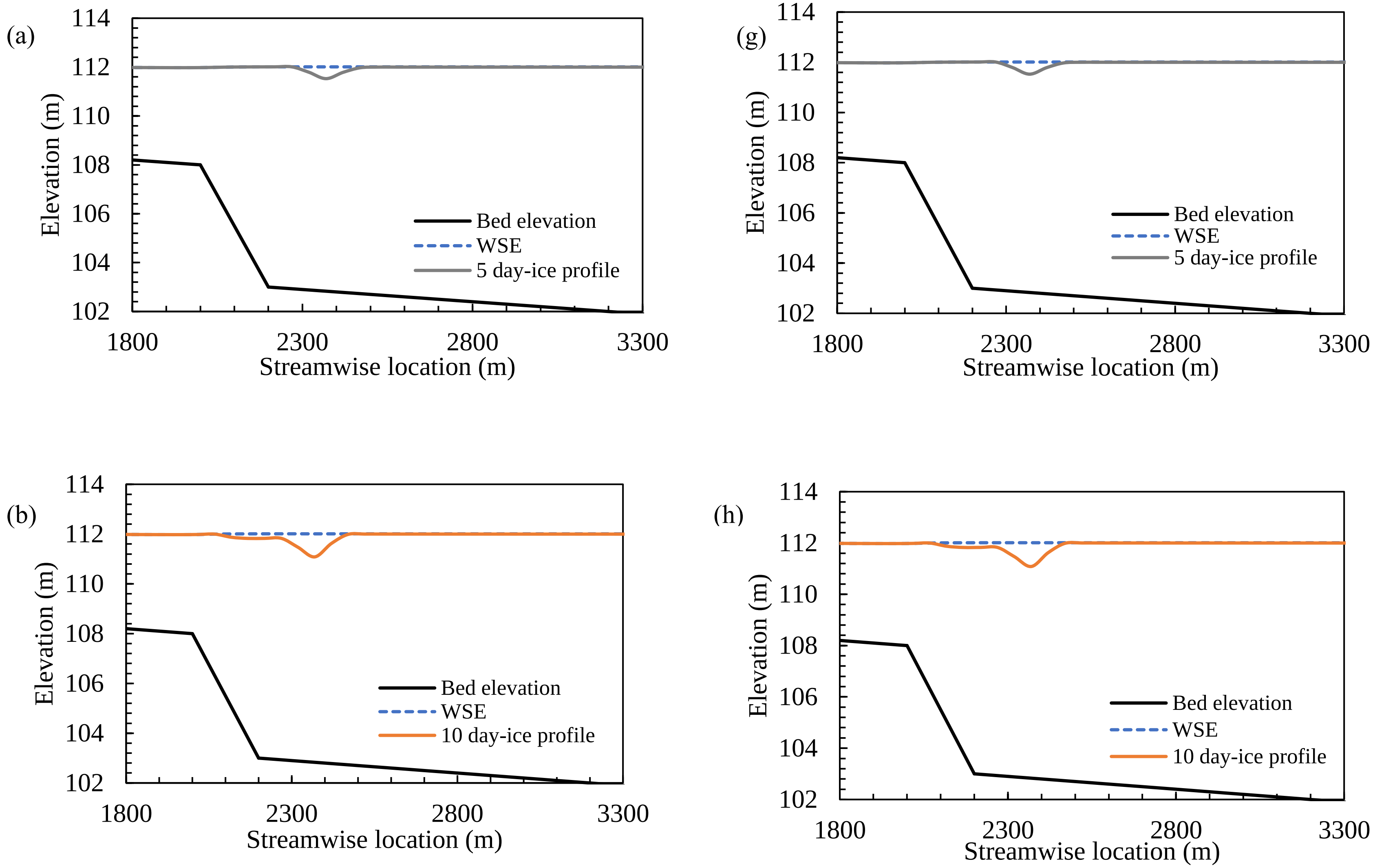
(a)
114
112
110
108
106
104
102
Elevation (m)
1800
2300
2800
3300
Streamwise location (m)
Bed elevation
WSE
5 day-ice profile
(g)
Bed elevation
WSE
5 day-ice profile
(b)
Bed elevation
WSE
10 day-ice profile
(h)
Bed elevation
WSE
10 day-ice profile

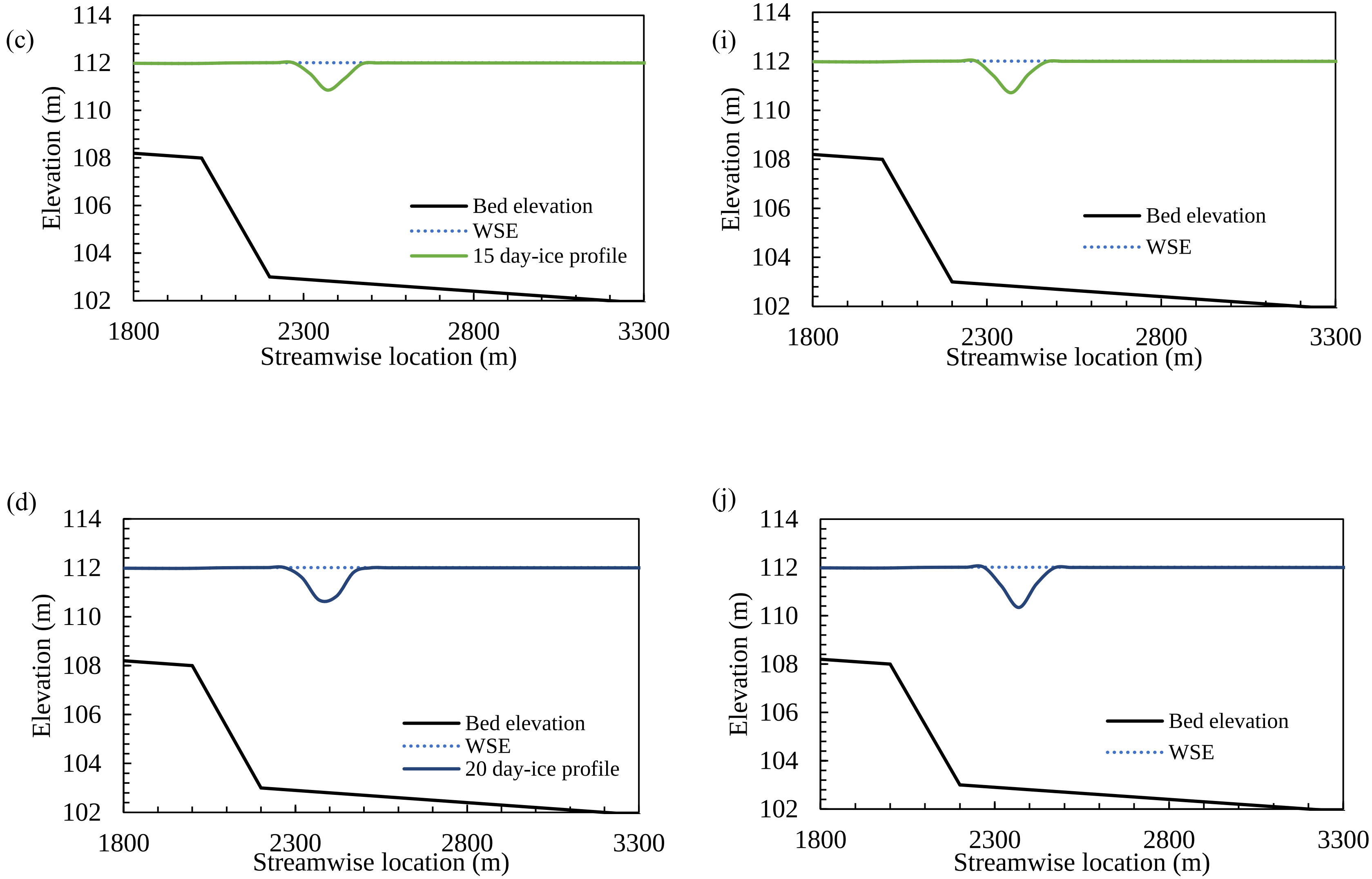

(c)
Elevation (m)
Streamwise location (m)
Bed elevation
WSE
15 day-ice profile
(i)
Elevation (m)
Streamwise location (m)
Bed elevation
WSE
(d)
Elevation (m)
Streamwise location (m)
Bed elevation
WSE
20 day-ice profile
(j)
Elevation (m)
Streamwise location (m)
Bed elevation
WSE

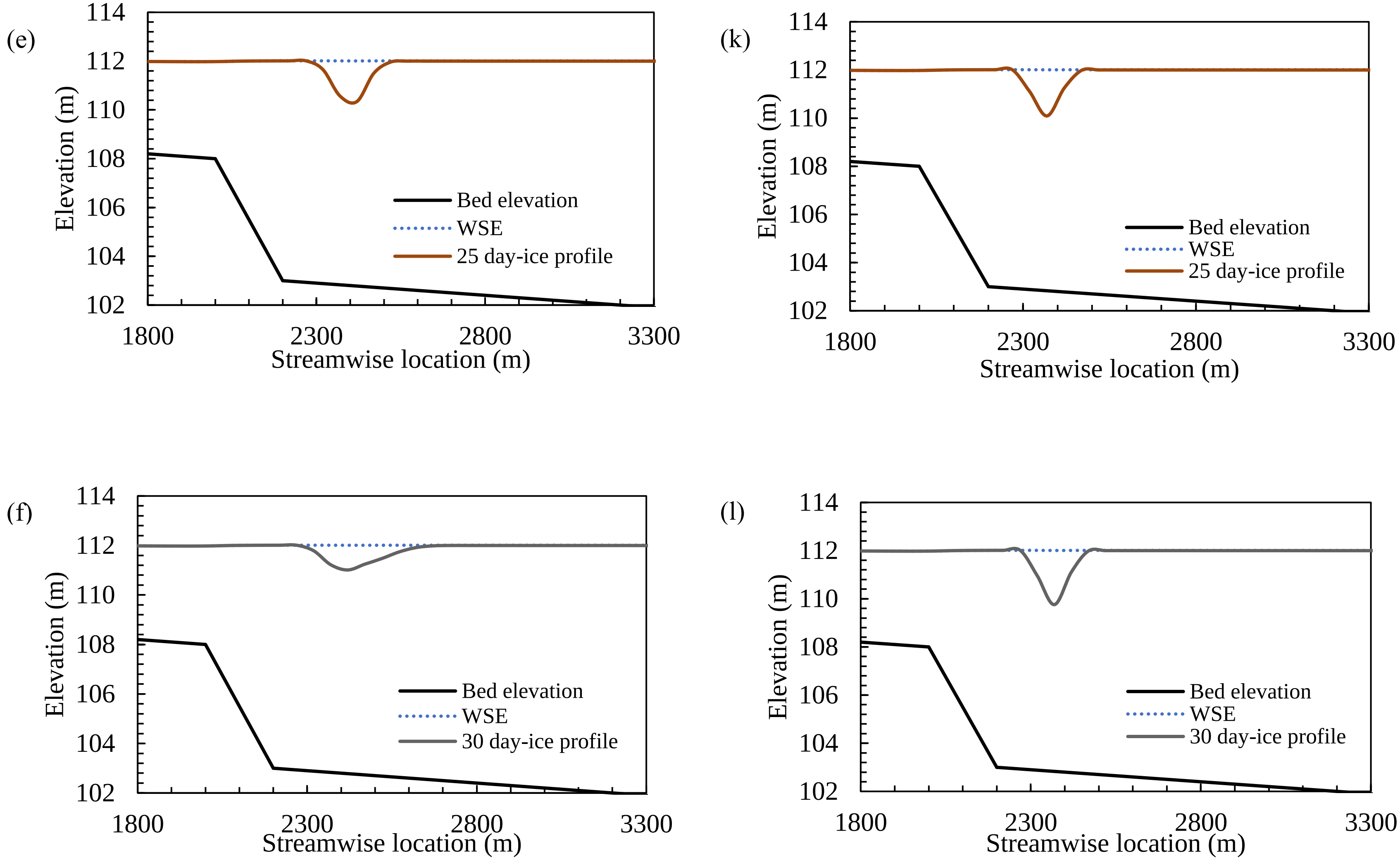


Figure 5.15. Streamwise ice deposition profiles for geometry 2 (ice cover at 2.4 km), Qi = 0.01 $m^3/s$ at 5, 10, 15, 20, 25 and 30 days; (a)-(f) $\Theta_c$= 0.041 simulations, (g)-(l) $\Theta_c$= 0.396 simulations.

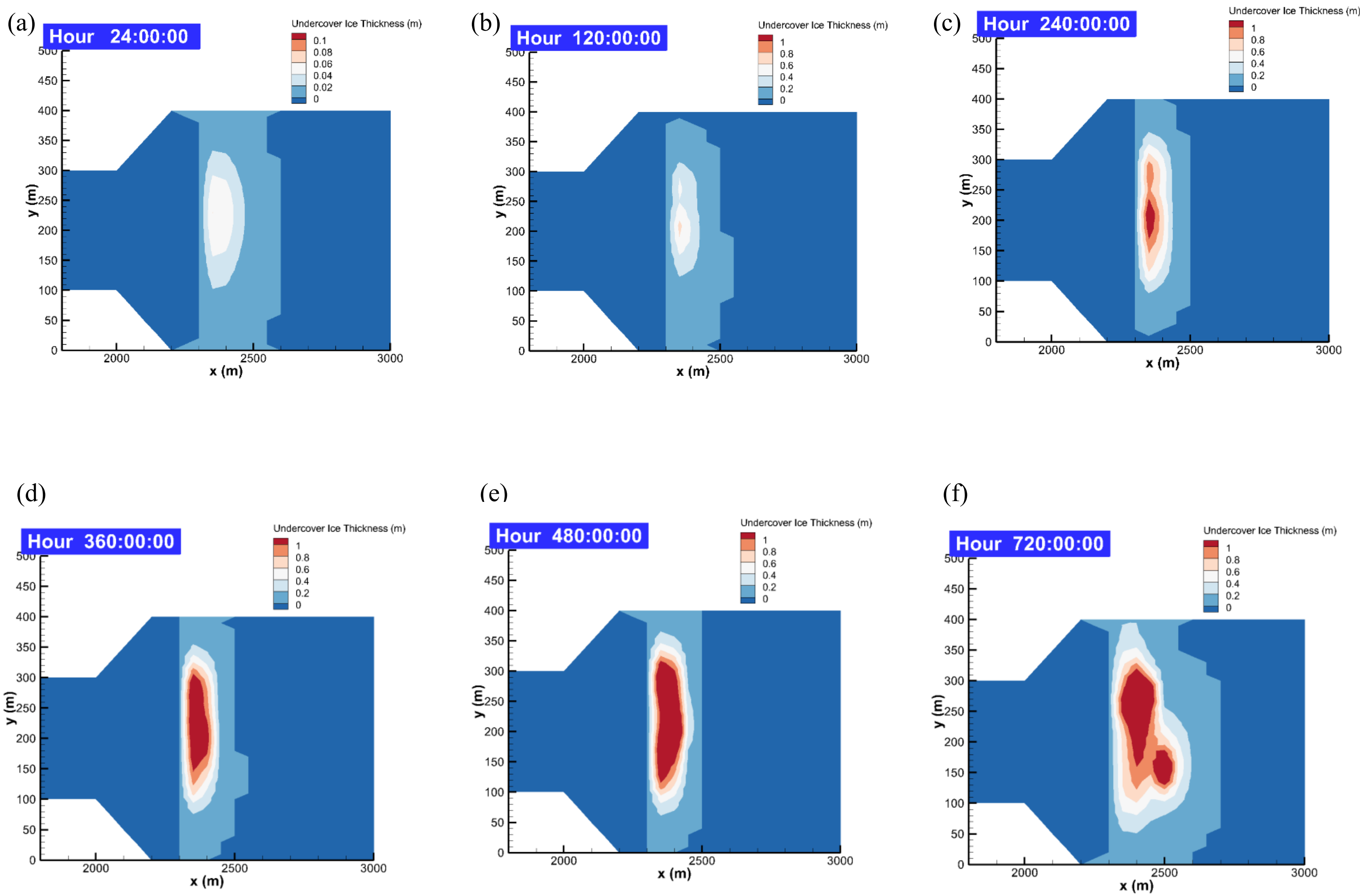


Figure 5.16. Plan view of the hanging dam for geometry 2 (ice cover at 2.4 km), Qi = 0.01 $m^3/s$ at 1, 5, 10, 15, 20 and 30 days; $\Theta_c$= 0.041 simulations.

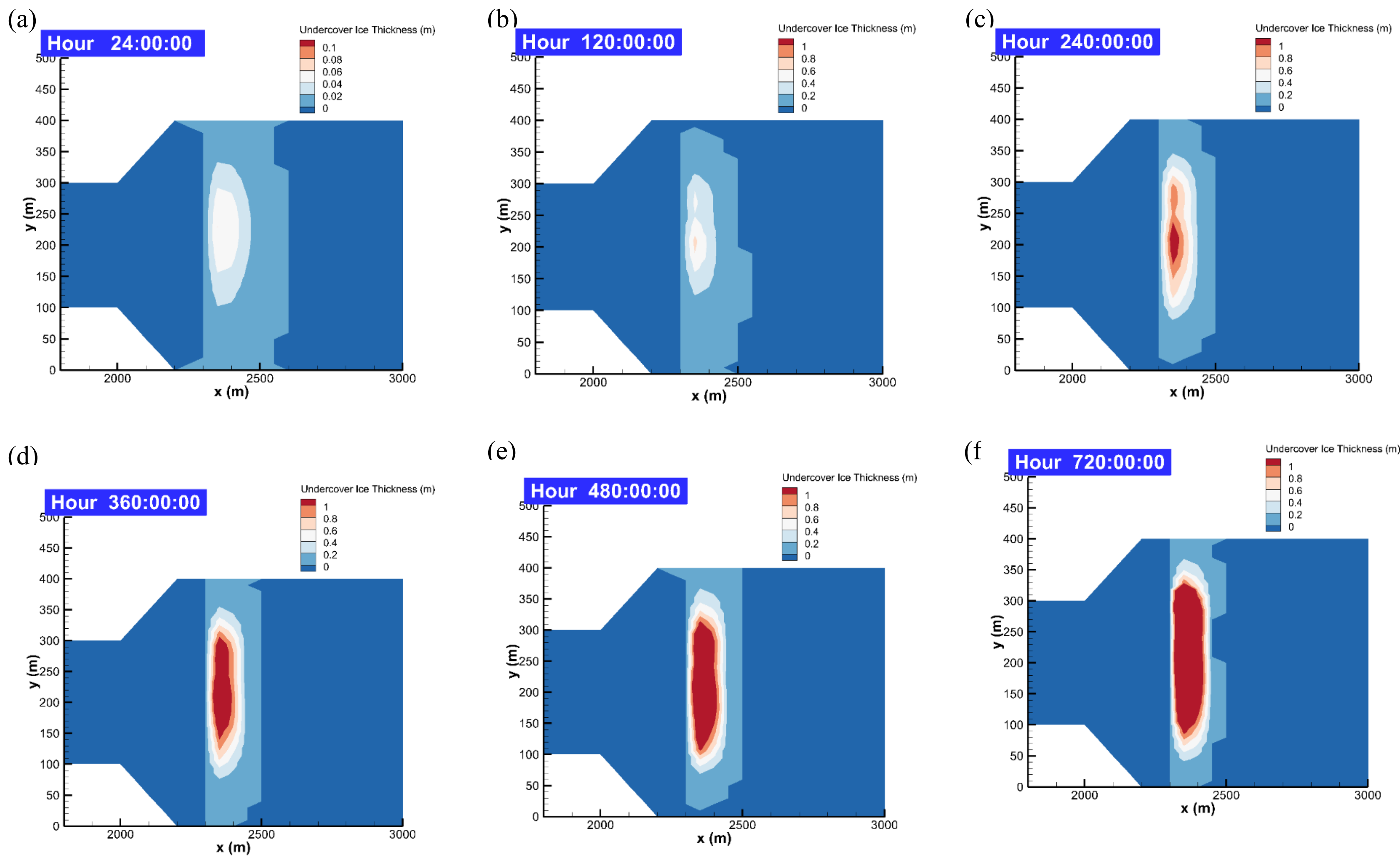


Figure 5.17. Plan view of the hanging dam for geometry 2 (ice cover at 2.4 km), Qi = 0.01 $m^3$/s at 1, 5, 10, 15, 20 and 30 days; $\Theta_c$= 0.396 simulation.

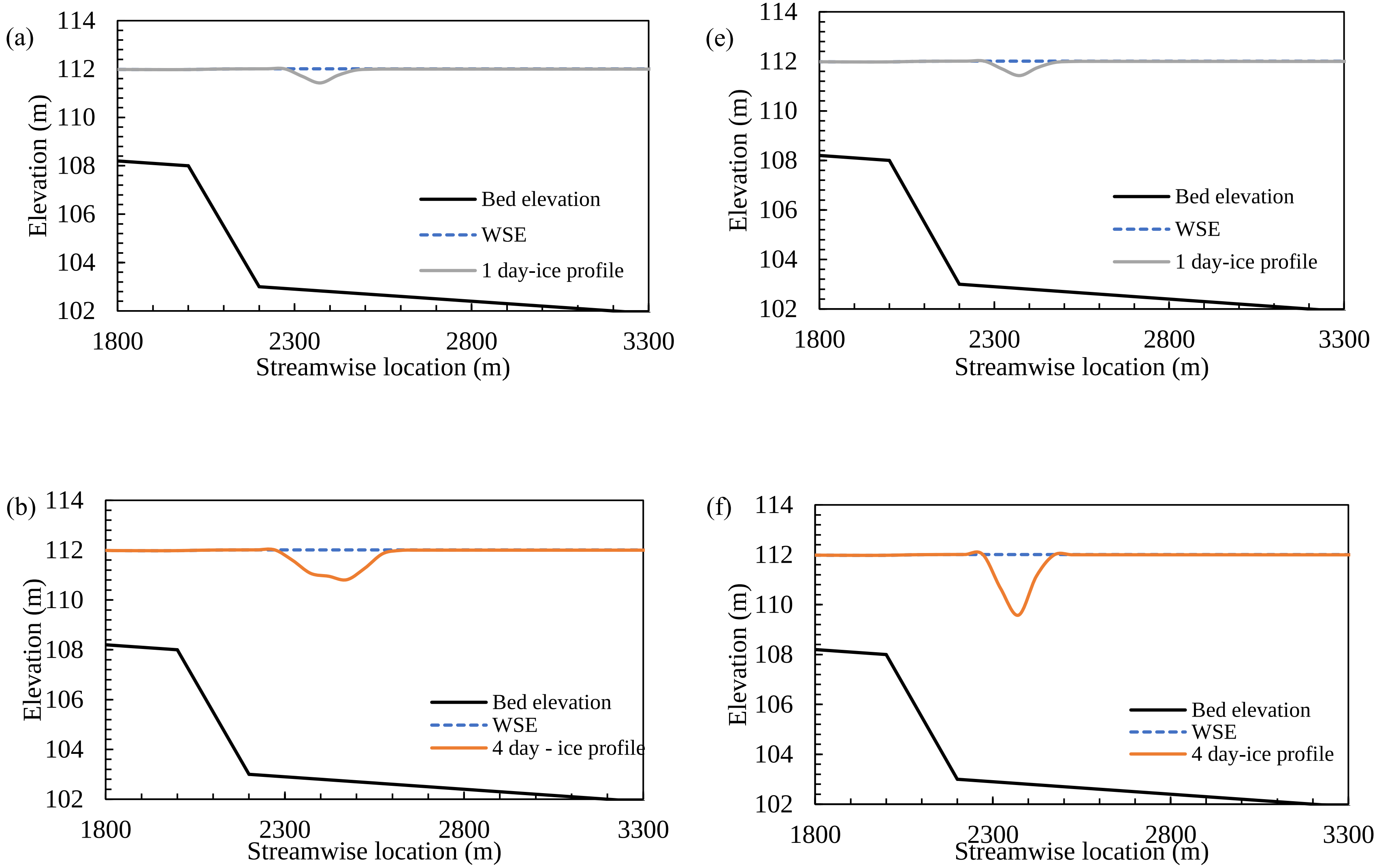

(a)
(e)
(b)
(f)
Elevation (m)
Streamwise location (m)
114
112
110
108
106
104
102
1800
2300
2800
3300
Bed elevation
WSE
1 day-ice profile
4 day - ice profile
4 day-ice profile

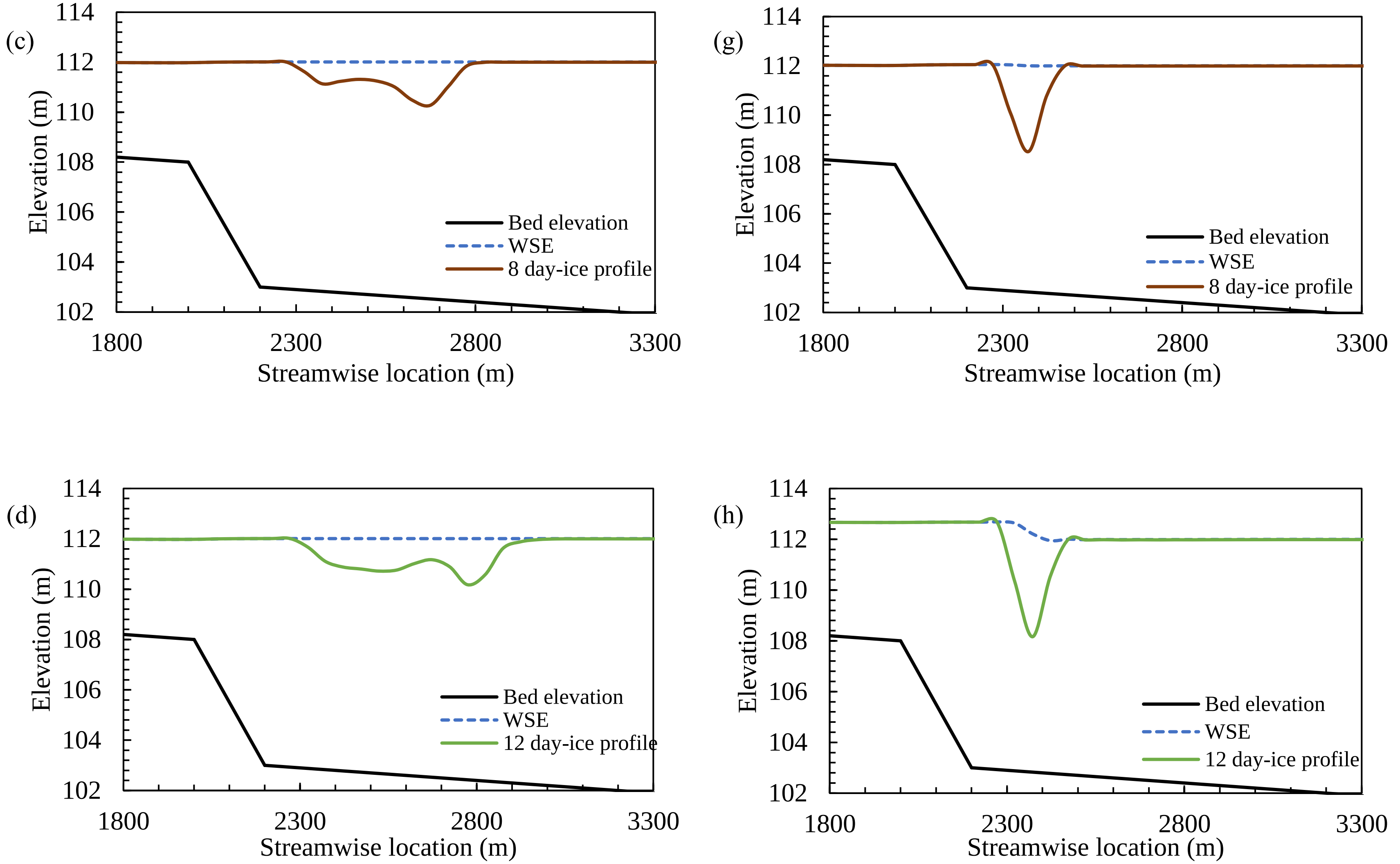


Figure 5.18. Streamwise ice deposition profiles for geometry 2 (ice cover at 2.4 km), Qi = 0.1 m$^3$/s at 1, 4, 8, 12 days; (a)-(d) $\Theta_c$= 0.041 simulations, (f)-(h) $\Theta_c$= 0.396 simulations.

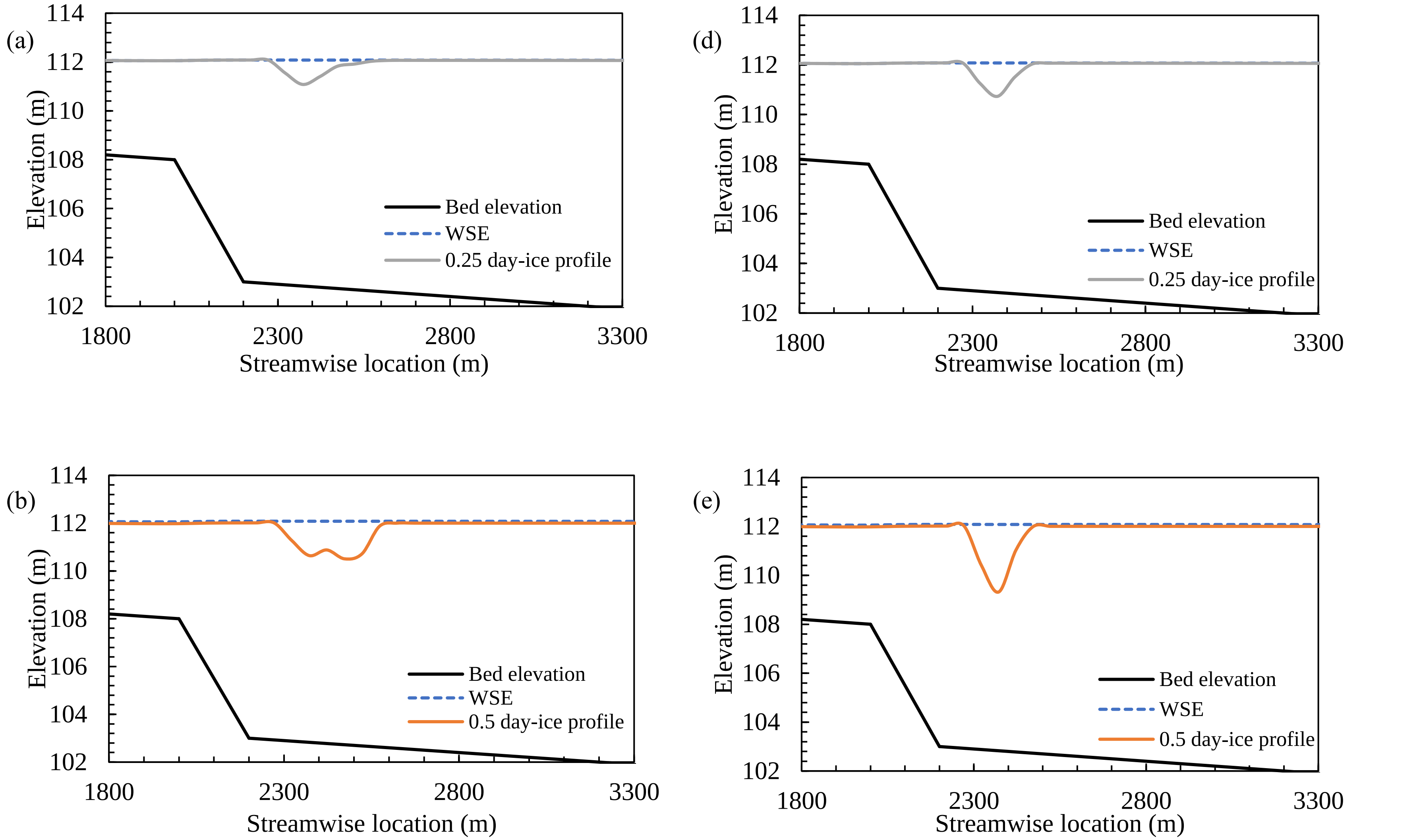
(a)
(b)
(d)
(e)
Elevation (m)
Streamwise location (m)
Bed elevation
WSE
0.25 day-ice profile
0.5 day-ice profile
114
112
110
108
106
104
102
1800
2300
2800
3300

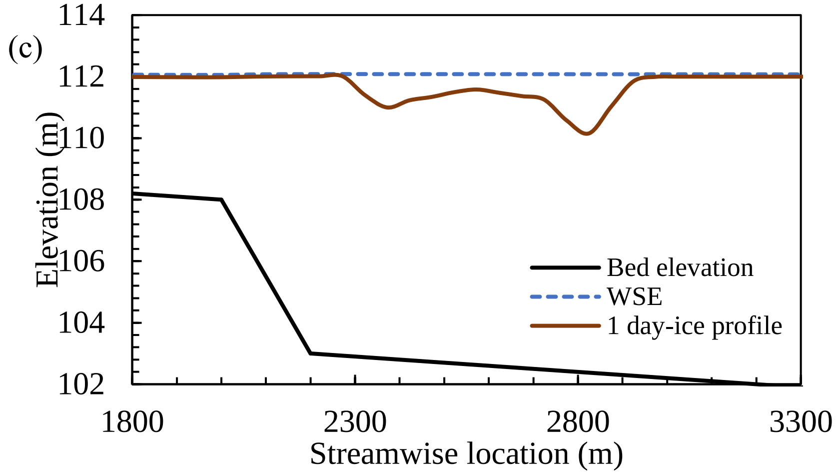


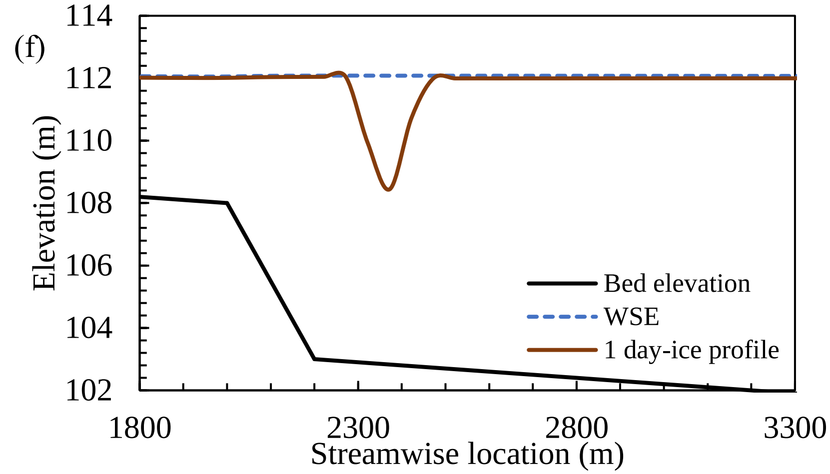


Figure 5.19. Streamwise ice deposition profiles for geometry 2 (ice cover at 2.4 km), Qi = 1 $m^3/s$ at 0.25, 0.5 and 1 day; (a)-(c) $\Theta_c$= 0.041 simulations, (d)-(f) $\Theta_c$= 0.396 simulations.

### 5.4.3 Model simulations to analyze the effect of approach Froude number

Model simulations were conducted to analyze the effect of approach Froude number on the maximum thickness of the hanging dam accumulation and its location using both Shen and Wang (1995) and Senarathbandara et al. (2024) equations. Similar to the previous section model simulations conducted using Shen and Wang (1995) equation are referred to as $\Theta_c$ = 0.041 simulations and the simulations conducted using Senarathbandara et al. (2024) equation are referred to as $\Theta_c$ = 0.396 simulations. Model conditions for approach Froude number simulations are presented in Table 5.3 and Table 5.4 below.

Table 5.3. Testing conditions for simulations to investigate the effect of approach Froude number on maximum ice thickness and its location for $\Theta_c$ = 0.041 simulations.

| Mesh geometry | Lake flow area ($m^2$) | River flow area ($m^2$) | Flow area ratio (-) | $Q_w$ ($m^3$/s) | Approach velocity (m/s) | Approach Fr (-) | $Q_i$ ($m^3$/s) |
|---|---|---|---|---|---|---|---|
| **Geometry 1** | 1800 | 800 | 2.25 | 500 | 0.63 | 0.10 | 0.2, 1.0 |
| | | | | 750 | 0.94 | 0.15 | |
| | | | | 900 | 1.13 | 0.18 | |
| | | | | 1000 | 1.25 | 0.20 | |
| | | | | 1200 | 1.50 | 0.24 | |
| **Geometry 2** | 3600 | 800 | 4.50 | 500 | 0.63 | 0.10 | 0.2, 1.0 |
| | | | | 750 | 0.94 | 0.15 | |
| | | | | 900 | 1.13 | 0.18 | |
| | | | | 1000 | 1.25 | 0.20 | |
| | | | | 1200 | 1.50 | 0.24 | |

Table 5.4. Testing conditions for simulations to investigate the effect of approach Froude number on maximum ice thickness and its location for $\Theta_c$ = 0.396 simulations.

| Mesh geometry | Lake flow area ($m^2$) | River flow area ($m^2$) | Flow area ratio (-) | $Q_w$ ($m^3/s$) | Approach velocity (m/s) | Approach Fr (-) | $Q_i$ ($m^3/s$) |
|---|---|---|---|---|---|---|---|
| **Geometry 1** | 1800 | 800 | 2.25 | 500 | 0.63 | 0.10 | 0.2, 1.0, 2.0 |
| | | | | 1000 | 1.25 | 0.20 | |
| | | | | 1500 | 1.88 | 0.30 | |
| | | | | 2000 | 2.50 | 0.40 | |
| | | | | 2500 | 3.13 | 0.50 | |
| | | | | 3000 | 3.75 | 0.60 | |
| | | | | 3500 | 4.38 | 0.70 | |
| **Geometry 2** | 3600 | 800 | 4.50 | 500 | 0.63 | 0.10 | 0.2, 1.0, 2.0 |
| | | | | 1000 | 1.25 | 0.20 | |
| | | | | 1500 | 1.88 | 0.30 | |
| | | | | 2000 | 2.50 | 0.40 | |
| | | | | 2500 | 3.13 | 0.50 | |
| | | | | 3000 | 3.75 | 0.60 | |
| | | | | 3500 | 4.38 | 0.70 | |

Due to the low value of $\Theta_c$ in the Shen and Wang equation, the ice depositions would erode even at low flow strength values. Since the model simulations at high Froude numbers did not produce an accumulation, the range of Froude numbers for Shen and Wang simulations were limited to 0.10 - 0.24. Since this was not an issue for the $\Theta_c$= 0.396 simulations, Froude numbers ranging from 0.1 to 0.7 were used for the model simulations.

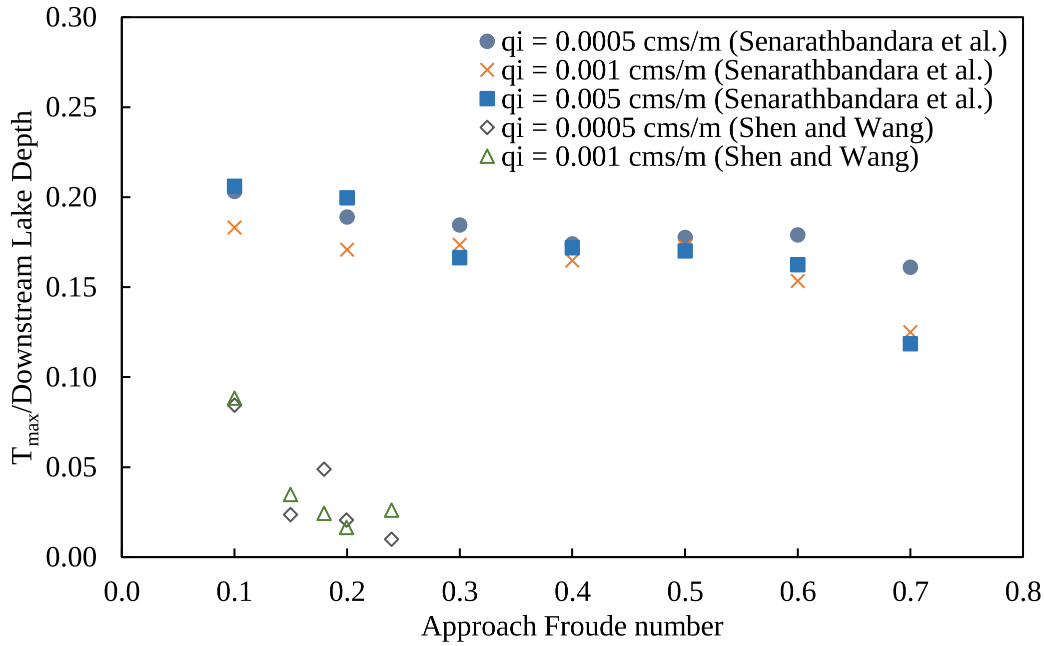


Figure 5.20. Maximum centerline thickness of the accumulation for geometry 1 simulations for various approach Froude numbers and incoming ice supply rates.

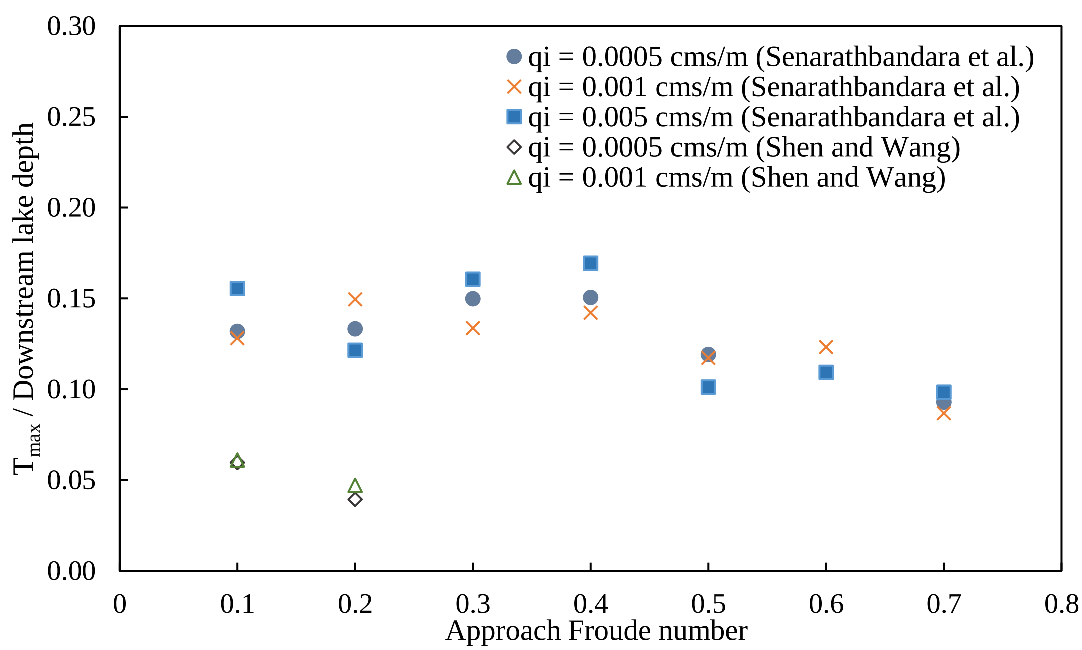


Figure 5.21. Maximum centerline thickness of the accumulation for geometry 2 simulations for various approach Froude numbers and incoming ice supply rates.

Figure 5.20 and Figure 5.21 show the variation of dimensionless maximum thickness of the under cover ice accumulation with the approach Froude number for both $\Theta_c$= 0.041 and $\Theta_c$= 0.396 simulations for both geometries 1 and 2, respectively. The under cover ice thickness along the centerline of the channel was considered in the analysis which is where the maximum deposition is expected. The dimensionless maximum thickness was obtained by dividing the maximum thickness of the accumulation by the respective water depth at the most downstream location of the channel.

The maximum thickness of the deposition decreased with increasing approach Froude number for both $\Theta_c$= 0.041 and $\Theta_c$= 0.396 simulations. The model results agreed with hanging dam laboratory experiments in Chapter 4 where a similar trend was observed when the approach Froude number was increased. The higher upstream channel velocity at high approach Froude numbers reduced the ice deposition rate causing the incoming ice to transport further away (in either streamwise, spanwise or both directions) from the lake inlet resulting in a decrease in the thickness of the hanging dam accumulation.

The location of maximum thickness for various approach Froude numbers and incoming ice supply rates for $\Theta_c$= 0.041 and $\Theta_c$= 0.396 simulations for geometry 1 and geometry 2 are shown in Figure 5.22 and Figure 5.23, respectively. In general for both geometry 1 and geometry 2, $\Theta_c$= 0.041 simulations show a distinct trend where the maximum thickness is located further downstream in the channel for increasing approach Froude numbers. The maximum thickness was located at the same streamwise location for $\Theta_c$= 0.396 simulations irrespective of the Froude number since the flow strength under the ice cover in these runs had not yet exceeded the critical dimensionless flow strength of 0.396 that is required to initiate incipient motion. For $\Theta_c$= 0.041 simulations, the maximum ice thickness was located further downstream in the channel for geometry 1 when compared to geometry 2. In geometry 2, the flow area expansion reduced the velocity downstream of the channel expansion interface providing a suitable condition for ice deposition closer to the lake inlet.

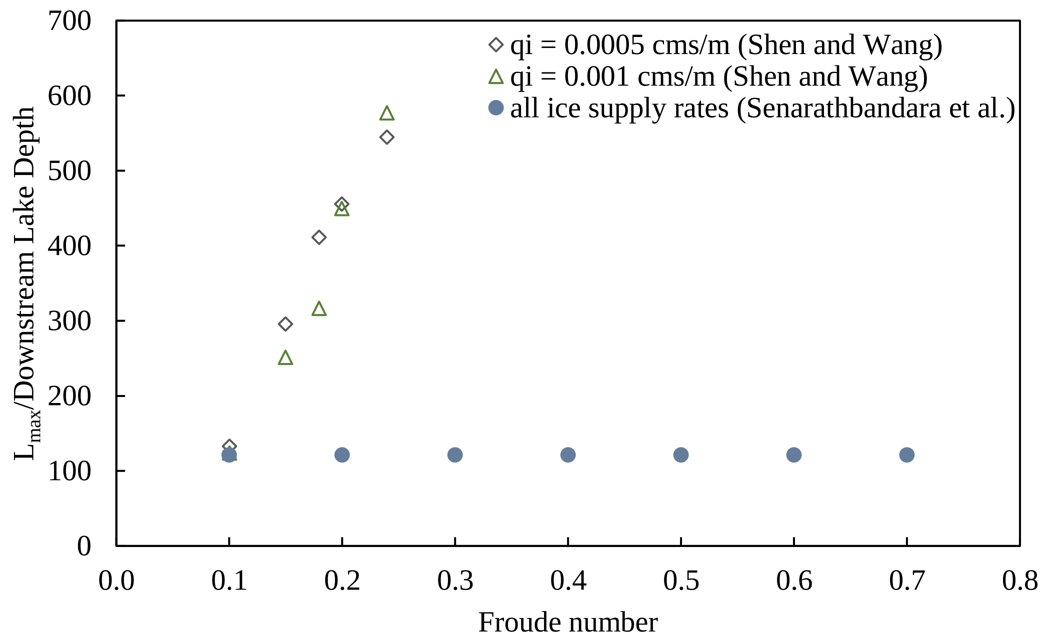


Figure 5.22 Location of maximum centerline thickness of the accumulation for geometry 1 model simulations for various approach Froude numbers and incoming ice supply rates.

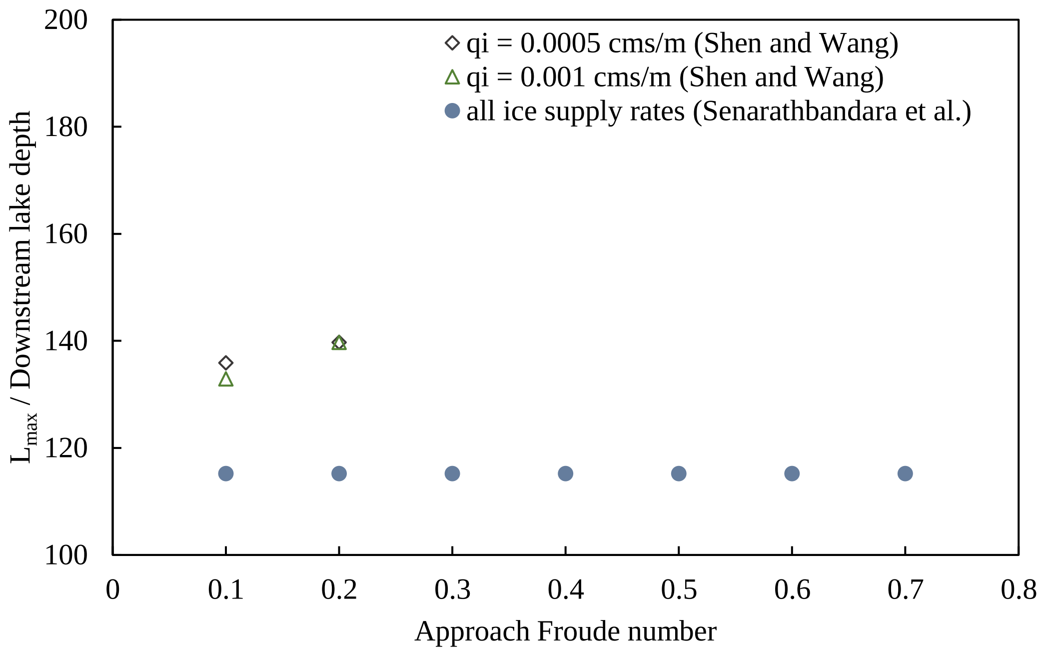


Figure 5.23 Location of maximum centerline thickness of the accumulation for mesh geometry 2 model simulations for various approach Froude numbers and incoming ice supply rates.

The trend of maximum thickness for $\Theta_c$= 0.396 simulations was similar to the laboratory experiments presented in Chapter 4, but the location of maximum thickness was not comparable to the experimental results. The ice deposition at the channel expansion interface did not undergo erosion due to the high critical flow strength of $\Theta_c$= 0.396 and the location of maximum thickness remained unchanged for all Froude number conditions for $\Theta_c$= 0.396 simulations. The ice accumulations for $\Theta_c$= 0.041 simulations were constantly evolving due to its low critical flow strength and the location of maximum thickness shifted downstream in the channel similar to the experimental results.

## 5.5 Conclusions

CRISSP2D model capabilities with respect to under cover ice transport and hanging dam formation using the existing numerical model formulation were analyzed in this chapter. The effect of incoming ice supply on under cover ice transport rate was evaluated by supplying various ice input rates for a range of flow strength conditions for an idealized channel. The model results showed that ice depositions occur at high incoming ice supply rates under low flow strength conditions since the flow is not capable of transporting the large quantity of ice coming from upstream. At low ice supply rates, the ice output from the model was closer to the ice supply from upstream, maintaining a condition closer to the equilibrium ice transport as the flow strength was adequate to transport the incoming ice supply. However, the deposition profiles generated by the model runs indicated model improvements are required to obtain a uniform ice deposition profile. The ice dynamic-hydrodynamic coupling time was identified as an important parameter that impacts the resulting ice deposition profile. Overall, the simulations showed that current numerical formulations in the CRISSP2D are capable of simulating under cover transport processes and the results are comparable to laboratory and field observations. It was determined that further numerical model formulations are required to improve the model response to varying incoming ice supply rates and enable the model to simulate the dynamic equilibrium and non-equilibrium conditions discussed in Chapter 3.

Under cover ice deposition was simulated in a channel with a channel expansion modelled as two different geometries to simulate a hanging dam formation using both the Shen and Wang (1995) and Senarathbandara et al. (2024) equations. The difference in hanging dam model results between the two equations highlighted the importance of critical dimensionless flow strength on deposition and erosion processes making a close comparison with the findings of Chapter 3. Geometry 1 simulations had thicker under cover depositions along the channel centerline compared to geometry 2 simulations, since the increased channel width in geometry 2 simulations allowed ice to transport in both streamwise and spanwise directions which reduced the ice thickness at the channel centerline. The model results show that critical dimensionless flow strength is an important parameter that has a significant effect on under cover transport processes. This parameter relates to the critical boundary shear stress which determines whether ice is depositing or eroding from a surface. Critical boundary shear stress depends on many factors including particle size, ice density, and the fall velocity coefficient. It is important to have an accurate estimate of these parameters when determining the $\Theta_c$ for a particular case/site. It is convenient to incorporate a customized $\Theta_c$ value which could fall within a range of possible flow strength values since this parameter can be easily changed through the parameter input file in CRISSP2D. The model simulations were conducted with two critical dimensionless flow strength values ($\Theta_c$ = 0.041 and $\Theta_c$ = 0.396). Model simulations with the higher $\Theta_c$ value showed a more concentrated deposition and formation of a hanging dam at the leading edge for longer duration model simulations. This is because the higher $\Theta_c$ had a high critical boundary shear stress value of 3.2 Pa, and the shear stress exerted on the ice cover boundary at the leading edge was lower than the critical value.

The analysis on the effect of Froude number on maximum hanging dam thickness and its location can be explained based on the effect of higher upstream channel velocity at high approach Froude numbers. The maximum thickness of the deposition decreased with increasing approach Froude number. A similar trend was observed in hanging dam laboratory results presented in Chapter 4. The higher upstream velocity at high approach Froude numbers transport ice away from the lake inlet resulting in a decrease in the thickness of the hanging dam accumulation.

# Chapter 6: Conclusions and Future Work

## 6.1 Summary and Conclusions

The first objective of this study was to develop a cover load transport formula using a series of comprehensive laboratory experiments. The effect of incoming ice supply rate on under cover ice transport processes was investigated to further understand under cover ice erosion and deposition processes. As the second objective, hanging dam physical properties (such as maximum centerline length, maximum width, maximum thickness and its location) were evaluated using a series of experiments in a laboratory physical model where water is issued from a narrow river to a wide lake. Lastly, the current numerical formulation of the under cover ice transport module in the CRISSP2D river ice numerical model was evaluated to assess the model capability to simulate under cover ice transport processes and hanging dam formation. The strengths of the model were identified along with a discussion on the ways to improve the current numerical formulation for under cover transport processes.

Chapter 1 presented an outline of the thesis with the motivation and background of the study, research objectives and the author's contributions to the research field.

Chapter 2 presented a literature review on under-cover ice transport processes, hanging dam formation and river ice numerical models capable of simulating under cover ice transport and hanging dam formation.

Chapter 3 presented a journal paper on the under cover ice transport laboratory experiments conducted to develop a cover load transport formula describing the relationship between dimensionless transport rate and dimensionless flow strength under equilibrium conditions. The formula was developed under uniform flow conditions under a range of flow strengths using HDPE pellets as simulated ice and bubble wrap as simulated ice cover. In the study, the critical dimensionless flow strength was determined by observing the incipient motion of HDPE pellets and was identified as an important parameter contributing to under cover transport rate estimation. A comparison of critical dimensionless flow strength was conducted for HDPE pellets and 1 mm diameter sand particles to highlight its dependency on particle size, density and buoyant velocity coefficient.

The relationship of equilibrium ice transport rate for a certain flow strength with the upstream ice supply was investigated in this paper. It was observed that the thickness of the initial ice cover remained constant without leading to major depositions when the incoming ice supply rate from upstream was equal to the equilibrium ice transport rate. There were no changes in the initial flow strength throughout the experimental duration since the under cover ice thickness did not change over time. Through a mass-balance analysis of a control volume it was determined the ice output rate from the reach (control volume) was equal to the ice supply rate to the reach from upstream.

The ice supply to the reach was varied to analyze the impact of incoming ice supply rate on dimensionless ice transport rate and dimensionless flow strength as well as deposition and erosion. When the incoming ice supply was lower than the equilibrium ice transport rate for a certain flow strength, the observed ice transport rates dropped below the line for equilibrium ice transport given by the developed cover load transport formula leading to erosion. Conversely, deposition occurred when the incoming ice supply was higher than the equilibrium ice transport rate. It was proposed that the developed cover load transport formula giving the equilibrium ice transport rate for a certain flow strength can be used as an initiation criterion for ice cover thickening and eventual hanging dam formation.

The laboratory experiments showed that flow strength tended towards the equilibrium flow strength when the ice supply was varied from the equilibrium ice supply rate. When the incoming ice supply rate was higher than the ice supply rate required for equilibrium, the ice thickness increased causing a net deposition in the flume. The water surface elevation and water surface slope increased due to ice depositions underneath the ice cover increasing the flow resistance. As a result, the dimensionless flow strength at the end of the experiment was higher than the initial dimensionless flow strength. When the incoming ice supply rate was lower than the equilibrium ice supply rate, there was continuous erosion of the ice cover which decreased the water surface elevation and water surface slope resulting in a reduction of resistance to flow. The dimensionless flow strength at the end of the experiment was lower than the initial dimensionless flow strength. An analysis of previously reported data from Hequ Reach (Wang, 1992) was presented in this paper which supported that the flow strength in a river has the potential to change when there is either insufficient ice supply or an abundant ice supply from upstream, making the conditions quite dynamic.

One of the main contributions of this chapter was the introduction of a cover load transport formula developed using laboratory experiments to estimate the equilibrium cover load transport for a certain flow strength condition in a river. The cover load transport formula presented in this chapter is known to be the only cover load formula that is developed exclusively using simulated ice that has similar physical properties to ice in a natural river. Introducing the concept of equilibrium ice transport rate using varying ice supply rate laboratory experiments to highlight the impact of incoming ice supply rate on ice transport rate can be recognized as a major contribution to the research field. This concept suggests the dynamic nature of under cover ice transport processes and was supported by experimental and field data on the change of flow strength when the incoming ice supply to a river is altered from the equilibrium ice supply rate. Altogether, the contributions of this chapter would help to improve and advance the present understanding on the under cover ice transport process which is one of the less investigated avenues of river ice research.

Chapter 4 of the thesis presented a journal paper on the hanging dam formation and evolution investigated using a laboratory experiment in a scaled-down physical model using HDPE pellets and bubble wrap as simulated ice and simulated ice cover, respectively. The effect of approach Froude number in the river and the incoming ice supply rate on hanging dam formation and evolution was analyzed using a series of experiments. It was observed that the hanging dam formed immediately or very close to the lake inlet at lower approach Froude numbers indicating that the low velocity of the river was not capable of transporting ice further downstream. At higher approach Froude numbers, the hanging dam accumulation formed further away from the lake inlet since the high velocity of the river did not allow ice deposition at the lake inlet.

The laboratory experiments showed that the maximum centerline length of the hanging dam for a certain ice volume increased with increasing approach Froude numbers while the maximum thickness of the hanging dam decreased with the increasing approach Froude numbers. The location of the maximum thickness of the hanging dam also shifted further downstream with increasing approach Froude numbers again demonstrating the high velocity effect of the river.

The aerial extent of the hanging dam was captured using a camera above the hanging dam flume, and the results showed the effect of incoming ice supply rate on the formation's aerial extent. For the same approach Froude number and the same total volume of simulated ice added to the model, the low incoming ice supply rates had a higher aerial extent compared to the high incoming ice supply rate experiments. The ice supply at low incoming ice supply rate experiments were not adequate to overcome the under ice erosion rate exerted by the flow of the river.

The hanging dam erosion caused by the high velocity of the river section exerting a high shear stress on the hanging dam accumulation was analyzed and discussed in this journal paper. The satellite imagery of the hanging dam at Dauphin River-Lake Winnipeg confluence was analyzed and compared to the laboratory results to provide a field insight to the phenomena. Satellite imagery from 2013 and 2023 of hanging dam formation downstream of Keeyask Generating Station was compared to observe a considerable reduction in the aerial extent of the hanging dam. The effects of flow control implemented by the generating station (i.e. lower Froude number) and cutoff of incoming ice supply by forming a competent ice cover upstream were identified and discussed as the main reasons for reduction in hanging dam size, highlighting the importance of considering the external factors that govern hanging dam formation.

This study on hanging dam formation and evolution relating the approach Froude number and incoming ice supply rate to the formation process is the first one of its kind in river ice research field. The observations of this study greatly improve the current state of knowledge of hanging dam formation and evolution process. The comparison of wall jet to hanging dam formation is beneficial for future efforts in numerical modelling related to hanging dam formation and evolution.

Chapter 5 of the thesis presented an evaluation of the under cover transport module of the CRISSP2D river ice numerical model with an emphasis on model capabilities to simulate under cover ice transport and hanging dam formation processes. While CRISSP2D is one of the most advanced river ice numerical models with the capability of simulating multitude of river ice processes, the under cover transport module is one of the least investigated components of the model. The main objectives of this chapter were to evaluate the current model formulation for under cover transport processes and hanging dam formation, to identify model strengths, and to propose modifications to improve the CRISSP2D model.

The laboratory experiments presented in Chapter 3 and Chapter 4 for under cover ice transport and hanging dam formation were used as the basis for numerical model simulations presented in this chapter. The model simulations for under cover ice transport processes were conducted using uniform flow conditions, and the effect of incoming ice supply on ice transport rate was tested by varying the ice input rate for a range of flow strength conditions. There were ice depositions in the channel, at high incoming ice supply rates under low flow strength conditions since the flow strength in the channel was not adequate to transport the large quantity of incoming ice. The ice output rates were closer to the ice input rate from upstream at low ice supply rates maintaining a condition closer to the equilibrium ice transport. The ice deposition profiles for uniform flow model runs suggested a possible improvement area of the model, since the depositions for current model simulations indicated a wave pattern of deposition that is related to under cover transport velocity and a user defined coupling time parameter. It was identified that the CRISSP2D model requires additional numerical formulations to simulate the dynamic equilibrium and non-equilibrium conditions that were introduced in Chapter 3, when the incoming ice supply to the model deviates from the equilibrium ice supply determined by the under cover transport equation.

The effect of critical dimensionless flow strength on hanging dam formation and evolution was investigated using an ideal channel with a channel expansion. Shen and Wang (1995) and Senarathbandara et al. (2024) cover load transport equations were used for the hanging dam model simulations. The critical dimensionless flow strength of the two equations has an order of magnitude difference, which can cause a significant difference in the predicted amount of erosion when the actual dimensionless flow strength is somewhere between these two critical values. The effect of critical dimensionless flow strength on deposition and erosion processes was clearly highlighted in the numerical model results. Simulations using the Senarathbandara et al. (2024) equation led to a thick hanging dam formation whereas Shen and Wang (1995) model simulations underwent continuous erosion as expected based on the much lower critical dimensionless flow strength. These model observations can be related to the findings presented in Chapter 3, where the critical dimensionless flow strength of HDPE pellets (simulated ice) was compared to 1 mm diameter sand particles to highlight the effect of specific gravity and fall/buoyant velocity on critical dimensionless flow strength. The model simulations on the effect of approach

Froude number on hanging dam physical properties demonstrated the impact of higher velocity of the upstream channel on the hanging dam accumulation. At higher approach Froude numbers, the higher velocity of the jet caused ice to transport further away from the lake inlet resulting in a decrease in the thickness of the hanging dam accumulation.

The following publications resulted from the work presented in the thesis. The first journal publication is on the further development of a cover load transport formula exclusively using laboratory experiments with simulated ice and ice cover. The paper also introduced the concept of equilibrium and non-equilibrium transport based on laboratory experiments and field data. The second journal publication is on hanging dam formation and evolution processes that is based on a series of laboratory experiments to investigate the effect of incoming ice supply rate and approach Froude number on hanging dam physical properties. The third, fourth and fifth publications are conference proceedings that were supplementary to the main findings of the journal publications. The third publication provided detailed methodology for obtaining the hanging dam physical properties using photogrammetry and it is presented in Chapter 4. The fourth publication is on the preliminary numerical model results of CRISSP2D numerical model for under cover ice transport and hanging dam simulations which is included in the model development of Chapter 5. The fifth publication is on laboratory experiments that were conducted for under cover ice transport and sediment transport.

- Senarathbandara R., Clark S.P., Dow K. (2024). Under Cover Ice Transport Processes under Equilibrium and Non-equilibrium Conditions. Cold Regions Science & Technology. Volume 219, 104124.

- Senarathbandara, R., Clark, S.P., Dow, K. (2023). Experimental Analysis on Hanging Dam Formation and Evolution. Water, 15, 4242.
- Senarathbandara R., Clark S.P., Dow K. (2023). Investigating the Effect of Incoming Ice Supply Rate on Hanging Dam Formation. 22nd Workshop on Hydraulics of Ice Covered Rivers, Canmore, Alberta, Canada.
- Senarathbandara R., Clark S.P., Dow K., Lees K. (2022). Numerical Simulation of Under Cover Ice Transport Processes and Hanging Dam Formation. 26th IAHR International Symposium on Ice. Montreal, Quebec, Canada.
- Senarathbandara, R., Clark, S.P., Dow, K. (2021). Laboratory Investigation on Under Cover Ice Transport Processes. 21st CRIPE Workshop on the Hydraulics of Ice Covered Rivers. Saskatoon, Saskatchewan, Canada.

## 6.2 Future Work

The recommendations for future work for laboratory and numerical components of this research are presented in the following sections.

### 6.2.1 Laboratory Experiments

1. Under cover ice transport rates for various flow conditions were quantified by volumetric measurements in this study. It would be beneficial to measure the velocity of an ice particle (HDPE pellet) along the ice-water boundary for different flow conditions. This velocity can be compared with the velocity calculated from the volumetric measurements and can be used to improve the velocity representation in the CRISSP2D numerical model.

2. Considering the difficulties of conducting a field study on hanging dam formation, obtaining the velocity measurements underneath the hanging dam formation in a laboratory experiment would be a significant contribution to the current knowledge state on hanging dam formation processes. Velocity underneath the ice cover (bubble wrap) and the velocity under the hanging dam formation were obtained using an acoustic Doppler velocimeter during preliminary stages of this study. However, the intrusive nature of these measurement techniques disrupted the hanging dam formation process. Non-intrusive measurement techniques like Large Scale Particle Image Velocimetry (LSPIV) can be adapted to quantify the surface velocities of the hanging dam formation based on the opaque nature of the bubble wrap. Under cover velocities will be a significant contribution to the knowledge of hanging dam formation and evolution processes.

### 6.2.2 Numerical Modelling

1. The importance of coupling time parameter is highlighted in Chapter 5 model results. Typically, the coupling time parameter of a CRISSP2D simulation is set to 900s (15 mins) to ensure fast computational time for a model run. The under cover transport simulations showed that 15 minutes is a substantially large coupling time to capture the dynamic nature of ice transport processes. The sensitivity analysis of under cover ice thickness variation with coupling time showed that by utilizing a small coupling time interval, the model can simulate ice deposition for a given flow strength. But the model had difficulty running at a low coupling time steps due to ice accumulation at model boundaries. While this issue was related to the model's treatment of ice at the boundaries instead of under cover ice transport processes itself, it is important to address this issue in order to improve the model capability

to generate an accurate ice deposition profile. Considering alternate numerical formulations to transport and deposit parcels over a coupling timestep would be beneficial to improve the under cover transport module in the CRISSP2D model.

2. The current numerical formulation for under cover transport velocity in the CRISSP2D model is based on the van Rijn (1984) sediment velocity formula. The current model formulation of using a sediment velocity formula for ice velocity estimation was justified based on the assumption that van Rijn (1984) formula takes density into account. There are certain differences between cover load and bed load transport processes despite the analogous nature of the two processes. Therefore, it is important to experimentally determine the under cover transport velocity to be used in the CRISSP2D model for under cover transport numerical model simulations for an accurate representation of this dynamic, natural process.

3. The performance of the CRISSP2D model with respect to under cover ice transport and hanging dam formation can be assessed by comparing the numerical model results to the laboratory experiment results presented in Chapter 3 and 4 of the thesis. Simulating under cover ice transport and hanging dam formation using a numerical model of the laboratory experiment setup would help to directly compare the processes. A field study with extensive amounts of data can also be used to assess the performance of the model in a natural environment. As discussed in Chapter 2, the frazil ice transport rates were quantified using field data and a complete heat budget approach in the field study at St. Raymond reach hanging dam of St. Anne River, Quebec by Vergeynst, Morse and Turcotte (2017). This study can be potentially used to evaluate the performance of CRISSP2D model. Similarly, a new field program can be designed at a suitable site to collect the

required data to compare numerical modeling results to field data from a natural river to evaluate the model performance.

4. Model simulations can be set up to investigate the model's capability to simulate the hanging dam erosion process. Simulations can be set up with an initial accumulation of ice parcels beneath a stable ice cover (simulating a hanging dam) and the water discharge to the model can be increased gradually to observe erosion under various flow conditions.

## References

Agisoft Metashape Professional Edition (Version 1.5) [Computer Software], 2019 Agisoft LLC.: St. Petersburg, Russia.

Aquaveo LLC., 2021. Surface-water Modeling System (Version 13.1) [Software]

Ashton, G.D., 1974. Froude criterion for ice block stability. J. of Glaciology 13: 307-313.

Badhan, M. A. 2020. An Experimental Investigation of Hanging Dam Formation. M.Sc. Thesis, University of Manitoba, Winnipeg, MB, Canada.

Bagnold, R.A., 1956. The flow of cohesionless grains in fluids. Philosophical Transactions. Royal Society, London, England, Series A, Vol 249, 235-297.

Bagnold, R. A., 1966. An approach to the sediment transport problem from general physics. Geological Survey Profile. Paper 422-I, U.S. Geological Survey, Washington, D.C.

Bagnold, R. A., 1973. The nature of saltation and of 'bed-load' transport in water. Philosophical Transactions. Royal Society, London, England, Series A, Vol 332, 473-504.

Beltaos, S., Dean, A.M., 1981. Field investigations of a hanging dam. In Proceedings of the IAHR Symposium on Ice, Quebec, QC, Canada, 27–31 July.

Beltaos, S., 2013. Ice Cover Formation. In River Ice Formation; Beltaos, S., Ed.; Committee on River Ice Processes and the Environment; Canadian Geophysical Union, Hydrology Section : Edmonton, AB, Canada, 181–251.

Blackburn, J., She, Y., 2019. A comprehensive public-domain river ice process model and its application to a complex natural river. Journal of Cold Regions Science and Technology, 163 (2019), 44-58. https://doi.org/10.1016/j.coldregions.2019.04.010

Bourgault, D.; Richards, C., Pawlowicz, R. A Matlab Package for Georectifying Oblique Digital Images (grect). Retrieved from GitLab. Available online: http://demeter.uqar.ca/g_rect/index.php/A_Matlab_package_for_georectifying_oblique_digital_images_(g_rect) (accessed on 10 May 2023).

Chien, N., 1956. The present status of research on sediment transport. Transactions, ASCE, Vol. 121.

Chien, N., 1980. A comparison of the bed load formulas. Journal of Hydraulic Engineering, Chinese Hydraulic Engineering Society, Beijing, No 4, 1-11.

Clark, S.P., Wall, A., 2016. Freeze-up monitoring on the Dauphin River, Manitoba, Canada. In Proceedings of the 23rd International Symposium on Ice, Ann Arbor, MI, USA, 31 May–3 June.

Coleman, H. W., & Steele, W. G., 1999. Experimentation and Uncertainty Analysis for Engineers (2nd ed.). Wiley.

Daly, S., 1984. Frazil ice dynamics (CRREL Monograph 84-1). Hanover, USA.

Gebre, S., Alfredsen, K., Lia, L., Stickler, M., & Tesaker, E., 2013. Review of Ice Effects on Hydropower Systems. Journal of Cold Regions Engineering, 27(4), 196–222. https://doi.org/10.1061/(ASCE)CR.1943-5495.0000059.

Gold, L.W., Williams, G.P., 1961. An unusual ice formation on the Ottawa River. J. Glaciol. 4, 569–573.

Groeneveld, J., Malenchak, J., Morris, M., 2017. Numerical Model Studies of Ice Conditions during the Design and Construction of the Keeyask Generating Station. In Proceedings of the 19th Workshop on the Hydraulics of Ice Covered Rivers, Whitehorse, Yukon, Canda, 9–12 July.

Groenevald, J., Damov, D., Snyder, G., O'Brien, S., 2022. Ice Management at the Muskrat Falls Project Before, During and After Construction. Proc. Canadian Dam Association Annual Conference, 17-19 October, St. John's, Newfoundland, and Labrador.

Hicks, F., 2009. An overview of river ice problems: CRIPE07 guest editorial. Cold Regions Science and Technology. 55(2), pp. 175–185. https://doi.org/10.1016/j.coldregions.2008.09.006.

Hopper, H.R., Raban, R.R., 1980 Hanging dams in the Manitoba Hydro system. In Proceedings of the Workshop on River Ice, Burlington, ON, Canada, 23–24 September; pp. 195–208.

ImageJ (Version 1.51) [Computer Software], 2018. National Institutes of Health and Laboratory for Optical and Computational Instrumentation (LOCI), University of Wisconsin: Madison, WI, USA.

KGS Group; North/South Consultants, 2014. Emergency Reduction of Lake Manitoba and Lake St. Martin Water Levels; Manitoba Infra-structure and Transportation: Winnipeg, MB , Canada.

Kivisild. H.R., 1959. Hanging ice dams. In Proceedings of the 8th Congress International Association for Hydraulic Research, Mon-treal, QC, Canada, 24–29 August, Volume 2, paper no. 23-F,-1-30.

Lal. A.M.W., Shen. H.T., 1990. Mathematical Model for River Ice Processes. Journal of Hydraulic Engineering. 117 (7), 851-867.

Launder, B.E., Rodi, W., 1981. The turbulent wall jet. Prog. Aerosp. Sci. 19, 81–128.

Lees, K.; Clark, S.P., Malenchak, J., Chanel, P., 2021. Characterizing ice cover formation during freeze-up on the regulated Upper Nelson River, Manitoba. Journal of Cold Regions Engineering, 35, 04021009.

Liu, L., Shen, H.T., 2011. CRISSP2D Version 1.1 Programmer's Manual. CEATI Report T012700-0401. Potsdam, New York, USA.

MacLachlan, D. W., 1926. Appendix E. In St. Lawrence Waterways Project Report; Joint Board of Engineers: Ottawa, Canada.

Peters, M. R., Clark, S. P., Dow, K., Malenchak, J., & Danielson, D., 2018. Flow Characteristics beneath a Simulated Partial Ice Cover: Effects of Ice and Bed Roughness. Journal of Cold Regions Engineering, 32(1). https://doi.org/10.1061/(ASCE)CR.1943-5495.0000143

Rijn, L.C. van, 1984. Sediment transport, Part I: bed load transport. Journal of Hydraulic Engineering, 110(10), pp. 1431-1456.

Rubey, W.W., 1993. Settling velocities of gravel, sand, and silt particles. American Journal of Science, 25(148), 325-338.

Senarathbandara, R., Clark, S.P., & Dow, K., 2021. Laboratory Investigation of Under Cover Ice Transport Processes, Proc. 21st Workshop on the Hydraulics of Ice Covered Rivers, Saskatoon, Saskatchewan, Canada.

Senarathbandara, R., Clark, S.P., & Dow, K, 2023. Investigating the effect of incoming ice supply rate on hanging dam formation. Proc. 22nd Workshop on the Hydraulics of Ice Covered Rivers, Canmore, AB, Canada, 9–13 July.

Shen, H. T. & Van Devalk, W.A., 1984. Field investigation of St. Lawrence River hanging dams. Proc. IAHR Symposium, Hamburg, Germany. 241-249.

Shen, H. T. & Wang, D. S., 1995. Under Cover Transportation and Accumulation of Frazil Granules, Journal of Hydraulic Engineering, 121(2), pp. 184–195.

Shen, H.T., 2000. River ice transport theories: past, present, and future. Proc. IAHR Ice Symposium, Gdansk. Vol. 2, 29–40.

Shen, H.T., 2002. Development of a Comprehensive River Ice Simulation System, in: Ice in the Environment: Proceedings of the 16th IAHR International Symposium on Ice. International Association of Hydraulic Engineering and Research, Dunedin, New Zealand.

Shen, H.T., Liu, L. and Chen, Y.-C., 2001. River ice dynamics and ice jam modeling. In Scaling Laws in Ice Mechanics and Ice Dynamics, Proc. IUTAM Symposium, Kluwer Academic Publishers 349–362

Shen, H.T., Wang, D.S., Lal, a. M.W., 1995. Numerical Simulation of River Ice Processes. J. Cold Reg. Eng. 9, 107–118. doi:10.1061/(ASCE)0887-381X(1995)9:3(107)

Sui, J., Hicks, F.M., Menounos, B., 2006. Observations of river bed scour under a developing hanging dam. Can. J. Civ. Eng. 33, 214-218.

Sun, Z., Yang, S. & Yao, K., 1986. Prototype observation and study of ice jam at Hequ section of the Yellow River. Proc. of IAHR Symposium, Iowa City, Iowa, Vol. II, 39-48.

Swamee, P.K., Ojha, C.S.P., 1991. Drag coefficient and fall velocity of non-spherical particles. Journal of Hydraulic Engineering, 117(5), 660-667.

Tatinclaux, J-C., Gogus , M., 1981. Stability of ice floes below a floating cover. Proc. 6th IAHR International Ice Symposium, Quebec City, Canada, Vol. 1: 298-311.

Tesaker, E., 1975. Accumulation of frazil ice in an intake reservoir. Proc. 3rd International Symposium on Ice Problems. Hanover, NH. 25-35.

Uzuner, M.S., 1977. Stability analysis of floating and submerged ice floes. ASCE J. of the Hydraulics Division 103: 713-722.

USGS Sentinel-2 EarthExplorer. Available online: https://apps.sentinel-hub.com/sentinel-playground (accessed on 7 June 2023).

USGS Landsat EarthExplorer. Available online: https://earthexplorer.usgs.gov (accessed on 8 June 2023).

Vergeynst, J., Morse, B., Turcotte, B., 2017. Quantifying frazil production, transport and deposition in a gravel-bed river: Case study of the St. Raymond hanging dam. Cold Reg. Sci. Technol. 141, 109–121.

Wang, D.S., 1992. Frazil Jam Evolution and Transport of Low Density Granules. Master’s thesis, Lulea University of Technology.

Wang, J., Wu, Y., Sui, J., Karney, B., 2019. Formation and Movement of Ice Accumulation Waves Under Ice Cover – An Experimental Study. J. Hydrol. Hydromech., 67, 2, 171-178.

Wazney, L.E., 2019. Investigation of River Ice Cover Formation Processes at Freeze-Up. Ph.D. Thesis, University of Manitoba, Winnipeg, MB, Canada.

Wu, W., and Wang, S.S.Y. (2006) Formulas for sediment porosity and settling velocity. Journal of Hydraulic Engineering, ASCE, 132(8), pp. 858-862.

Zbigniewicz, H.S., 1997 Lake Winnipeg Regulation Ice Stabilization Program. In Proceedings of the Workshop on River Ice, Fredericton, NB, Canada, 24–26 September; pp. 43–53.

# Appendix A Mesh Sensitivity Analysis

A mesh discretization sensitivity analysis was conducted using three finite element meshes as listed in Table A.1 given below. The finite element mesh had a length of 10 km, and a width of 200 m. The first 1 km of the channel was set up as an open water section and the ice-covered section was set from 2 km to 10 km with a stationary ice cover of thickness 0.01 m.

Table A.1. Mesh categories for sensitivity analysis.

| Mesh Category | Streamwise Discretization (m) | Spanwise Discretization (m) | Number of nodes | Number of elements |
|---|---|---|---|---|
| **Fine** | 10 | 20 | 10511 | 20000 |
| **Medium** | 50 | 20 | 2111 | 4000 |
| **Coarse** | 100 | 20 | 1061 | 2000 |

$Q_w$ = 350 $m^3/s$ and $Q_{in}$ = 0.5 $m^3/s$ were used as the upstream boundary conditions. The normal depth for a water discharge of 350 $m^3/s$ was used as the downstream boundary condition. The water surface elevation for the downstream boundary condition was determined according to the Manning's equation according to the methodology presented in section 5.3 in the thesis.

The mass of under cover ice parcels entering the model domain (ice covered section of the channel) and the mass of under cover ice parcels exiting the model domain for the three mesh categories are shown in Figure A.1 and Figure A.2, respectively. The model results for fine and medium meshes are closely comparable, while the results for coarse mesh deviate from the fine and medium meshes.

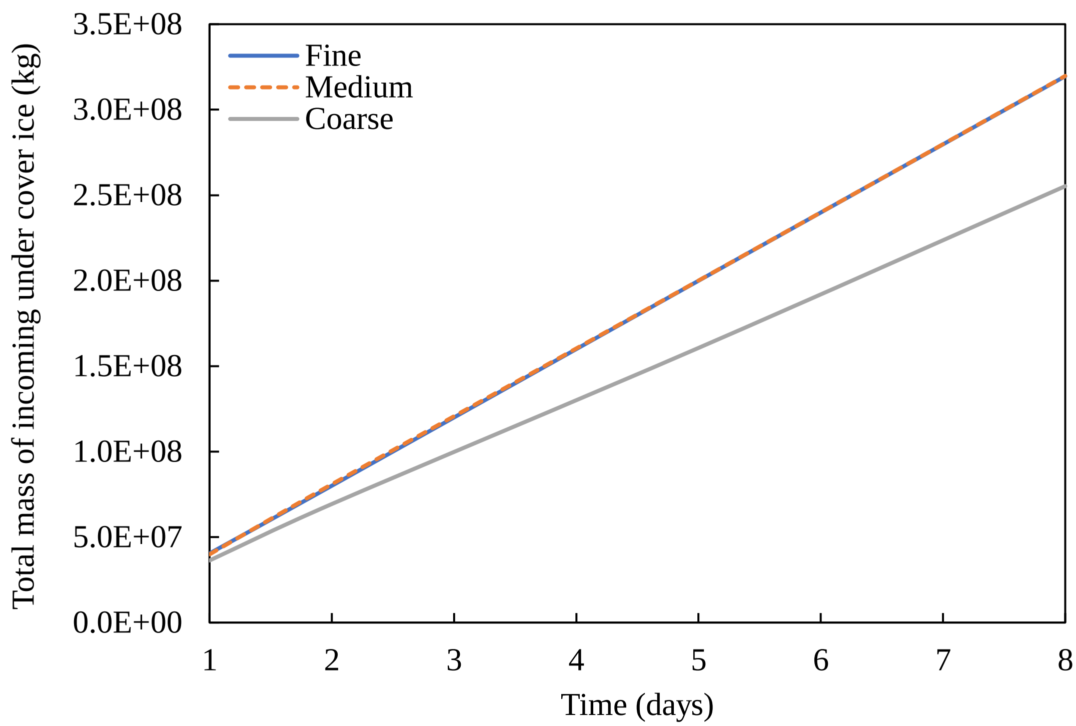


Figure A.1. Total mass of incoming under cover ice entering the model domain.

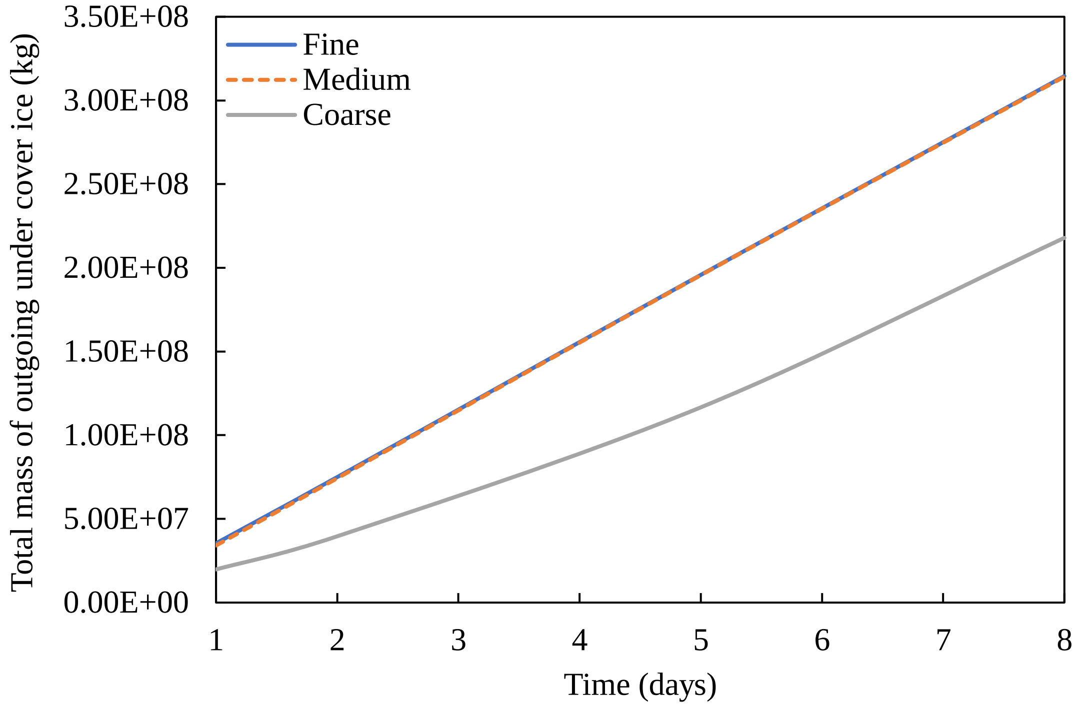


Figure A.2. Total mass of outgoing under cover ice exiting the model domain.

The simulation time to run a 24-hour simulation for each of the mesh categories is summarized in Table A.2 below.

Table A.2. Simulation time for a 24-hour simulation for different mesh categories.

| Mesh Category | Time (hours) |
|---|---|
| **Fine** | 5.5 |
| **Medium** | 1.0 |
| **Coarse** | 0.5 |

Based on the model accuracy and computational efficiency, the medium mesh with 50 m streamwise and 20 m spanwise spatial discretization was selected for the model simulations presented in the thesis.

# Appendix B Plan View of Hanging Dam

The plan view of hanging dam for $\Theta_c$= 0.041 and $\Theta_c$= 0.396 simulations with Qi = 0.1 and 1.0 m$^3$/s for both geometry 1 and 2 at 15 min coupling time step are presented in the following figures.

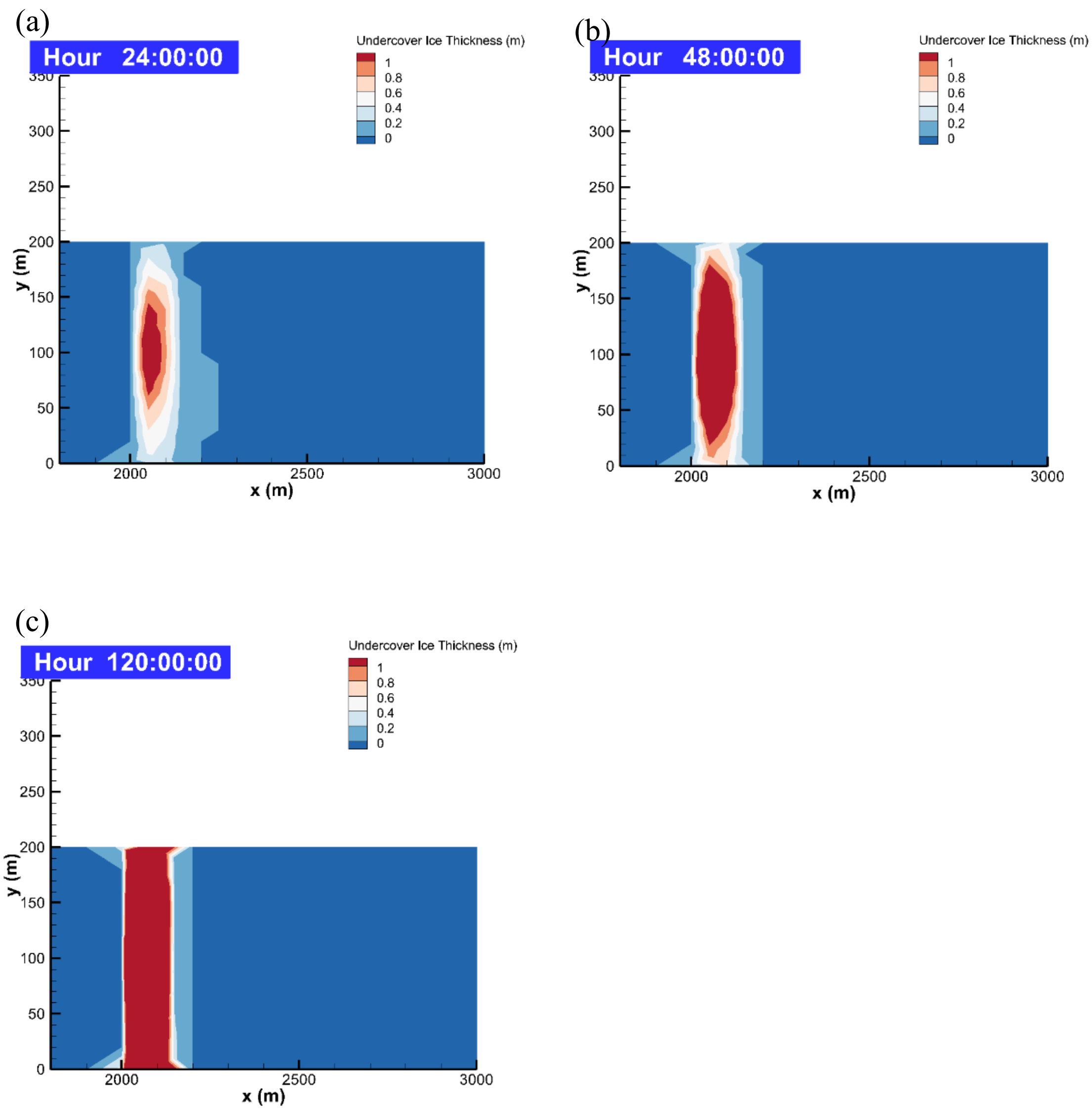


Figure B.1. Plan view of the hanging dam for geometry 1 (ice cover at 2.0 km), Qi = 0.1 m$^3$/s for $\Theta_c$= 0.396 simulations.

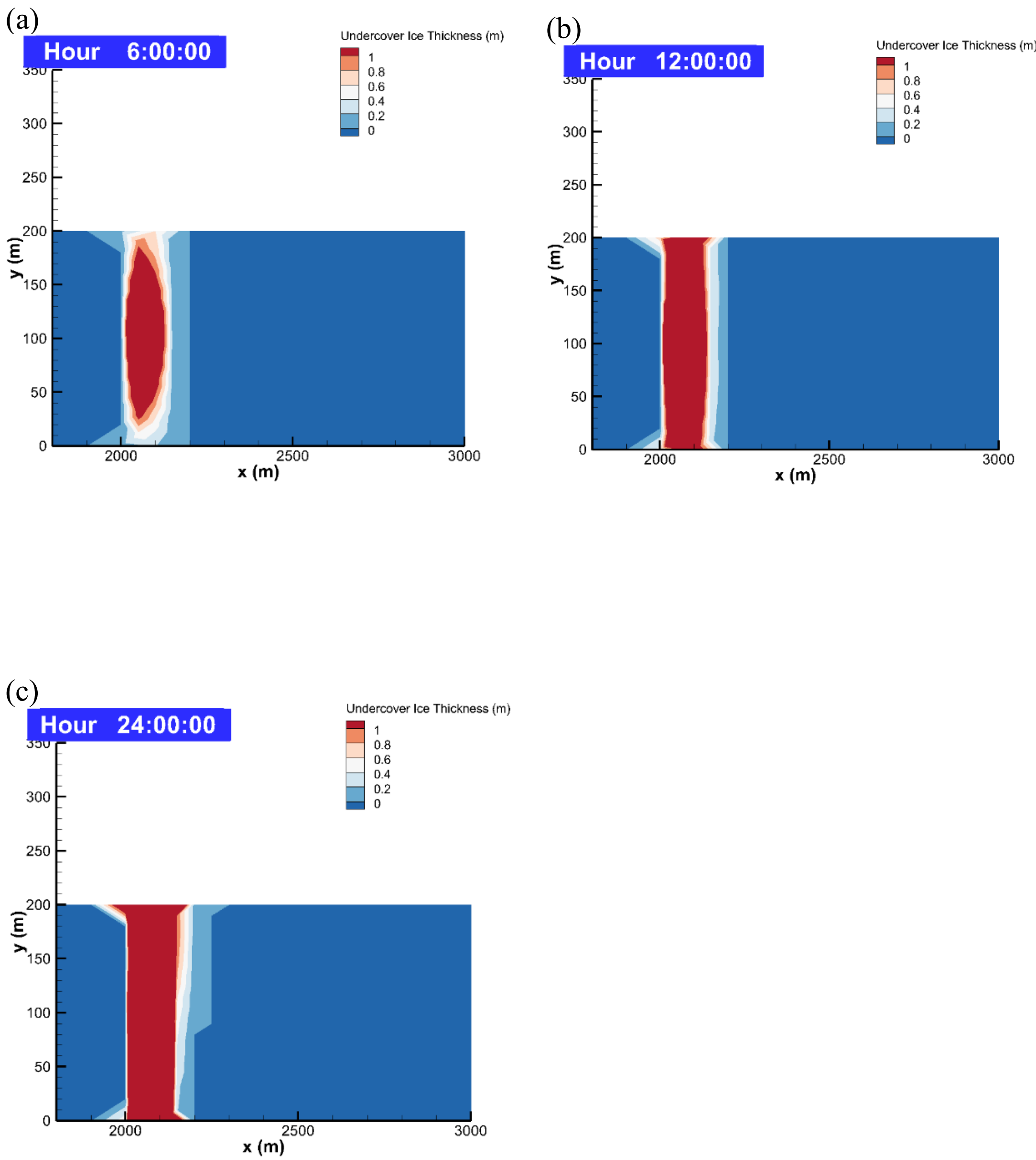


Figure B.2. Plan view of the hanging dam for geometry 1 (ice cover at 2.0 km), Qi =1.0 $m^3/s$ for $\Theta_c$= 0.396 simulations.

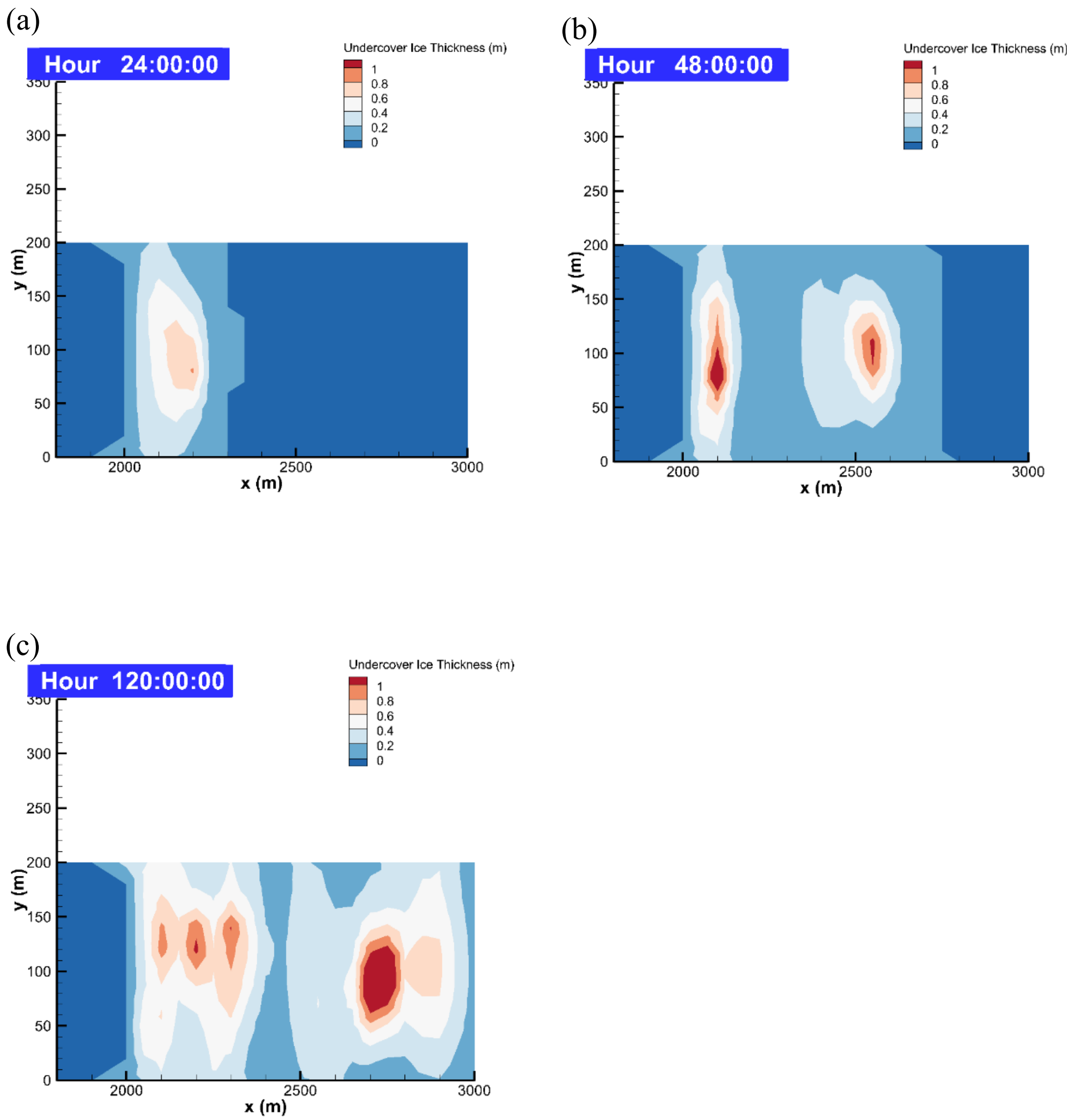


Figure B.3. Plan view of the hanging dam for geometry 1 (ice cover at 2.0 km), Qi = 0.1 $m^3/s$ for $\Theta_c$= 0.041 simulations.

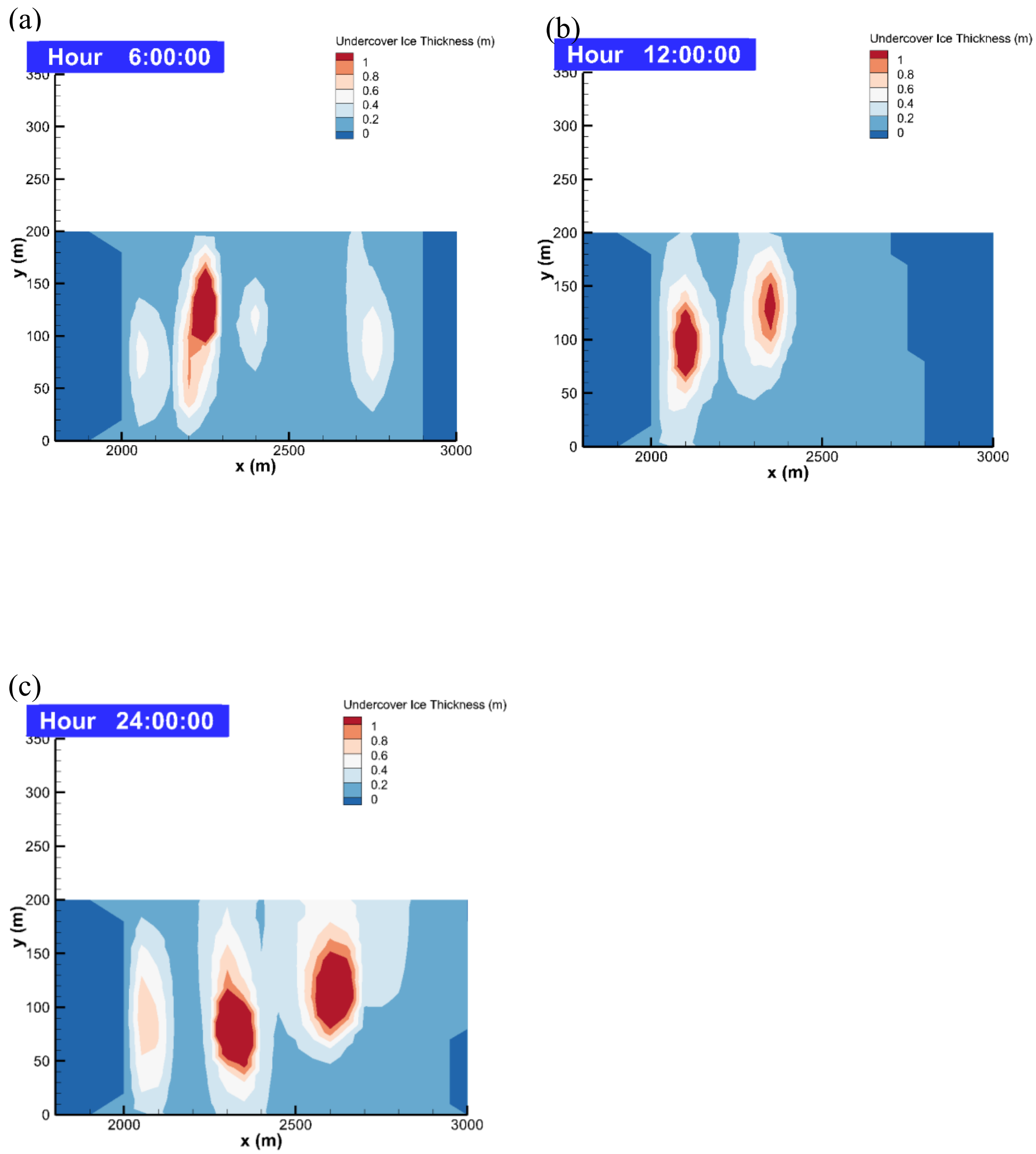


Figure B.6. Plan view of the hanging dam for geometry 1 (ice cover at 2.0 km), Qi =1.0 m$^3$/s for $\Theta_c$= 0.041 simulations.

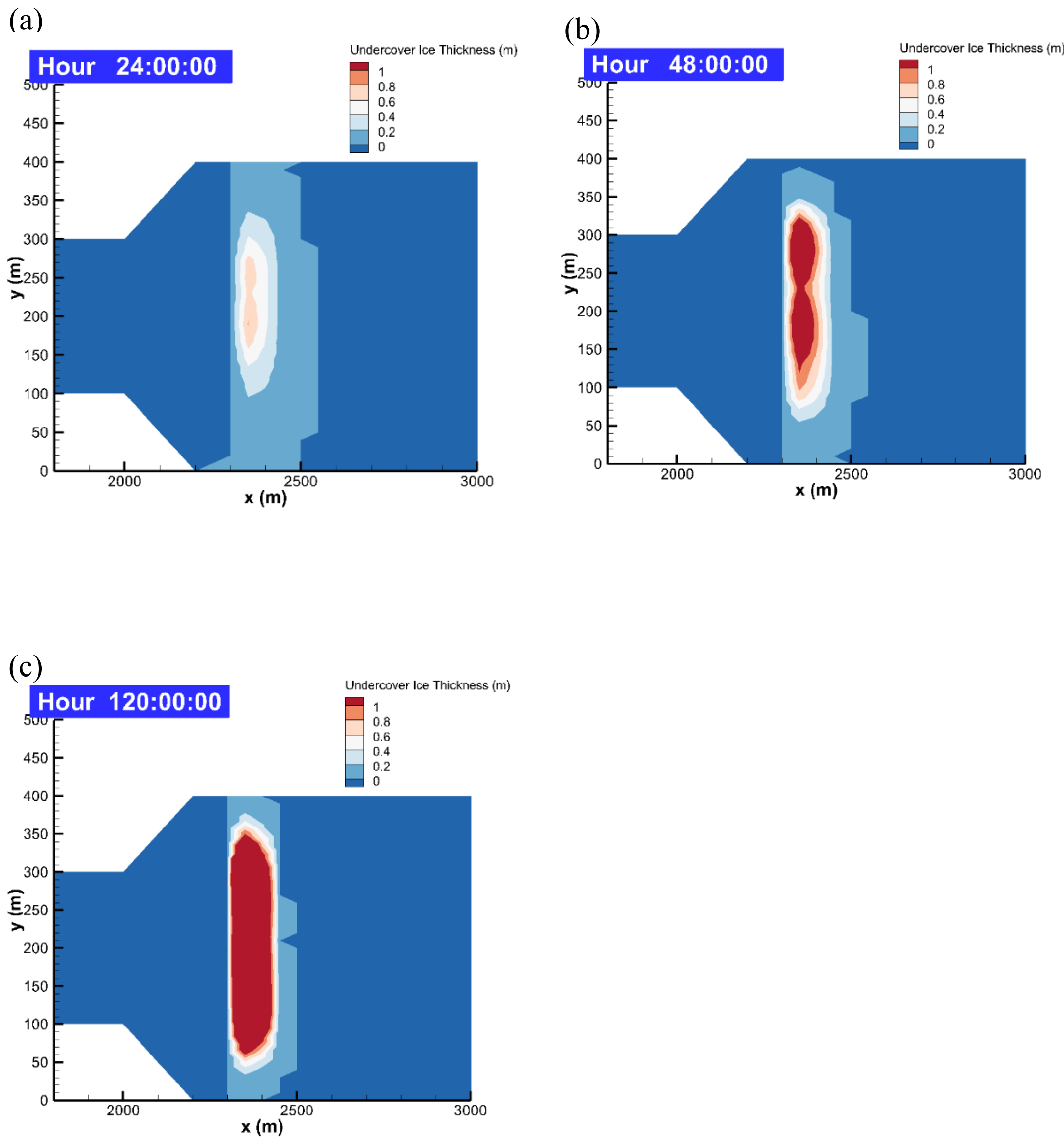


Figure B.5. Plan view of the hanging dam for geometry 2 (ice cover at 2.4 km), Qi = 0.1 $m^3/s$ for $\Theta_c$= 0.396 simulations.

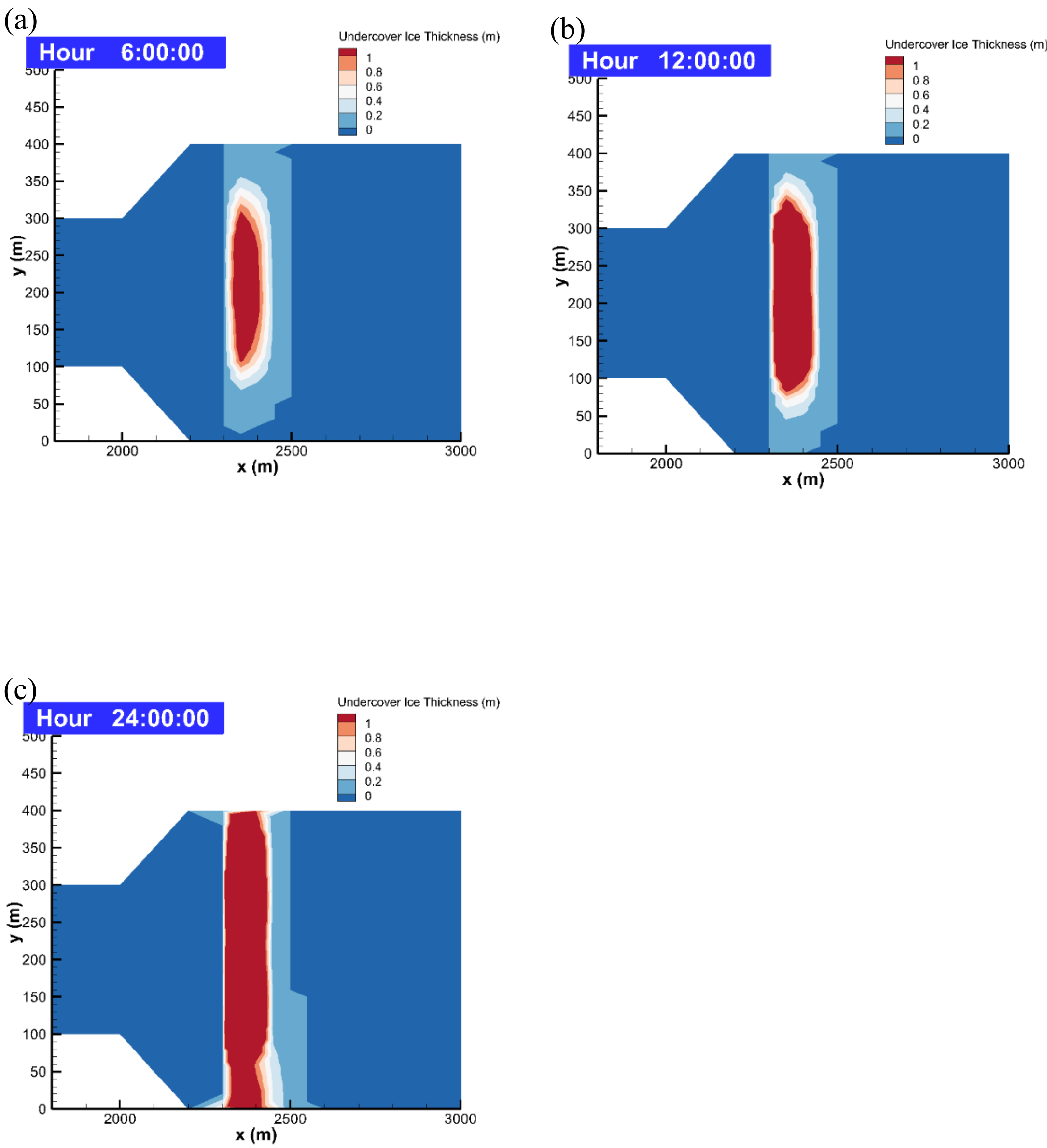


Figure B.6. Plan view of the hanging dam for geometry 2 (ice cover at 2.4 km), Qi =1.0 $m^3/s$ for $\Theta_c$= 0.396 simulations.

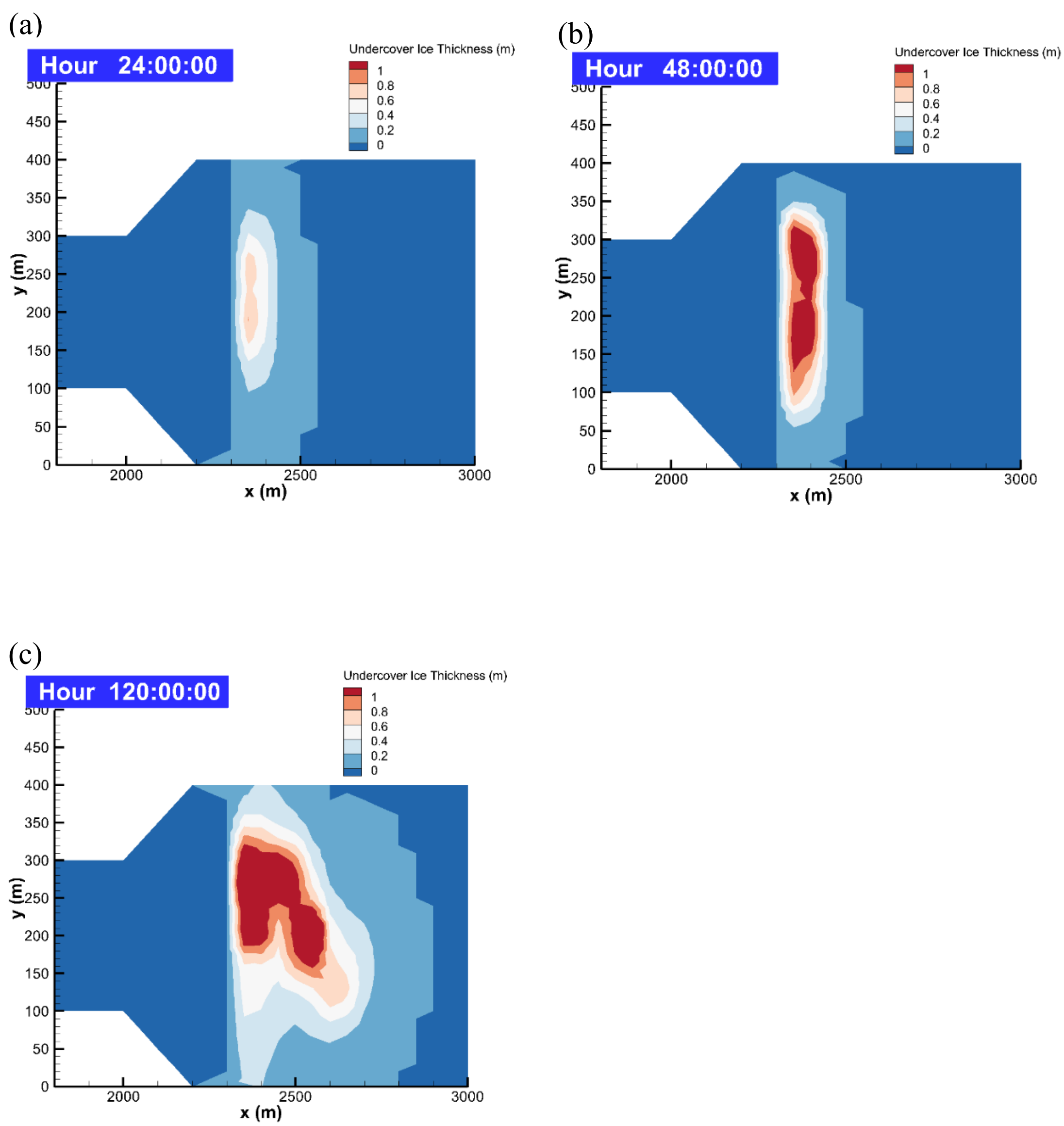


Figure B.7. Plan view of the hanging dam for geometry 2 (ice cover at 2.4 km), Qi = 0.1 $m^3/s$ for $\Theta_c$= 0.041 simulations.

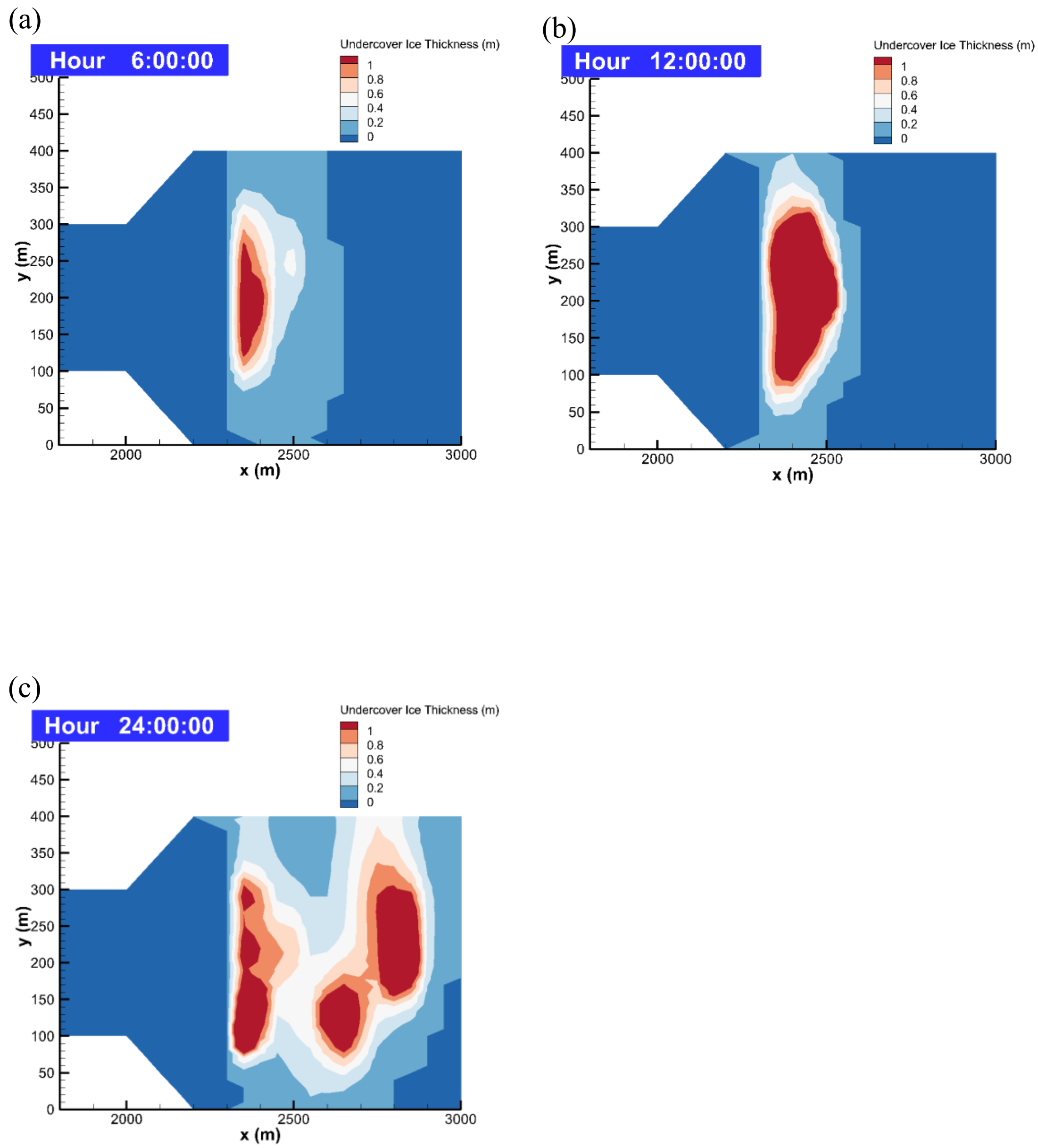


Figure B.8. Plan view of the hanging dam for geometry 2 (ice cover at 2.4 km), Qi =1.0 $m^3/s$ for $\Theta_c$= 0.041 simulations.